

Self-Assembling Peptide Hydrogels for Articular Cartilage Repair

James Phillip Warren

Submitted in accordance with the requirements for the
degree of Doctor of Philosophy

The University of Leeds

School of Mechanical Engineering

January 2017

The candidate confirms that the work submitted is his/her own. The candidate confirms that appropriate credit has been given within the thesis where reference has been made to the work of others.

This copy has been supplied on the understanding that it is copyright material and that no quotation from the thesis may be published without proper acknowledgement.

© 2017 The University of Leeds and James Phillip Warren

The right of James Phillip Warren to be identified as Author of this work has been asserted by him in accordance with the Copyright, Designs and Patents Act 1988

Acknowledgments

Firstly I would like to say thank you to my supervisor, Dr Stuart Warriner, for his infinite patience and support. His knowledge and guidance over the past three years has made this work possible. Hopefully from now on I will get a ChemDraw structure correct first time. I would also like to express my gratitude to my co-supervisors, Professor Eileen Ingham and Professor John Fisher CBE, for their amazing support, guidance and patience during my PhD. Without them, this work would also not have been possible. My supervisory team was made up of truly inspirational people, whom I will forever be indebted to for everything over these past three years.

Secondly I would like to thank various lab groups across different faculties for their support throughout my PhD. The various members of iMBE, along with the members of the group in lab 1.49 and 3.13 in the School of Chemistry, whom have helped me in some way have enabled me to survive my PhD with some of my sanity still intact, specifically Tom, Ivona, Zoe and Dan. Special acknowledgements go to Dr Phil Davies and Dr Hazel Fermor for their support over the years and the patience to listen and correct my ramblings and misconceptions.

Thirdly I would like to thank my family and friends, in particular my girlfriend Emma, mum, dad and brother, whom have been an ever present source of encouragement, support and understanding. Without them I would not have been able to accomplish this work for which I am eternally grateful.

Finally, I would like to thank the EPSRC for funding my PhD through the Doctoral Training Centre for Tissue Engineering and Regenerative Medicine (DTC-TERM) whom gave me the chance to undertake this body of work.

Abstract

Osteoarthritis affects millions of people globally, with damage to articular cartilage causing pain and altered mechanics during articulation. The treatment for late stage osteoarthritis is surgical intervention ultimately leading to total joint replacements. These treatments are not ideal for younger or more active patients so there is a clinical need for an early stage intervention treatment to reduce or stop the progression of osteoarthritis. It has been reported that there is a correlation between the loss of glycosaminoglycans (GAGs) from within osteoarthritic cartilage and the changes in biomechanics of the cartilage. It is hypothesized that the re-introduction of GAGs into early stage osteoarthritic cartilage through the use of permanent linkage and integration into a self-assembling peptide hydrogel matrix which could penetrate the cartilage tissue would potentially restore the resistance to deformation observed in osteoarthritic cartilage.

Initially synthetic self-assembling peptide-chondroitin sulfate (CS) conjugates were synthesized through utilizing copper-catalyzed click chemistry and subsequently characterized.

The chosen peptide-CS conjugates were then incorporated into self-assembling peptide hydrogels and the morphologies and gel properties were investigated and evaluated in terms of the closest resemblance to the natural properties of the surrounding cartilage into which the hydrogels would be eventually injected.

The best hydrogel candidates were then taken forward to be injected into a GAG depleted early stage osteoarthritic porcine cartilage model developed by Andres Barco (University of Leeds) where a severely GAG depleted state had been produced through a succession of surfactant and phosphate buffered saline washes. The hydrogels were doped with fluorescently labelled material which integrated into the hydrogel matrix, then injected into the cartilage tissue in a monomeric state. The hydrogels then self-assembled *in situ* and the deformation of the tissue was measured through creep indentation. The introduction of the peptide-CS conjugate showed significant restoration of resistance to deformation.

Table of Contents

Contents

Self-Assembling Peptide Hydrogels for Articular Cartilage Repair	i
Acknowledgments.....	iii
Abstract.....	iv
List of Tables	xiii
List of Figures	xv
Abbreviations.....	xxiii
1. General Introduction.....	1
1.1 Hyaline articular cartilage	2
1.1.1 Function of hyaline articular cartilage	2
1.1.2 Composition and structural features of hyaline articular cartilage.....	2
1.1.3 Collagen.....	2
1.1.4 Glycosaminoglycans and proteoglycans	4
1.1.4.1 Chondroitin sulfate	7
1.1.5 Other molecules.....	8
1.1.6 Microstructure and extracellular matrix of articular cartilage	8
1.1.6.1 Pericellular matrix.....	8
1.1.6.2 Territorial matrix.....	9
1.1.6.3 Inter-territorial matrix.....	9
1.1.7 Macrostructure of articular cartilage.....	9
1.1.7.1 Surface – lamina splendens	10
1.1.7.2 Superficial zone.....	10
1.1.7.3 Transitional zone.....	11
1.1.7.4 Deep zone	11
1.1.7.5 Calcified cartilage zone	11
1.1.8 Lubrication mechanism of hyaline cartilage	12

1.1.8.1	Fluid film lubrication	12
1.1.8.2	Boundary lubrication.....	13
1.1.8.3	Mixed lubrication	13
1.1.8.4	Biphasic model	13
1.1.8.5	Triphasic model.....	14
1.1.9	Wear of cartilage.....	16
1.1.9.1	Mechanical wear	16
1.1.9.2	Biochemical wear	17
1.2	Articular cartilage defects.....	18
1.3	Osteoarthritic cartilage	19
1.3.1	Pathophysiology of osteoarthritis.....	19
1.3.2	Animal models	22
1.3.3	Differences between healthy and osteoarthritic cartilage	22
1.3.3.1	Histological changes.....	22
1.3.3.2	Molecular changes	23
1.4	Intervention for early stage cartilage defects.....	26
1.4.1	Surgical procedures.....	26
1.4.2	Tissue engineering approaches to cartilage repair and regeneration	28
1.4.2.1	Cell sources	28
1.4.3	Scaffold material	30
1.4.3.1	Synthetic material.....	31
1.4.3.2	Natural materials	33
1.4.4	Potential uses of self-assembling peptides in regenerative medicine applications	
	34	
1.5	Self-assembling peptides	36
1.5.1	Self-assembling peptides as biomaterials.....	37
1.5.1.1	Hydrogel scaffolds.....	37
1.6	Self-assembly mechanism.....	38

1.6.1	External effects on self-assembly	40
1.6.1.1	pH	40
1.6.1.2	Ionic strength	40
1.6.1.3	Temperature	41
1.7	Different classes of self-assembling peptides.....	41
1.7.1	Self-assembling peptides forming helical structures	42
1.7.1.1	Helical peptides.....	42
1.7.2	Self-assembling peptides forming β -sheet like structures.....	43
1.7.2.1	Amphiphiles	43
1.7.2.2	Fmoc dipeptides.....	44
1.7.3	Self-assembling peptides forming tape or β -sheet structures.....	46
1.7.3.1	RADA	46
1.7.3.2	MAX peptides.....	46
1.7.3.3	P ₁₁ - X tape based peptides.....	47
1.8	Project aims.....	49
2.1	Materials	51
2.1.1	Equipment.....	51
2.1.2	Glassware	51
2.1.3	Plastic ware	51
2.1.4	Reagents.....	51
2.1.5	Cells.....	51
2.1.6	General stock solutions.....	52
2.1.6.1	Phosphate buffered saline (PBS).....	52
2.1.6.2	Baby hamster kidney (BHK) cell culture medium	52
2.1.6.3	L929 cell line culture medium.....	52
2.2	General methods	53
2.2.1	Sterilisation	53
2.2.1.1	Dry heat sterilisation.....	53

2.2.1.2 Moist heat/ autoclave sterilisation	53
2.2.1.3 Measurement of pH	53
2.2.1.4 Lyophilisation of samples	53
2.3 Chemical methods	54
2.3.1 Synthetic methods	54
2.3.2 Gel preparation	65
2.3.3 Liquid chromatography-mass spectrometry (LC-MS) analysis.....	65
2.3.4 Mass spectrometry analysis.....	65
2.3.5 Fourier transformed infra-red (FTIR) analysis.....	65
2.3.6 Nuclear magnetic resonance (NMR) analysis	66
2.3.7 Transmission electron microscopy	66
2.3.8 Rheological analysis	66
2.3.9 Flame atomic absorption spectroscopy.....	67
2.4 Biochemical methods.....	67
2.4.1 Papain Digestion	67
2.4.2 DMMB photometric assay	67
2.4.3 Stains-all photometric assay	68
2.4.3 Extract cytotoxicity	69
2.4.4 ATP-lite photometric assay	69
2.5 Biological methods.....	70
2.5.1 Tissue culture	70
2.5.2 Dissection of cartilage tissue.....	71
2.5.3 GAG depletion method	71
2.5.4 Cartilage layer retrieval.....	72
2.5.5 Cryo-sectioning	72
2.5.6 Histological methods	72
2.5.6.2 Paraffin wax embedding	72
2.5.7 Immunohistochemical staining.....	74

2.5.8 Optical microscopy.....	75
2.5.9 Peptide injection	75
2.5.10 Confocal microscopy	76
2.6 Biomechanical methods.....	77
2.6.1 PMMA cementing	77
2.6.2 Creep indentation	77
2.6.2.1 Calibration.....	77
2.6.3 Needle indentation for cartilage thickness measurement	79
2.7 Statistical analysis	79
2.7.1 Confidence limits	79
2.7.2 Statistical analysis	79
2.7.3 Arcsin transformation	79
3.1 Introduction	80
3.1.1 Peptide chemistry	80
3.1.2 Carbohydrates.....	84
3.1.3 Click chemistry	86
3.2 Results.....	89
3.2.1 Synthesis of P ₁₁₋₄ and P ₁₁₋₈ peptide fragments.....	89
3.2.1.1 P ₁₁₋₄ : Unidecamer or Dodecamer	90
3.2.1.2 Effects on self-assembly and morphology	96
3.2.1.3 Final peptide structure.....	99
3.2.2 Chondroitin Sulfate conjugate synthesis	103
3.2.2.1 Reductive amination method	103
3.2.2.2 Oxime formation method	104
3.2.3 P ₁₁₋₄ -CS conjugate: Click reaction optimization	105
3.2.4 Cu cytotoxicity.....	118
3.3 Discussion.....	123
3.3.1 Functionalised peptide synthesis.....	123

3.3.2	Modified chondroitin sulfate synthesis	124
3.3.3	P ₁₁ -4-CS conjugate: Click reaction optimization	125
3.3.4	Cu cytotoxicity.....	126
3.4	Conclusion.....	126
4.1	Introduction	128
4.1.1	Self-assembling systems	128
4.1.2	Self-assembling peptide hydrogels.....	129
4.1.3	Methods of morphological analysis.....	129
4.1.4	Physical testing of hydrogels.....	131
4.2	Results.....	135
4.2.1	Morphologies of different P ₁₁ -4 gels at different ionic strengths.....	135
4.2.1.1	P ₁₁ -4 only.....	135
4.2.1.2	P ₁₁ -4 + CS.....	137
4.2.1.3	P ₁₁ -4 + P ₁₁ -4-PEG-Hex-CS.....	139
4.2.2	Morphologies of different P ₁₁ -8 gels at different ionic strengths.....	143
4.2.2.1	P ₁₁ -8 only.....	143
4.2.2.2	P ₁₁ -8 + CS.....	144
4.2.2.3	P ₁₁ -8 + P ₁₁ -8-PEG-Hex-CS.....	145
4.2.3	Mechanical properties of P ₁₁ -4 gels at different ionic concentrations.....	150
4.2.4	Mechanical properties of P ₁₁ -8 gels at different ionic concentrations.....	153
4.2.5	P ₁₁ -4 Series at an increased concentration (30 mg ml ⁻¹ or ~18mM)	155
4.2.6	P ₁₁ -8 Series at an increased concentration (30 mg ml ⁻¹ or ~18mM)	157
4.3	Discussion and Conclusion.....	159
4.3.1	Morphologies of different P ₁₁ -4 gels at different ionic concentrations	159
4.3.2	Morphologies of different P ₁₁ -8 gels at different ionic concentrations	160
4.3.3	Mechanical properties of different P ₁₁ -4 gels at different ionic concentrations.....	161
4.3.4	Mechanical properties of different P ₁₁ -8 gels at different ionic concentrations.....	161

4.3.5 Mechanical properties of different P ₁₁ -4 gels at different ionic concentrations at 30 mg ml ⁻¹	162
4.3.6 Mechanical properties of different P ₁₁ -8 gels at different ionic concentrations at 30 mg ml ⁻¹	163
4.3.7 Conclusion	163
5.1 Introduction	165
5.1.1 Osteoarthritic cartilage models	165
5.1.1.1 Choice of animal model	165
5.1.1.2 Model development and disease simulation	167
5.2 Results	168
5.2.1 Severe osteoarthritic model validation	168
5.2.1.1 Histological validation of GAG depleted cartilage model	169
5.2.1.2 Immunohistochemical validation of GAG depleted cartilage model	170
5.2.1.3 Quantitative validation of GAG depleted cartilage model	171
5.2.1.4 Detection of residual SDS using a Stains-All assay	172
5.2.3 Confirming self-assembly in the tissue	174
5.2.3.1 Confocal imaging	175
5.2.2 Mechanical testing of osteoarthritic tissue model	183
5.2.2.1 Indentation testing	183
5.2.2.2 Cartilage thickness measurements	184
5.2.2.3 Deformation during indentation tests	187
5.3 Discussion and conclusion	192
5.3.1 GAG depleted cartilage model	192
5.3.3 Confirming self-assembly within the tissue	192
5.3.2 Mechanical testing of GAG depleted tissue model	193
5.3.4 Conclusion	194
6.1 General Discussion	195
6.2 Detailed approach to future work	199

6.2.1 Effect of peptide-GAG interaction on self-assembly	199
6.2.2 Contact cytotoxicity of peptide-GAG conjugate	200
6.2.3 Tribological testing.....	200
6.2.4 Analysis of peptide-GAG conjugate penetration within cartilage tissue	200
6.2.5 Investigating the structure of the peptide-GAG conjugate upon self-assembly	200
6.3 Conclusion.....	201
Appendix 1	221
Table 1: Equipment	221
Table 2: Chemical Reagents	224
Appendix 2: Rheological data.....	226
P ₁₁ -4 only.....	226
P ₁₁ -4 + CS.....	227
P ₁₁ -4 + P ₁₁ -4-CS.....	231
P ₁₁ -8 only.....	239
P ₁₁ -8 + CS.....	241
P ₁₁ -8 + P ₁₁ -8-CS.....	245

List of Tables

TABLE 1.1: THE CONCENTRATION RANGES FOR VARIOUS IONIC SOLUTES FOUND WITHIN THE SUPERFICIAL AND DEEP ZONES OF ARTICULAR CARTILAGE.	2
TABLE 1.2: THE DIFFERENT TYPES OF GAGS FOUND IN ARTICULAR CARTILAGE AND THEIR ASSOCIATED CHARACTERISTICS, WHERE RESIDUE A AND B REFER TO THE REPEATING UNITS WITHIN A POLYSACCHARIDE CHAIN AND WHERE +/- INDICATES THE PRESENCE OR ABSENCE OF THE DESCRIBED CHARACTERISTIC (ADAPTED FROM(SALTZMANN, 2004)). ...	5
TABLE 1.3: GRADES AND DESCRIPTIONS OF THE DIFFERENT CLASSIFICATIONS OF ARTICULAR CARTILAGE DEFECTS AS CATERGORISED BY ICRS. (ADAPTED FROM PERERA ET AL., 2012).....	18
TABLE 1.4: IMMUNOHISTOLOGICAL OBSERVATIONS OF OSTEOARTHRITIC CARTILAGE AT VARYING STAGES OF DISEASE PROGRESSION. (ADAPTED FROM LORENZ AND RICHTER, 2006).....	24
TABLE 1.5: BIOCHEMICAL OBSERVATIONS OF OSTEOARTHRITIC CARTILAGE AT VARYING STAGES OF DISEASE PROGRESSION. (ADAPTED FROM LORENZ AND RICHTER, 2006).	25
TABLE 1.6: THE DIFFERENT CELL SOURCES THAT HAVE BEEN INVESTIGATED TO ENGINEER CARTILAGE TISSUE (ADAPTED FROM WARREN, 2013).	29
TABLE 1.7: THE DIFFERENT SYNTHETIC POLYMERS THAT HAVE BEEN USED AS SCAFFOLD MATERIALS FOR CARTILAGE TISSUE ENGINEERING (ADAPTED FROM WARREN, 2013).	32
TABLE 1.8: THE DIFFERENT NATURAL POLYMERS AND MOLECULES THAT HAVE BEEN USED AS SCAFFOLD MATERIALS FOR CARTILAGE TISSUE ENGINEERING (ADAPTED FROM WARREN, 2013).....	33
TABLE 2.1: CELLS USED DURING THE STUDY.....	51
TABLE 2.2: LIST OF REAGENTS FOR PAPAIN DIGESTION OF CARTILAGE SAMPLES.....	67
TABLE 2.3: LIST OF REGENTS FOR DMMB PHOTOMETRIC ASSAY	68
TABLE 2.4: LIST OF REAGENTS FOR STAINS-ALL ASSAY.....	68
TABLE 2.5: LIST OF REAGENTS FOR GAG DEPLETION OF CARTILAGE TISSUE	71
TABLE 2.6: LIST OF REAGENTS FOR SAFRANIN O/FAST GREEN STAINING	73
TABLE 2.7: LIST OF REAGENTS FOR IMMUNOHISTOCHEMICAL LABELLING FOR CS	74
TABLE 3.1: A SUMMARY OF THE VARIOUS METHODS AND CONDITIONS EMPLOYED IN THE ATTEMPT TO SUCCESSFULLY SYNTHESIZE THE PEPTIDE FRAGMENT – OTHER THAN METHOD 5, ALL METHODS WERE EMPLOYED FOR PEPTIDES 2 AND 3.....	91
TABLE 3.2: AVERAGE LOADING CYCLES REQUIRED TO ACHIEVE COMPLETE LOADING FOR DIFFERENT COMBINATIONS OF RESINS AND COUPLING REAGENTS.	94
TABLE 3.3: VARIOUS CONDITIONS INVESTIGATED FOR THE CUAAC REACTION BETWEEN P ₁₁ -X-PEG-HEX-N ₃ AND ALKYNE-CS FRAGMENTS.	110
TABLE 4.1: SUMMARY OF THE DIFFERENT SAMPLES, PEPTIDE TYPE, CS INTRODUCTION MANNER, BUFFER TYPE, MOLAR RATIO AND PEPTIDE CONCENTRATION.	134
TABLE 4.2: THE FIBRILLAR LENGTHS AND WIDTHS FOR P ₁₁ -4 ONLY SAMPLES AT TWO DIFFERENT IONIC STRENGTH BUFFERS (\pm S.D).	136
TABLE 4.3: THE FIBRILLAR LENGTHS AND WIDTHS FOR P ₁₁ -4 +CS SAMPLES AT TWO DIFFERENT MOLAR RATIOS AND IONIC STRENGTH BUFFERS (\pm S.D).....	138

TABLE 4.4: THE FIBRILLAR LENGTHS AND WIDTHS FOR P ₁₁₋₄ + P ₁₁₋₄ -CS SAMPLES AT TWO DIFFERENT MOLAR RATIOS AND IONIC STRENGTH BUFFERS (\pm S.D).....	140
TABLE 4.5: THE FIBRILLAR LENGTHS AND WIDTHS FOR P ₁₁₋₈ ONLY SAMPLES AT TWO DIFFERENT IONIC STRENGTH BUFFERS (\pm S.D).	143
TABLE 4.6: THE FIBRILLAR LENGTHS AND WIDTHS FOR P ₁₁₋₈ +CS SAMPLES AT TWO DIFFERENT MOLAR RATIOS AND IONIC STRENGTH BUFFERS (\pm S.D).....	145
TABLE 4.7: THE FIBRILLAR LENGTHS AND WIDTHS FOR P ₁₁₋₈ +P ₁₁₋₈ -CS SAMPLES AT TWO DIFFERENT MOLAR RATIOS AND IONIC STRENGTH BUFFERS (\pm S.D).....	146
TABLE 4.8: SUMMARY OF THE DIFFERENT FIBRILLAR LENGTHS AND WIDTHS (NM) FOR EACH DIFFERENT PEPTIDE SAMPLE FROM BOTH THE P ₁₁₋₄ AND P ₁₁₋₈ SERIES (\pm S.D).....	149
TABLE 4.9: SUMMARY OF THE G' AND G'' VALUES OF THE P ₁₁₋₄ SERIES OF HYDROGELS, ALONG WITH THE PARAMETERS USED TO OBTAIN THE VALUES FROM THE FREQUENCY SWEEP.	152
TABLE 4.10: SUMMARY OF THE G' AND G'' VALUES OF THE P ₁₁₋₈ SERIES OF HYDROGELS AT 10 MG ML ⁻¹ , ALONG WITH THE PARAMETERS USED TO OBTAIN THE VALUES FROM THE FREQUENCY SWEEP.	154
TABLE 4.11: SUMMARY OF THE G' AND G'' VALUES OF THE P ₁₁₋₄ SERIES OF HYDROGELS AT 30 MG ML ⁻¹ , ALONG WITH THE PARAMETERS USED TO OBTAIN THE VALUES FROM THE FREQUENCY SWEEP.	155
TABLE 4.12: SUMMARY OF THE G' AND G'' VALUES OF THE P ₁₁₋₈ SERIES OF HYDROGELS AT 30 MG ML ⁻¹ , ALONG WITH THE PARAMETERS USED TO OBTAIN THE VALUES FROM THE FREQUENCY SWEEP.	157
TABLE 5.1: PROS AND CONS OF TISSUE TYPES COMMONLY USED IN <i>IN VITRO</i> TESTING. THE PROS AND CONS OF EACH DIFFERENT TISSUE IS SUMMARISED IN TERMS OF PRACTICALITY AND COST EFFECTIVENESS.	166
TABLE 5.2: THE DIFFERENT CONTROL GROUPS TESTED USING THE INDENTATION RIG TO MEASURE THE EFFECTS OF DEFORMATION OBSERVED WITHIN NATIVE AND DEPLETED CARTILAGE SAMPLES.	184
TABLE 5.3: THE MEASURED AND LITERATURE VALUES FOR BOTH MEDIAL AND LATERAL CARTILAGE THICKNESSES, WITH SDS TREATED MEASURED SAMPLES ALSO SHOWN (N=12) WHERE THE RESULTS ARE PRESENTED AS THE MEAN \pm 95% CL (P<0.05 STUDENT T-TEST).....	187
TABLE 5.4: SUMMARY OF RESTORATION OF DEFORMATION RESISTANCE IN VARIOUS CONTROLS GROUPS. THE DATA SHOWN IS SPLIT INTO TWO DATA SETS – MEDIAL (TOP) AND LATERAL (BOTTOM)WHERE THE DATA IS THE MEAN RESTORATION (N=3) \pm 95 % CL. (P<0.05, STUDENT T-TEST)	190

List of Figures

FIG 1.1: A SCHEMATIC SHOWING THE VARIOUS INTERMEDIATE STRUCTURES DURING COLLAGEN PRODUCTION, AS WELL AS TYPICAL DIMENSIONS.....	3
FIG 1.2: A SCHEMATIC REPRESENTATION OF AGGREGAN, G1, G2 AND G3 REPRESENT GLOBULAR DOMAINS INVOLVED IN CHONDROCYTE APOPTOSIS, BINDING OF HYALURONAN, CELL ADHESION AND AGGREGATION.	6
FIG 1.3: THE BASIC STRUCTURE OF CHONDROITIN-6-SULFATE.	8
FIG 1.4: THE MACROSTRUCTURE OF ARTICULAR CARTILAGE, WITH THE CHONDROCYTE MORPHOLOGY AND LOCALISATION (A) AND COLLAGEN ORIENTATION (B) OF THE CORRESPONDING ZONE SHOW (REPRODUCED WITH COPYRIGHT PERMISSION FROM JAZRAWI ET AL., 2011).....	10
FIG 1.5: THE DIFFERENT PHASES ASSOCIATED WITH THE TRIPHASIC MODEL, WHERE FOR THE BIPHASIC MODEL ONLY THE FLUID AND SOLID COMPONENTS ARE MODELLED.....	15
FIG 1.6: THE VARIOUS LUBRICATION REGIMES ASSOCIATION WITH ARTICULATION OF ARTICULAR JOINTS (REPRODUCED FROM HTTP://BIO.MECH.KYUSHU-U.AC.JP/SPR/RESEARCH-EN.HTML , ACCESSED 20/07/2014).....	16
FIG 1.7: THE PATHWAY FOR WEAR AND POTENTIAL DEVELOPMENT OF OSTEOARTHRITIS IN ARTICULAR CARTILAGE (ADAPTED FROM BURR AND GALLANT, 2012).....	20
FIG 1.8: PATHOPHYSIOLOGICAL CHANGES IN OSTEOARTHRITIC ARTICULAR CARTILAGE WHEN MECHANICAL LOADING IS APPLIED.	21
FIG 1.9: THE VARIOUS SURGICAL TECHNIQUES CURRENTLY EMPLOYED TO TREAT ARTICULAR CARTILAGE DEFECTS (REPRODUCED WITH COPYRIGHT PERMISSION FROM HUEY ET AL., 2012).....	26
FIG 1.10: DIAGRAMS AND IMAGES OF SAP'S WHICH HAVE FORMED INTO DIFFERENT STRUCTURES THROUGH DIFFERENT METHODS OF SELF-ASSEMBLY AND DIFFERENT APPLICATIONS. ROUTE A SHOWS HOW IONIC SELF-COMPLEMENTARY PEPTIDES UNDERGO SELF-ASSEMBLY TO FORM A HYDROGEL SCAFFOLD. ROUTE B SHOWS HOW SURFACTANT-LIKE PEPTIDES CAN SELF-ASSEMBLE TO FORM NANOTUBES AND NANO-VESICLES. ROUTE C SHOWS HOW PEPTIDES CAN BE USED TO NANO-COAT A SURFACE USING A FUNCTIONAL GROUP SUCH AS A THIOL ONTO A GOLD SURFACE FOR NANOTECHNOLOGY APPLICATIONS. ROUTE D SHOWS HOW CONTROLLING THE ENVIRONMENT IN WHICH SECONDARY PEPTIDE ASSEMBLY OCCURS, PEPTIDES CAN BE EXPLOITED FOR USE AS NANO-SWITCHES DEPENDING UPON EXTERNAL STIMULI (REPRODUCED WITH COPYRIGHT PERMISSION FROM ZHANG, 2003).....	35
FIG 1.11: THE DIFFERENT INTERMEDIATES OF SELF-ASSEMBLY FOR THE P11-X CLASS OF PEPTIDES EXPERIENCE WHEN UNDER A CONCENTRATION DEPENDENT REGIME.	39
FIG 1.12: THE DIFFERENT SECONDARY STRUCTURES ADOPTED BY SELF-ASSEMBLING PEPTIDES (BOYLE AND WOOLFSON, 2011). (A) REPRESENTS THE RANDOM COIL STATE OF UNASSEMBLED SAPS, WHERE UPON SELF-ASSEMBLING (B) IS A B-STRAND WHERE AN ENTROPIC LOSS IS ASSOCIATED WITH THIS STATE AND (C) IS AN A-HELIX. THESE TWO DIFFERENT SECONDARY STRUCTURES UNDERGO FURTHER SELF-ASSEMBLY TO FORM (D) WHICH IS A B-SHEET OR (E) AND (F) WHICH ARE MULTIPLE INTERACTING A-HELICES (REPRODUCED WITH COPYRIGHT PERMISSION FROM BOYLE AND WOOLFSON, 2011).....	42
FIG 1.13: THE REPEATING UNITS WITHIN A HELICAL FORMING SELF-ASSEMBLING PEPTIDE (O'LEARY, 2011).	43
FIG 1.14: TYPICAL AMPHIPHILIC PEPTIDE (SARGEANT, 2008).	44

FIG 1.15: REPRESENTATION OF THE TWO TYPES OF INTERACTIONS INVOLVED IN THE SELF-ASSEMBLY OF FMOC DIPEPTIDES – HYDROGEN BONDING AND π - π STACKING.	45
FIG 1.16: TWO DIFFERENT AMINO ACIDS ARE COVALENTLY BOUND TO FORM THE FMOC DIPEPTIDE (WILLIAMS, 2008B)....	45
FIG 1.17: THE REPEATING STRUCTURE OF A RADA PEPTIDE CHAIN (HORII, 2007B).....	46
FIG 1.18: A MAX PEPTIDE, WHERE V = VALINE AND K = LYSINE (RAJAGOPAL, 2006B).	47
FIG 1.19: THE TYPICAL STRUCTURE OF A P11-X PEPTIDE, THE EXAMPLE ABOVE IS KNOWN AS P11-4 (KIRKHAM ET AL., 2007).....	47
FIG 1.20: THE BASIC DESIGN PARAMETERS OF THE P11-X PEPTIDE FAMILY.	48
FIG 1.21: A REPRESENTATION OF THE AIM TO FORM AN AGGREGAN LIKE BRUSH STRUCTURE USING THE PEP-GAG CONJUGATES.....	49
FIG 2.1: VOLTAGE AGAINST SLIP DISC HEIGHT CALIBRATION PLOT.	78
FIG 2.2: VOLTAGE AGAINST SLIP DISC WEIGHT CALIBRATION PLOT.	78
FIG 3.1: A REPRESENTATION OF FMOC-SPPS OF A PEPTIDE AMIDE WHERE THE LOADING STAGE USES A RESIN WHICH HAS A TERMINAL AMINO GROUP, WITH A SINGLE SYNTHETIC CYCLE SHOWN.	81
FIG 3.2: VARIOUS TERMINAL N AND SIDE CHAIN PROTECTING GROUPS.	82
FIG 3.3: i) HATU METHOD MECHANISM USING HCTU, WHERE THE BASE IS DIPEA ii) HOBt METHOD MECHANISM USING HOBt AND DIC iii) HOBt METHOD MECHANISM USING OXYMA PURE [®] AND DIC.	83
FIG 3.4: DIFFERENT NATURAL POLYSACCHARIDES, WHERE CHITOSAN CONSISTS OF A SINGLE REPEATING UNCHARGED SACCHARIDE UNIT (β -(1-4)- LINKED D-GLUCOSAMINE WITH RANDOM GLUCOSAMINE RESIDUES BEING ACETYLATED), WHILST HYALURONIC ACID (ALTERNATING β -(1-3) AND β -(1-4)-LINKED D- GLUCURONIC ACID AND D-N-ACETYLGLUCOSAMINE) AND CHONDROITIN SULFATE (D-GLUCURONIC ACID AND D-N-ACETYL GALACTOSAMINE WITH RANDOM SULFATION OF HYDROXYL GROUPS) CONSIST OF A REPEATING ANIONIC DISACCHARIDE UNIT.	84
FIG 3.5: A REPRESENTATION OF AGGREGAN, WITH THE GAG CHAINS ARRANGED IN A BRUSH-LIKE STRUCTURE AROUND A PROTEIN BACKBONE. A MORE DETAILED DESCRIPTION CAN BE FOUND IN CHAPTER 1.	85
FIG 3.6: THE EQUILIBRIUM STATE OF THE REDUCING END OF A SACCHARIDE AND REDUCTIVE AMINATION VIA THE FORMATION OF AN IMINE.	86
FIG 3.7: AN EXAMPLE OF A P11-X PEPTIDE AND THE ACETYLATED TERMINUS HIGHLIGHTED.	86
FIG 3.8: VARIOUS TYPES OF “CLICK” REACTIONS, WITH THE CORRESPONDING RATE CONSTANTS SHOWN.....	87
FIG 3.9: THE GENERAL SYNTHETIC STRATEGY FOR THE TOTAL SYNTHESIS OF A PEPTIDE-CS CONJUGATE BASED ON SYNTHESIZING TWO FRAGMENTS: AN AZIDE FUNCTIONALISED PEPTIDE FRAGMENT AND A FUNCTIONALISED CS FRAGMENT.	88
FIG 3.11: STRUCTURE OF FUNCTIONALISED P11-4 OR “P12-4” – DODECAMER.....	90
FIG 3.12: STRUCTURE OF FUNCTIONALISED P11-4 – UNIDECAMER.....	90
FIG 3.13: MASS SPECTRUM ANALYSIS INDICATING THAT SEQUENTIAL DELETION OF AMINO ACIDS DURING THE P ₁₁ -4 SYNTHESIS WHICH RESULTED FROM INCOMPLETE LOADING OF THE RESIN WITH THE INITIAL AMINO ACID – GLN.	92
FIG 3.14: THE STRUCTURES OF THE TWO DIFFERENT RESINS MAINLY EMPLOYED – PEGA RINK AMIDE AND NOVAGEL [®] RINK AMIDE RESINS.....	93

FIG 3.15: MASS SPECTRA OF BOTH FUNCTIONALISED P ₁₁ -4 IN CRUDE FORM, A – P ₁₁ -4 AND B – “P ₁₂ -4” WHERE THE HIGHLIGHTED PEPTIDE PEAK IN B HAD THE TRP RESIDUE CARBOXYLATED. THIS RESIDUAL CO ₂ GROUP WAS REMOVED BY TREATMENT WITH ACOH AND LYOPHILISATION.	94
FIG 3.16: MASS SPECTRA SHOWING THE TEST SCALE (TOP) AND FULL SCALE (BOTTOM) PURIFICATION ATTEMPTS OF THE FUNCTIONALISED P ₁₁ -4 PEPTIDES VIA UV DIRECTED RP HPLC.....	95
FIG 3.17: MASS SPECTRUM OF THE PURIFICATION ATTEMPT OF FUNCTIONALISED P ₁₁ -4 VIA CHROMATOGRAPHY ON A UV-DIRECTED BIOTAGE INSTRUMENT, WHERE THE PEPTIDE PEAK IS HIGHLIGHTED.....	96
FIG 3.18: TEM MICROGRAPHS OF TWO DIFFERENT ISOMERS OF P ₁₁ -4-CS AT DIFFERENT MOLAR RATIOS WITHIN P ₁₁ -4 HYDROGELS (~6 MM). A) P ₁₁ -4 + P ₁₁ -4-PEG-LYS (MCA)-HEX-CS 32-1 RATIO 230 MM NA ⁺ BUFFER, 4000X MAGNIFICATION B) P ₁₁ -4 + P ₁₁ -4-PEG-LYS (MCA)-HEX-CS 64-1 RATIO 230 MM NA ⁺ BUFFER, 6000X MAGNIFICATION C) P ₁₁ -4 + P ₁₁ -4-LYS (MCA)-PEG-HEX-CS 32-1 RATIO 230 MM NA ⁺ BUFFER, 5000X MAGNIFICATION C) P ₁₁ -4 + P ₁₁ -4-LYS (MCA)-PEG-HEX-CS 64-1 RATIO 230 MM NA ⁺ BUFFER, 4000X MAGNIFICATION, SCALE BAR – 500 NM.....	97
FIG 3.19: THE DIFFERENT FIBRIL DIMENSIONS, A) EFFECT ON FIBRIL LENGTH FOR THE DIFFERENT VARIANTS AT 130 MM AND 230 MM NA ⁺ CONCENTRATIONS, B) EFFECT ON FIBRIL WIDTH FOR DIFFERENT VARIANTS AT 130 MM AND 230 MM NA ⁺ CONCENTRATIONS. ERROR BARS: ± STANDARD DEVIATION, N = 100.....	98
FIG 3.20: STRUCTURE OF P ₁₁ -4-PEG-HEX-N ₃	99
FIG 3.21: THE DIFFERENCES BETWEEN THE TWO TYPES OF RESIN: (TOP) REQUIRES LOW TFA CONTENT TO CLEAVE THE PEPTIDE FROM THE SOLID SUPPORT WHILST LEAVING THE SIDE GROUPS PROTECTED (BOTTOM) HIGH TFA CONTENT TO CLEAVE THE PEPTIDE CAUSES THE SIDE GROUPS TO BE DEPROTECTED AS WELL AS CLEAVING THE SOLID SUPPORT.	100
FIG 3.22: A) ANALYTICAL HPLC TRACE B) ACCURATE MASS MS TRACE FOR SYNTHESIZED PEPTIDE 3 (P ₁₁ -4-PEG-HEX-N ₃), WITH THE 1+ AND 2+ SPECIES SHOWN.	101
FIG 3.23: STRUCTURE OF SYNTHESIZED PEPTIDE 4 (P ₁₁ -8-PEG-HEX-N ₃).	102
FIG 3.24: STRUCTURAL DETERMINATION OF PEPTIDE 4 (P ₁₁ -8-PEG-HEX-N ₃) WITH A) ANALYTICAL HPLC TRACE B) ACCURATE MASS MS TRACE.	102
FIG 3.25: SYNTHETIC PATHWAY OF ALKYNYL SUBSTITUTED HYDROXYLAMINE LINKER AS HYDROCHLORIDE SALT.....	103
FIG 3.26: GENERAL SCHEME FOR REDUCTIVE ANIMATION SYNTHETIC PATHWAY.	104
FIG 3.27: SYNTHETIC PATHWAY OF CHONDROITIN SULFATE CONJUGATE VIA THE ANILINE CATALYSED OXIME LIGATION ROUTE.	105
FIG 3.28: GENERIC REACTION SCHEME OF CUAAC REACTION LINKING FUNCTIONALIZED PEPTIDE WITH EITHER 4-ETHYNYLBENZYLALCOHOL 1, AMINOXY 4 OR FUNCTIONALIZED CS 5 UNDER VARIOUS CONDITIONS.....	106
TABLE 3.3: VARIOUS CONDITIONS INVESTIGATED FOR THE CUAAC REACTION BETWEEN P ₁₁ -X-PEG-HEX-N ₃ AND ALKYNE-CS FRAGMENTS.	107
TABLE 3.3: VARIOUS CONDITIONS INVESTIGATED FOR THE CUAAC REACTION BETWEEN P ₁₁ -X-PEG-HEX-N ₃ AND ALKYNE-CS FRAGMENTS.	108
TABLE 3.3: VARIOUS CONDITIONS INVESTIGATED FOR THE CUAAC REACTION BETWEEN P ₁₁ -X-PEG-HEX-N ₃ AND ALKYNE-CS FRAGMENTS.	109

FIG 3.29: MASS SPECTRA FOR STARTING PEPTIDE 3 (P ₁₁ -4-PEG-HEX-N ₃) MATERIAL (TOP) AND CLICK REACTION PRODUCT CONJUGATE 1 WITH ETHYNYL BENZYL ALCOHOL (BOTTOM) UNDER REACTION 13 CONDITIONS.....	111
FIG 3.30: THE ¹ H NMR SPECTRUM OF THE PRODUCT OF AN ETHYNYL BENZYL ALCOHOL – P ₁₁ -4-PEG-HEX-N ₃ CLICK REACTION – CONJUGATE 1 USING REACTION 13 CONDITIONS. THE CHARACTERISTIC TRIAZOLE PROTON PEAK IS ~8 PPM.	112
FIG 3.31: MASS SPECTRA FOR STARTING PEPTIDE 3 (P ₁₁ -4-PEG-HEX-N ₃) MATERIAL (TOP) AND CLICK REACTION PRODUCT CONJUGATE 3 WITH AMINOXY INTERMEDIATE 4 (BOTTOM) UNDER REACTION 13 CONDITIONS.....	113
FIG 3.32: UV TRACE OF CONJUGATE 5 (P ₁₁ -4-PEG-HEX-(TRIAZOLE)-CS) REACTION BEFORE (ABOVE) AND AFTER (BOTTOM) COMPLETION. THERE WAS NO PRESENCE OF THE STARTING PEPTIDE MATERIAL INDICATING THE REACTION HAS GONE TO COMPLETION WITH THE UV PEAK AT 1.9 MIN HAVING DISAPPEARED.....	114
FIG 3.33: ¹ H NMR TRACE COMPARING PEPTIDE 3 (P ₁₁ -4-PEG-HEX-N ₃), CONJUGATE 3 (P ₁₁ -4-PEG-HEX-BENZYL) AND CONJUGATE 5 (P ₁₁ -4-PEG-HEX-CS), WITH THE CHARACTERISTIC TRIAZOLE PROTON ~8 PPM.....	114
FIG 3.34: SEC-MALLS TRACE – UV TRACE (TOP) AND LS TRACE (BOTTOM) WITH CS (BLUE) AND CONJUGATE 5 (P ₁₁ -4-PEG-HEX-CS) (ORANGE).....	116
FIG 3.35: UV TRACE OF CONJUGATE 6 (P ₁₁ -8-PEG-HEX-CS) REACTION BEFORE (ABOVE) AND AFTER (BOTTOM) COMPLETION. THERE WAS NO PRESENCE OF THE STARTING PEPTIDE MATERIAL INDICATING THE REACTION HAS GONE TO COMPLETION WITH THE UV PEAK AT 1.5 MIN HAVING DISAPPEARED.....	117
FIG 3.36: ¹ HNMR TRACE COMPARING PEPTIDE 4 (P ₁₁ -8-PEG-HEX-N ₃), CONJUGATE 4 (P ₁₁ -8-PEG-HEX-BENZYL) AND CONJUGATE 6 (P ₁₁ -8-PEG-HEX-CS), WITH THE CHARACTERISTIC TRIAZOLE PROTON ~8PPM.....	117
FIG 3.37: SEC-MALLS TRACES FOR CONJUGATE 6 (P ₁₁ -8-PEG-HEX-CS) (RED) COMPARED TO CS ONLY (BLUE). UV TRACE (TOP) AND LS TRACE (BOTTOM).	118
FIG 3.39: EXTRACT CYTOTOXICITY RESULTS FOR RESIDUAL CU (I) AND CU (II) CONCENTRATIONS USING BHK AND L929 CELL LINES. (UPPERMOST) BHK CELLS EXPOSED FOR 48 HR TO CU ₂ SO ₄ AT VARIOUS CONCENTRATIONS. (UPPER MIDDLE) BHK CELLS EXPOSED FOR 48 HR TO CUCL AT VARIOUS CONCENTRATIONS. (LOWER MIDDLE) L929 CELLS EXPOSED FOR 48 HR TO CU ₂ SO ₄ AT VARIOUS CONCENTRATIONS. (LOWERMOST) L929 CELLS EXPOSED FOR 48 HR TO CUCL AT VARIOUS CONCENTRATIONS. = SIGNIFICANT DIFFERENCE TO NEGATIVE CONTROL (MEDIA) (A = 0.95).	121
FIG 4.1: STAGES OF SELF-ASSEMBLY AND HYDROGEL FORMATION FOR P ₁₁ -X CLASS OF SELF-ASSEMBLING PEPTIDES (REPRODUCED WITH COPYRIGHT PERMISSION FROM AGGELI <i>ET AL</i>)	130
FIG 4.2: A SCHEMATIC OF A TYPICAL TRANSMISSION ELECTRON MICROSCOPE	131
FIG 4.3: A SCHEMATIC REPRESENTATION OF A STRAIN CONTROLLED RHEOLOGICAL EXPERIMENT.....	132
FIG 4.4: A SCHEMATIC REPRESENTATION OF A STRESS CONTROLLED RHEOLOGICAL EXPERIMENT.....	132
FIG 4.5: THE VARIOUS CONFIGURATIONS OF MEASUREMENT INTERFACES POSSIBLE WITH RHEOLOGICAL EXPERIMENTS	133
FIG 4.6: AN EXAMPLE TEM MICROGRAPH TO HIGHLIGHT HOW THE FIBRIL LENGTHS AND WIDTHS WERE MEASURED – WHERE THE LENGTH WAS THE PERSISTENCE LENGTH AND THE WIDTH WAS THE WIDTH OF THE FIBRIL AT THE WIDEST POINT (TO AVOID ANY VARIATION IN OTHER UNMEASURED DIMENSIONS SUCH AS PITCH TWIST). SCALE BAR – 500 NM.	135
FIG 4.7: TEM IMAGES OF P ₁₁ -4 (~6 μM) GELS IN DIFFERENT IONIC STRENGTH BUFFERS. A) 230 mM Na ⁺ BUFFER, 4000X MAGNIFICATION, SCALE BAR - 500NM. B) 130 mM Na ⁺ BUFFER, 4000X MAGNIFICATION, SCALE BAR – 500NM..	136
FIG 4.8: IMAGE OF P ₁₁ -4 GELS ONLY AT 230 mM Na ⁺ (LEFT) AND 130 mM Na ⁺ (RIGHT)	136

FIG 4.9: TEM IMAGES OF P ₁₁₋₄ + CS (~5.85MM) GELS IN DIFFERENT IONIC STRENGTH BUFFERS. A) P ₁₁₋₄ + CS 32-1 RATIO 230 MM NA ⁺ BUFFER, 4000X MAGNIFICATION, SCALE BAR - 500NM. B) P ₁₁₋₄ + CS 64-1 RATIO 230 MM NA ⁺ BUFFER, 4000X MAGNIFICATION, SCALE BAR - 500NM. C) P ₁₁₋₄ + CS 32-1 130 MM NA ⁺ BUFFER, 4000X MAGNIFICATION, SCALE BAR - 500NM. D) P ₁₁₋₄ + CS 64-1 130 MM NA ⁺ BUFFER, 4000X MAGNIFICATION, SCALE BAR - 500NM.	137
FIG 4.10: IMAGE OF P ₁₁₋₄ + CS GELS AT 230 MM NA ⁺ AT BOTH 32:1 (FAR LEFT), 64:1 (LEFT) MOLAR RATIOS AND 130 MM NA ⁺ AT BOTH 32:1 (FAR RIGHT), 64:1 (RIGHT) MOLAR RATIOS.	139
FIG 4.11: TEM IMAGES OF P ₁₁₋₄ + P ₁₁₋₄ -CS (~5.85MM) GELS IN DIFFERENT IONIC STRENGTH BUFFERS. A) P ₁₁₋₄ + P ₁₁₋₄ -CS 32-1 RATIO 230 MM NA ⁺ BUFFER, 4000X MAGNIFICATION, SCALE BAR - 500NM. B) P ₁₁₋₄ + P ₁₁₋₄ -CS 64-1 RATIO 230 MM NA ⁺ BUFFER, 4000X MAGNIFICATION, SCALE BAR - 500NM. C) P ₁₁₋₄ + P ₁₁₋₄ -CS 32-1 130 MM NA ⁺ BUFFER, 4000X MAGNIFICATION, SCALE BAR - 500NM. D) P ₁₁₋₄ + P ₁₁₋₄ -CS 64-1 130 MM NA ⁺ BUFFER, 4000X MAGNIFICATION, SCALE BAR - 500NM.	140
FIG 4.12: IMAGES OF P ₁₁₋₄ + P ₁₁₋₄ -CS GELS AT 230 MM NA ⁺ AT BOTH 32:1 (FAR LEFT), 64:1 (LEFT) MOLAR RATIOS AND 130 MM NA ⁺ AT BOTH 32:1 (RIGHT), 64:1 (FAR RIGHT) MOLAR RATIOS.	141
FIG 4.13: COMPARISON OF THE DIFFERENT FIBRILLAR LENGTHS AND WIDTHS FOR EACH DIFFERENT P ₁₁₋₄ SAMPLE. A) FIBRILLAR LENGTHS OF EACH P ₁₁₋₄ SAMPLE. B) FIBRILLAR WIDTHS OF EACH P ₁₁₋₄ SAMPLE. (ERROR BARS = ± S.D).	142
FIG 4.14: TEM IMAGES OF P ₁₁₋₈ (~5.85MM) GELS IN DIFFERENT IONIC STRENGTH BUFFERS. A) 230 MM NA ⁺ BUFFER, 4000X MAGNIFICATION, SCALE BAR - 500NM. B) 130 MM NA ⁺ BUFFER, 4000X MAGNIFICATION, SCALE BAR - 500NM.	143
FIG 4.15: IMAGE OF P ₁₁₋₈ GELS ONLY AT 230 MM NA ⁺ (LEFT) AND 130 MM NA ⁺ (RIGHT)	144
FIG 4.16: TEM IMAGES OF P ₁₁₋₈ + CS (~5.85MM) GELS IN DIFFERENT IONIC STRENGTH BUFFERS. A) P ₁₁₋₈ + CS 32-1 RATIO 230 MM NA ⁺ BUFFER, 4000X MAGNIFICATION, SCALE BAR - 500NM. B) P ₁₁₋₈ + CS 64-1 RATIO 230 MM NA ⁺ BUFFER, 4000X MAGNIFICATION, SCALE BAR - 500NM. C) P ₁₁₋₈ + CS 32-1 130 MM NA ⁺ BUFFER, 4000X MAGNIFICATION, SCALE BAR - 500NM. D) P ₁₁₋₈ + CS 64-1 130 MM NA ⁺ BUFFER, 4000X MAGNIFICATION, SCALE BAR - 500NM.	144
FIG 4.17: IMAGE OF P ₁₁₋₈ + CS GELS AT 230 MM NA ⁺ AT BOTH 32:1 (FAR LEFT), 64:1 (LEFT) MOLAR RATIOS AND 130 MM NA ⁺ AT BOTH 32:1 (RIGHT), 64:1 (FAR RIGHT) MOLAR RATIOS.	145
FIG 4.18: TEM IMAGES OF P ₁₁₋₈ + P ₁₁₋₈ -CS (~5.85MM) GELS IN DIFFERENT IONIC STRENGTH BUFFERS. A) P ₁₁₋₈ + P ₁₁₋₈ -CS 32-1 RATIO 230 MM NA ⁺ BUFFER, 4000X MAGNIFICATION, SCALE BAR - 500NM. B) P ₁₁₋₈ + P ₁₁₋₈ -CS 64-1 RATIO 230 MM NA ⁺ BUFFER, 4000X MAGNIFICATION, SCALE BAR - 500NM. C) P ₁₁₋₈ + P ₁₁₋₈ -CS 32-1 130 MM NA ⁺ BUFFER, 4000X MAGNIFICATION, SCALE BAR - 500NM. D) P ₁₁₋₈ + P ₁₁₋₈ -CS 64-1 130 MM NA ⁺ BUFFER, 4000X MAGNIFICATION, SCALE BAR - 500NM.	146
FIG 4.19: IMAGES OF P ₁₁₋₈ + P ₁₁₋₈ -CS GELS AT 230 MM NA ⁺ AT BOTH 32:1 (FAR LEFT), 64:1 (LEFT) MOLAR RATIOS AND 130 MM NA ⁺ AT BOTH 32:1 (RIGHT), 64:1 (FAR RIGHT) MOLAR RATIOS.	147
FIG 4.20: COMPARISON OF THE DIFFERENT FIBRILLAR LENGTHS AND WIDTHS FOR EACH DIFFERENT P ₁₁₋₈ SAMPLE. A) FIBRILLAR LENGTHS OF EACH P ₁₁₋₈ SAMPLE. B) FIBRILLAR WIDTHS OF EACH P ₁₁₋₈ SAMPLE. (ERROR BARS = ± S.D).	148

FIG 4.21: AN EXAMPLE ILLUSTRATING THE LVER REGION FROM TWO AMPLITUDE SWEEPS: 1 Hz (LEFT) AND 20 Hz (RIGHT), WHERE THE PLATEAU REGION IS APPARENT.	150
FIG 4.22: AN EXAMPLE OF WHICH VALUE INDICATES THE G' AND G'' MODULI, WHICH ARE OBTAINED FROM THE FREQUENCY SWEEPS AT THE SELECTED STRAIN CHOSEN FROM THE AMPLITUDE SWEEPS FOR THE LVER REGION OF THE SAMPLE. .	151
FIG 4.23: A COMPARISON OF THE G' AND G'' VALUES FOR EACH OF THE P ₁₁₋₄ SAMPLES, WITH THE MODULI AXIS IN A LOG SCALE TO SHOW THE RELATIVE MAGNITUDES.	153
FIG 4.24: A COMPARISON OF THE G' AND G'' VALUES FOR EACH OF THE P ₁₁₋₈ SAMPLES, WITH THE MODULI AXIS (Y-AXIS) IN A LOG SCALE TO SHOW THE RELATIVE MAGNITUDES.	155
FIG 4.25: A COMPARISON OF THE G' AND G'' VALUES FOR EACH OF THE P ₁₁₋₄ SAMPLES INCLUDING THE 30 MG ML ⁻¹ SAMPLES, A) THE MODULI AXIS IN A NUMERICAL SCALE, B) WITH THE MODULI AXIS IN A LOG SCALE TO SHOW THE RELATIVE MAGNITUDES.	156
FIG 4.26: A COMPARISON OF THE G' AND G'' VALUES FOR EACH OF THE P ₁₁₋₈ SAMPLES INCLUDING THE 30 MG ML ⁻¹ SAMPLES, A) THE MODULI AXIS IN A NUMERICAL SCALE, B) WITH THE MODULI AXIS IN A LOG SCALE TO SHOW THE RELATIVE MAGNITUDES.	158
FIG 5.1: FLOWCHART ILLUSTRATING THE GAG DEPLETING PROCEDURE. THE PROCEDURE INVOLVED SDS AND PBS WASHES AT VARYING LENGTHS, WHILST BEING AGITATED AT 240 RPM, 37 °C.	168
FIG 5.2: SAFRANIN O AND FAST GREEN STAINED SECTIONS OF NATIVE AND GAG DEPLETED PORCINE CARTILAGE. TOP LEFT (A) – NATIVE HEALTHY MEDIAL CARTILAGE. TOP RIGHT (B) – GAG DEPLETED MEDIAL CARTILAGE. BOTTOM LEFT (C) – NATIVE HEALTHY LATERAL CARTILAGE. BOTTOM RIGHT (D) – GAG DEPLETED LATERAL CARTILAGE. SCALE BAR = 500 μM.	169
FIG 5.3 : IMMUNOHISTOCHEMICAL MICROGRAPHS OF NATIVE AND GAG DEPLETED CARTILAGE. CS SELECTIVE STAINING FOR NATIVE AND GAG DEPLETED SAMPLES INDICATING THE PRESENCE OF CS WHERE THE DENSE BROWN COLOURATION IS LOCATED. A) NATIVE MEDIAL SAMPLE. B) GAG DEPLETED MEDIAL SAMPLE. C) NATIVE LATERAL SAMPLE. D) GAG DEPLETED LATERAL SAMPLE. SCALE BAR = 500 MM.	171
FIG 5.4: QUANTIFICATION OF GAG CONTENT OF NATIVE AND GAG DEPLETED CARTILAGE. DATA IS SHOWN AS THE MEAN (N=6) ± 95% CL. * INDICATES SIGNIFICANT (P<0.05, STUDENTS T-TEST).	172
FIG 5.5: STRUCTURE OF STAINS-ALL DYE.	172
FIG 5.6: QUANTITATIVE MEASUREMENTS OF AVERAGE SDS LEVELS IN VARIOUS WASHES OF MEDIAL (TOP) AND LATERAL (BOTTOM) TISSUE SAMPLES (N=3). WAVELENGTH READ AT 447NM. RESULTS ARE THE MEAN READINGS (N=3) ± 95 % CL, WHERE SIGNIFICANCE (P<0.05) IS INDICATED BY *.	173
FIG 5.7: IMAGES OF P ₁₁₋₄ ONLY HYDROGELS (10MGML ⁻¹) IN THE PRESENCE OF SDS AT 0.1 % STARTING SDS CONCENTRATION.	174
FIG 5.8: FLUORESCENCE MICROGRAPH OF PEPTIDE INJECTED TISSUE. GEL WAS P ₁₁₋₄ :P ₁₁₋₄ -CS 32:1 (P ₁₁₋₄ -FLUORESCIN DOPED 150:1) INJECTED GAG DEPLETED TISSUE.	175
FIG 5.9: CONFOCAL IMAGES OF FLUORESCIN ONLY CONTROL WITHIN ARTICULAR PORCINE CARTILAGE AND FRAP RECOVERY DATA. A) PRE-BLEACHING MICROGRAPH WITH THE POSITIVE CONTROL CIRCLED IN BLUE, WHILE THE NEGATIVE CONTROL CIRCLED IN RED. B) POSITIVE CONTROL AREA HAS BEEN PHOTO-BLEACHING USING 100% POWER FOR 488NM LASER.	

C) POST-BLEACHING SHOWS RECOVERY OF FLUORESCENCE AFTER ~50 MS. GRAPH REPRESENTS FLUORESCENCE RECOVERY RATE OF OVER 100 MS FOLLOWING PHOTO BLEACHING OF CONTROL AREA. SCALE BAR = 50 MM.	176
FIG 5.10: STRUCTURE OF FLUORESCIN LABELLED P ₁₁ -4 USED IN THE FRAP EXPERIMENTS.	177
FIG 5.11: CONFOCAL MICROGRAPHS OF P ₁₁ -4 ONLY CONTROLS INJECTED WITHIN ARTICULAR PORCINE CARTILAGE AND FRAP RECOVERY DATA. A) PRE-BLEACHING MICROGRAPH WITH THE POSITIVE CONTROL CIRCLED IN BLUE, WHILE THE NEGATIVE CONTROL CIRCLED IN RED. B) POSITIVE CONTROL AREA HAS BEEN PHOTO-BLEACHING USING 100% POWER FOR 488NM LASER. C) POST-BLEACHING SHOWS SOME RECOVERY OF FLUORESCENCE AFTER ~50 MS. GRAPH REPRESENTS FLUORESCENCE RECOVERY RATE OF OVER 100 MS FOLLOWING PHOTO BLEACHING OF CONTROL AREA. SCALE BAR = 20 MM.	178
FIG 5.12: CONFOCAL IMAGES OF P ₁₁ -4-CS CONTROL WITHIN ARTICULAR PORCINE CARTILAGE AND FRAP RECOVERY DATA. A) PRE-BLEACHING MICROGRAPH WITH THE POSITIVE CONTROL CIRCLED IN BLUE, WHILE THE NEGATIVE CONTROL CIRCLED IN RED. B) POSITIVE CONTROL AREA HAS BEEN PHOTO-BLEACHING USING 100% POWER FOR 488NM LASER. C) POST-BLEACHING SHOWS RECOVERY OF FLUORESCENCE AFTER ~50 MS. GRAPH REPRESENTS FLUORESCENCE RECOVERY RATE OF OVER 100 MS FOLLOWING PHOTO BLEACHING OF CONTROL AREA. SCALE BAR = 50 MM.	180
FIG 5.13: FLUORESCIN LABELLED CS MOLECULE USED IN THE FRAP EXPERIMENTS.	181
FIG 5.14: CONFOCAL IMAGES OF FLUORESCENTLY LABELLED CS ONLY CONTROL WITHIN ARTICULAR PORCINE CARTILAGE AND FRAP RECOVERY DATA. A) PRE-BLEACHING MICROGRAPH WITH THE POSITIVE CONTROL CIRCLED IN BLUE, WHILE THE NEGATIVE CONTROL CIRCLED IN RED. B) POSITIVE CONTROL AREA HAS BEEN PHOTO-BLEACHING USING 100% POWER FOR 488NM LASER. C) POST-BLEACHING SHOWS RECOVERY OF FLUORESCENCE AFTER ~50 MS. GRAPH REPRESENTS FLUORESCENCE RECOVERY RATE OF OVER 100 MS FOLLOWING PHOTO BLEACHING OF CONTROL AREA. SCALE BAR = 50 MM.	182
FIG 5.15: TYPICAL SCHEMATIC OF CARTILAGE THICKNESS MEASUREMENT (TOP) AND REAL DATA INTERPRETATION (BOTTOM). A REPRESENTATION OF THE DATA ANALYSIS AND THE CORRESPONDING REGIONS OF THE CARTILAGE SAMPLE (TOP). THE THICKNESS OF THE CARTILAGE LAYER IS CALCULATED FROM THE INTERCEPTION POINT FROM THE GRADIENTS CHOSEN WHERE THE BOUNDARIES OF THE CARTILAGE ARE – THE EXAMPLE SHOWN IS FOR A MEDIAL SAMPLE WHERE THE CALCULATED CARTILAGE THICKNESS = 2.01 MM.	186
FIG 5.16: SUMMARY OF MEAN DEFORMATION DATA AFTER 1HR. DEFORMATION WAS SHOWN OVER 1HR (3600s) FOR EACH CONTROL GROUP SEPARATED FOR THE TWO CONDYLES – MEDIAL SAMPLES (TOP) AND LATERAL SAMPLES (BOTTOM) WITH DATA REPRESENTING MEAN (N=3) ± 95% CL. LABELS – M = MEDIAL, L = LATERAL, H = NATIVE (HEALTHY), S = SDS GAG DEPLETED, HN = NATIVE NEEDLE ONLY, HS = NATIVE SHAM INJECTION, S + P = GAG DEPLETED + P ₁₁ -4-CS 10 MGML ⁻¹ INJECTED, S + CS = GAG DEPLETED + CS ONLY INJECTED, S + P ₁₁ -4 30 = GAG DEPLETED + P ₁₁ -4 30 MGML ⁻¹ ONLY, S + P ₁₁ -4-CS 30 = GAG DEPLETED + P ₁₁ -4-CS 30 MGML ⁻¹ , S + P ₁₁ -8-CS 30 = GAG DEPLETED + P ₁₁ -8-CS 30 MGML ⁻¹	188
FIG 5.17: PERCENTAGE DEFORMATION AT EQUILIBRIUM END POINT. THE DATA SHOWS THE PERCENTAGE DEFORMATION ONCE THE TISSUE HAS REACHED AN EQUILIBRATED STATE ~ 1HR. THE DATA IS SPLIT INTO TWO DATA SETS, MEDIAL (TOP) AND LATERAL (BOTTOM) SAMPLES, WITH THE MEAN VALUES (N=3) ± 95 % CL SHOWN, WHERE SIGNIFICANCE (P<0.05, STUDENT T-TEST) IS INDICATED BY *. LABELS – M = MEDIAL, L = LATERAL, H = NATIVE (HEALTHY), S = SDS GAG DEPLETED, HN = NATIVE NEEDLE ONLY, HS = NATIVE SHAM INJECTION, S + P = GAG DEPLETED + P ₁₁ -4-CS	

10 MGML⁻¹ INJECTED, S + CS = GAG DEPLETED + CS ONLY INJECTED, S + P₁₁₋₄ 30 = GAG DEPLETED + P₁₁₋₄

30 MGML⁻¹ ONLY, S + P₁₁₋₄-CS 30 = GAG DEPLETED + P₁₁₋₄-CS 30 MGML⁻¹, S + P₁₁₋₈-CS 30 = GAG DEPLETED +

P₁₁₋₈-CS 30 MGML⁻¹. 189

Abbreviations

ACI	Anterior cruciate ligament
AFM	Atomic force microscopy
ANOVA	Analysis of variance
BHK	Baby hamster kidney
BSA	Bovine serum albumin
CL	Confidence level
CS	Chondroitin sulfate
DIAD	Diisopropyl azodicarboxylate
DMEM	Dulbecco's modified eagle's media
DMF	Dimethylformamide
DMMB	1,9-dimethylmethylene blue
DMSO	Dimethyl sulphoxide
ECM	Extracellular matrix
EDTA	Ethylenediaminetetraacetic acid
FBS	Foetal bovine serum
FT-IR	Fourier transformed infrared spectroscopy
GAG	Glycosaminoglycans
GalNAc	N-acetyte galactosamine
GlcUA	Glucuronate
GMEM	Glasgow's minimal essential media
HA	Hyaluronan (Hyaluronic acid)
ICRS	International Cartilage Repair Soceity
LC-MS	Liquid-chromatography – mass spectroscopy
LVDT	Linear variable differential transducer
Mca	Methylcoumarin
MS	Mass spectroscopy
NMR	Nuclear magnetic resonance spectroscopy
OA	Osteoarthritis
PBS	Phosphate buffered saline
PCL	Poly (ϵ caprolactone)

PEG	Polyethylene glycol
PGA	Poly glycolic acid
PLA	Poly lactic acid
PLLA	Poly (L) lactic acid
PPD	<i>P</i> -phenylene diamine
PVA	Poly vinyl alcohol
SAPs	Self-assembling peptides
SD	Standard deviation
SDS	Sodium dodecyl sulfate
SEC-MALLS	Size exclusion chromatography – multi angle laser light scatter
SFZ	Superficial zone
TBS	Tris buffered saline
TEM	Transmission electron microscopy
TPB	Tryptone phosphate broth

Chapter 1

Introduction

1. General Introduction

Cartilage is a connective tissue, which is found throughout the body, in particular surrounding hard tissues such as bone. The tissue has a sparse cell distribution of chondrocytes, contributing only a small volume within adult tissue (Foundation, 2002), which are found within an extracellular matrix (ECM) mainly comprised of collagen, proteoglycans (PGs) such as aggrecan, glycosaminoglycans (GAGs) such as chondroitin sulfate (CS) and hyaluronan and water. It can be described as a “stiff, inelastic tissue” (Fisher, 2013). Unlike other tissues, it is avascular, alymphatic and aneural and thus it has a low nutrient influx which is maintained through physical processes such as diffusion and mechanical stimulation – compression and expansion. This lack of blood supply gives rise to the low regenerative nature of cartilage after injury and damage (Jahn et al., 2016).

There are different types of cartilage: hyaline, elastic and fibrocartilage (Lee, 2007). Hyaline cartilage is found in the endplates of vertebrae, intervertebral discs and articulating joints – where it is known as articular cartilage. Elastic cartilage is found within tendon and ligament insertion sites such as found around the knee and the outer ear. Fibrocartilage is the type of cartilage found within the annulus fibrosis of intervertebral discs as well as the menisci in the knee joint, but as discussed later on it can form after trauma and surgery to articular cartilage. Each type of cartilage has a different basic function and thus has a different composition in terms of the components found within the ECM (Eslahi et al., 2016). Hyaline or articular cartilage is mainly responsible for providing the near frictionless surface necessary for diarthrodal joints to function correctly and efficiently. The function of elastic cartilage is to support and maintain the shape and form of the tissue surrounding it. The function of fibrocartilage is to provide a very flexible and compressible basis for other tissue types to form around, in the case of the annulus fibrosis for example.

In terms of extracellular components, hyaline cartilage consists of mainly collagen and PGs such as aggrecan, while elastic cartilage incorporates elastic fibres such as elastin. Fibrocartilage is similar to hyaline cartilage in consisting predominately of collagen and PGs but the proportions of each differ, in that it has a lower proteoglycan and higher collagen content (Verma, 2001, Bhattacharjee et al., 2015).

1.1 Hyaline articular cartilage

1.1.1 Function of hyaline articular cartilage

Hyaline articular cartilage is the predominant type of cartilage found within articulating joints such as the knee. It provides protection between the two articulating surfaces of the bones from abrasion due to its near frictionless properties thus ensuring a smooth movement of the bones over one another and helps minimise the impact damage experienced by the joint during situations such as jumping and/or falling by distributing the weight evenly over the joint instead of on a specific point of the joint (Pearle, 2005, Sophia Fox, 2009).

1.1.2 Composition and structural features of hyaline articular cartilage

Articular cartilage comprises two different components in essence: a solid component and a fluidic component, where the interactions between these two components are paramount in determining the mechanical properties and in turn the function of articular cartilage.

The fluidic component is water at physiological pH ~ 7 , along with physiological concentrations of ionic solutes such as Na^+ , K^+ , Ca^{2+} and Cl^- which are summarised in **Table 1.1** (Kienle et al., 2015, Boettcher et al., 2016).

Species	Concentration in Superficial Zone (mM)	Concentration in Deep Zone (mM)	Ref.
Na^+	210-230	260-320	(Kienle et al., 2015, Urban, 1994)
K^+	7	9-11	
Ca^{2+}	4-6	8-15	
Cl^-	100-110	70-90	

Table 1.1: The concentration ranges for various ionic solutes found within the superficial and deep zones of articular cartilage.

This contributes to 75-80% of the wet weight of articular cartilage (Maroudas, 1979). The solid component consists of approximately 1-2% chondrocytes but depending on the source chondrocytes may contribute up to 10%, up to 95 % collagen – mainly type II, 3-10% PGs, $\sim 10\%$ lipids and small amounts of glycoproteins – which are polypeptide chains functionalised with carbohydrate groups typically found on cellular membranes (2004, Saltzmann, 2004).

1.1.3 Collagen

Collagen is the most abundant structural protein found in articular cartilage and accounts for approximately 90 – 95 % of the dry weight of cartilage. There are various types of collagen with different structures depending on the tissue location.

The various types of collagen all have the same fundamental unit within the structure: a triple helical motif that forms through the molecular interactions between three polypeptide chains. Each of the polypeptide chains consists of ~1000 amino acid residues, and each type of collagen has a specific set of three polypeptide chains within its makeup (Pearle, 2005, Ofek et al., 2008, Saltzmann, 2004). There are no fewer than 29 different polypeptide chains which make up the 15 distinct types of collagen found within cartilage including types I, IV, V, VI, IX and XI in small amounts (< 5%) and type II. Each polypeptide chain consists mainly of glycine and proline residues and hydroxyproline helps stabilise the structures (Saltzmann, 2004, Hunziker et al., 2015).

Collagen is produced by chondrocytes. The cells secrete procollagen molecules which undergo enzymatic cleavage within the extracellular environment to form a triple helix. The triple helices can undergo further organisation *via* inter and intra molecular bonds such as hydrogen bonding from hydroxyproline residues and disulfide bridges from cysteine residues to form fibrils and fibres, which are stabilised by crosslinking between lysine residues (Ofek et al., 2008, Pearle, 2005). A schematic showing the production of collagen and the various intermediates is shown in **Fig 1.1**.

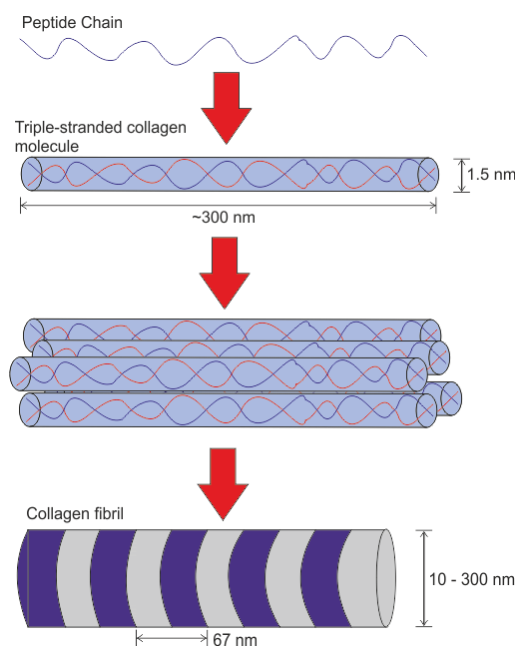


Fig 1.1: A schematic showing the various intermediate structures during collagen production, as well as typical dimensions.

Fibril forming types of collagen include type I, II and III. Type II is the collagen predominately found in articular cartilage accounting for 60 % of the dry weight. It is made up of three $\alpha 1$ (II) polypeptide chains and consists of high levels of 4-hydroxylysine and carbohydrate. These fibrils are thinner than those formed by type I collagen (Ofek et al., 2008, Pearle, 2005). Type I collagen

consists of two $\alpha 1(I)$ chains and one $\alpha 2(I)$ chain, and features low levels of 5-hydroxylysine and carbohydrate and the fibrils formed are broad. Type III collagen differs from the previous two, in that it is made up of three $\alpha 1(III)$ chains but has high levels of 4-hydroxyproline and low levels of 5-hydroxylysine and carbohydrate but this type is not found within articular cartilage tissue and is found mainly in elastic cartilage within skin, blood vessels and internal organs (Pearle, 2005, Hosseininia et al., 2016).

Articular cartilage also contains other collagen types that form fibrils and globular like structures such as types V, VI, IX and XI (Pearle, 2005, Saltzmann, 2004, Hunziker et al., 2015). The roles of these types of collagen are still not fully understood but hypotheses have been put forward to suggest that they play a role in interactions between molecules and help modulate the macrostructure of collagen type II (Saltzmann, 2004) Type X, which is found predominately within calcified cartilage (see below), appears to be involved in the process of cartilage mineralisation at the interface between the cartilage and the underlying subchondral bone (Ofek et al., 2008, Pearle, 2005, Saltzmann, 2004).

1.1.4 Glycosaminoglycans and proteoglycans

Glycosaminoglycans (GAGs) are high molecular weight polysaccharides which, due to being heavily sulfated, are negatively charged. Every GAG is a poly (disaccharide) of two regularly repeating sugar residues which are characteristic of the GAG (Fajardo et al., 2014). The different sugar residues of the GAGs found within articular cartilage as well as other characteristics associated with each GAG are summarised in **Table 1.2**.

GAG	MW (kDa)	Residue A	Residue B	Sulfated	Covalently Linked to proteins	Contains other sugar residues	Tissue
Hyaluronic Acid	4 – 8,000	D-glucuronic acid	N-acetyl-D-glucosamine	-	-	-	Cartilage, synovial fluid, connective tissue, vitreous body, skin
Chondroitin Sulfate	5 – 50	D-glucuronic acid	N-acetyl-D-galactosamine	+	+	+	Cartilage, skin, cornea, bone, arteries
Keratan Sulfate	4 - 19	D-galactose	N-acetyl-D-glucosamine	+	+	+	Cartilage, intervertebral discs, cornea

Table 1.2: The different types of GAGs found in articular cartilage and their associated characteristics, where residue A and B refer to the repeating units within a polysaccharide chain and where +/- indicates the presence or absence of the described characteristic (Adapted from Saltzmann, 2004 with permission from Oxford University Press).

Most sulfated GAGs contain other sugar residues, which creates further complexity in the linear chemical structure. GAGs are unbranched, inflexible but very soluble in water, allowing adoption of a random coil conformation. This conformation allows the GAGs to occupy a large volume in aqueous media. Each GAG chain extends within the space and interacts with other GAG chains to form further structures, thus causing the formation of highly hydrated gels at relatively low concentrations of GAGs. In physiological aqueous media, counter ions such as Na^+ surround the sulfated GAG chains, creating an osmotic pressure which pulls further water molecules into the gel. Due to this action, tissues such as cartilage which are high in sulfated GAGs have high resistance to compression (Athanasίου, 2009, Pearle, 2005, Saltzmann, 2004). With the exception of hyaluronic acid, GAGs covalently bind to a core protein forming macromolecular structures called proteoglycans.

Proteoglycans are one of the largest groups of macromolecules in the ECM, representing between 10-15% of the wet weight. Each proteoglycan can consist of one or more GAG types, such as aggrecan which consists predominately of chondroitin sulfate and a smaller quantity of keratan sulfate that are covalently bound to a core protein through linker proteins. Aggrecan

consists of ~ 130 GAG chains, and the molecular weight of the core protein is 210kDa (Athanasίου, 2009, Pearle, 2005, Saltzmann, 2004). The global structure of aggrecan, in a schematic form, is shown in **Fig 1.2**.

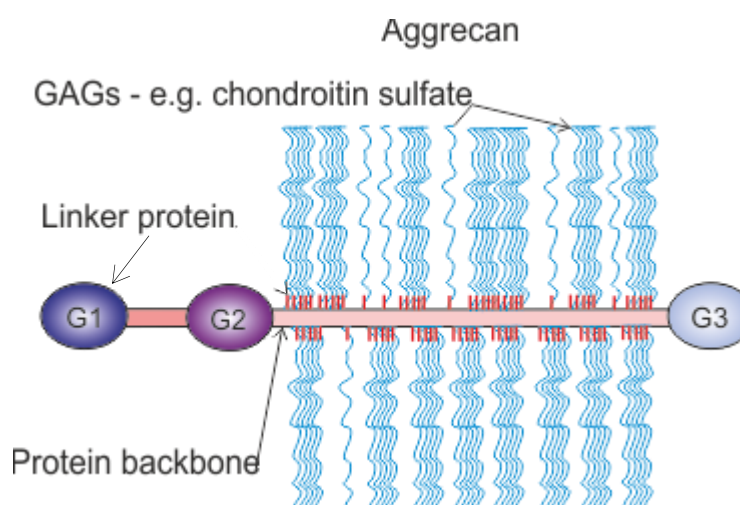


Fig 1.2: A schematic representation of aggrecan, G1, G2 and G3 represent globular domains involved in chondrocyte apoptosis, binding of hyaluronan, cell adhesion and aggregation.

Aggrecan is the most abundant and largest proteoglycan found within articular cartilage, and it is characterised by the ability to further assemble by aggregating with hyaluronic acid through linker proteins to form large proteoglycan aggregates.

Aggrecan fills the interfibrillar space of the articular cartilage ECM, and due to the negative charge on the GAG chains and the counter ions, the osmotic pressure formed – called the Donnan osmotic pressure, is critical to the compressive resistance of articular cartilage. This negative charge is called a “fixed charge density” when applied to the cartilage ECM, and the osmotic pressure imbibes fluids into the tissue to help maintain equilibrium (Athanasίου, 2009, Pearle, 2005, Saltzmann, 2004). The equilibrium is between the swelling of the tissue by the influx of fluids and the restraint imposed by the inelastic nature of the collagen network. When the cartilage is loaded, after the load has been displaced the fluid within cartilage is restored to equilibrium and this helps dissipate the force throughout the entire tissue. This is explained by the biphasic theory which will be discussed in later sections (Athanasίου, 2009, Pearle, 2005, Saltzmann, 2004).

This equilibrium is also important to the functional properties of cartilage when under pressure since function is highly dependent on the fluid pressure within the tissue (Athanasίου, 2009, Pearle, 2005, Saltzmann, 2004). Due to the fact that GAGs give rise to this osmotic pressure, a loss of GAGs would result in a loss of fluid pressure within the tissue, therefore impairing the mechanical function of the cartilage (Saltzmann, 2004; Pearle *et al.*, 2005; Athanasίου *et al.*,

2009). This breakdown in function has been reported in advancing stages of diseases such as osteoarthritis which will be discussed in later sections (Athanasίου, 2009, Pearle, 2005, Saltzmann, 2004).

Articular cartilage contains other proteoglycans which do not form aggregates, and are characterised by the ability to interact with the collagen network. These proteoglycans include decorin, biglycan and fibromodulin, which are all smaller than aggrecan but are present in similar molar quantities to aggrecan (Athanasίου, 2009, Pearle, 2005, Saltzmann, 2004). These all have similar protein structures, only varying in the GAG composition and the function of the proteoglycan. Biglycan and decorin possess 2 and 1 dermatan sulfate, another type of GAG, respectively, while fibromodulin possesses multiple keratan sulfate chains (Athanasίου, 2009, Pearle, 2005, Saltzmann, 2004). The function of each differs; decorin and fibromodulin interact with type II collagen fibrils in the ECM and are involved in fibrillogenesis and the interactions between fibrils. Biglycan on the other hand is found around chondrocytes and interacts with collagen type VI (Athanasίου, 2009, Pearle, 2005, Saltzmann, 2004).

1.1.4.1 Chondroitin sulfate

Chondroitin sulfate is the most abundant GAG in articular cartilage, which, as shown in **Table 1.2**, is made up of two repeating saccharide molecules: D-glucuronic acid and N-acetylgalactosamine. The two saccharides are linked through an $\alpha(1\rightarrow3)$ covalent bond, where the 1 and 3 represent the carbon bearing the oxygen through which the bond forms. Each of the repeating disaccharide molecules are linked through either a $\beta(1\rightarrow4)$ or $\beta(1\rightarrow3)$ covalent bond (Bali, 2001). The core structure of chondroitin sulfate is shown in **Fig 1.3**. Chondroitin sulfate gains the sulfate part of its name from the fact the galactosamine residues are sulfated in one of two places; position 4 or position 6 giving rise to two different isomers of chondroitin sulfate – chondroitin 4 sulfate and chondroitin 6 sulfate. The ratio of these two isomers is different depending on the type of cartilage as well as the age and health of the cartilage. As cartilage ages, the amount of these saccharide molecules that are sulfated in the two positions changes. In adolescent cartilage, there is up to a four times greater concentration of the 4-sulfated chondroitin sulfate in the deeper regions of the cartilage compared to the upper residues. This changes as the cartilage matures and ages with the predominant residue becoming chondroitin 6 sulfate rather than chondroitin 4 sulfate (Bali et al., 2001, Bayliss, 1999).

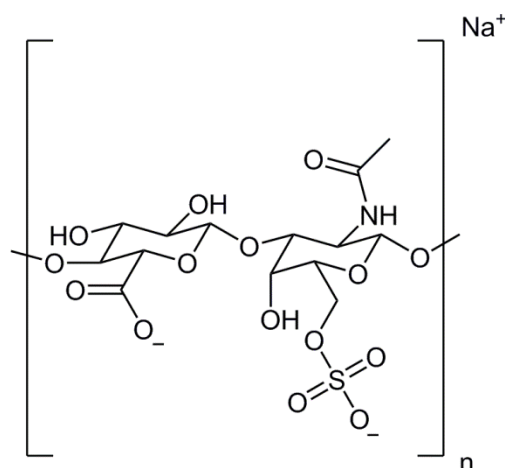


Fig 1.3: The basic structure of chondroitin-6-sulfate.

1.1.5 Other molecules

Articular cartilage, in addition to collagen, GAGs and proteoglycans contains small amounts of noncollagenous proteins such as fibronectin, tenascin, cartilage oligomeric protein, chondrocalcin, superficial zone protein, thrombospondin and matrix-GLA (glycine, leucine, and alanine) protein (Athanasίου, 2009, Pearle, 2005, Saltzmann, 2004), lipids, phospholipids, glycoproteins and inorganic crystal compounds such as hydroxyapatite within calcified cartilage (Athanasίου, 2009, Pearle, 2005, Saltzmann, 2004, Bhattacharjee et al., 2015). The functions of these components are unclear currently, but theories exist speculating that they are involved in organising and maintaining the macromolecular structure of the ECM.

1.1.6 Microstructure and extracellular matrix of articular cartilage

As discussed above, the make-up of articular cartilage ECM consists of a varying amount of collagen, proteoglycans and non-collagenous proteins (Fisher, 2013). The biomechanical properties of articular cartilage are aided by organisation of the tissue structure which comprises of the pericellular, territorial and inter-territorial matrices. The force being exerted upon the tissue is transmitted throughout the three matrices before reaching the chondrocytes, thus assisting in regulating the strains observed at the cellular level (Athanasίου, 2009).

1.1.6.1 Pericellular matrix

The pericellular matrix is a thin layer encapsulating the cell membrane of chondrocytes within articular cartilage. It comprises fine collagen fibres, a high concentration of proteoglycans, some glycoproteins, other noncollagenous proteins, and a small amount of fibronectin and collagen type VI (Athanasίου, 2009, Sophia Fox, 2009, Wilusz et al., 2014). The precise function of the matrix is currently unknown but evidence indicates it may have two functions:

1. Protect the physical integrity of the articular chondrocytes during compressive loading (Athanasίου, 2009).
2. Play a functional role of initiating signal transduction within articular cartilage when load bearing (Sophia Fox, 2009).

1.1.6.2 Territorial matrix

The territorial matrix surrounds the pericellular matrix and is thicker and comprises similar molecular components to the surrounding extracellular matrix, predominantly collagen type II and proteoglycans (Athanasίου, 2009, Hosseininia et al., 2016). The amount of proteoglycans in the territorial matrix is higher than the surrounding extracellular matrix. The collagen structure is also finer, forming a basket-like network around the chondrocytes (Sophia Fox, 2009). The function of the territorial matrix is thought to be to protect the chondrocytes from mechanical stresses and it may be partially responsible for the resilience of the articular cartilage structure and its resistance to high loads (Sophia Fox, 2009).

1.1.6.3 Inter-territorial matrix

The inter-territorial matrix is the largest of the three matrices, contributing to the biomechanical properties of the tissue (Sophia Fox, 2009), (Athanasίου, 2009, Hosseininia et al., 2016). It comprises large collagen type II fibres orientated in different planes depending on the zone of the inter-territorial matrix; parallel to the surface in the superficial zone, obliquely in the middle zone and perpendicular to the surface in the deep zone (Sophia Fox, 2009), (Athanasίου, 2009). The concentration of proteoglycans varies within this matrix; depending on the zone (Sophia Fox, 2009), (Athanasίου, 2009).

1.1.7 Macrostructure of articular cartilage

Hyaline cartilage has a macro structure in which, morphologically, there are four separate zones as mentioned above, in increasing depth: the superficial zone, transitional zone, middle or deep zone and calcified cartilage zone (Bhosale, 2008, Pearle, 2005, Athanasίου, 2009, Gaut and Sugaya, 2015).

The composition and structure of the extracellular matrix along with the composition, structure and function of the chondrocytes within each zone changes due to the different roles each plays within the whole cartilage structure (Bhosale, 2008). The macrostructure of articular cartilage is illustrated in **Fig 1.4**.

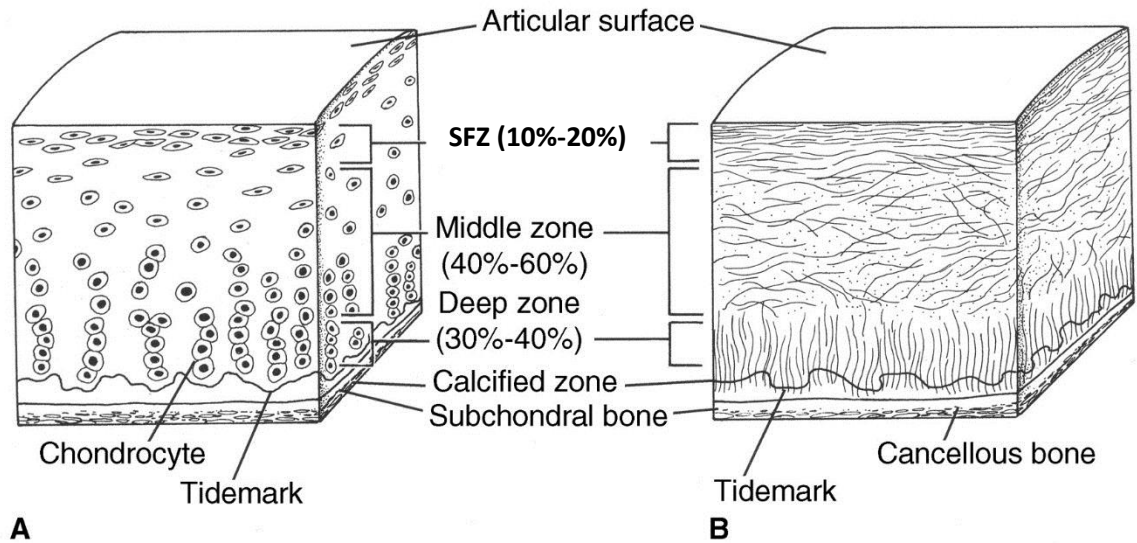


Fig 1.4: The macrostructure of articular cartilage, with the chondrocyte morphology and localisation (A) and collagen orientation (B) of the corresponding zone show (reproduced from Jazrawi et al., 2011 with permission from Journal of the American Academy of Orthopaedic Surgeons).

1.1.7.1 Surface – lamina splendens

The surface of articular cartilage, ranging from between hundreds of nanometres to several microns, is covered by a proteinaceous layer called the *lamina splendens* (Athanasίου, 2009). The *lamina splendens* is an acellular, predominantly non-fibrous region, the function of which is not precisely known but there are several hypotheses which have been suggested ranging from an added layer of protection for the cartilage surface through supporting proteins involved in lubrication such as lubricin, hyaluronan-aggreccan aggregates, collagen type II and fibronectin through to acting as a surface anchor for collagen networks to form microstructures within the cartilage structure called arcades of benninghoff (Athanasίου, 2009, Glowacki and Thornhill, Andresen Eguiluz et al., 2015).

1.1.7.2 Superficial zone

The superficial zone (SFZ) or tangential zone, as it is sometimes called, is the upper most region of articular cartilage. This zone is reported to protect the deeper zones from damage caused by shear, tensile and compressive forces and stresses (Sophia Fox, 2009). One theory behind how this zone may protect the deeper zones is through the collagen fibril content and alignment. Here the fibres have a small diameter and are densely packed and are orientated in a highly ordered fashion parallel to the articular surface (Athanasίου, 2009, Pearle, 2005, Sophia Fox, 2009).

The collagen in this zone is mainly type II and IX (Sophia Fox, 2009). The appearance, shape and function of the chondrocytes within this region also contributes to the protecting function as

the chondrocytes are small in size and are flattened with a parallel orientation to the surface (Kheir, 2009, Gaut and Sugaya, 2015).

The chondrocytes in the superficial zone express proteins which have a lubricating and protective function specifically superficial zone protein (SZP), while secreting relatively low levels of proteoglycans (Pearle, 2005). The majority of the tensile properties of articular cartilage result from this region, where the compressive modulus is the lowest of the zones and can deform up to 25 times more than the zone below it – the transitional or middle zone.

1.1.7.3 Transitional zone

The transitional or middle zone acts as a “functional and anatomic bridge” (Sophia Fox, 2009) between the superficial and deep zones by being the first line of resistance to compressive forces. The compressive modulus is higher compared to the superficial zone, partially due to the orientation of the collagen fibrils that are also thicker than the superficial zone fibrils. The less organized arrangement is exhibited by an “arcade-like structure” (Athanasίου, 2009) interspersed with random obliquely orientated fibres (Athanasίου, 2009, Pearle, 2005, Sophia Fox, 2009).

The amount of proteoglycans is at a higher level in the middle zone and the shapes of the chondrocytes are different. The chondrocytes are larger; more rounded and arranged either singly or in isogenous groups, but the density of the cells is lower than in the superficial zone (Athanasίου, 2009, Pearle, 2005, Sophia Fox, 2009, Kheir, 2009).

1.1.7.4 Deep zone

The deep zone is the last purely hyaline tissue region. It provides the majority of the compressive force resistance, which arises from the orientation of the collagen fibrils which are larger in diameter and sit in a perpendicular orientation to the surface with anchors to the subchondral bone lying underneath (Athanasίου, 2009, Pearle, 2005, Sophia Fox, 2009).

The amount of proteoglycans is at a maximum in the deep zone, while having the lowest water content and cell density. The chondrocytes in the deep zone are larger and group into a columnar organization, being parallel to the collagen fibres and perpendicular to the joint surface (Athanasίου, 2009, Pearle, 2005, Sophia Fox, 2009, Kheir, 2009, Gaut and Sugaya, 2015).

1.1.7.5 Calcified cartilage zone

There is a thin line between the deep zone and the calcified zone called the “tidemark” (Athanasίου, 2009, Pearle, 2005, Sophia Fox, 2009). The calcified zone is where the tissue undergoes a transition into subchondral bone, and aids in maintaining the structural integrity of the articular cartilage by securing the collagen fibrils of the deep zone to the subchondral

bone underneath (Athanasίου, 2009, Pearle, 2005, Sophia Fox, 2009). It minimises the stiffness gradient experienced between stiff, rigid bone and softer, more pliable cartilage (Athanasίου, 2009, Pearle, 2005, Sophia Fox, 2009). The chondrocytes scarcely populate this region and are in a state of hypertrophy (Athanasίου, 2009, Pearle, 2005, Sophia Fox, 2009, Kheir, 2009).

1.1.8 Lubrication mechanism of hyaline cartilage

In articulating joints, despite the resistance articular cartilage has inherently due to its structure, there is a need for lubrication. The joint comprises of three components: the two corresponding ends of the bone involved in the joint and the synovial fluid and membrane. The synovial fluid is a non-newtonian fluid that surrounds the joint and is involved in lubricating the joint to achieve two main objectives: help dissipate the force experienced when the joint is under loading and to help dissipate the heat generated through friction during articulation. The actual mechanism through which the synovial fluid and cartilage surface interact to achieve adequate lubrication has been studied and developed over many decades (Majd et al., 2014, Daniel, 2014).

1.1.8.1 Fluid film lubrication

Various theories have been proposed over the years on how articular cartilage undergoes lubrication during articulation. These theories originated with the fluid film lubrication regime, and its subsequent variations, which were proposed initially in 1886 by Reynolds (Reynolds, 1886). The basic idea of the regime was that the synovial fluid supported the entire joint when articulation occurred thus lubricating the joint and preventing contact from occurring (Jin and Dowson, 2011). This mechanism regime occurs when two articulating surfaces are partitioned entirely by a film of thin fluid which enables the joint to articulate while experiencing very low friction.

As fluids are incompressible, when a pressure is applied the fluid supports the load experienced by the surfaces. One key feature for this mechanism to work is that the thickness of the fluid film is at least three times greater than the height of the combined surface projections or asperities.

Over the past seven decades, there have been five variations of the fluid film regime proposed: hydrodynamic (Ateshian et al., 1997, Dowson, 1967), elasto-hydrodynamic/micro-elastohydrodynamic (Dowson and Jin, 1986, Daniel, 2014), squeeze film (Ateshian et al., 1997), boosted (Walker *et al.*, 1968; Langfield *et al.*, 1969) and weeping/hydrostatic lubrication (McCutchen, 1959).

1.1.8.2 Boundary lubrication

The inherent problem with the fluid film lubrication regime theory was highlighted by Sir John Charnley in 1960 (Charnley, 1960). He proposed that the speeds and loads experienced within the joint were not appropriate to generate a hydrodynamic lubricating film. He in turn proposed the boundary lubrication regime (Jin and Dowson, 2011). The basic idea of the boundary film regime is that instead of the synovial fluid supporting the whole joint, the fluid interacts with molecules produced during articulation because the local pressure exerted on the joint causes thermal degradation of the surface. The mono or multilayer of synovial fluid is adsorbed on to the surface which prevents direct contact of the surfaces to occur. Boundary lubrication regime takes over from fluid film when the combined surface roughness of the surfaces is greater than the thickness of the fluid film. Synovial fluid comprises of many different molecules, in particular hyaluronic acid (Gomis et al., 2004, Kobayashi et al., 2004, Lohmander et al., 1996, Puhl et al., 1993), lubricin (Jay et al., 2007, Schumacher et al., 1994), surface phospholipids (Basalo et al., 2007a, Forsey et al., 2006, Ozturk et al., 2004) and chondroitin sulfate (Basalo et al., 2007a). All of these, apart from chondroitin sulfate, have been proposed to be responsible as the lubricant responsible for this regime and studied in great detail. Chondroitin sulfate has been studied the least (Daniel, 2014).

1.1.8.3 Mixed lubrication

Mixed lubrication was proposed to explain how synovial joints are lubricated through a combination of both fluid film and boundary lubrication regimes.

The two different regimes were combined in 1967, when Dowson (Dowson, 1967) noticed a combination of the two regimes was probably responsible in equal parts: the film fluid regime involved in entraining and squeeze-film actions and the boundary film regime protecting the surface during extreme loads or during periods of inactivity (Jin and Dowson, 2011). The fluid film regime dominates until it breaks down when extreme or unfavourable loading conditions are experienced and then boundary lubrication dominates to help maintain the low friction between surfaces.

This is the most probable mechanism by which synovial joints are lubricated when under normal physiological conditions, but the other mechanisms may come into play under non-physiological or extreme loading conditions (Zhang et al., 2015).

1.1.8.4 Biphasic model

The previous lubrication regimes were based at the level of the synovial joint, being influenced by the composition and biochemical makeup of the joint surfaces. The biphasic lubrication model is based upon the intrinsic properties and structure of the articular cartilage itself. The

reason for this mechanism being termed biphasic is that articular cartilage is considered to have two distinct phases; a solid phase which constitutes a collagen-proteoglycan network, and a fluid phase which is the interstitial fluid (Zhang et al., 2015).

The biphasic model is a two component version of the mixed lubrication model. It was formulated by Mow *et al* in 1980 (Mow, 1980) based on the idea of interstitial fluid within cartilage being involved in the load bearing properties as proposed in 1959 by McCutchen (McCutchen, 1959). The model is based on the collagen-proteoglycan matrix being proposed to be intrinsically incompressible and a porous-permeable solid with the interstitial fluid modelled as an incompressible fluid (Ateshian et al., 2004).

The physical properties of the solid phase were assumed to be linearly elastic and permeable with a constant value throughout the entire tissue. The permeability was later modified to include strain-dependent permeability to improve the model (Lai et al., 1991). The reason articular cartilage is well suited to the biphasic regime is it is highly porous with pore sizes <10nm (Dowson, 1990).

The solid collagen-proteoglycan network is highly charged which allows the permeability to be very low $< 10^{-15} \text{m}^4 \text{Ns}^{-1}$ (Ateshian et al., 1997). The interstitial fluid, which moves upon exudation when under load, has a large drag force when flowing. These forces cause pressurisation of the interstitial fluid and allow it to be capable of bearing a load until the load pushes all the fluid into the unloaded regions. This then causes the solid collagen-proteoglycan phase to take over, which allows a low friction coefficient during motion to be maintained until the interstitial fluid can be regenerated to support the load again.

1.1.8.5 Triphasic model

The biphasic model was expanded further by Lai *et al* in 1991 (Lai et al., 1991) to include proteoglycans. The negatively charged proteoglycans are modelled as a negative charge density which is fixed to a solid matrix and the corresponding counter ions in the interstitial fluid modelled as additional fluid phases (Huang et al., 2005, Mow and Huijkes, 2005). The counter ions consist of monovalent cations present in the interstitial fluid that balance the negative charge on the collagen-proteoglycan network. The addition of this phase allowed greater accuracy when modelling and predicting cartilage tissue deformations (Lu, 2004). The different phases and the corresponding aspects within cartilage are shown in **Fig 1.5**.

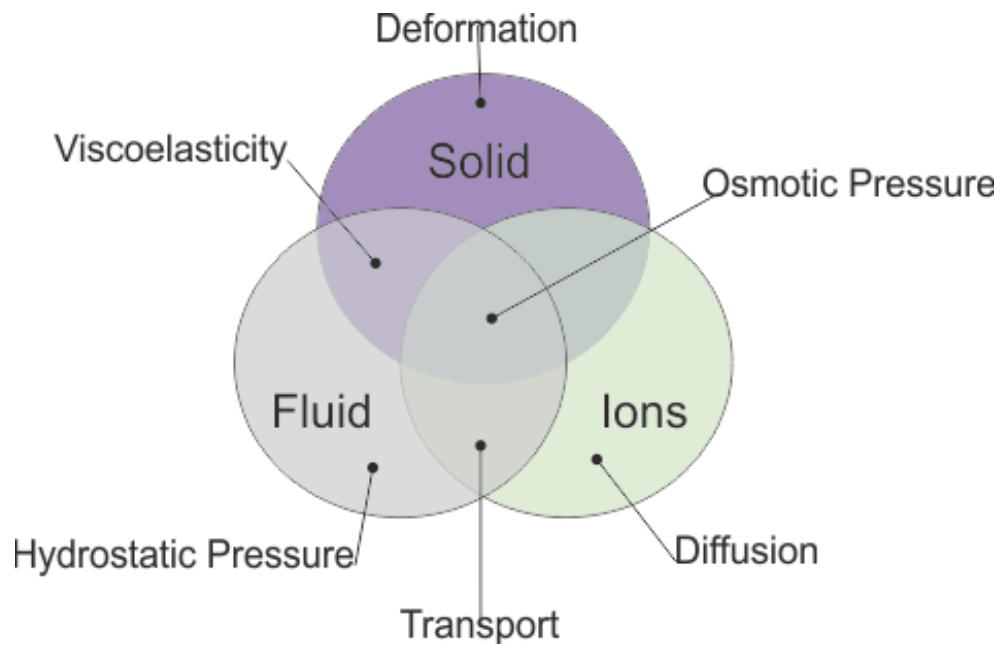


Fig 1.5: The different phases associated with the triphasic model, where for the biphasic model only the Fluid and Solid components are modelled.

From researching the various studies and results of these different components, the consensus of this author is that neither one of these components is the sole lubricant that allows boundary lubrication to occur. It is also this author's opinion that the lubrication regime responsible for lubricating articular joints is in fact the mixed lubrication regime as shown in **Fig 1.6**. During locomotion and articulation of the joint, there is a steady ingress and egress of synovial fluid within the joint which is explained through elastohydrodynamic lubrication – which is the extension and compression of components such as GAGs and proteins such as lubricin from the exertion of pressure upon the fluid (Daniel, 2014). However once locomotion has ceased and the joint becomes stationary the flow of synovial fluid ceases. When motion occurs again there is a “start-up” phase where different lubrication regimes are hypothesized to be involved. A mixed regime occurs to begin with where a combination of boundary and gel hydration lubrication occurs which ultimately leads to a weeping type lubrication regime to occur. It is these varying regimes that make the overall lubrication of cartilage so efficient and effective during locomotion.

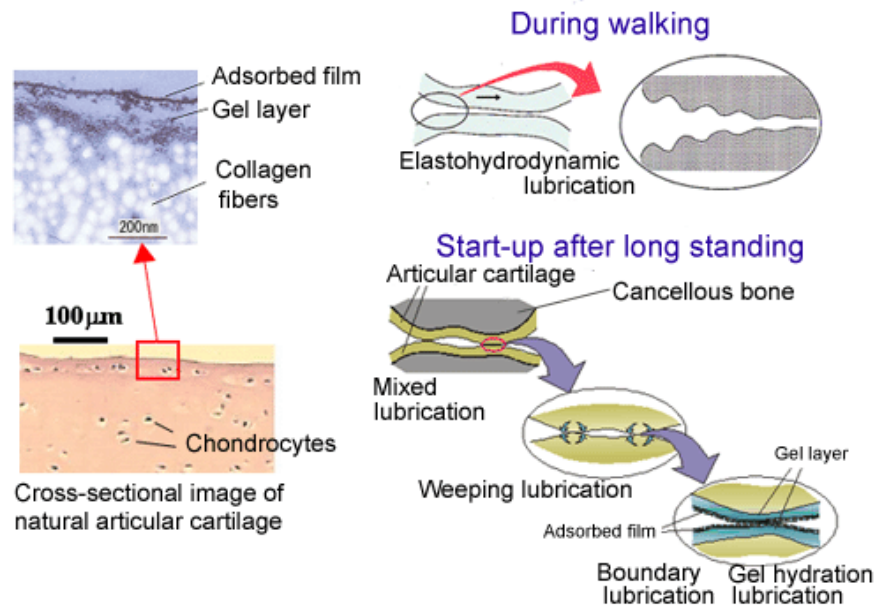


Fig 1.6: The various lubrication regimes association with articulation of articular joints (reproduced from <http://bio.mech.kyushu-u.ac.jp/SPR/research-en.html>, accessed 20/07/2014)

1.1.9 Wear of cartilage

Articular cartilage can wear through two mechanisms: mechanical and biochemical. In the basic definition wear is the removal of material from a surface or object through a repeating mechanical action of the surface against another surface or object.

This applies to articular cartilage due to the fact it is a “mechanical” joint in terms of the mechanics involved during articulation, but due to it being a biological tissue it can degrade through disease or due to biochemical agents. This may relate to the disruption of the collagen network, loss of proteoglycans or changes in the ionic equilibrium in both the tissue and synovial fluid.

Normal articular cartilage can undergo years of articulation with minimal wear due to the various features it possesses and mechanisms of lubrication. When abnormal conditions are applied to the tissue and/or joint such as trauma, disease or excessive biomechanical loading then the tissue cannot respond to the changes and wear occurs which can lead to irreparable damage.

1.1.9.1 Mechanical wear

There are two types of wear that articular cartilage may be subject to: fatigue wear and interfacial wear.

Fatigue wear is independent of the lubrication regime involved in the joint as it has been reported to occur because of cyclic stresses and strains that the application of repetitive loading causes during motion. The typical human joint undergoes 1-3 million cycles annually, and these

repetitive cycles have been shown to cause cyclic stresses and strains to form which can cause failure in the bulk material (Cawston and Wilson, 2006, Kienle et al., 2015).

The stresses and strains cause disruptions in the bone and cartilage structure which starts a cascade of reactions that potentially end with the onset of osteoarthritis as described below (Cawston and Wilson, 2006). The disruptions in the bone and cartilage result from interfacial wear.

Interfacial wear is when two or more surfaces come into proximity and solid-solid contact occurs. There are two types of interfacial wear: adhesive wear and abrasive wear (Cawston and Wilson, 2006). Adhesive wear occurs when two opposing surfaces form a junction when contact is made. When the junction is stronger than the inherent cohesive strength of each material then particles of the weaker material can tear off and adhere to the stronger material. Abrasive wear occurs in a similar way but it is when the two surfaces make contact and the softer material is damaged by the asperities of the harder material, which may be either the other surface or particles formed through other wear mechanisms (Cawston and Wilson, 2006, Kienle et al., 2015).

1.1.9.2 Biochemical wear

Biochemical wear occurs when the tissue enters a pathological state caused by conditions such as rheumatoid arthritis or collagen metabolic disorders. This type of degradation may also be a natural effect of chondrocytes aging which may alter the makeup of the ECM in terms of GAG molar ratios. These changes have been reported to cause the biomechanical properties of the cartilage tissue to deteriorate leading to degradation (Pecchi et al., 2012, Trevino et al., 2016).

1.2 Articular cartilage defects

There are three main types of defect associated with articular cartilage: superficial matrix disruption, partial thickness defects and full thickness defects. These can be expanded to five classifications to include normal cartilage and defects between partial and full thickness defects (Matsiko et al., 2013). The five classifications are shown in **Table 1.3**.

Grade	Description
0	Normal, healthy cartilage
I	Cartilage with visible swelling and softening
II	Partial thickness defect < 50% total cartilage thickness with no exposure of subchondral bone
III	Partial thickness defect > 50% total cartilage thickness with no exposure of subchondral bone
IV	Total loss of cartilage with subchondral bone exposed

Table 1.3: Grades and descriptions of the different classifications of articular cartilage defects as categorised by ICRS. (Adapted from Perera et al., 2012 with permission from the Royal College of Surgeons of England)

Grade I defects occur when microfractures form within the cartilage structure which can cause loss of GAGs in the superficial zone. These microfractures also cause thinning of the articular cartilage and in turn thickening of the calcified cartilage layer (Nukavarapu and Dorcemus, 2013). These types of defects occur when blunt trauma damages the ECM, but the chondrocytes can synthesise new matrix through aggregating into clusters near the site of damage (Matsiko et al., 2013).

Grade II defects occur when the articular cartilage is damaged beyond the superficial layer but only up to the middle zone. Grade III is when the articular cartilage damage extends into the calcified cartilage layer. Both grades are not self-repairable unlike grade I defects, meaning surgery or other treatments are required to prevent further degeneration (Matsiko et al., 2013, Nukavarapu and Dorcemus, 2013).

Grade IV defects occur when the entire cartilage layer is damaged and the subchondral bone is either exposed or damaged. This happens in extreme trauma cases or through progressive degradation usually through disease such as osteoarthritis (Matsiko et al., 2013, Nukavarapu and Dorcemus, 2013).

1.3 Osteoarthritic cartilage

Osteoarthritis is the most common type of arthritis in the modern world. It is a degenerative disease that causes the integrity of articular cartilage to become compromised (Pitsillides and Beier, 2011).

It was considered for a long time to be a “wear and tear” disease which was the only outcome from any process that led to increased pressure on a single joint (Berenbaum, 2013).

Osteoarthritis can affect any articulating joint, and it often results in decreased quality of life such as the inability to work. One of the problems with the disease is that it is usually only diagnosed in the advanced stages, by which point non-surgical treatments are generally ineffective and limited.

1.3.1 Pathophysiology of osteoarthritis

As mentioned in previous sections, cartilage lacks significant regenerative capabilities because it is avascular and has limited nutrient supply. This limited regenerative ability means that only small defects in the cartilage matrix such as loss of ECM components or deterioration of the collagen organisation can be repaired. In large defects the limits of this repairing ability are reached and the damage becomes permanent (Lorenz and Richter, 2006). Osteoarthritis has certain typical features in the form of degeneration or progressive loss of the functional structure of articular cartilage.

The causes of osteoarthritis can be classified as either primary or secondary. Primary osteoarthritis is generally related to aging and general “wear and tear” of daily life where there is no detectable structural deformities or abnormalities (Aury-Landas et al., 2016). The pathway for development of osteoarthritis, both primary and secondary, is shown in **Fig 1.7**.

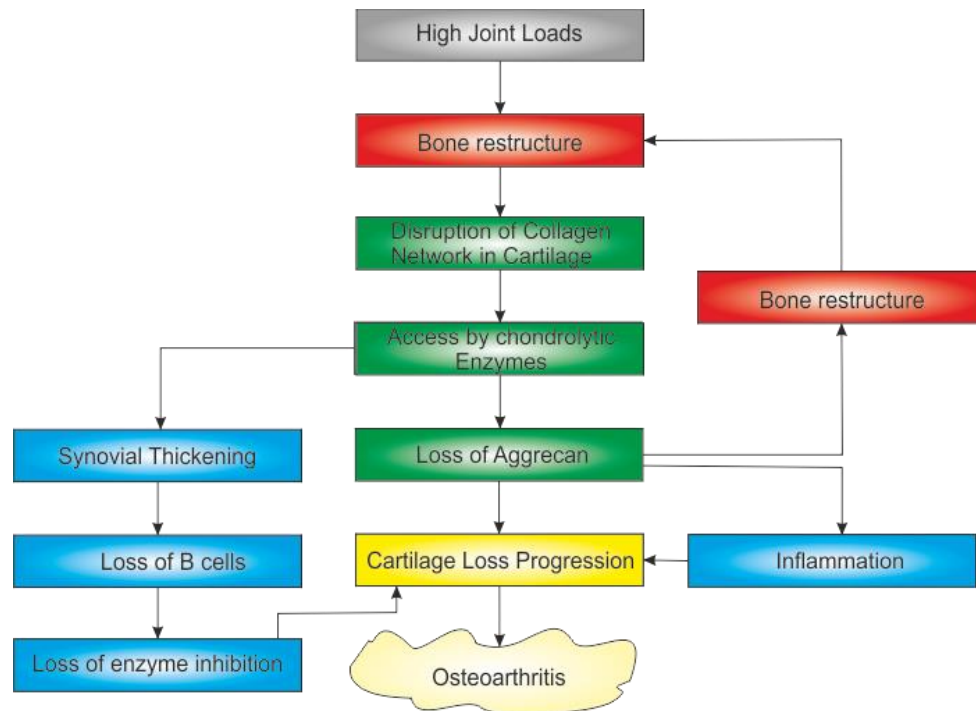


Fig 1.7: The pathway for wear and potential development of osteoarthritis in articular cartilage (Adapted from Burr and Gallant, 2012 with permission from the Nature Publishing Group).

Not everyone develops osteoarthritis but the older someone becomes the more likely that person is to develop the disease (Dieppe and Lohmander, 2005, Doherty et al., 1983, Sarzi-Puttini et al., 2005, Aury-Landas et al., 2016). Secondary osteoarthritis is caused by non-physiological motions either through obesity overloading the joints or an injury to the joint or any of the supportive soft tissues associated with the joint (Dieppe and Lohmander, 2005, Doherty et al., 1983, Sarzi-Puttini et al., 2005, Aury-Landas et al., 2016)

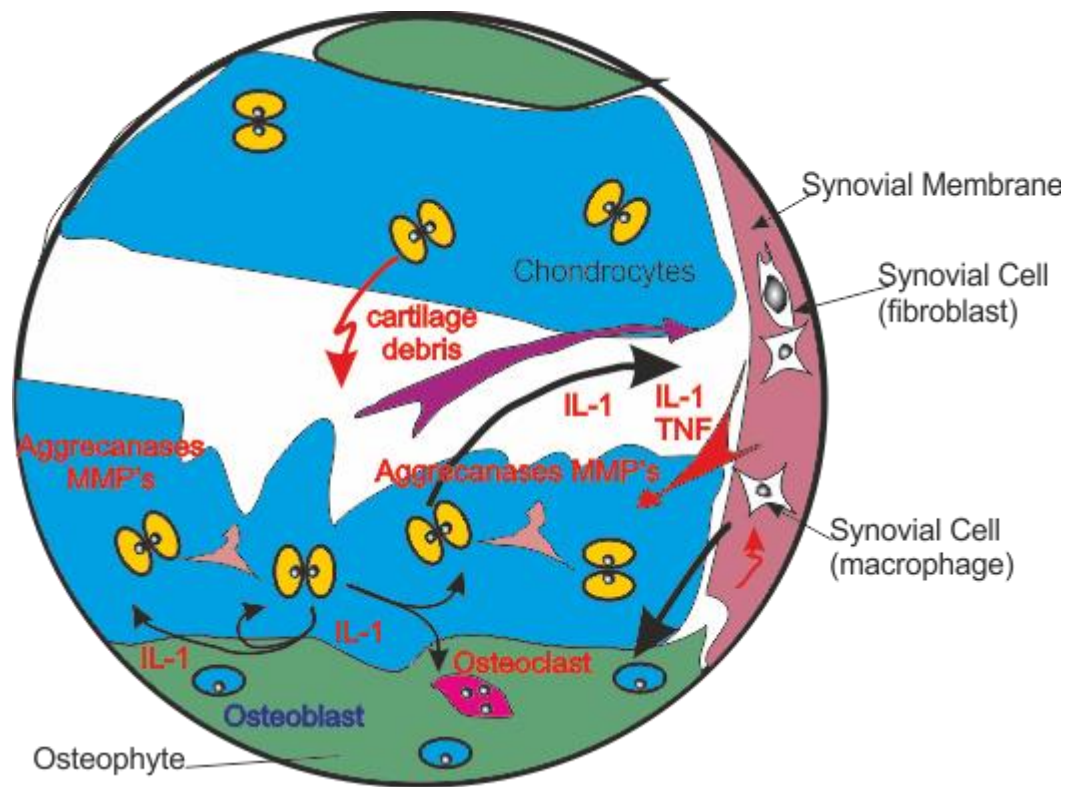


Fig 1.8: Pathophysiological changes in osteoarthritic articular cartilage when mechanical loading is applied.

As the disease progresses the physical appearance of articular cartilage changes from a normally white/silvery colour, hard tissue to a yellow, soft, damaged tissue. The damage of the tissue appears as fissures and pits which increase in size through both mechanical wear and molecular degradation, as mentioned in section 2 (Martel-Pelletier et al., 2008, Xia et al., 2014). The disease manifests as an imbalance between anabolic and catabolic processes within the tissue, in which both processes are accelerated and enhanced (Lorenz and Richter, 2006). The precise mechanisms of degradation of articular cartilage are still unclear, but many theories of complex interactions between genetic, environmental, metabolic and biochemical factors have been proposed as illustrated in **Fig 1.8**. There is enhanced production of matrix-degrading enzymes which result in the progressive loss of collagen and proteoglycans/GAGs from the ECM. The chondrocytes initially proliferate, synthesize and secrete increased amounts of matrix molecules. This increased synthesis is overcome as osteoarthritis progresses and cartilage degradation continues (Lorenz and Richter, 2006).

Within osteoarthritic cartilage, many different cytokines and growth factors are present, some of which are involved in chondrogenesis. These molecules are produced by chondrocytes and the synovium (Xia et al., 2014).

Anabolic processes such as matrix synthesis are facilitated by the secretion of growth factors such as insulin-like growth factor (IGF)-1, transforming growth factor (TGF) – β , fibroblast

growth factors (FGFs) and bone morphogenetic proteins (BMPs). In contrast, catabolic processes such as matrix degradation are promoted by proteases, but in particular matrix metalloproteinases (MMPs) such as MMP-1, -8 and -13 which have been shown to lead to the degradation of GAGs as mentioned above (Lorenz and Richter, 2006, Martel-Pelletier, 1998, Martel-Pelletier et al., 2008, Xia et al., 2014).

1.3.2 Animal models

Various animal models have been developed over the years in order to study the complex nature of osteoarthritis. These models include approaches involving spontaneous, mechanical and chemically induced osteoarthritis in a variety of animals including dogs, rabbits, sheep (Dumond et al., 2004, Gaffen et al., 1997, Liu et al., 2011, Marijnissen et al., 2002, Young et al., 2005, Cook et al., 2014, Ahern et al., 2009).

These models have enabled a time point for the onset of osteoarthritis to be identified and a progressive timescale for particular prominent events as osteoarthritis progresses to be constructed.

The limitations of using animal models are the different timescales for the onset and progression of osteoarthritis. The different biomechanics and lifetimes of different species is an uncontrollable variable, and makes comparison of the results difficult e.g. dogs are quadrupeds and the loading on joints during motion is different to humans who are bipeds (Lorenz and Richter, 2006).

1.3.3 Differences between healthy and osteoarthritic cartilage

There are many biological differences between healthy and osteoarthritic cartilage. In order to classify the differences they can be grouped into two categories: histological changes and molecular changes.

1.3.3.1 Histological changes

The early stage of osteoarthritic cartilage is categorised by a rougher surface than healthy cartilage. GAGs remain distributed in a homogenous manner and slight fibrillation can occur within the superficial zone (Miosge et al., 2004). This fibrillation can increase as the disease progresses to a degree where the cellular structure changes and there is a noticeable decreased concentration of proteoglycans (Fernandes, 1998, Lorenz and Richter, 2006, McDevitt et al., 1977).

The morphology of the chondrocytes in the superficial zone changes from flat to round and they become hypertrophic, eventually disappearing from the tissue completely. The chondrocytes in the middle and deep zones also become mildly hypertrophic (Fernandes, 1998, Lorenz and

Richter, 2006). Other observations include clusters of multi-cellular chondrocytes which contain enlarged nuclei found within the tangential zone along with necrotic chondrocytes with pyknotic nuclei in the radial zone as well as the transitional zone (Bluteau et al., 2001).

In the advanced stages of osteoarthritis, there is an observed complete breakdown of the cartilaginous tissue (Lorenz and Richter, 2006). The breakdown consists of fissures and holes which can penetrate the entire thickness of the tissue so that the calcified zone is exposed (Pfander, 1999). Around these fissures, chondrocytes congregate in clusters in the early stages of advanced osteoarthritis, ultimately disappearing completely (Miosge et al., 2004).

The internal collagen and ECM organisation becomes completely disorganised and disordered and the articular cartilage is replaced by fibrocartilage in the form of scar tissue with a cell phenotype similar to fibroblasts (Miosge et al., 2004). In extreme cases, the fissures penetrate beyond the calcified zone to expose the subchondral bone below (Hayami et al., 2003).

1.3.3.2 Molecular changes

Molecular changes have been analysed using different methods: immunohistochemistry and biochemistry.

Immunohistochemistry

In early and mild osteoarthritic cartilage there is a change in collagen organisation and distribution. Within the deep cartilage zone, the production of collagen type II increases but in the superficial zone a shift occurs and collagen type I is produced within osteoarthritic cartilage (Miosge et al., 2004, Young et al., 2005, Xia et al., 2014).

In advanced osteoarthritis, collagen type II is still produced but only in clusters and collagen type I is still present but the production of collagen in general slows as osteoarthritis progresses (Pfander, 1999, Young et al., 2005).

The specific changes have been collated and presented in **Table 1.4**.

		Early or Mild Osteoarthritis	Advanced Osteoarthritis	
Collagen type I	Increase	(Miosge et al., 2004, Teshima et al., 2004)	Increase	(Miosge et al., 2004)
Collagen type II	Decrease Increase	(Young et al., 2005) (Pfander, 1999)	No change Decrease	(Nerlich et al., 1993) (Pfander, 1999)
Collagen type III	Increase	(Aigner et al., 1993)	-	
Collagen type VI	Increase	(Hambach, 1998)	No change	(Hambach, 1998)
Collagen type X	Increase	(Von der Mark et al., 1992)	-	
Fibronectin	Increase	(Pfander, 1999)	Increase	(Pfander, 1999)
MMP1	Increase	(Fernandes, 1998)	-	
MMP9	Increase	(Hayami et al., 2003)	-	
MMP13	Increase	(Fernandes, 1998, Hayami et al., 2003)	-	

Table 1.4: Immunohistological observations of osteoarthritic cartilage at varying stages of disease progression.

(Adapted from Lorenz and Richter, 2006 with permission from Elsevier).

Biochemical

As the disease progresses, various biochemical changes are observed, some of which are directly related to the immunohistological changes mentioned above. A loss of proteoglycans occurs due to an increased rate of degradation while the rate of proteoglycan production

changes very little. This is due to the increased production of MMPs which degrade proteoglycans. This reduction in proteoglycans causes an increased content of water within the tissue due to the formation of an osmotic gradient (Appleyard, 2003, Little et al., 1996). The different proteoglycans are affected in different ways, but the most noticeable effect is lower levels of chondroitin sulfate (Carney et al., 1992, Carney et al., 1984, Lorenz and Richter, 2006). The different biochemical effects and symptoms have been collated and presented in **Table 1.5**. The synthesis of collagen increases up until a certain point where the rate of synthesis decreases resulting in an unchanged, balanced content in terms of production and degradation (Little et al., 1996).

	Early or Mild Osteoarthritis		Advanced Osteoarthritis	
Water content	Increase	(Appleyard, 2003, Little et al., 1996)	Decrease	(Mankin and Lippiello, 1971)
Collagen content	No change	(Appleyard, 2003)	No change	(Lippiello et al., 1977)
Collagen production	Increase	(Floman, 1980)	Increase	(Squires et al., 2003)
Collagen degradation	Increase	(Squires et al., 2003)	-	
Proteoglycan content	Decrease	(Little et al., 1996)	Decrease	(Squires et al., 2003)
Proteoglycan production	Increase/ no change	(Carney et al., 1992, Carney et al., 1984) / (Little et al., 1996)	-	
Proteoglycan degradation	Increase	(Carney et al., 1992, Carney et al., 1984)	-	

Table 1.5: Biochemical observations of osteoarthritic cartilage at varying stages of disease progression. (Adapted from Lorenz and Richter, 2006 with permission from Elsevier).

1.4 Intervention for early stage cartilage defects

Osteoarthritis is a debilitating disease. Intervention at the early stages when initial damage occurs may prevent disease progression.

There are currently only limited surgical methods of early intervention, however current research within the field of tissue engineering could provide alternative methods of intervention. These methods will be addressed and discussed in this section.

1.4.1 Surgical procedures

There are four groups of repair procedures for cartilage damage: arthroscopic lavage and debridement for very small defects; marrow stimulating techniques; osteochondral autografts and allografts and, more recently, cell-implantation based procedures (Muzzarelli et al., 2012, Balakrishnan and Banerjee, 2011, Abarategi et al., 2010, Campbell et al., 2016). The various techniques are shown in **Fig 1.9**.

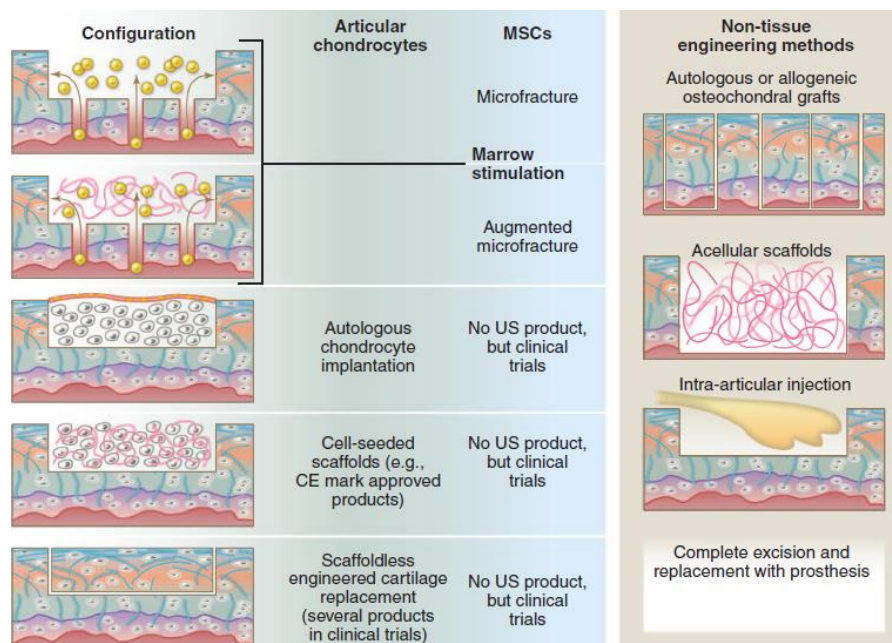


Fig 1.9: The various surgical techniques currently employed to treat articular cartilage defects (Reproduced from Huey et al., 2012 with permission from AAAS).

Arthroscopic lavage and debridement are termed palliative treatments and are the least invasive in that they involve surgically removing loose, damaged cartilage fragments from the damaged joint. When the synovial membrane becomes irritated and excessive growth occurs it can develop fronds which are inflamed and release cytokines and enzymes which can cause further damage to the surrounding joint. It is the inflamed and damaged sections of the synovial membrane that are removed during lavage and debridement (Thiede et al., 2012, Matsiko et al., 2013, Nukavarapu and Dorcemus, 2013, Campbell et al., 2016).

Microfracture is termed a reparative treatment and is employed to treat cartilage defects in active patients. This technique involves drilling holes through the articular cartilage defect into the bone marrow of the subchondral bone. The holes are between 0.5-1mm diameter and approximately 3mm deep and 3-5mm apart (Matsiko et al., 2013, Nukavarapu and Dorcemus, 2013, Perera et al., 2012). The holes allow influx of the mesenchymal stem cells from the bone marrow into the cartilage tissue to promote differentiation into chondrocytes (Matsiko et al., 2013, Nukavarapu and Dorcemus, 2013, Perera et al., 2012, Campbell et al., 2016).

Autograft and allograft transplantation is usually reserved for lesions larger than 2cm² diameter. These techniques are used when lavage, debridement and microfracture have failed and the patient has high demand on the joint, such as an athlete. Autografts, which are taken from a non-load bearing area of the joint, are used for small to medium chondral and osteochondral defects which are 2-3cm² in area. Allografts are taken from another, non-genetically identical patient and are used on larger defects > 3cm² (Matsiko et al., 2013, Nukavarapu and Dorcemus, 2013, Perera et al., 2012).

Autologous chondrocyte implantation or ACI was first developed in 1994 by Brittberg *et al.*, when it was described in treating full thickness articular cartilage defects of a human knee (Perera et al., 2012). This involves a two-stage procedure in which the first stage is an arthroscopic biopsy of a healthy area of articular cartilage and the chondrocytes are isolated and cultured. The second stage involves debridement of the osteochondral lesion which is then covered by a periosteal flap. The lesion is then implanted with the cultured cells (Matsiko et al., 2013, Nukavarapu and Dorcemus, 2013, Perera et al., 2012, Thiede et al., 2012, Huey et al., 2012).

The surgical techniques outlined above are successful in terms of relieving pain and restoring some improved joint motion and function (Balakrishnan and Banerjee, 2011), but the cartilage formation promoted by these techniques is usually fibrocartilage composed of collagen type I instead of type II. Cartilage containing collagen type I is inferior to hyaline cartilage containing collagen type II in terms of biochemical and mechanical properties (D. W. Jackson., 2001).

It is because of this inferior cartilage production that there remains a clinical need to promote the formation hyaline cartilage. The field of tissue engineering is providing potential alternatives to the current treatments. The ideal treatment would be one in which early cartilage defects are repaired by promoting the formation of hyaline cartilage *in vivo*. Other ways of treating cartilage damage, in the short term, would be to reduce the degradation of cartilage or to restore the biomechanical properties of the damaged cartilage.

1.4.2 Tissue engineering approaches to cartilage repair and regeneration

Tissue engineering is the field of science that aims to synthetically reproduce human tissue through the combined use of cells, cellular components i.e. growth factors, a scaffold material and physical stimuli. The field has shown some great leaps forward in producing tissue that has pioneered tissue replacements. Various research groups around the world are currently investigating different approaches for nearly every tissue type in the human body.

The complicated structure of articular cartilage, which has many different zones that have different orientations of collagen and chondrocytes, gives rise to different biomechanical properties. This has led to difficulties in creating living tissue constructs which recapitulate both the biological and biomechanical characteristics of articular cartilage.

A variety of approaches have been undertaken by an enormous number of different groups globally to overcome these difficulties, in which different cell types and different scaffold materials have been investigated. The literature in this area of research is beyond the scope of this review.

The following sections will attempt to summarise some of the major areas of investigation various groups have taken to tissue engineer cartilage.

1.4.2.1 Cell sources

Various sources of cells have been investigated for use in cartilage tissue engineering. The optimal cell source is still currently unknown (C. Chung., 2008, Makris et al., 2015). The various sources are shown in **Table 1.6**.

The ideal source of cells would be chondrocytes, as pre-differentiation *in vitro* would not be required, thus potentially decreasing the economic cost of using cellular based treatments. The difficulty in using chondrocytes is that when expanding chondrocytes *in vitro*, dedifferentiation can occur. This is an issue which growth factors or the material of the scaffold upon which the chondrocytes are seeded, may help to overcome.

Cell Source	Reference of examples	Reason for choice	Issues
Chondrocytes	-	Chondrocytes are a natural choice as a cell source.	The main concern with selecting chondrocytes as the cell type is the
Articular	(J. M. Mesa., 2006, Y. Li., 2004)	These have been extensively studied in the past. Specifically their role in producing, maintaining and remodelling the ECM found in native cartilage (C. Chung., 2008).	low quantities of these cells present within cartilage ~ 1-10% depending on the source, thus expansion prior to use is required.
Auricular	(G. J. V. M. van Osch., 2004, A. Panossian., 2001)		Expansion in monolayer causes dedifferentiation typically resulting in decreased rates of proteoglycan synthesis and collagen type II production along with an increased rate of collagen type I production (C. Chung., 2008).
Costal	(A. G. Tay., 2004, T. S. Johnson., 2004)		
Fibroblasts	(M. M French., 2004, K. H. Lee., 2001)	Fibroblasts are more readily obtained in larger quantities than chondrocytes and can be directed to express a chondrogenic phenotype (C. Chung., 2008).	The issue with fibroblasts is that differentiation <i>in vitro</i> prior to implantation is required (C. Chung., 2008).
Stem cells		Stem cells have been studied in depth in recent years due to possessing “multi-lineage potential” (C. Chung., 2008) These cells can be extracted from a multitude of different tissues. They can then be expanded without losing the potential to differentiate through several pathways and mechanisms (C. Chung., 2008).	The issue with using bone-marrow derived stem cells is that the extracellular matrix they produce when undergoing induced chondrogenesis is mechanically weaker than that produced by native chondrocytes. For adipose-derived stem cells, the expression rate of collagen type II and lower concentrations of cartilage-specific matrix proteins are the main issues that limit their potential within cartilage tissue engineering.
• Bone-marrow derived	• (W. J. Li., 2005, J. W. Chen., 2005)		
• Adipose-derived	• (J. I. Huang., 2004, G. R. Erickson., 2002)		

Table 1.6: The different cell sources that have been investigated to engineer cartilage tissue (Adapted from Warren, 2013).

1.4.3 Scaffold material

Scaffold materials can be classed into three groups: synthetic, natural or hybrid which combines both synthetic and natural materials. Synthetic materials are generally synthetic polymers that can be produced on an industrial scale *via* chemical polymerization reactions initiated either by radiation or catalysis. They can be formulated in many different compositions which affects mechanical properties, chemical modification and rates of degradation both *in vitro* and *in vivo* (Lee and Shin, 2007, Makris et al., 2015).

Some of these polymers are biocompatible and biodegradable (Kon et al., 2015). These include poly (glycolic acid) (PGA), poly (D, L lactic acid) (PLA), poly (caprolactone) (PCL) and poly(lactic co-glycolic acid) (PLGA) (Lee and Shin, 2007); (Lee et al., 2009, Muzzarelli et al., 2012). There are also biocompatible polymers such as poly (ethylene glycol) (PEG) that is not biodegradable (Lee and Shin, 2007, Balakrishnan and Banerjee, 2011, Muzzarelli et al., 2012).

Natural materials are biomaterials that are naturally occurring in nature and include collagen, gelatin and various polysaccharides such as chitosan and hyaluronic acid (Lee and Shin, 2007, Kon et al., 2015). Collagen type I and hyaluronic acid make excellent choices for scaffold materials because they occur naturally in the structure of native articular hyaline cartilage. Chitosan is a polysaccharide derived from chitin, which is found in the shells of crustaceans (Li et al., 2016).

The reasons for use are shown in **Tables 1.7** and **1.8** for synthetic and natural polymers respectively, along with brief descriptions of results beneficial to cartilage tissue engineering. For a complete investigation into the potential materials upon which cells can be cultured decellularized tissue also deserves mention. In comparison to natural or synthetic scaffold materials, decellularized tissue is tissue that has had the cellular components removed through a variety of washes and treatments which aims to remove any immunogenic material to prevent an immunological response upon implantation (Gilbert, 2006). Various tissue types have been investigated, from connective tissue such as ligaments and tendons to organ tissue or even whole organs (Ott et al., 2010, Petersen et al., 2010, Song and Ott, 2011) but to date, there has been little success in decellularization of natural cartilage.

1.4.3.1 Synthetic material

Polymer	References	Reason for use	Results
PGA	(J. C. Becker., 2005, J. K. Mouw., 2005)	PGA scaffolds have been shown to have high rates of degradation as well as a high porosity. They have also been shown to be biocompatible.	The high porosity and rates of degradation allowed an initially high cellular growth, while the function of differentiated chondrocytes was maintained (Lee and Shin, 2007). The production and secretion of an ECM that was similar to that which is produced by healthy normal articular cartilage was also maintained (Lee and Shin, 2007).
PLA	(S. E. Kim., 2003, S. I. Jeong., 2005)	PLA scaffolds have been shown to possess similar properties to PGA scaffolds in regards to their porosity and rate of degradation.	PLA scaffolds showed a decreased propensity for cellular growth and matrix synthesis when compared to PGA(Lee and Shin, 2007).
PCL	(S. E. Kim., 2003, S. I. Jeong., 2005, J. C. Becker., 2005, Q. Huang., 2002)	PCL can be copolymerized with either PGA or PLA, and this improves the resulting polymer's elastic properties.	PCL scaffold, when in combination with growth factor TGF- β 1 and mesenchymal stem cells, showed potential as a scaffold material because hyaline cartilage formed following implantation into a subject, along with the seeded cells producing glycosaminoglycans after a four week period(Q. Huang., 2002).
PEG	(B. S Yoon., 2004, J. Elisseeff., 2001, A. J. DeFail., 2006)	PEG is not a biodegradable polymer but is used widely in clinical instruments and other medical devices as it is biocompatible. The lack of biodegradation is overcome by the safe excretion <i>via</i> metabolic process from the body. This is because of the low molecular weight < 10,000 (Lee and Shin, 2007).	PEG, after being cross-linked into hydrogels, has been shown to support chondrogenesis. This can be improved by the addition of bioactive peptides and hydrolysable units, such as lactic acid units, to the scaffold. The improvement was seen in terms of increased cell proliferation and ECM deposition (C. Chung., 2008, J. Elisseeff., 2001).

PLGA	(J. Elisseeff, 2001, A. J. DeFail., 2006, X. B. Yang., 2004, H. J. Shin., 2006)	PLGA is a block copolymer produced from lactic acid and glycolic acid. It has similar properties to that of the individual polymers; PGA and PLA.	PLGA scaffolds have been shown to support cell differentiation and successful induced chondrogenesis <i>in vivo</i> within a 12 week period post-implantation (K. Uematsu., 2005).
------	---	---	--

Table 1.7: The different synthetic polymers that have been used as scaffold materials for cartilage tissue engineering (Adapted from Warren, 2013).

1.4.3.2 Natural materials

Material	References	Reason for use	Results
Collagen	(B. Wambach., 2000, Ushida., 2002, Kawamura., 1998, Nehrer., 1997)	A. Naturally found in cartilage tissue. It has been shown to be an integral part of providing strength and flexibility to the tissue.	Collagen type I, when combined with other synthetic polymers such as PLLA, has been shown to promote articular chondrocytes to proliferate and support them whilst secretion of matrix components specific to cartilage occurred (Balakrishnan and Banerjee, 2011). The chondrocytes were also shown to express collagen type II molecules when in the presence of collagen type I (J. Elisseeff., 2001).
Hyaluronic acid	(J. Aigner., 1998, Chung., 2009)	C. Naturally found in cartilage tissue. It has been shown to help distribute any “shock” throughout the joint. It also helps in maintaining the structural and functional properties of the matrix of cartilage (Muzzarelli et al., 2012). It is involved in cell proliferation, leading to the conclusion it would make a potential good biomaterial choice for scaffolds (C. Chung., 2008).	Hyaluronic acid has been shown, when combined with other natural materials such as gelatin to form a hydrogel. When the hydrogel was seeded with mesenchymal stem cells is showed favourable formation of elastic hyaline-like cartilage when applied to a defect in the surface of hyaline cartilage. The new cartilage showed good integration into the surrounding native cartilage (C. Chung., 2009). Also when hyaluronic acid was combined with another natural material - chitosan and then seeded with chondrocytes, hyaline-like cartilage was again formed when compared to that of a control where fibrocartilage formed in a defect (Muzzarelli et al., 2012).
Chondroitin Sulfate	(Q. Li., 2004, B. Amsden., 2007)	G. Naturally found in cartilage tissue. It provides a substantial amount of the cartilage tissue’s resistance to compression.	Chondroitin sulfate has been combined with many other polymers to produce scaffolds or hydrogels. When combined with PEG to form a hydrogel and seeded with mesenchymal stem cells, an enhanced rate of ECM deposition was observed along with an increase rate of chondrogenic marker expression (Spiller et al., 2011).

Table 1.8: The different natural polymers and molecules that have been used as scaffold materials for cartilage tissue engineering (Adapted from Warren, 2013).

Although tissue engineering shows some promise, as yet no group has successfully produced a tissue engineered cartilage with the composition and biomechanical function of natural articular cartilage. Moreover, tissue engineering approaches involving the use of living cells will require extensive development before being used to treat patients and will be regulated as advanced therapeutic medicinal products leading to high development costs.

A more practical approach would be to use a cell-free method as an early stage intervention. A novel class of materials called self-assembling peptides (SAPs) are of particular interest for tissue engineering applications.

1.4.4 Potential uses of self-assembling peptides in regenerative medicine applications

SAPs have the potential to be used in a plethora of ingenious ways within the field of tissue engineering and regenerative medicine because of the chemical and physical properties they inherently possess. The reversible ability of these molecules to form stable, self-supporting gels *via* controllable stimuli such as pH, temperature, ionic strength and concentration/dilution makes them potentially useful and quite a versatile tool within a difficult field of science (Aggeli, 1997).

As shown in **Fig 1.10**, the proposed applications of SAPs will vary depending on the chemical structure and sequence of the base-level peptide before secondary self-assembly occurs.

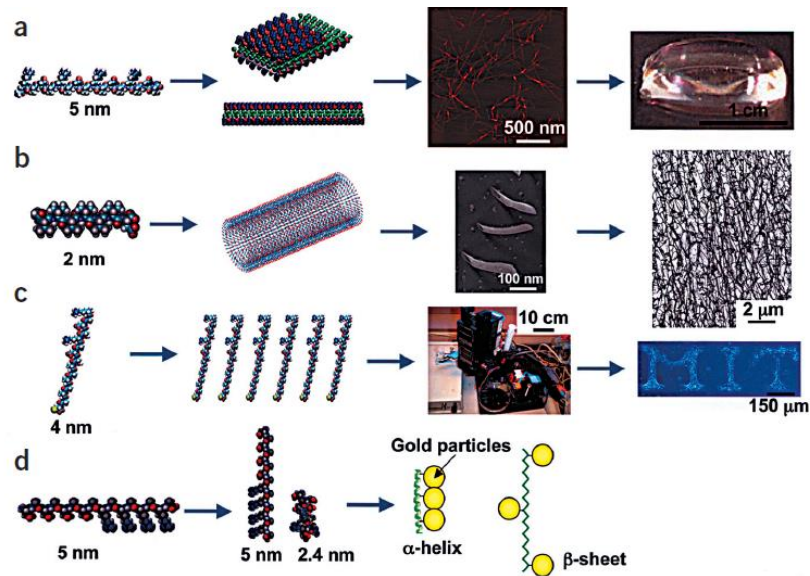


Fig 1.10: Diagrams and images of SAP's which have formed into different structures through different methods of self-assembly and different applications. Route A shows how ionic self-complementary peptides undergo self-assembly to form a hydrogel scaffold. Route B shows how surfactant-like peptides can self-assemble to form nanotubes and nano-vesicles. Route C shows how peptides can be used to nano-coat a surface using a functional group such as a thiol onto a gold surface for nanotechnology applications. Route D shows how controlling the environment in which secondary peptide assembly occurs, peptides can be exploited for use as nano-switches depending upon external stimuli (reproduced from Zhang, 2003 with permission from the Nature Publishing Group).

These inherent properties of SAPs can be exploited for uses within regenerative medicine and tissue engineering ranging from biomaterials to potential carriers for either pharmacological agents or proteins for a variety of therapies. A greater insight into each of these uses is discussed below.

1.5 Self-assembling peptides

Self-assembling peptides (SAPs) are chains of amino acids that are covalently linked through an amide bond which is known as a peptide bond. The chains can undergo association that is governed by thermodynamics which allows a spontaneous process known as self-assembly to occur. This self-assembling process allows the peptides to form structures that are ordered in a hierarchical manner. The assembly is reversible, where the driving force for assembly is the formation of favourable interactions either intramolecularly or intermolecularly and the establishment of a thermodynamic equilibrium (Carrick, 2007a). These interactions, in the order of strongest to weakest, are hydrogen bonding, electrostatic/ columbic interactions, hydrophobic/ π - π stacking interactions, Van der Waal interactions and solvent mediated hydrogen bonding (Zhang, 2003). Covalent bonding can also occur in SAPs. This type of bonding is stronger than those mentioned above but because covalent bond formation may interfere with the reversible processes required for self-assembly these bonds are usually formed post self-assembly during crosslinking steps (Zhang, 2003).

The hierarchical nature of the structures formed through self-assembly is similar to that observed within nature in organisms. The first level of structural assembly is a simple peptide chain which straightens from a random coil to an entropically unfavourable β -strand– known as 1-D primary self-assembly. The second level of self-assembly is known as secondary and this involves the formation of either an α -helical structure or a β -sheet like structure from β -strands through non-covalent interactions. Tertiary self-assembly is based on interactions of side chains from amino acid residues between secondary structures to form 3-D structures which form tape and subsequently ribbons with a twisted structure which is the result of hydrophobic interactions between aromatic and uncharged residues to decrease the entropic penalty from ordering within the solvent. The fourth and final level, which is known as quaternary self-assembly, is the formation of fibrillar structures which are bundles of ribbons to further reduce the entropic penalty from ordering.(Aggeli, 2001a). These fibrils can further associate to form fibers, which are micron-scale structures of entwined fibrils, and these fibers are similar to the structure of connective components such as collagen.

In the case of the tape-like structure assembly to produce ribbons, fibrils and fibers when favourable physiological conditions occur, the density of peptides increases alongside the dimensions of the structure (Aggeli, 2003b). These tape-based structures also occur naturally in diseases that are termed Amyloid diseases which include Alzheimer's and Huntington's and result from mutations such as amino acid deletion or aberrant protein folding or processing (Krysmann, 2008).

The potential uses of SAPs in regenerative medicine range from simple biomaterials to potential drug carriers.

1.5.1 Self-assembling peptides as biomaterials

SAPs are ideal biomaterials because of their relatively simple chemical synthesis within a chemistry lab *ex vivo* or recombinant production in micro-organisms. They are advantageous over other natural materials because the morphology that is adopted can be controlled and reversed under certain conditions, as well as being modifiable post-synthesis (Holmes, 2002). The advantage SAPs have over synthetic materials is that they can be designed to promote a minimal host response and limit or eliminate any potential cytotoxicity. There are “general” criteria for potential materials for use in regenerative medicine (Holmes, 2002): 1) the material is customisable in terms of structure and function to suit specified range requirements, 2) the material possesses a pre-determinable rate of degradation, 3) the rate of degradation of the material is controllable once determined, 4) the material is chosen with the aim of limiting cytotoxicity problems, 5) the material possesses favourable properties that promote interactions between the cells and material itself, 6) or in contrast to the point above, inhibits said interactions, 7) the material is chosen with the aim of promoting a minimal or non-existent immunological response *in vivo* upon implantation, 8) the possibility of scaling up synthesis and functionalization of the material on an industrial and thus clinical scale, 9) the material is soluble in aqueous solutions if required to be, 10) the material is compatible with human physiology under physiological conditions in terms of pH ~ 7.4 and temperature ~37°C.

1.5.1.1 Hydrogel scaffolds

The term hydrogel refers to a gel that is predominantly water, in which the water is entrapped in a matrix of interconnecting projections. SAPs can form gels with a fibrillar structure which fits the description of a hydrogel. This entrapment arises from the hydrophilic side chains of the peptide forming favourable interactions with water molecules that are trapped between “pockets” of hydrophobic regions that repel the water molecules (Liu, 2011).

As mentioned in below, SAP assemble through one of two specific mechanisms. These mechanisms can be exploited within regenerative medicine to allow an injectable material which upon injection into a patient will undergo self-assembly, and due to the fact that self-assembly occurs post injection a greater level of tissue penetration is possible compared to attempting to inject an already assembled hydrogel. This ability makes SAPs unique in terms of other hydrogel scaffold materials. The SAPs are prepared in a monomeric state, which when subjected to physiological conditions or through three different processes by which SAPs can be triggered to self-assemble (Chow, 2008):

1. External stimuli such as changes in ionic strength, pH or temperature of the immediate environment
2. Chemical processes such as irradiation, enzymatic catalysis or polymerisation through radical or photonic can cause crosslinking
3. Physical processes causes similar crosslinking

1.6 Self-assembly mechanism

The classes of SAPs mentioned in the previous section all self-assemble *via* either one of two mechanisms: nucleated growth self-assembly or complementary self-assembly. Nucleated growth self-assembly occurs in a single component system and involves monomers that are in a random coil state orientating in space so that a favourable conformation for self-assembling is achieved (Kyle et al., 2012).

For example, a monomeric peptide will change from a random coil conformation to a β -strand conformation when the peptide conformation transition energy; $\varepsilon_c K_B T$ is reached. This energy requirement is mainly due to the entropy loss which is associated with the peptide straightening out from the random coil to the β -strand.

Once in the β -strand conformation, further self-assembly can only occur once the tape scission energy; $\varepsilon_\beta K_B T$ is reached. This energy requirement is mainly due to the gain of enthalpy which stems from the intermolecular peptide backbone complementary hydrogen bonds and interactions between peptide side chains such as hydrophobic, complementary hydrogen bonds and columbic interactions. These two energies direct self-assembly of peptides to form β -sheet structures or a similar structure in the case of certain classes mentioned above. To form a stable β -sheet there are however further factors which need to be taken into consideration. Even if $\varepsilon_\beta K_B T$ is reached, the concentration of the peptides has to be greater than a specific concentration – critical tape concentration of c^* . This concentration is the point when the peptides can nucleate to form a stable nucleus upon which other peptides can continue to grow.

Even when the energetics for self-assembly are met, if:

$c < c^*$ - small tapes are not stable at these low concentrations so the peptides are all in a monomeric state

$c \sim c^*$ - nucleated self-assembly starts

$c > c^*$ - tape growth occurs

When the concentration dependent mechanism is involved, the monomeric peptide chains form structures based on the hierarchical pattern mentioned in a previous section. The monomers form tape-like structures at a critical concentration (c^*) so that hydrogen bonding

and electrostatic interactions order the monomers once the aromatic groups align the peptides for 1-D self-assembly. The tape-like structure then forms a ribbon once the concentration increases to the required amount. This is the result from the presence of more hydrogen donating or receiving groups on the additional monomers. At higher concentrations, the ribbons can interact with one another through additional hydrogen bonding and electrostatic interactions to form fibrils which then can also go on to form fibres as shown in **Fig 1.11** (Aggeli, 2001b). The monomers are affected by external stimuli such as changes in pH or ionic strength of salt ions in solution. During a pH change, for example from basic to acidic, the various side chains on the peptide sequence are protonated. This affects the self-assembly by either promoting it or disrupting it depending on the peptide sequence. The ionic strength of the salt also influences the self-assembly as the mono and divalent positively charged salt ions screen the negatively charged side groups of the peptide sequence (Kirkham et al., 2007).

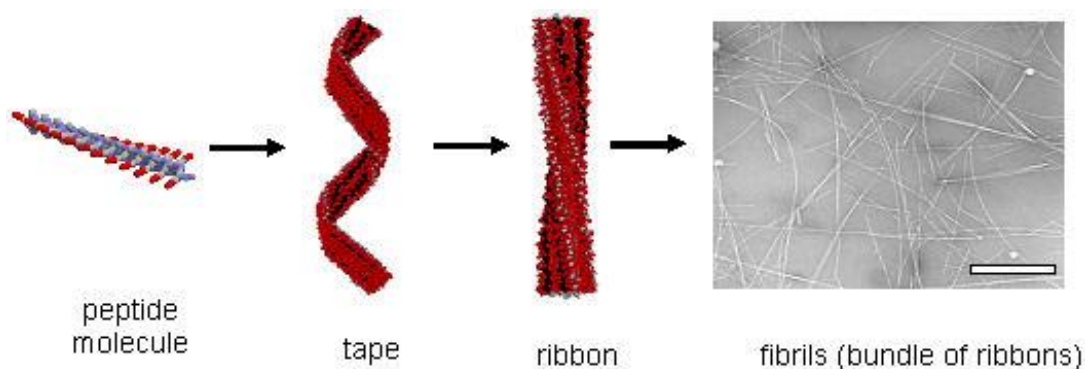


Fig 1.11: The different intermediates of self-assembly for the P11-X class of peptides experience when under a concentration dependent regime.

In the case of the complementarity mechanism for self-assembly, the peptides are a binary pair that have been rationally designed in such a way that self-assembly can only occur between the peptides when two complementary peptides are in the presence of one another (Kyle et al., 2012). Once this requirement is met then the peptides can be triggered by a pH change, thermal or mechanical process to start the self-assembling process. The two monomers will only associate as a complementary pair and not with identical monomers of each type. The difficulty with designing peptide system that self-assembly *via* this type of mechanism is that the two monomeric peptides have to have be triggered by a similar stimulus, e.g. monomeric at a similar pH and switch to a polymeric gel at a similar pH.

In the case of two peptides from the P₁₁-X family designed by the Aggeli group – P₁₁-13 (CH₃CO-Gln-Gln-Glu-Phe-Glu-Trp-Glu-Phe-Glu-Gln-Gln-NH₂) and P₁₁-14 (CH₃CO-Gln-Gln-Orn-Phe-Orn-

Trp-Orn-Phe-Orn-Gln-Gln-NH₂) there are varying interactions which cause the onset of self-assembly (Kyle et al., 2012).

The phenylalanine (Phe) and tryptophan (Trp) residues are hydrophobic so promote hydrophobic interactions between the side chains and intermolecular π - π interactions. The Ornithine (Orn) and Glutamic acid (Glu) residues are hydrophilic and promote strong columbic and complementary electrostatic interactions where one side of the surface of the β -sheet is more hydrophilic than the other because of the Gln, Orn and Glu residues (Kyle et al., 2012).

1.6.1 External effects on self-assembly

There are external stimuli that can affect self-assembly in terms of affecting the system physically such as change in temperature or physio-chemistry such as change in pH or ionic strength of the solution in which the peptides are dissolved.

1.6.1.1 pH

By changing the pH of the solution in which the peptides are dissolved, different side chains are either protonated or deprotonated. In the case of P₁₁₋₄, another peptide designed by the Aggeli group (Riley et al., 2009, Knapman et al., 2008, Maude et al., 2011, Carrick et al., 2007, Aggeli et al., 2001, Maude et al., 2012, Kyle et al., 2009, Kyle et al., 2010, Kirkham et al., 2007, Bell et al., 2006, Davies et al., 2006, Davies and Aggeli, 2011), changing the pH caused changes in the glutamic acid residue in positions 5,7 and 9 of the sequence (Carrick et al., 2007). At low pH \sim 3, P₁₁₋₄ has fully self-assembled into a β -sheet and has an overall net charge of +1 due to the arginine (Arg) residue being protonated. As the pH increases to \sim 3.4, the electrical charge on the Arg residue is neutralised by the glutamic acid and insoluble, self-assembled aggregates known as flocculates form. When the pH is increased above 4 the glutamic acid becomes further deprotonated and the gel changes to a viscous weakly nematic fluid. The increasing negative net charge causes repulsion between the fibrils and fibres such that more of the peptides enter a monomeric state. Once the pH is above 8, then the β -sheet completely disintegrates and all the peptide chains become monomeric (Carrick et al., 2007).

These changes in peptide structure and self-assembly by changing pH occur with all SAPs as the side chains are susceptible to protonation/deprotonation because of their biological nature.

1.6.1.2 Ionic strength

The ionic strength of the solution has also been shown to affect the self-assembling mechanism, in that it increases the pH range over which a self-assembled structure can form. It does not affect the protonation/ deprotonation of amino acid side chains, implying it affects the self-assembly by screening the electrostatic repulsion between positive and negatively charged side

chains. The charge of the salt also affects the ionic strength as divalent cations such as calcium, which have a larger debye radius than univalent cations such as sodium or potassium, means screening of the electrostatic interactions over a larger range can occur (Carrick et al., 2007). This larger debye radius can also cause unfavourable interactions between calcium ions within a fibril which can disrupt self-assembly (Carrick et al., 2007).

1.6.1.3 Temperature

Physical changes such as temperature will have multiple effects on both monomeric peptides and the self-assembled gels. As the temperature increases, the rate of association/dissociation of the side chains changes so that it causes protonation/deprotonation to change when the pH is changed. The increased thermal energy also causes the individual molecules to vibrate and rotate more so the hydrogen bonds formed between the peptides weaken and the self-assembled gel disintegrates.

The physical change from the gel to a fluid is fully reversible upon cooling, as the hydrogen bonds are restored and self-assembly reoccurs (Carrick et al., 2007).

1.7 Different classes of self-assembling peptides

In current research and literature, there are a variety of different broad 'classes' of SAPs. These classes differ from each other dependent on the chemistry of the self-assembling mechanism and the chemical make-up of the peptide chain. The chemical make-up of the classes can include:

- Different distinct regions within the peptide such as hydrophobic and hydrophilic regions
- A specific sequence of amino acids
- Or a different number of specific amino acid

There are two secondary structures these peptide classes can adopt; β -sheets (as mentioned previously) or helices. The different stages of secondary self-assembly are shown in **Fig 1.12**.

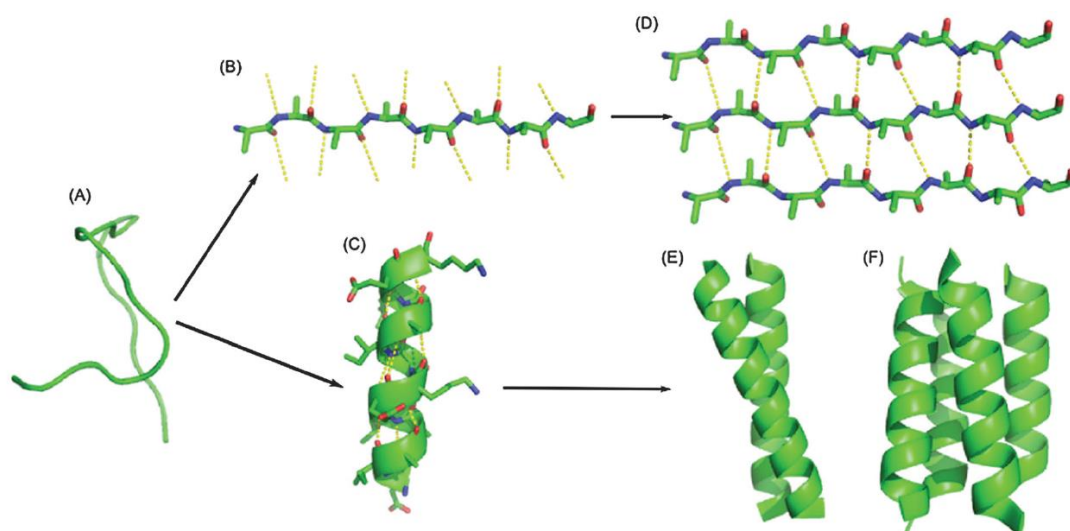


Fig 1.12: The different secondary structures adopted by self-assembling peptides (Boyle and Woolfson, 2011). (A) represents the random coil state of unassembled SAPs, where upon self-assembling (B) is a β -strand where an entropic loss is associated with this state and (C) is an α -helix. These two different secondary structures undergo further self-assembly to form (D) which is a β -sheet or (E) and (F) which are multiple interacting α -helices (reproduced from Boyle and Woolfson, 2011 with permission from the Royal Society of Chemistry).

1.7.1 Self-assembling peptides forming helical structures

1.7.1.1 Helical peptides

Helical SAPs are different from the previous classes mentioned in this review in that the structures are not based around forming a β -sheet secondary structure but instead based around forming a helical secondary structure which then assembles into bundles. The hydrogen bonding involved in stabilising the α -helix is localised intramolecularly in contrast to that witnessed in β -sheet based peptide structures where it is predominately intermolecular hydrogen bonding that is responsible for the self-assembly.

In helical structures the pitch twist is typically smaller compared to β -sheet based structures, with 3.6 residues per turn. This results in a smaller fibrillar structure when compared to a similar β -sheet forming peptide chain (Boyle, 2012, Boyle and Woolfson, 2011, Boyle and Woolfson, 2012, Bromley, 2010, Fletcher, 2012, Yoshizumi, 2011).

In this class the number of amino acids residues in the self-assembling units can vary from as few as seven up to as many as twenty eight, but the amino acids within the chains do not vary a great deal as they usually contain proline, lysine and glutamic acid. An example of helical forming self-assembling peptides is shown in **Fig 1.13**.

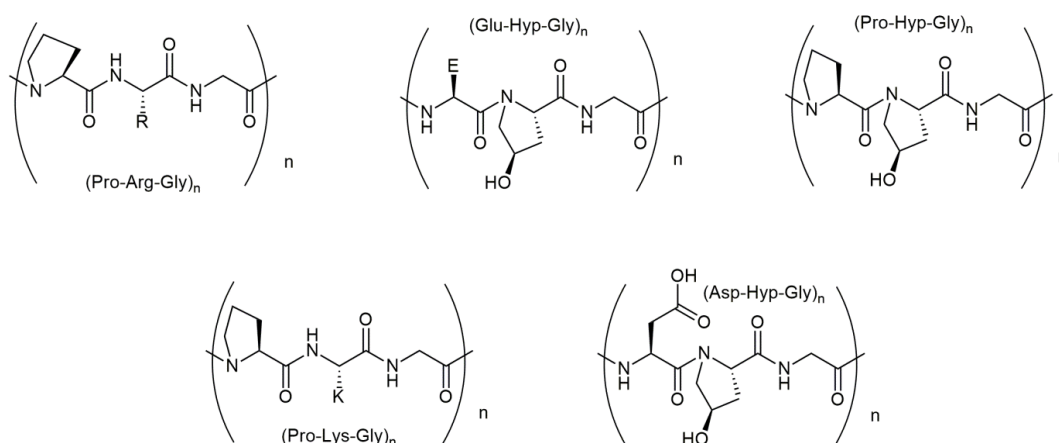


Fig 1.13: The repeating units within a helical forming self-assembling peptide (O'Leary, 2011).

The residues adopt a repeating backbone which have dihedral angles of φ -60° and ψ - 45°, where this repeating pattern leads to the formation of a tight, right handed helix to form. The helix is stabilised through hydrogen bonds from carbonyl and amide groups of the amino acids, these groups though are spaces four residues apart along the peptide chain. As mentioned above, the average number of residues in each turn is 3.6 which causes the side groups of the amino acids that are usually four residues apart into close proximity in space which interact through hydrogen bonds of polar groups as well as π - π stacking and hydrophobic interactions of aromatic groups. The incorporation of the strained proline residues aids in projecting these side groups of nearby residues to be able to interact through aforementioned interactions (Boyle and Woolfson, 2011).

Helical peptides have been used for tissue engineering as scaffolds for cell culture but have neither the versatility nor ease of structural modification for use as part of a cell-free early stage intervention (Boyle and Woolfson, 2011).

1.7.2 Self-assembling peptides forming β -sheet like structures

1.7.2.1 Amphiphiles

Amphiphilic peptides or peptidic amphiphiles (PAs) are a family of SAPs that are sequences of amino acids that form a hydrophilic region and a hydrophobic region. The hydrophilic region of the peptide chain is made up of polar, charged amino acids while the hydrophobic region is made up of aromatic or uncharged amino acids. This structure causes the peptide chains to assemble in the way surfactants do to form micelle-like structures, in which the core is composed of the hydrophobic regions that interact mainly through hydrophobic forces and the outer surface comprises of hydrophilic regions which interact with the surrounding aqueous

solution through hydrogen bonding. A diagram of a typical amphiphilic peptide is shown in **Fig 1.14**.

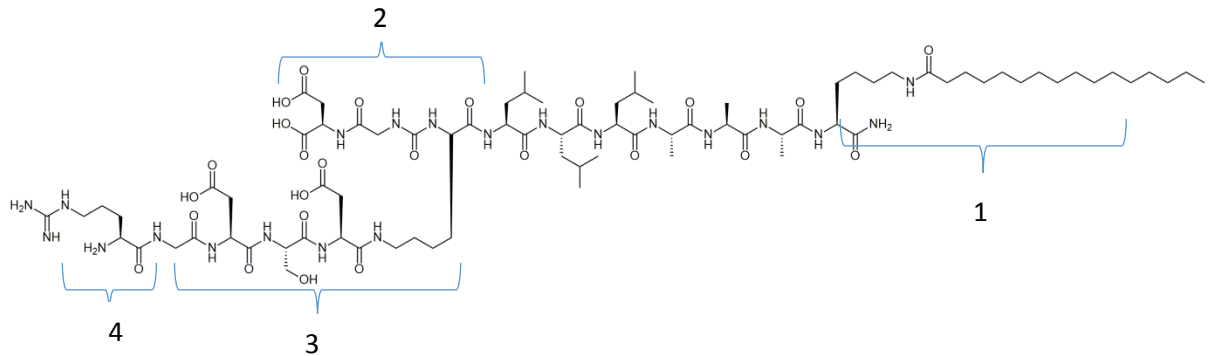


Fig 1.14: Typical amphiphilic peptide (Sargeant, 2008).

The structure of PAs can be divided into four distinct regions that require consideration during the design stage (CUI, 2010b):

1. Hydrophobic section – usually an alkyl chain of medium length
2. Short sequence of amino acids that when the appropriate pH is attained can form intra and intermolecular hydrogen bonding
3. Hydrophilic section – amino acids that are polar and charged that assist by increasing the solubility of the peptide and increase the sensitivity of the peptide to changes in pH
4. A region in which selected ligands can be attached for bioactive signalling

PAs have been used extensively under the umbrella term of regenerative medicine and these applications have included a scaffold material which incorporated Ti-6Al-4V foam that formed a nanofiber matrix which altered the bioactivity of the matrix so that it could be a potentially active scaffold construct (Sargeant, 2008). PAs, as well as RADA peptides, have been involved in studies on human MSCs (Sargeant, 2012). The final application which is the most pertinent to the objective of this review is that of PAs promoting the mineralisation of hydroxyapatite, which resembled the extracellular matrix established by proliferating osteoblasts (Hartgerink, 2001).

1.7.2.2 Fmoc dipeptides

Fmoc dipeptides are a class of self-assembling peptides that are formed by the coupling of two different amino acid residues, in which one amino acid is protected by a fluorenylmethyloxycarbonyl (Fmoc) group on the N terminus. This simple design allows for effective block polymeric chains to be produced (Orbach, 2009, Jayawarna, 2009, Das, 2009, Jayawarna, 2006, Mart, 2006, Williams, 2008).

These SAPs assemble through hydrogen bonding and electrostatic interactions. The amino acid side chains can be either hydrophilic or hydrophobic, in which the strength of assembly depends on the number of hydrogen bonds formed between hydrogen bond accepting residues and carbonyl groups of the amide bond or hydrogen bond donating residues and amine groups of the amide bond of two dipeptides. Other than hydrogen bonding, π - π stacking occurs because of the Fmoc group present. The delocalised electrons in the Fmoc groups align one another to minimise the unfavourable entropic penalty that interactions with the aqueous solvent causes. This alignment of the Fmoc groups is the first stage during self-assembly which forms a template upon which hydrogen bonding can form. The stacking forms a tubular column of planar Fmoc molecules, around which the hydrophilic side chains branch out to form intra and intermolecular hydrogen bonds as illustrated in **Fig 1.15**.

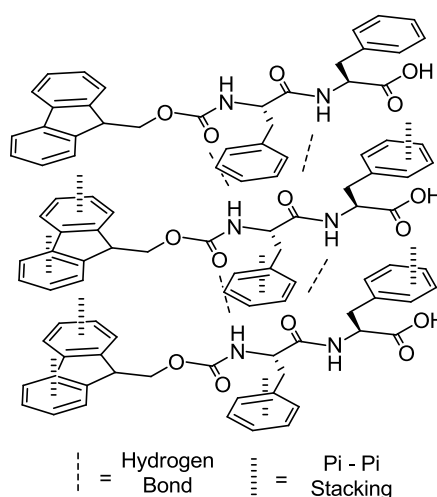


Fig 1.15: Representation of the two types of interactions involved in the self-assembly of Fmoc dipeptides – hydrogen bonding and π - π stacking.

A diagram showing how the two amino acids form the Fmoc dipeptide is shown in **Fig 1.16**.

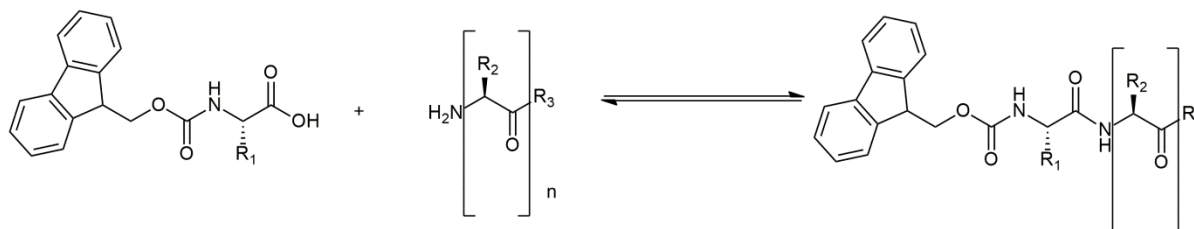


Fig 1.16: Two different amino acids are covalently bound to form the Fmoc dipeptide (Williams, 2008b).

Fmoc peptides have been used in many applications in the field of tissue engineering. Some studies have involved the Fmoc dipeptides forming hydrogels in which cells were promoted to proliferate and differentiate into neurons selectively (Jayawarna, 2006), as seen with studies carried out using the PAs and RADA classes of SAPs. Another application, is the promotion of

proliferation and differentiation of chondrocytes, in which different protected amino acids were shown to affect chondrocytes when seeded onto a scaffold constructed of these amino acids (Jayawarna, 2009).

1.7.3 Self-assembling peptides forming tape or β -sheet structures

1.7.3.1 RADA

The RADA class of self-assembling peptide, which is shown in **Fig 1.17**, is a peptide with a sequence of four repeating amino acids: arginine (R), alanine (A), aspartic acid (D) and alanine (A) to form a four amino acid chain with alternating hydrophilic side chain containing residues - arginine and aspartic acid, and hydrophobic side chain containing residues - alanine. The number of repeats of these four amino acids can range from one group up to four groups resulting in a sixteen amino acid containing peptide sequence (Horii, 2007a, K. Chen., 2012, Wu, 2011, Chau, 2008, Holmes, 2000b, Hamada, 2007, E. Genove., 2005).

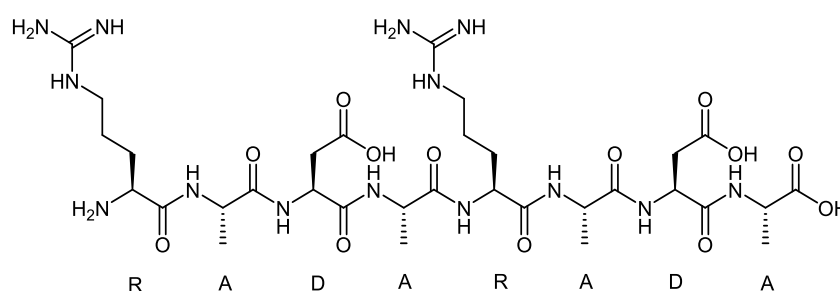


Fig 1.17: The repeating structure of a RADA peptide chain (Horii, 2007b).

RADA SAPs have been studied extensively within the field of tissue engineering as a scaffold material for various cell types such as: bone marrow derived mesenchymal stem cells (Genove, 2005); (Hamada K., 2007), neurites (Holmes, 2000a), and osteoblasts (Horii, 2007b).

1.7.3.2 MAX peptides

MAX self-assembling peptides are similar to RADA self-assembling peptides with alternating hydrophilic and hydrophobic amino acids in the sequence. The difference is that the choice of amino acids is not restricted to only arginine, aspartic acid or alanine residues when being designed. The sequence tends to be longer than RADA peptides in that the sequence is approximately 20 amino acids long. A diagram of a MAX peptide is shown in **Fig 1.18**.

MAX peptides consist of two domains that are linked through a spacer made up of the amino acids residues: valine, proline and tyrosine, which form a β -turn (Krysmann, 2008, Nagy, 2011, Rajagopal, 2006, Guvendiren, 2012, Nowak, 2002, Rajagopal, 2009, Ozbas, 2007).

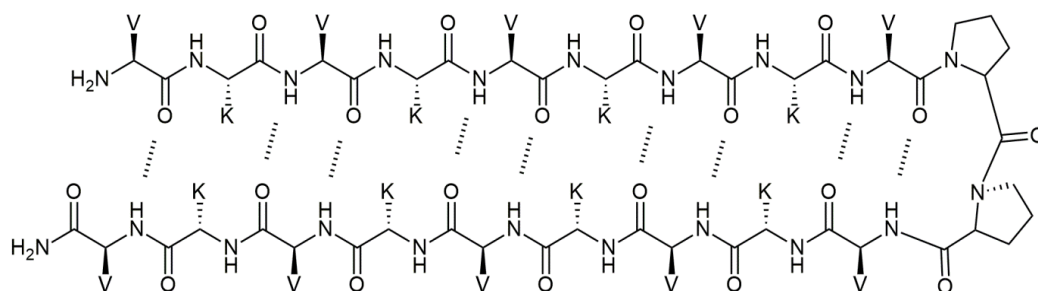


Fig 1.18: A MAX peptide, where V = Valine and K = Lysine (Rajagopal, 2006b).

This class of SAPs have been used within tissue engineering research to form scaffolds and hydrogel structures upon which cells can proliferate and differentiate. These SAPs have shown minimal cytotoxicity, and are cytocompatible with fibroblasts, osteoblast progenitor cells, MSCs, hepatocytes and articular chondrocytes (Guvendiren *et al.*, 2012).

1.7.3.3 P₁₁-X tape based peptides

P₁₁-X peptides are based on a sequence of eleven amino acids which are either hydrophilic/polar or hydrophobic except for three amino acid residues which form an aromatic core consisting of phenylalanine and tryptophan residues. A typical structure of a P₁₁-X peptide is shown in **Fig 1.19**. The basic design of this class of SAPs is shown in **Fig 1.20**.

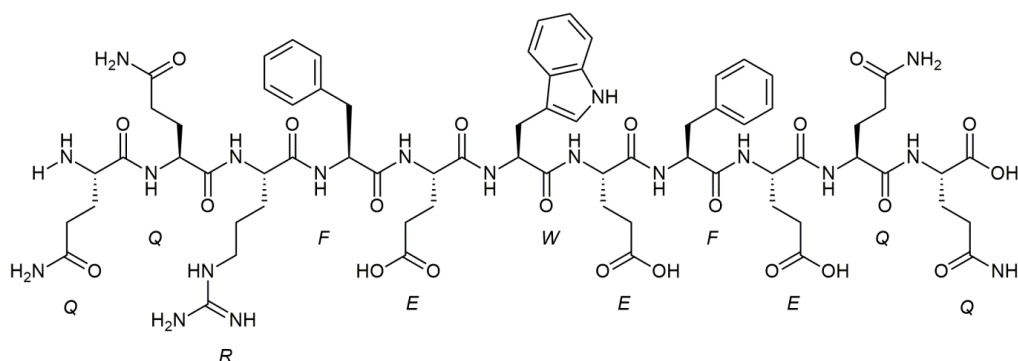


Fig 1.19: The typical structure of a P₁₁-X peptide, the example above is known as P11-4 (Kirkham *et al.*, 2007).

The choice of amino acid residues also dictates the pH at which the monomeric form exists as they change the overall charge of the peptide chain. These peptides can self-assemble through one of two mechanisms: 1) concentration dependency or 2) complementarity (Aggeli, 1997, Aggeli, 2001a, Aggeli, 2003a, Aggeli, 2001b, Bell, 2006, Carrick, 2007b, Kirkham *et al.*, 2007, Kyle, 2009, Kyle, 2010, Riley, 2009).

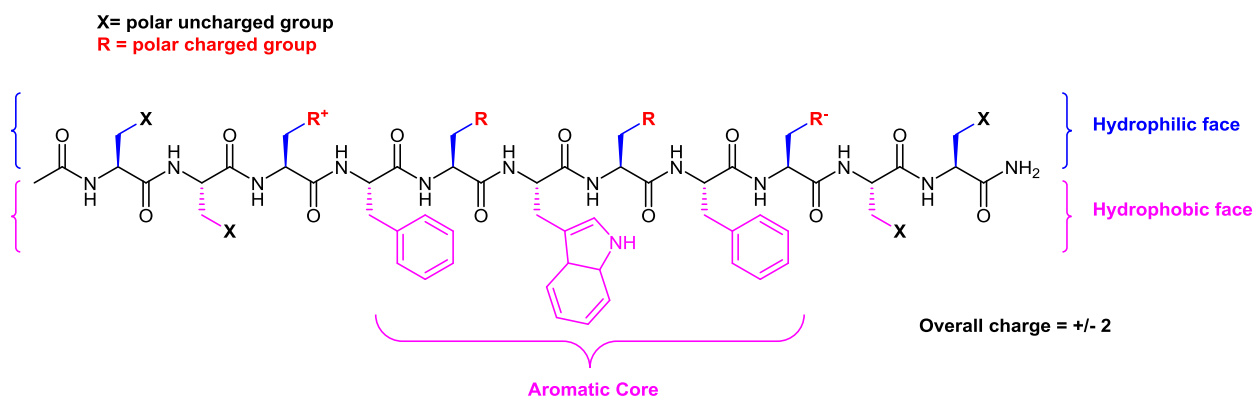


Fig 1.20: The basic design parameters of the P11-X peptide family.

This class of SAPs has already been used in cell-free studies by the Aggeli group in the past. One application which this class of SAP has been used for is to promote enamel remineralisation in the treatment of dental caries. Kirkham *et al.* used P₁₁-4 to promote hydroxyapatite to mineralise in dental caries. The study showed that the crystal structure of P₁₁-4 was perfect for hydroxyapatite due to the distance between the glutamic acid residues being the same as the crystal lattice structure of hydroxyapatite (Kirkham *et al.*, 2007).

The most relevant application involved the investigation into the potential application as injectable lubricants for osteoarthritic joints. Bell *et al.* showed that the P₁₁-X series could be used in the treatment of osteoarthritis. P₁₁-X peptides, in particular P₁₁-9 which resembled hyaluronic acid the closest, were used to investigate whether the application *via* injection into damaged articular cartilage had any measureable restoration of the biomechanical properties of the cartilage samples when compared to healthy articular cartilage. The results showed that the application of P₁₁-9 restored some of the lubrication properties but was still less efficient when compared to hyaluronic acid. It showed that this class of peptides had potential to act as a cell-free therapeutic material for the early stage treatment of osteoarthritic cartilage (Bell *et al.*, 2005).

1.8 Project aims

The link between the loss of GAGs within articular cartilage and the onset and progression of osteoarthritis raises led us to ask: if GAGs can be stably reintroduced into the tissue, would the onset and progression of OA be slowed or stopped?

Previous studies have been carried out to investigate whether simply injection GAGs into osteoarthritic joints had any significant effect on restoring the biomechanical properties of the tissue, but it was noted that applying physiological loads to the tissue caused expulsion of the GAGs. The lack of permanence in the integration of the GAGs into the stable matrix clearly prevents them from improving the biomechanical properties of the tissue. If the GAGs can be trapped within the tissue somehow, could an improvement of biomechanical properties be observed?

We considered that the use of self-assembling peptides could provide a solution to this problem. The formation of a self-supporting stable hydrogel with a cross-linking network of fibrils entwined within one another could be a suitable platform for entrapping GAGs within cartilage tissue.

To ensure the full entrapment of GAGs within the SAPs matrix, it was envisaged that the GAGs could be bound covalently to the SAP matrix through the synthesis of a GAG functionalised SAP with the GAG linked to the peptide through the use of click chemistry. The idea was to mimic the structure of aggrecan, with the covalently bound GAGs projected out from the SAP core similar to the protein core found within aggrecan, but rather than the use of a linker protein to bind the two fragments together, a triazole motif would be used. As illustrated in **Fig 1.21**, the idea for the design of the Pep-GAG conjugate is that upon *in situ* self-assembly within the cartilage tissue to ensure penetration, the self-assembling peptides, both non-functionalised and functionalised variants, will assembly into an aggrecan-like brush structure where the CS chains project out from the core which would comprise of the self-assembling peptide strands.

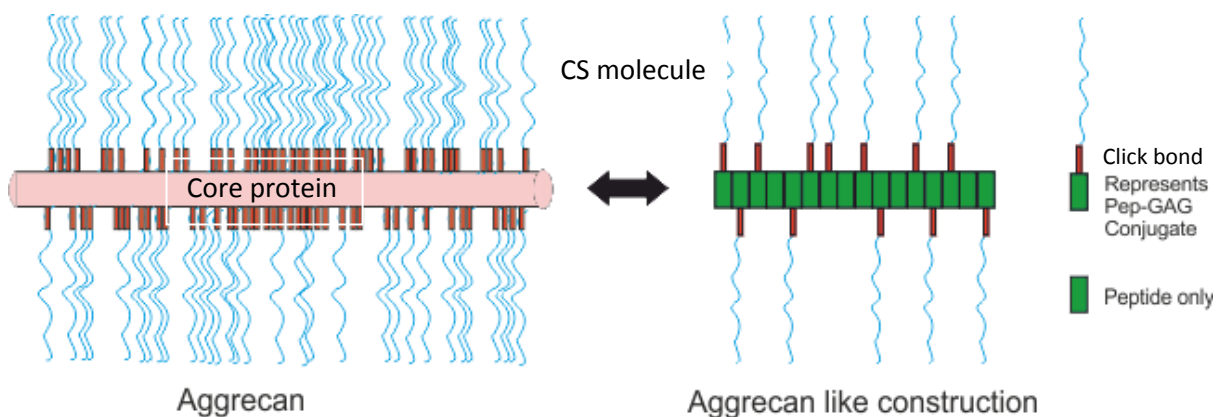


Fig 1.21: A representation of the aim to form an aggrecan like brush structure using the Pep-GAG conjugates.

A proof of concept project was carried out in house by a group of researchers led by Kainmuller (unpublished). However, although small quantities of the SAP-GAG conjugate were obtained, it could not be fully characterised. This made quantification and analysis of the effect of introducing the conjugate into both self-assembled gels and biologically derived materials difficult to perform on scale and made results inconclusive. The aim of this project were:

1. To design, develop and optimise the synthesis of a SAP-GAG conjugate
2. To characterise the effect of incorporating the conjugate within a SAP hydrogel matrix.
3. Once the most suitable conditions have been identified, to develop and produce an osteoarthritic porcine cartilage model to enable the response of the biomechanical properties to incorporation to the peptide GAG conjugate to be measured.

The different stages are described in the following Chapters.

- Chapter 3 describes the optimisation of the chemical synthesis of self-assembling peptides and their functionalisation by covalently linking chondroitin sulfate utilizing click chemistry
- Chapter 4 discusses the effects of mixing the SAP/GAG conjugates and SAPs at varying molar ratios (1:64 and 1:32) on the self-assembly, biomechanical and biophysical properties of the resulting materials.
- Chapter 5 investigates the biomechanical properties of the GAG depleted articular cartilage treated with SAPs/GAGs.

Chapter 2

Material and methods

2.1 Materials

2.1.1 Equipment

A list of general laboratory equipment used during the study including the suppliers is presented in Appendix 1.

2.1.2 Glassware

All laboratory glassware was purchased from Fisher Scientific (Loughborough, UK) unless otherwise stated. Glassware was cleaned by either immersion in a 1 % (v/v) solution of Neutracon® for one hour and was then rinsed with tap water and dried or sterilised using dry heat (for biological or tissue work) or cleaned with detergent, then rinsed with tap water, then acetone and dried or placed in an oven (~60-70 °C) until required (for chemical synthesis).

2.1.3 Plastic ware

All non-sterile and sterile disposable plastic ware was purchased from Scientific Laboratory Supplies Ltd. (Nottingham, UK) unless otherwise stated. All plastic ware was stored as per suppliers' instruction.

2.1.4 Reagents

All chemical reagents, Cat No's and supplier information are listed in Appendix 1.

2.1.5 Cells

The cell lines used during this study, along with suppliers, are listed in **Table 2.1**.

Cells	Type	Species	Supplier	
BHK	Fibroblasts	Hamster	Health Agency	Protection
L929	Fibroblasts	Murine	Health Agency	Protection

Table 2.1: Cells used during the study.

2.1.6 General stock solutions

2.1.6.1 Phosphate buffered saline (PBS)

One PBS tablet was dissolved in 100 ml distilled water. The pH was adjusted to pH 7.2 -7.4 using 6M hydrochloric acid (HCl) or 6M sodium hydroxide (NaOH) solution.

2.1.6.2 Baby hamster kidney (BHK) cell culture medium

Glasgow's minimal essential media (GMEM) 82 ml was used with 5 % (v/v) foetal bovine serum (FBS) 5 ml, 10 % (v/v) tryptone phosphate broth (TPB) 10 ml, 2 mM L- glutamine 1 ml, 100 U.ml⁻¹ penicillin and 100 U.ml⁻¹ streptomycin – 2 ml total volume.

2.1.6.3 L929 cell line culture medium

Dulbecco's modified Eagle's medium (DMEM) 87 ml was used with 10 % (v/v) FBS 10 ml, 2 mM L-glutamine 1 ml, 100 U.ml⁻¹ penicillin and 100 U.ml⁻¹ streptomycin – 2 ml total volume

2.2 General methods

2.2.1 Sterilisation

2.2.1.1 Dry heat sterilisation

Equipment or glassware to be sterilised was placed in suitable containers or wrapped in tinfoil and placed into a hot air oven (190°C for 4 hours). Items were allowed to cool and then removed, with care being taken to maintain sterile conditions.

2.2.1.2 Moist heat/ autoclave sterilisation

Solutions and equipment such as plastic ware not suitable for dry heat sterilisation were sterilised using an autoclave. Items were placed into autoclave bags and labelled with autoclave tape. Items were autoclaved (121°C for 20 minutes at 15 psi). Items were allowed to cool and were then removed with care being taken to maintain sterility.

2.2.1.3 Measurement of pH

The pH meter used was either a Jenway 3020 pH meter, Satorius Docu-pH meter or WPA CD720 pH meter. The meter was calibrated using purchased standard solutions of pH 4, 7, and 10. The pH of solutions was measured at room temperature using temperature compensation. The pH of solutions was changed by the drop-wise addition of 6 M HCl or 6 M NaOH whilst being stirred unless otherwise stated.

2.2.1.4 Lyophilisation of samples

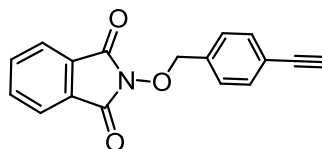
Samples were lyophilised differently depending on whether the samples were chemical or biological in nature. Chemical samples were placed in freeze-able glass vials and frozen by immersion in liquid nitrogen (N₂). The vial caps were then pierced and placed in a freeze dryer (Thermo, Heto Powerdry LL1500 or VirTis, Benchtop BTP 8ZL) at -101 °C, 0.15 - 0.1 mbar until completely lyophilised.

For biological samples such as cartilage tissue, the cartilage tissue was cut away from the subchondral bone and macerated. Samples were then placed in suitable containers and weighed three times with mean wet weight calculated. Samples were placed in a freeze dryer (Thermo, Savant ModulyoD) at -50 °C, 0.15 - 0.2 mbar, and the weight measured every 24 hr until constant (48 - 72 hr).

2.3 Chemical methods

2.3.1 Synthetic methods

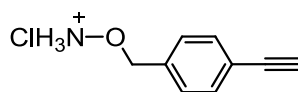
Compound 3



4-ethynylbenzylalcohol (500 mg, 3.78 mmol, 1 eq), N-hydroxyphthalimide (925 mg, 5.67 mmol, 1.5 eq) and PPh_3 (1.5 g, 5.67 mmol, 1.5 eq) were suspended in dry THF (10 ml) under N_2 , cooled to 0 °C, and DIAD ($\rho=1.027$, 1.1 ml, 5.67 mmol, 1.5 eq) was added dropwise. After the addition was complete the reaction mixture was warmed up to rt and the clear/slightly yellow solution was stirred under N_2 overnight, during which some product precipitated from the mixture, it was isolated by filtration and the filtrate was concentrated to dryness under reduced pressure. The residue was purified by recrystallization from hot MeOH/EtOAc to yield **compound 3** (814 mg, 78%) as slightly yellow crystals.

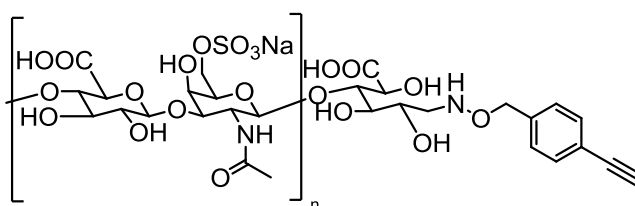
δ_{H} (500MHz, CDCl_3) 7.85-7.80 (2H, m, Ar_{Phthalimide}), 7.75-7.70 (2H, m, Ar_{Phthalimide}), 7.50 (4H, s, Ar_{Benzyl}), 5.22 (2H, s, CH_2), 3.12 (1H, s, Alkyne H). δ_{C} (75MHz, CDCl_3) 163.4, 134.5, 134.3, 132.3, 129.6, 128.9, 123.5, 123.1, 83.2, 79.2, 78.0. m/z (ESI⁻) 300.1 ($[\text{M}+\text{Na}]^+$ 100%); found MNa^+ 300.0734, $\text{C}_{17}\text{H}_{11}\text{NO}_3\text{Na}$ requires 300.0631.

Compound 4



JW1-5 (1.6g, mmol, 1eq) was suspended in DCM (20ml), hydrazine monohydrate ($\rho=1.032$, 560 μl , 5.67mmol, 2eq) was added and the reaction mixture heated under reflux overnight. After filtration, 1.0M HCl in Et_2O was added to the filtrate until $\text{pH}<2$. The colourless precipitate was isolated by filtration, washed with DCM and dried to yield **compound 4** (941mg, 84%) as a colourless powder.

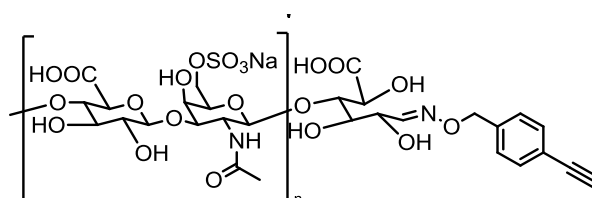
δ_{H} (500MHz, DMSO) 11.1 (3H, s, NH_3), 7.54 (2H, d, J 8.2, Ar), 7.45 (2H, d, J 8.2, Ar), 5.08 (2H, s, CH_2), 4.27 (1H, s, Alkyne H). δ_{C} (75MHz, DMSO) 134.4, 132.0, 129.5, 122.4 82.9, 81.5, 75.1. m/z (EI⁺) found M^+ 147.0682, $\text{C}_9\text{H}_9\text{NO}$ requires M 147.0684.

Compound 5

Chondroitin 6-sulphate (50mg, $\sim 2.8\mu\text{mol}$, 1eq) and **compound 4** (25.5mg, 0.14mmol, 50eq) in DMSO/AcOH 85:15 (5ml) (pH 3-3.3) was stirred at 40°C for 1.5-2hr then NaBH_3CN (87.3mg, 1.4mmol, 500eq) in H_2O (5ml) was then added to the mixture. The solution was stirred overnight (pH 3.5-3.7). During this process, gas formation (HCN) occurred. The gas was bubbled through aqueous NaOH (pH 11-11.5) and later destroyed together with any cyanide containing waste by addition of bleach. After 1, 2 and 3d more NaBH_3CN (3x 87.3mg, $\Sigma 1500\text{eq}$) was added and after 6d the crude mixture was purified by dialysis over 2 days. The solution was concentrated after each change using TLC (KMnO_4 and H_2SO_4 in MeOH). The resulting mixture was freeze dried to yield **compound 5** (48mg) as a colourless solid.

$\nu_{\text{max}}/\text{cm}^{-1}$ (DMSO) 3450 (br, O-H). 2950-3050 (m, C-H), 1830 (m, C=O, acid), 1755 (s, C=O, amide I), 1630 (m, N-H, amide II)

$\nu_{\text{max}}/\text{cm}^{-1}$ (Solid) 2910-2930 (m, C-H), 1738 (m, C=O, acid), 1652 (s, C=O, amide I), 1553 (m, N-H, amide II).

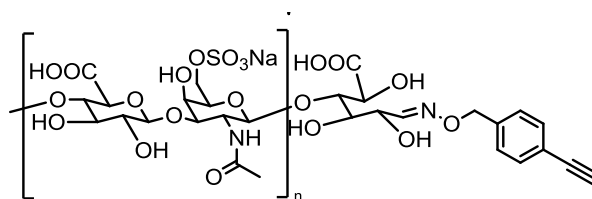
Compound 6 –Protocol 1

Chondroitin 6-sulphate (50mg, $\sim 2.8\mu\text{mol}$, 1eq) and **compound 4** (25.5mg, 0.14mmol, 50eq) in 10 mM aqueous Aniline solution (2 ml), 100 mM NaOAc buffer(2 ml) (pH 4) and 1mM aqueous Na Ascorbate (1 ml) was stirred at 40°C overnight. The crude mixture was purified by dialysis over 2 days. The solution was monitored after each dialysis change using TLC (KMnO_4 and H_2SO_4 in MeOH). The resulting mixture was freeze dried to yield **compound 6** (45mg) as a colourless solid.

δ_{H} (500MHz, DMSO) 9.1 (1H, s, HC=N), 7-7.3 (4H, m, aromatic), 4.2-5 (multiple, m, CS chains)

$\nu_{\text{max}}/\text{cm}^{-1}$ (DMSO) 3450 (br, O-H). 2950-3050 (m, C-H), 1830 (m, C=O, acid), 1755 (s, C=O, amide I), 1630 (m, N-H, amide II).

$\nu_{\text{max}}/\text{cm}^{-1}$ (Solid) 2910-2930 (m, C-H), 1738 (m, C=O, acid), 1652 (s, C=O, amide I), 1553 (m, N-H, amide II).

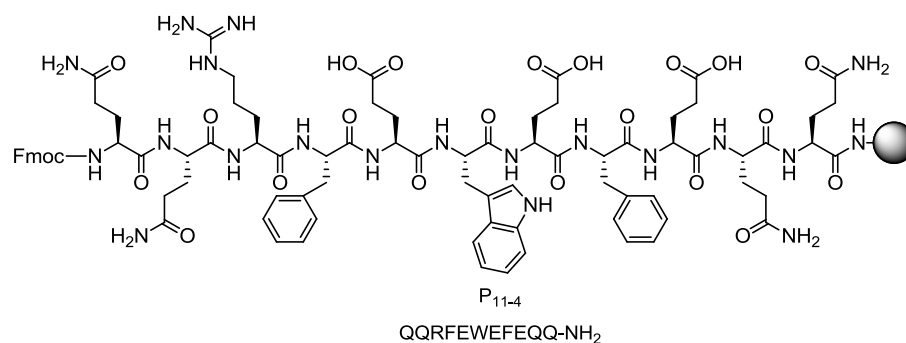
Compound 6 –Protocol 2

Chondroitin 6-sulphate (50mg, $\sim 2.8\mu\text{mol}$, 1eq) and **compound 4** (25.5mg, 0.14mmol, 50eq) in 10 mM aqueous *p*-phenylenediamine solution (2 ml), 100 mM NaOAc buffer(2 ml) (pH 4) and 1mM aqueous Na Ascorbate (1 ml) was stirred at 40°C for 1 hr. The crude mixture was purified by dialysis over 2 days. The solution was monitored after each dialysis change using TLC (KMnO_4 and H_2SO_4 in MeOH). The resulting mixture was freeze dried to yield **compound 6** (45mg) as a colourless solid.

δ_{H} (500MHz, DMSO) 9.1 (1H, s, HC=N), 7-7.3 (4H, m, aromatic), 4.2-5 (multiple, m, CS chains)

$\nu_{\text{max}}/\text{cm}^{-1}$ (DMSO) 3450 (br, O-H). 2950-3050 (m, C-H), 1830 (m, C=O, acid), 1755 (s, C=O, amide I), 1630 (m, N-H, amide II).

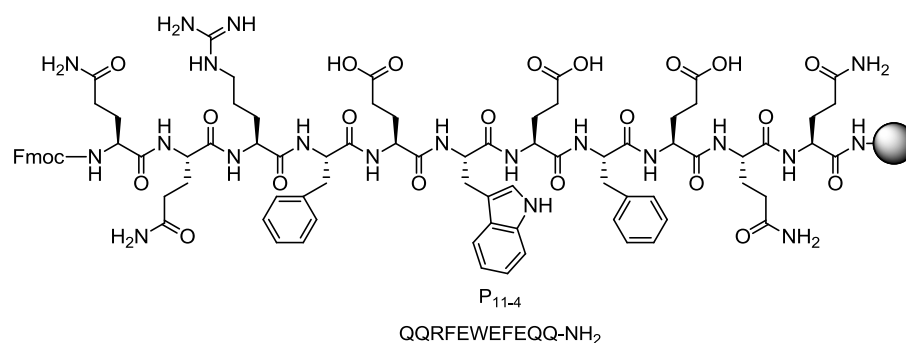
$\nu_{\text{max}}/\text{cm}^{-1}$ (Solid) 2910-2930 (m, C-H), 1738 (m, C=O, acid), 1652 (s, C=O, amide I), 1553 (m, N-H, amide II).

Base peptide 1 (P₁₁₋₄) Protocol 1

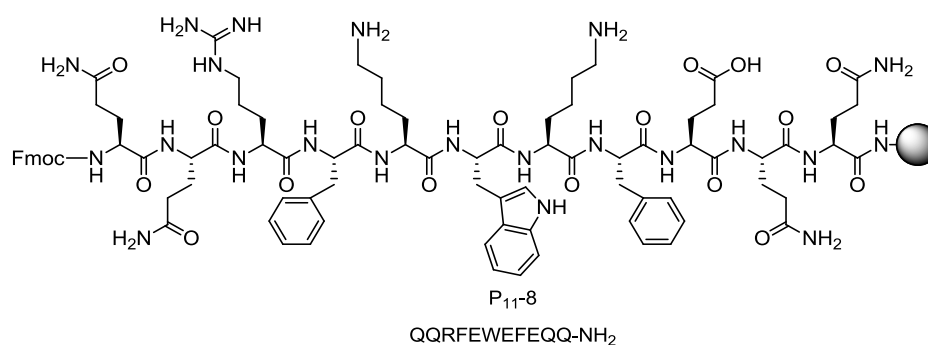
Rink Amide PEGA (loading 0.35 mmol/g) or Rink Amide Novagel (loading 0.63 mmol/g) were swollen in DMF for 1 hr and then either washed with DMF (5 \times). Fmoc-Gln(Trt)-OH (5.0 eq) and HCTU (5.0 eq) were dissolved in DMF and DIPEA (10.0 eq) was added to the solution. The mixture was inverted to mix and then added to the resin and agitated for 1 hr. Consecutive couplings (Q (Fmoc-Gln(Trt)-OH), E (Fmoc-Glu(OtBu)-OH), F (Fmoc-Phe-OH), E (Fmoc-Glu(OtBu)-OH), W (Fmoc-Trp(Boc)-OH), E (Fmoc-Glu(OtBu)-OH), F (Fmoc-Phe-OH), R (Fmoc-Arg(Pbf)-OH), Q (Fmoc-Gln(Trt)-OH), Q (Fmoc-Gln(Trt)-OH)) were carried out using an automated peptide synthesizer (Liberty CEM 12 908505). The resin was filtered then sequential washes of DMF (5 \times 2min), 20% Piperidine in DMF (5min), DMF (2min), 20% Piperidine in DMF (5min), DMF

(2min), 20% Piperidine in DMF (5min) and DMF (5x2min) to carry out Fmoc deprotection. The next amino acid (5.0 eq) and HCTU (5.0 eq) were dissolved in DMF, addition of DIPEA (10.0 eq) to the solution and the mixture was added to the resin and agitated for 20 min under microwave assistance except for the Arginine residue where a normal coupling of 1hr without microwave assistance was carried out.. Once the final amino acid had been coupled, the resin was washed with DMF (5x2ml) then stored in DMF until required for further functionalisation.

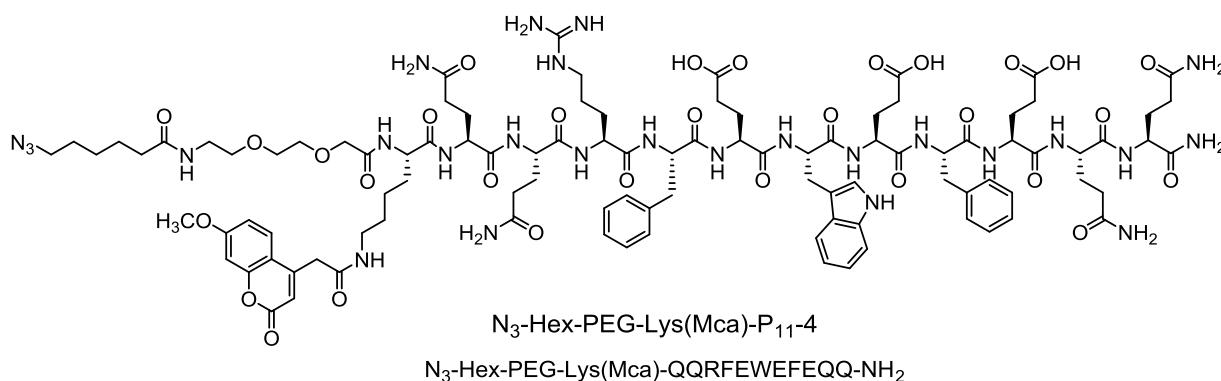
Base peptide 1 (P₁₁₋₄) Protocol 2



NovaSyn TG Sieber (loading 0.1-0.25 mmol/g) were swollen in DMF for 1 hr and then activated by addition of 20% Piperidine in DMF (3x2 min) and then washed with DMF (5x 2min). Fmoc-Gln(Trt)-OH (5.0 eq) and Oxyma Pure (5.0 eq) were dissolved in DMF and DIC (5.0 eq) was added to the solution. The mixture was inverted to mix and then added to the resin and agitated for 1 hr. Consecutive couplings (Q (Fmoc-Gln(Trt)-OH),E (Fmoc-Glu(OtBu)-OH),F (Fmoc-Phe-OH),E (Fmoc-Glu(OtBu)-OH),W (Fmoc-Trp(Boc)-OH),E (Fmoc-Glu(OtBu)-OH),F (Fmoc-Phe-OH),R (Fmoc-Arg(Pbf)-OH),Q (Fmoc-Gln(Trt)-OH),Q (Fmoc-Gln(Trt)-OH)) were carried out using an automated peptide synthesizer (Liberty CEM 12 908505). The resin was filtered then sequential washes of DMF (5x 2min), 20 % Piperidine in DMF (5 min), DMF (2 min), 20% Piperidine in DMF (5 min), DMF (2 min), 20 % Piperidine in DMF (5 min) and DMF (5x2 min) to carry out Fmoc deprotection. The next amino acid (5.0 eq) and Oxyma Pure (5.0 eq) were dissolved in DMF, addition of DIC (5.0 eq) to the solution and the mixture was added to the resin and agitated for 20 min under microwave assistance except for the Arginine residue where a normal coupling of 1hr without microwave assistance was carried out. Once the final amino acid had been coupled, the resin was washed with DMF (5x2 ml) then stored in DMF until required for further functionalisation.

Base peptide 2 (P₁₁₋₈)

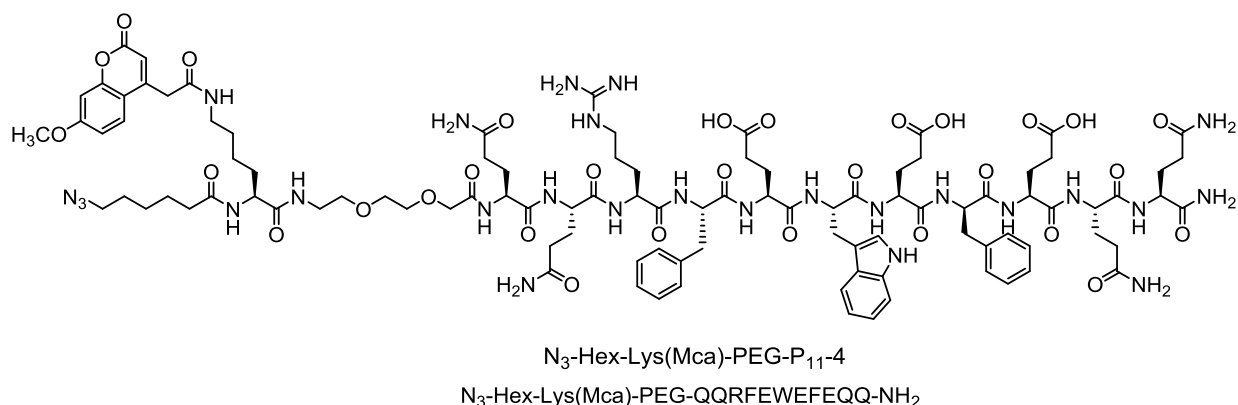
NovaSyn TG Sieber (loading 0.1-0.25 mmol/g) were swollen in DMF for 1 hr and then activated by addition of 20% Piperidine in DMF (3x2 min) and then washed with DMF (5x 2min). Fmoc-Gln(Trt)-OH (5.0 eq) and Oxyma Pure (5.0 eq) were dissolved in DMF and DIC (5.0 eq) was added to the solution. The mixture was inverted to mix and then added to the resin and agitated for 1 hr. Consecutive couplings (Q (Fmoc-Gln(Trt)-OH), E (Fmoc-Glu(OtBu)-OH), F (Fmoc-Phe-OH), O (Fmoc-Orn(Boc)-OH), W (Fmoc-Trp(Boc)-OH), O (Fmoc-Orn(Boc)-OH), F (Fmoc-Phe-OH), R (Fmoc-Arg(Pbf)-OH), Q (Fmoc-Gln(Trt)-OH), Q (Fmoc-Gln(Trt)-OH)) were carried out by an automated peptide synthesizer (Liberty CEM 12 908505). The resin was filtered then sequential washes of DMF (5x2 min), 20% Piperidine in DMF (5 min), DMF (2 min), 20% Piperidine in DMF (5 min), DMF (2 min), 20% Piperidine in DMF (5 min) and DMF (5x2 min) to carry out Fmoc deprotection. The next amino acid (5.0 eq) and Oxyma Pure (5.0 eq) were dissolved in DMF, addition of DIC (5.0 eq) to the solution and the mixture was added to the resin and agitated for 20 min under microwave assistance except for the Arginine residue where a normal coupling of 1 hr without microwave assistance was carried out. Once the final amino acid had been coupled, the resin was washed with DMF (5x2 ml) then stored in DMF until required for further functionalisation.

Peptide 1

P₁₁₋₄ on Rink Amide Novagel resin (0.1 mmol) was coupled with Fmoc-Lys(Mca)-OH (175.6 mg, 0.3 mmol, 3 eq) using HCTU (121 mg, 0.29 mmol, 2.9 eq) and DIPEA ($p=0.74$, 105 μ l, 0.6 mmol,

6 eq) in DMF (3 ml) overnight. Next, Fmoc-PEG-COOH (119 mg, 0.21 mmol, 2.1 eq) was introduced using HCTU (83.2 mg, 0.2 mmol, 2 eq) and DIPEA ($\rho=0.74$, 73.5 μl , 0.42 mmol, 4.2 eq) in DMF (3 ml) overnight. For the attachment of 6-bromohexanoic acid, the acid (195 mg, 1 mmol, 10 eq) and DIC ($\rho=0.81$, 78.1 μl , 0.5 mmol, 5 eq) were dissolved in dry DCM (5 ml) at 0 °C under N_2 . After 30 min, the solvent was removed under reduced pressure and the colourless needles were redissolved in warm DMF (4 ml) and added to the solid phase. The mixture was agitated overnight, filtered and the resin was washed with DMF (5x2 min) and DMSO (5x2 min). For introduction of the azide, NaN_3 (52 mg, 0.8 mmol, 8 eq) was dissolved in DMSO (5 ml) and reacted with the resin overnight. After filtration and washing of the solid phase with DMSO (5x2 min), DMSO/ H_2O 1:1 (5x2 min), DMF (5x2 min) and DCM (5x2 min) the peptide was cleaved using TFA/TIPS/DCM 95:2.5:2.5 (1 ml). The mixture was agitated for 6 hr, filtered and the filtrate concentrated under reduced pressure. The crude peptide was precipitated by addition of cold Et_2O , centrifuged and the pellet suspended in 1% NH_3 solution and lyophilised. Complete removal of the Trp-COOH protecting group was achieved by repetitive re-suspension of the peptide in 1% AcOH and lyophilisation. The peptide was purified by a reverse phased UV-directed Biotage system with 0.1% NH_3 in H_2O as solvent A and 0.1% NH_3 in CH_3CN as solvent B with a gradient 10% \rightarrow 90% solvent B over 20 min. R_t (HPLC-MS column 1 positive) 1.752 min, m/z (ESI⁺) $[\text{M}+2\text{H}]^{2+}$ -1092.2048 100%, $\text{C}_{100}\text{H}_{136}\text{N}_{26}\text{O}_{30}$ requires $[\text{M}+2\text{H}]^{2+}$ 1092.2056.

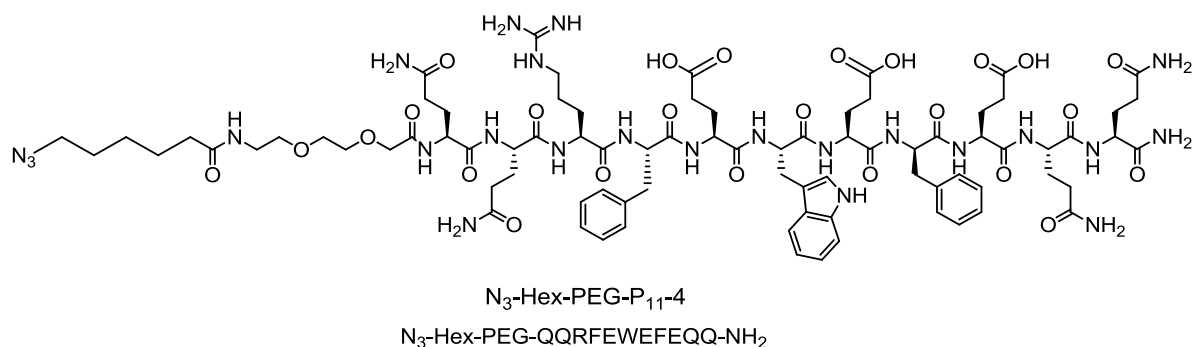
Peptide 2



$\text{P}_{11\text{-}4}$ on Rink Amide Novagel resin (0.1 mmol) was coupled with Fmoc-PEG-COOH (119mg, 0.21 mmol, 2.1 eq) was introduced using HCTU (83.2 mg, 0.2 mmol, 2eq) and DIPEA ($\rho=0.74$, 73.5 μl , 0.42 mmol, 4.2 eq) in DMF (3ml) Next, Fmoc-Lys(Mca)-OH (175.6 mg, 0.3 mmol, 3 eq) using HCTU (121 mg, 0.29 mmol, 2.9 eq) and DIPEA ($\rho=0.74$, 105 μl , 0.6 mmol, 6 eq) in DMF (3 ml) was coupled overnight. For the attachment of 6-bromohexanoic acid, the acid (195 mg, 1 mmol, 10 eq) and DIC ($\rho=0.81$, 78.1 μl , 0.5 mmol, 5 eq) were dissolved in dry DCM (5 ml) at

0 °C under N₂. After 30 min, the solvent was removed under reduced pressure and the colourless needles were redissolved in warm DMF (4 ml) and added to the solid phase. The mixture was agitated overnight, filtered and the resin was washed with DMF (5x2 min) and DMSO (5x2 min). For introduction of the azide, NaN₃ (52 mg, 0.8 mmol, 8 eq) was dissolved in DMSO (5 ml) and reacted with the resin overnight. After filtration and washing of the solid phase with DMSO (5x2 min), DMSO/H₂O 1:1 (5x2 min), DMF (5x2 min) and DCM (5x2 min) the peptide was cleaved using TFA/TIPS/DCM 95:2.5:2.5 (1 ml). The mixture was agitated for 6 hr, filtered and the filtrate concentrated under reduced pressure. The crude peptide was precipitated by addition of cold Et₂O, centrifuged and the pellet suspended in 1% NH₃ solution and lyophilised. Complete removal of the Trp-COOH protecting group was achieved by repetitive resuspension of the peptide in 1% AcOH and lyophilisation. The peptide was purified by a reverse phased UV-directed Biotage system with 0.1% NH₃ in H₂O as solvent A and 0.1% NH₃ in CH₃CN as solvent B with a gradient 10% → 90% solvent B over 20 min. R_t (HPLC-MS column 1 positive) 1.710 min, *m/z* (ESI⁺) [M+2H]²⁺-1092.2057 100%, C₁₀₀H₁₃₆N₂₆O₃₀ requires [M+2H]²⁺ 1092.2056.

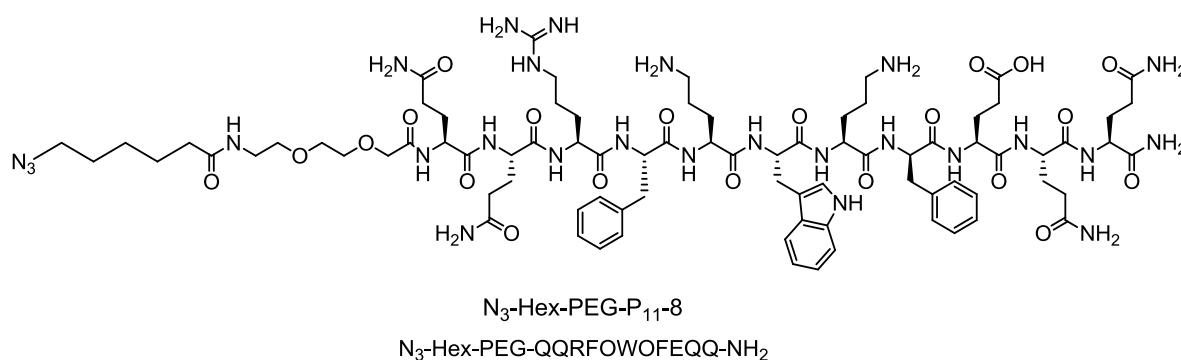
Peptide 3



P₁₁-4 on NovaSyn TG Sieber resin (0.1 mmol) was coupled with Fmoc-PEG-COOH (119 mg, 0.21 mmol, 2.1 eq) was introduced using Oxyma Pure (59.6 mg, 0.42 mmol, 4.2 eq) and DIC (ρ=0.815, 102.9 μl, 0.42 mmol, 4.2 eq) in DMF (3 ml). For the attachment of 6-bromohexanoic acid, the acid (195 mg, 1 mmol, 10 eq) and DIC (ρ=0.81, 78.1 μl, 0.5 mmol, 5 eq) were dissolved in dry DCM (5 ml) at 0 °C under N₂. After 30min, the solvent was removed under reduced pressure and the colourless needles were redissolved in warm DMF (4 ml) and added to the solid phase. The mixture was agitated overnight, filtered and the resin was washed with DMF (5x2 min) and DMSO (5x2 min). For introduction of the azide, NaN₃ (52 mg, 0.8 mmol, 8 eq) was dissolved in DMSO (5 ml) and reacted with the resin overnight. After filtration and washing of the solid phase with DMSO (5x2 min), DMSO/H₂O 1:1 (5x2 min), DMF (5x2 min) and DCM (5x2 min) the peptide was cleaved using TFA/TIPS/DCM 95:2.5:2.5 (1 ml). The mixture was

agitated for 6 hr, filtered and the filtrate concentrated under reduced pressure. The crude peptide was precipitated by addition of cold Et₂O, centrifuged and the pellet suspended in 1% NH₃ solution and lyophilised. Complete removal of the Trp-COOH protecting group was achieved by repetitive resuspension of the peptide in 1% AcOH and lyophilisation. The peptide was purified by a reverse phased UV-directed Biotage system with 0.1% NH₃ in H₂O as solvent A and 0.1% NH₃ in CH₃CN as solvent B with a gradient 10% → 90% solvent B over 20 min. R_t (HPLC-MS column 1 positive) 2.335 min, *m/z* (ESI⁺) [M+2H]²⁺- 919.9373 100%, C₈₂H₁₁₆N₂₄O₂₅ requires [M+2H]²⁺ 919.9384.

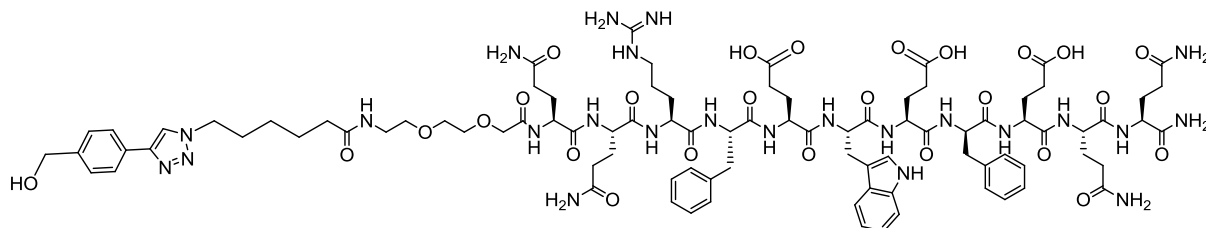
Peptide 4



P₁₁-8 on NovaSyn TG Sieber resin (0.1 mmol) was coupled with Fmoc-PEG-COOH (119 mg, 0.21 mmol, 2.1 eq) was introduced using Oxyma Pure (59.6 mg, 0.42 mmol, 4.2 eq) and DIC ($\rho=0.815$, 102.9 μ l, 0.42 mmol, 4.2 eq) in DMF (3 ml). For the attachment of 6-bromohexanoic acid, the acid (195 mg, 1 mmol, 10 eq) and DIC ($\rho=0.81$, 78.1 μ l, 0.5 mmol, 5 eq) were dissolved in dry DCM (5 ml) at 0 °C under N₂. After 30 min, the solvent was removed under reduced pressure and the colourless needles were redissolved in warm DMF (4 ml) and added to the solid phase. The mixture was agitated overnight, filtered and the resin was washed with DMF (5x2 min) and DMSO (5x2 min). For introduction of the azide, NaN₃ (52 mg, 0.8 mmol, 8 eq) was dissolved in DMSO (5 ml) and reacted with the resin overnight. After filtration and washing of the solid phase with DMSO (5x2 min), DMSO/H₂O 1:1 (5x2 min), DMF (5x2 min) and DCM (5x2 min) the peptide was cleaved using TFA/TIPS/DCM 95:2.5:2.5 (1 ml). The mixture was agitated for 6 hr, filtered and the filtrate concentrated under reduced pressure. The crude peptide was precipitated by addition of cold Et₂O, centrifuged and the pellet suspended in 1% NH₃ solution and lyophilised. Complete removal of the Trp-COOH protecting group was achieved by repetitive resuspension of the peptide in 1% AcOH and lyophilisation. The peptide was purified by a reverse phased UV-directed Biotage system with 0.1% TFA in H₂O as solvent A and 0.1% TFA in CH₃CN as solvent B with a gradient 10% → 90% solvent B over 20 min. R_t

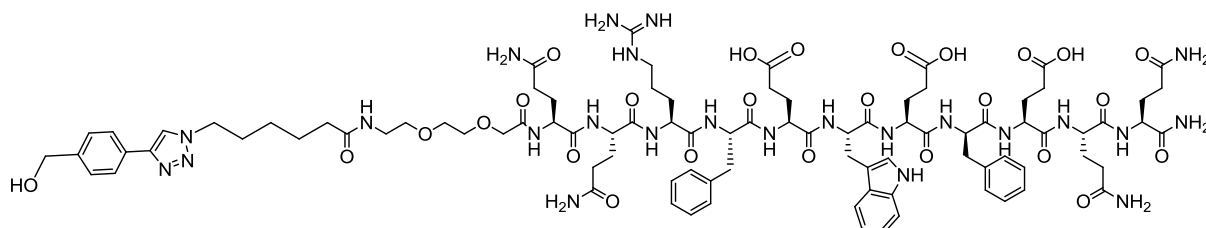
(HPLC-MS column 1 positive) 1.1824 min, m/z (ESI⁺) [M+2H]²⁺- 1077.0440 100%, C₁₀₂H₁₄₆N₂₈O₂₆ requires [M+2H]²⁺ 1077.0431.

Conjugate 1 Protocol 1



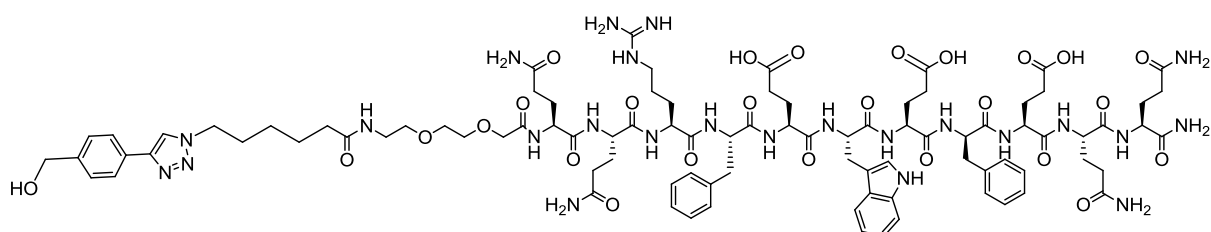
In this order, 0.15 mM ethynyl benzyl alcohol (100 μ l, 1 eq) in DMSO (**Compound 1**), 0.3 mM **peptide 3** (100 μ l, 2 eq) in DMSO, 1 mM CuSO₄·5H₂O (100 μ l, 6 eq) in H₂O and 10 mM Na-Ascorbate in H₂O (100 μ l, 60 eq) were added together after being degassed with N₂ to H₂O (600 μ l). The reaction mixture was left for 90 hr. Upon completion, the mixture was purified by six rounds of dialysis (1 hr) (MWCO 14 kDs), additional H₂O was added and lyophilised. White powder was obtained – **conjugate 1** in ~20 % conversion based on LC-MS analysis.

Conjugate 1 Protocol 2



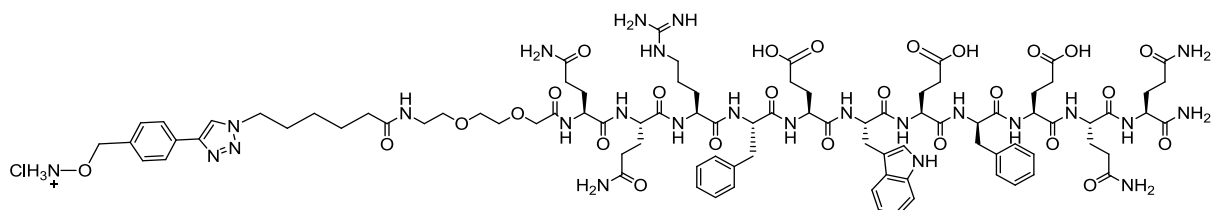
In this order, 1 mM **peptide 3** (100 μ l, 1 eq) in DMSO, 1 mM TCEP in H₂O (100 μ l, 1 eq) in H₂O, 1 mM CuSO₄·5H₂O in H₂O (100 μ l, 1 eq), 1mM TBTA in DMSO (100 μ l, 1 eq) and 5 mM ethynyl benzyl alcohol (100 μ l, 5 eq) in DMSO (**Compound 1**) were added together after being degassed with N₂ to 100 mM sodium phosphate buffer (500 μ l). The reaction mixture was left for 90 hr. Upon completion, the mixture was purified by six rounds of dialysis (1 hr) (MWCO 14 kDa), additional H₂O was added and lyophilised. White powder was obtained – **conjugate 1** in ~80 % conversion based on LC-MS analysis.

Conjugate 1 Protocol 3



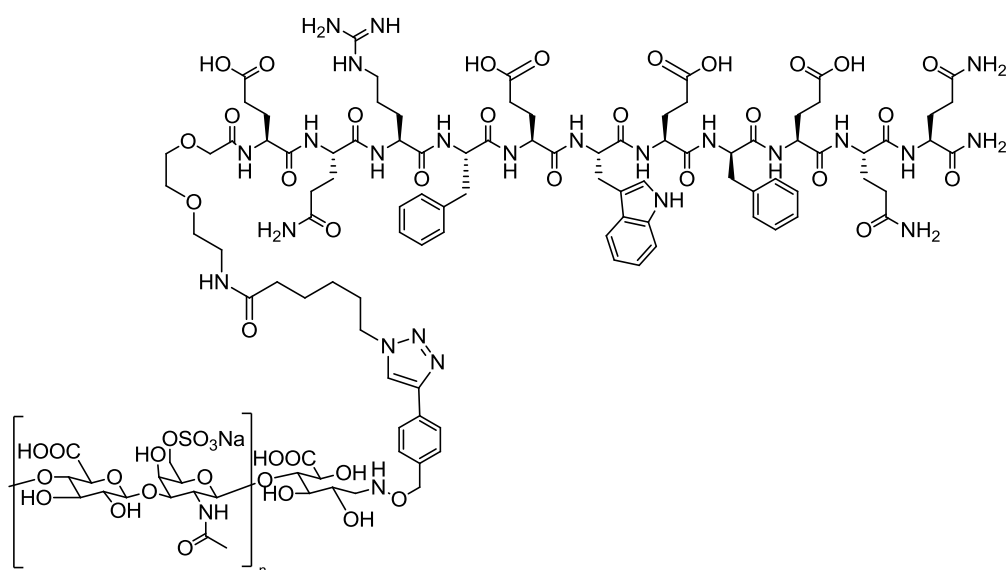
In this order, 1 mM **peptide 3** (100 μ l, 1 eq) in DMSO, 1 mM ethynyl benzyl alcohol (100 μ l, 1 eq) in DMSO (**Compound 1**), 1 mM Na-Ascorbate (100 μ l, 1 eq), 1mM TBTA in DMSO (100 μ l, 1 eq) and 1 mM $\text{CuSO}_4 \cdot 5\text{H}_2\text{O}$ in H_2O (100 μ l, 1 eq) were added together after being degassed with N_2 to 100 mM sodium phosphate buffer (500 μ l). The reaction mixture was left for 90 hr. Upon completion, the mixture was purified by six rounds of dialysis (1 hr) (MWCO 14 kDa), additional H_2O was added and lyophilised. White powder was obtained – **conjugate 1** in ~90 % conversion based on LC-MS analysis.

Conjugate 2



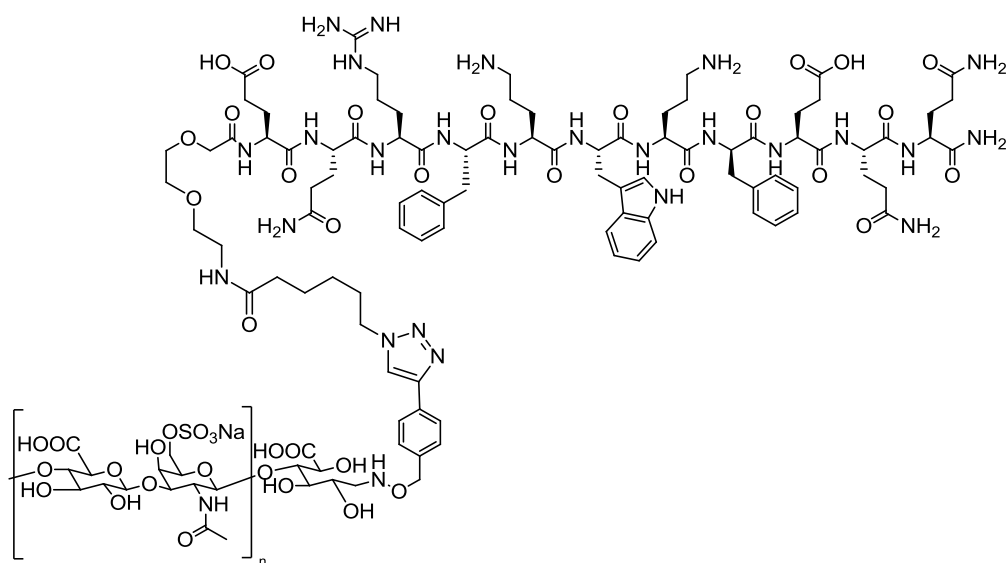
In this order, 1 mM **peptide 3** (100 μ l, 1 eq) in DMSO, 1 mM **Compound 4** (100 μ l, 1 eq) in DMSO, 1 mM Na-Ascorbate (100 μ l, 1 eq), 1mM TBTA in DMSO (100 μ l, 1 eq) and 1 mM $\text{CuSO}_4 \cdot 5\text{H}_2\text{O}$ in H_2O (100 μ l, 1 eq) were added together after being degassed with N_2 to 100 mM sodium phosphate buffer (500 μ l). The reaction mixture was left for 90 hr. Upon completion, the mixture was purified by six rounds of dialysis (1 hr) (MWCO 14 kDa), additional H_2O was added and lyophilised. White powder was obtained – **conjugate 2** in ~70 % conversion based on LC-MS analysis.

Conjugate 3



In this order, 1 mM **peptide 3** (100 μ l, 1 eq) in DMSO, 1 mM **Compound 5** (100 μ l, 1 eq) in DMSO, 1 mM Na-Ascorbate (100 μ l, 1 eq), 1mM TBTA in DMSO (100 μ l, 1 eq) and 1 mM $\text{CuSO}_4 \cdot 5\text{H}_2\text{O}$ in H_2O (100 μ l, 1 eq) were added together after being degassed with N_2 to 100 mM sodium phosphate buffer (500 μ l). The reaction mixture was left for 90 hr. Upon completion, the mixture was purified by six rounds of dialysis (1 hr) (MWCO 14 kDa), additional H_2O was added and lyophilised. White powder was obtained – **conjugate 3** in ~80 % conversion based on LC-MS analysis.

Conjugate 4



In this order, 1 mM **peptide 4** (100 μ l, 1 eq) in DMSO, 1 mM **Compound 5** (100 μ l, 1 eq) in DMSO, 1 mM Na-Ascorbate (100 μ l, 1 eq), 1mM TBTA in DMSO (100 μ l, 1 eq) and 1 mM $\text{CuSO}_4 \cdot 5\text{H}_2\text{O}$ in H_2O (100 μ l, 1 eq) were added together after being degassed with N_2 to 100 mM

sodium phosphate buffer (500 μ l). The reaction mixture was left for 90 hr. Upon completion, the mixture was purified by six rounds of dialysis (1 hr) (MWCO 14 kDa), additional H₂O was added and lyophilised. White powder was obtained – **conjugate 4** in ~70 % conversion based on LC-MS analysis.

2.3.2 Gel preparation

Lyophilised peptide, and either **conjugate 3** or **4** or CS only at varying quantities (~5 mg for 1:64 ratio or ~10 mg for 1:32 ratio) were weighed out into glass vials and reconstituted in monomerising solution – either 1 M sodium acetate buffer at pH 4 or 1 M sodium phosphate buffer at pH 10 (1 ml), vortexed for 30 sec and sonicated for 5 min. The sample was then frozen in liquid N₂ and then lyophilised. Once fully lyophilised the sample was reconstituted in pH adjusted (pH 7.4) buffer (1 ml), vortexed for 30 sec and sonicated for 5 min and stored in a cool, dark place until required for testing.

2.3.3 Liquid chromatography-mass spectrometry (LC-MS) analysis

If the sample was dry, then 5-10 mg was dissolved in either methanol or water (1 ml) if possible, or DMSO (1 ml) as an alternative. If the sample was in solution, then 10 μ L was taken and made up to 1 ml with the solvents mentioned above, depending on the sample. LC-MS analysis (Bruker HCT-Ultra) was then carried out with 10 μ L of sample injected using one of two techniques: small molecular weight sample C18 column – positive procedure with acidic solvents 20-80% MeOH in H₂O, and for large molecular weight sample peptide C18 column– high mass positive peptide column with acidic solvents 20-80% MeOH in H₂O. Once the sample had been processed by the mass spectrometer then the data was analysed on Bruker Data analysis 4.0 software.

2.3.4 Mass spectrometry analysis

The sample (5 mg) was dissolved in methanol or water (1 ml). The solution was then injected into the mass spectrometer (Bruker MaXis Impact spectrometer) (10 μ L) (without LC separation) and run through a high mass electrospray ionisation procedure. The data was analysed on Data analysis 4.1 SRI software.

2.3.5 Fourier transformed infra-red (FTIR) analysis

The sample (~2-3 mg) was placed on the diamond cell of the spectrometer (Perkin Elmer Spectrum 100S) and an infrared spectrum was produced. The spectrum was analysed using Omnic software to assign the relative peaks and the associated functional groups.

2.3.6 Nuclear magnetic resonance (NMR) analysis

The sample (~10 mg) was dissolved in either deuterated water, deuterated chloroform or deuterated DMSO. The solution was then placed in a 5mm NMR tube and analysed. A variety of methods were then carried out on each sample. The 400 MHz apparatus (Bruker Avance 400) was used to run low resolution proton NMR, large scan number proton NMR and 2-D NMR experiments while the 500 MHz apparatus (Bruker Avance 500) was used to run high resolution proton NMR and carbon NMR experiments. The spectra produced was analysed on Mestrenova software to assign the relative peaks and corresponding species environment, depending on the experiment run.

2.3.7 Transmission electron microscopy

Transmission electron microscopy was carried out using a JEOL 1400 electron microscope. Electron microscope (EM) grids (copper hexagonal 400 mesh) pre-coated with a carbon film from mica sheets prepared in house. The peptide solutions remained in contact with the grids for one minute, the excess was then removed. The grids were negatively stained by absorption of 2 % (w/w) aqueous uranyl acetate solution for 20 seconds. The excess was removed and left to air dry. Images were obtained, with the TEM operating at 80 kV accelerating voltage, immediately after sample preparation to avoid artefacts and destruction of the sample.

2.3.8 Rheological analysis

All the rheological measurements were performed on a Malvern Kinexus Pro rheometer with a plate-plate of geometry (diameter: 25 mm, gap: 0.033 mm). All the tests were performed at 37 °C, utilizing a solvent trap with the atmosphere being kept saturated to minimize evaporation of the peptide samples.

Amplitude sweeps were performed at 0.01-100 % shear strain in a controlled mode. Two amplitude sweeps were carried out for each sample (250 μ L) (1 Hz and 20 Hz) and a strain level was chosen at which the elastic/storage modulus (G') and viscous/loss modulus (G'') were independent of strain amplitude at the two different frequency levels.

The dynamic moduli of the hydrogels were measured as a function of frequency with the sweeps carried out between 1 and 20 Hz. Peptide samples (250 μ L) were allowed to equilibrate for 15 minutes once loaded on to the plate prior to the start of testing.

rSpace for Kinexus 1.10 (Malvern Instruments) was used to control the rheometer and to export the raw data into Origin 9.1 (OriginLab Corporation, USA) which was used to process and plot the results.

2.3.9 Flame atomic absorption spectroscopy

In order to calculate the concentration of residual copper following click reactions, the solutions absorbance were measured using a Perkin Elmer Analyst 200 flame atomic absorption spectrophotometer. A calibration curve was required so CuSO₄ standards were made up in distilled water in 100 ml volumetric flasks at the following concentrations 0.001, 0.005, 0.01, 0.05, 0.1, 0.5, 1, 2 and 5 mM. The standards were measured three times to obtain an average and then a calibration curve was plotted using Microsoft Excel of absorbance versus known concentration. The unknown samples were then measured in triplicate also and the average absorbance was used for each unknown to calculate the residual concentration.

2.4 Biochemical methods

2.4.1 Papain Digestion

For sulphated proteoglycan quantification, macerated, freeze-dried tissues were digested using papain.

Reagents listed in **Table 2.2**.

Reagents	Substituents
Digestion buffer (pH 6.0)	0.788 g L-cystine hydrochloride
	1.8612 g EDTA
	1 L PBS
Digestion solution	1250 U papain
	25 ml digestion buffer

Table 2.2: List of reagents for papain digestion of cartilage samples

Papain digestion solution (5 ml) was added to 10 - 20 mg (dry weight) lyophilised cartilage in a bijou and incubated in a water bath at 60 °C for 36 - 48 hr, until fully digested.

2.4.2 DMMB photometric assay

Reagents listed in **Table 2.3**.

Reagents	Substituents
Phosphate buffer (pH 6.8)	137 ml sodium di-hydrogen orthophosphate (0.1 M)

	63 ml di-sodium hydrogen orthophosphate (0.1 M)
DMMB dye (pH 3.0)	16 mg DMMB
	5 ml ethanol
	2 ml formic acid
	2 g sodium formate

Table 2.3: List of reagents for DMMB photometric assay

Made up to 1 L with distilled water

Method:

Tissues were lyophilised (Section 2.2.1.4) and papain digested (Section 2.4.1). Standard calibration solutions of chondroitin sulfate were made up in phosphate buffer at 0, 3.125, 6.25, 12.5, 25, 50, 100, 150 and 200 $\mu\text{g}\cdot\text{ml}^{-1}$. Test samples were diluted 1:100, in phosphate buffer. Each standard and sample (40 μl) were added to a clear, 96 well flat bottomed plate in triplicate, to which 250 μl DMB dye was added. Plates were gently agitated for 2 min on a plate shaker at 50 rpm before the optical density of each well was measured at 525 nm using a micro plate spectrophotometer. A standard curve was plotted of the absorbance of the chondroitin sulfate standards vs concentration. Dilution factors were then accounted for, and the concentration of GAG was determined for tissue dry weight.

2.4.3 Stains-all photometric assay

Reagents listed in **Table 2.4**.

Stock Stains-all solution 0.1 % (w/v) in formamide

Reagent	Substitutents
Stains-all dye working solution (pH 8.8)	0.005 % (w/v) Stains-all stock solution
	10 % (v/v) formamide
	25 % (v/v) isopropanol
	15 mM Trizma-HCl, pH 8.8
	65 % H ₂ O

Table 2.4: List of reagents for Stains-all assay

Made up to 100 ml with distilled water

Method:

Standard calibration solutions of SDS were made up in distilled water at 0, 1.95, 3.91, 7.82, 15.63, 31.25, 62.5, 125, 250, 500, 1000 and 2000 $\mu\text{g}\cdot\text{ml}^{-1}$. Test samples were diluted 1:100, in phosphate buffer. Each standard and sample (40 μl) were added to a clear, 96 well flat bottomed plate in triplicate, to which 50 μl Stains-all dye was added. Plates were gently agitated for 2 min on a plate shaker at 50 rpm before the absorbance of each well was measured at 447 nm using a micro plate spectrophotometer. A standard curve was plotted of the absorbance of the SDS standards vs concentration. Dilution factors were then accounted for, and the concentration of SDS was determined.

2.4.3 Extract cytotoxicity

Each copper salt (CuSO_4 and CuCl_2) was weighed and was added to BHK and L929 media to create test solutions that would give varying concentration (0.001 - 5 mM) during the cytotoxicity testing.

Two cell lines, L929 and BHK cells, were sub-cultured and re-suspended in cell culture medium; DMEM based medium for L929 cells (Section 2.1.7.3) and GMEM based medium for BHK cells (Section 2.1.7.2). Cells were seeded at an appropriate cell density to achieve 80 % confluence in a 96 well plate. The cell suspension (200 μl) was added to the wells of a 96 well plate and incubated for 48 hours at 37°C in 5 % (v/v) CO_2 in air. The cell culture medium was aspirated from the cells and replaced with 100 μl of fresh L929 and BHK cell culture medium. 100 μl of test solution or control (positive, standard cell culture medium with 40 % DMSO; negative, standard cell culture medium) was added and incubated at 37°C in 5 % (v/v) CO_2 in air for 72 hours. Six samples of each peptide were tested. The level of ATP was then measured using the ATPLite-M[®] assay described in Section 2.4.4. The results were collected and plotted as the mean value with 95 % confidence limits (Section 2.7.1). Data was analysed for significant difference by one-way ANOVA.

2.4.4 ATP-lite photometric assay

ATPLite-M[®] assay reagents, lyophilised substrate solution, substrate buffer and mammalian cell lysis solution, were allowed to equilibrate to room temperature. The vial of lyophilised substrate solution was reconstituted by the addition of 5 ml of substrate buffer.

The medium was aspirated from each well of the 96 well plate and replaced with 100 μl of fresh cell culture medium. To each well 50 μl of mammalian cell lysis solution was added and agitated at 500 rpm for five minutes. To each well 50 μl of substrate solution was added; the wells were covered in tin foil to prevent photo-bleaching and agitated at 500 rpm for five minutes. The luminescence was determined using a Chameleon Plate Reader. The data was exported into

Microsoft® Excel 2013, then the results are normalised against the readings for the blank wells.

2.5 Biological methods

2.5.1 Tissue culture

Cells were cultured in cell culture medium (Section 2.1.6). All cell culture work was performed aseptically in a class II safety cabinet. Cultures were incubated at 37 °C in 5 % CO₂ (v/v) in air. Before use, all culture media and additives were equilibrated to 37 °C.

2.5.1.1 Resurrection and maintenance of cells

Following removal from liquid N₂ storage, cells were thawed in a 37 °C water bath. Thawed cell stock (2 ml) was added to a T75 cell culture flask containing 13 ml of the appropriate, pre-warmed cell culture medium. Flasks were incubated for at least 18 hr at 37 °C in 5 % CO₂ (v/v) in air to allow cells to attach to the culture plastic. Culture medium was changed every 48-72 hr until cells were confluent and could be passaged.

2.5.1.2 Cell passaging

Cell culture medium was aspirated and the monolayer gently washed two times with 10 ml PBS without calcium or magnesium. Trypsin/EDTA (1.5 ml) was added to the flask and incubated for 5 min at 37 °C in 5 % CO₂ (v/v) in air. Flasks were gently tapped to detach cells and 10 ml culture medium was added to suspend cells and inhibit trypsin activity. The cell suspension was then centrifuged for 10 min at 150 G. The supernatant was carefully aspirated from the cell pellet, which was then re-suspended in 5 ml culture medium. Following a count of viable cells (Section 2.5.1.3), the appropriate cell density was seeded into a fresh flask with culture medium and the medium replaced every 2-3 days until confluent and ready for further passage.

2.5.1.3 Cell viability

In order to test the viability of cells, trypan blue was added to cell suspensions before counting. Trypan blue is able to enter dead cells due to a loss of membrane potential, so live cells microscopically appeared transparent while dead cells appeared blue and could therefore be excluded from cell counts.

To perform a cell count, 20 µl cell suspension was added to 20 µl trypan blue and added to an Improved Neubauer counting chamber. Viable cells were counted in *n* number of grids which resulted in a cell count. The total number of cells per ml suspension was calculated as follows:

$$\text{Number of cells / ml} = \frac{\text{Number of viable cells}}{4} \times 10^4 \times \text{Dilution factor}$$

Where n = number of grids used in count

And Dilution factor = correction required due to dilution of cell suspension in trypan blue (in this case Dilution factor = 2)

2.5.2 Dissection of cartilage tissue

Porcine legs were supplied by local abattoirs, usually within 24 hr of slaughter. Pigs were aged ~ 6 months. Joints were used fresh, or stored at 4 °C overnight for dissection the following day.

Excess flesh was removed from the skeletal structures to allow easier access and manoeuvrability. Joints were exposed by cutting the surrounding tissue and extracapsular ligaments, then the joint capsule was excised. All ligaments were severed and the menisci removed from the knee so that all joint surfaces were exposed. Excess tissue was removed to ensure as clean a surface as possible was achieved prior to any further processing. The femoral condyles were then removed using an oscillating saw. Any exposed cartilage surfaces were kept hydrated throughout by covering in PBS soaked tissue. Harvested tissue was then kept at 4 °C overnight in PBS soaked tissue or carried forward through the 0.1 % SDS washes for GAG depletion.

2.5.3 GAG depletion method

Reagents listed in **Table 2.5**.

Reagents	Constituents
0.1 % SDS	2 g SDS 2 l distilled water
PBS	See Section 2.1.7.1

Table 2.5: List of reagents for GAG depletion of cartilage tissue

Femoral porcine condyles were placed in 250 ml plastic containers. Sequential washes in the order or and for duration described - 2 × 0.1 % SDS (200 ml) wash overnight, 3 × PBS (200 ml) washes and 1 × PBS (200 ml) wash overnight. Upon completion of the cycle, the tissue was

covered in PBS soaked tissue and either treated with peptide hydrogel samples (Section 2.5.6) or stored overnight at 4 °C until treatment or tested the following day.

2.5.4 Cartilage layer retrieval

Osteochondral pins 9 mm in diameter and ~12 mm deep were extracted from cartilage surfaces of the medial and lateral condyles. The pins were initially marked out then a power drill with a specialist corer drill bit was used to cut into the subchondral bone. A handheld corer was then used to loosen the pin and extract it from the joint. The cartilage layer was removed using a scalpel from the pin and placed in a plastic cassette for fixation processed or frozen in optimal cutting temperature (OCT) fluid for cryo-sectioning.

2.5.5 Cryo-sectioning

Cartilage samples were kept frozen until required. The cryostat (Leica CM3050 S) was pre-cooled to -28 °C. The embedded cartilage samples were then frozen using OCT fluid on to a metal stub and then placed in to a stainless steel holder. The excess frozen OCT fluid was removed and then 100 µm sections were taken and placed on to Superfrost Plus slides then immersed in 70 % (v/v) ethanol for 30 sec to fix the tissue. Once fixed the sections covered in tin foil and were stored at -15 °C until visualised using microscopy.

2.5.6 Histological methods

2.5.6.1 Fixation

Cartilage layer samples were placed in a 250 ml plastic container with 200 ml 1M zinc acetate for 24 hr to achieve complete fixation.

2.5.6.2 Paraffin wax embedding

Cartilage samples were placed in plastic cassettes (Histocette®) and cycled in the Leica TP 120 automated tissue processor. Cassettes containing the cartilage tissue were processed by immersion in 70 % (v/v) ethanol for 1 hr followed by 1 hr in 90 % (v/v) ethanol. Cassettes containing the cartilage tissue were then immersed in absolute ethanol for 2 hr 20 min, 3 hr 20 min then 4 hr 20 min sequentially. Immersion in xylene followed for cycles of 1 hr, 1 hr 30 min and 2 hr sequentially. Cassettes containing the cartilage tissue were then embedded with molten paraffin wax for 1 hr 30 min then 2 hr. Tissue cassettes were taken from the automated processor, tissues removed and orientated cut-surface-down in moulds. Samples were covered in molten wax, left to set overnight at room temperature, after which, excess wax was trimmed away.

2.5.6.3 Sectioning and slide preparation

Wax embedded tissues were sectioned on a microtome (Leica RM2125RTF) to a thickness of 10 μm . Using forceps and a brush, sections were carefully placed in a water bath at 40 °C. The wax sections were then transferred onto Superfrost Plus slides and placed directly onto a hotplate at 45 °C to bake on and dry overnight.

2.5.6.4 Dewaxing and rehydration

Sections were dewaxed in xylene for 10 min, then in fresh xylene for another 10 min. Sections were then dehydrated in 3 successive immersions in 100% (v/v) ethanol for 3 min, 2 min then 2 min followed by immersion in 70% (v/v) ethanol for 2 min. Slides were then placed under running tap water for 3 min to rehydrate the sections.

2.5.6.5 Dehydration and mounting

Stained sections were dehydrated by immersion in 70% (v/v) ethanol for 5 sec, followed by successive washes in 100% ethanol for 1 min, 2 min and 3 min. Sections were then immersed twice in xylene for 10 min each time. Cover slips were mounted to slides using a drop of DPX mountant, avoiding bubbles. Slides were left to dry in a fume hood overnight before visualizing using microscopy.

2.5.6.6 Safranin O/fast green staining

Reagents listed in **Table 2.6**.

Reagent	Substitutents
0.1 % (w/v) Safranin O	0.1 g Safranin O 100 ml distilled water
0.02 % (w/v) Fast green	0.02 g fast green 100 ml distilled water

Table 2.6: List of reagents for Safranin O/fast green staining

Safranin O stains proteoglycans while fast green stains collagen, nuclei are stained with Weigert's haematoxylin. Following dewaxing and rehydration, sections were immersed in Weigert's haematoxylin for 3 min then running tap water for 10 min. Sections were differentiated in 1 % (v/v) acid alcohol for 1 min then rinsed for 3 min in running tap water. Sections were immersed in fast green for 5 min before being rinsed in acetic acid for 10-15 sec.

2.5.7 Immunohistochemical staining

2.5.7.1 Reagents

Reagents listed in **Table 2.7**.

Reagent	Substituents
Hydrogen peroxide solution (3 % v/v)	20 ml hydrogen peroxide (30 % v/v) 180 ml PBS
Tris buffer (2 M, pH 7.6)	242.26 g Trizma base 758 ml distilled water
Sodium chloride solution (3M)	175.32 g sodium chloride 1 L distilled water
Tris buffered saline (TBS)	25 ml Tris buffer (2 M) 50 ml sodium chloride solution (3 M) 925 ml distilled water
TBS containing 0.05 % (w/v) Tween 20 (TBS-T)	500 µl Tween 20 1 L TBS
Bovine serum albumin (BSA; 5 % w/v)	2.5 g BSA 500 ml PBS 6 ml Sodium azide (1 % w/v)
Antibody diluent	300 µl BSA (5 % w/v) 54 ml TBS 1 L distilled water

Table 2.7: List of reagents for immunohistochemical labelling for CS

2.5.7.2 Sample preparation

Fresh and GAG depleted cartilage tissue (n=3) were fixed in 0.1M zinc acetate, wax embedded, sectioned and transferred onto slides as described in Sections 2.5.4.1 – 2.5.4.2, sections were then dewaxed and rehydrated as described in Section 2.5.6.4.

2.5.7.3 Antigen retrieval

As tissues had been zinc acetate fixed, antigen retrieval was performed to re-expose tissue epitopes for antigen binding. Following dewaxing and rehydration, each section was circled using a hydrophobic marker and proteinase K solution applied drop wise until sections were fully covered. Sections were incubated at room temperature for 20 min.

2.5.7.4 Labelling of tissue sections using monoclonal antibodies

Following sample preparation (Section 2.5.7.2) sections were immersed in hydrogen peroxide (3 %, v/v) in PBS for 10 min at room temperature to block endogenous peroxidase activity, and

then washed for 3 min in running tap water. Sections were briefly washed with TBS on a plate rocker. Following antigen retrieval (Section 2.5.7.3) dual endogenous enzyme block (25 µl) from the Ultra vision kit was added to block non-specific background staining, and sections were incubated for 10 minutes, followed by two ten min washes in TBS on a plate rocker. The primary antibody specific for chondroitin sulfate – CS-56 (Rabbit) was then applied at working concentration and incubated at room temperature for 1 hr. Sections were then washed twice for 10 min in TBS-T, then twice for 10 min in TBS on a plate rocker. Labelled polymer-HRP (20 µl) from the Ultra vision kit was then added to each section and incubated for 30 min in the dark at room temperature. Sections were again washed twice for 10 min in TBS-T, then twice for 10 min in TBS on a plate rocker. Excess buffer was tapped off before substrate chromogen (20 µl liquid 3,3-diaminobenzidine (DAB) chromagen plus 1 ml substrate buffer) was added to each section and incubated at room temperature for 10 min. Sections were rinsed four times in distilled water before being immersed in haematoxylin (Mayer's) for 10 sec. Sections were washed for 3 min in running tap water before being dehydrated and mounted in DPX mountant, as described in Section 2.5.6.5. To verify specific antibody binding, an isotype control was performed on native and GAG depleted tissue sections using IgG (Rabbit) in place of the primary antibody at the same concentration as the primary antibody had been used. An antibody-free negative control was also included, in which sections were incubated in antibody diluent alone in place of the primary and secondary antibody. Once dry, sections were viewed using normal light microscopy.

2.5.8 Optical microscopy

Bright-field microscopy was carried out using an Olympus BX40 microscope. Fluorescence microscopy was carried out with the fluorescent vertical illuminator (BX51-RFA) and appropriate filters using the same microscope. Images were captured using an attached Olympus digital camera controlled through Cell^B software (image capture and digitalisation).

2.5.9 Peptide injection

Reconstituted peptide solution as described in Section 2.3.2, was drawn up into a 1 ml syringe through a 30 G needle. The areas of injection on the GAG depleted condyles were circled using a hydrophobic pen. 20 injections were then carried out injecting approximately 50 µl into each site and the sample placed in a suitable container, covered in tin foil to avoid photo bleaching and left overnight in the dark at 4 °C to equilibrate and self-assemble *in situ*.

2.5.10 Confocal microscopy

The samples were imaged in a thawed state and were placed on a glass histology slide (Superfrost plus). The samples were imaged using a Zeiss LSM 510 META inverted confocal microscope using a FITC filter. Fluorescence recovery after photo bleaching experiments were carried out by selecting two regions on a live image of the section. The positive control was imaged every 1 ms until 5 ms then photo bleached using 100 % power of the 488 nm laser. The regions were then imaged every 1 ms for 100 ms. Images were collected using the associated image software (Carl Zeiss ZEN) and were analysed using LSM image browser.

2.6 Biomechanical methods

2.6.1 PMMA cementing

In order to carry out both creep and needle indentation the porcine condyles needed to be cemented. The cementing was carried out in stainless steel cylinders, where 2 stages were prepared. A ratio of 2:1 Cold Cure™ rapid repair powder: Cold Cure™ repair liquid was prepared in straight sided glass beakers. The first stage was poured, allowed to cure for 30 min and then the condyles were placed on the cured cement and the second stage was poured around the condyles to ensure majority of the condyles were covered with the area of interest left exposed. The cement was left to fully cure for 30 min and then removed from the cylinders and covered in PBS soaked tissue ready for testing, or left in 4 °C overnight for testing the following day.

2.6.2 Creep indentation

In order to assess the time dependent biomechanical behaviour of articular cartilage, femoral condyles underwent creep indentation. Condyles were secured in a stainless steel cylindrical sample holder and submerged in PBS to maintain cartilage hydration. An impermeable, stainless steel, cylindrical indenter (2.5 mm diameter) was used with an added 20.5 g weight added to indent the cartilage with a load of 2.54 N over 1 h. The indenter was positioned ~ 1 mm above the cartilage surface and the lowering of the indenter shaft was controlled via a silicone oil filled dashpot, to reduce the speed of impact, the full load was applied within 0.2 sec. The displacement of the indenter was measured using a linear variable differential transducer (LVDT; RDP D5-200H, ElectroSense, PA, USA) and the resistance force measured using a piezo-electric force transformer (Part No. 060-1896-02, ElectroSense, PA, USA). LabView 8 software (National Instruments, TX, USA) was used to collect and store data produced by the force transducer and LVDT.

2.6.2.1 Calibration

Calibration was required to convert the voltage outputs of the LVDT and force transducer into millimetres and Newtons respectively. Standard steel slip gauges were used to calibrate the LVDT, the voltage was recorded for each height increase following the addition of slip gauges. Voltage was plotted against slip gauge height and the linear trend line calculated, the equation of which was used as a calibration factor (**Fig 2.1**).

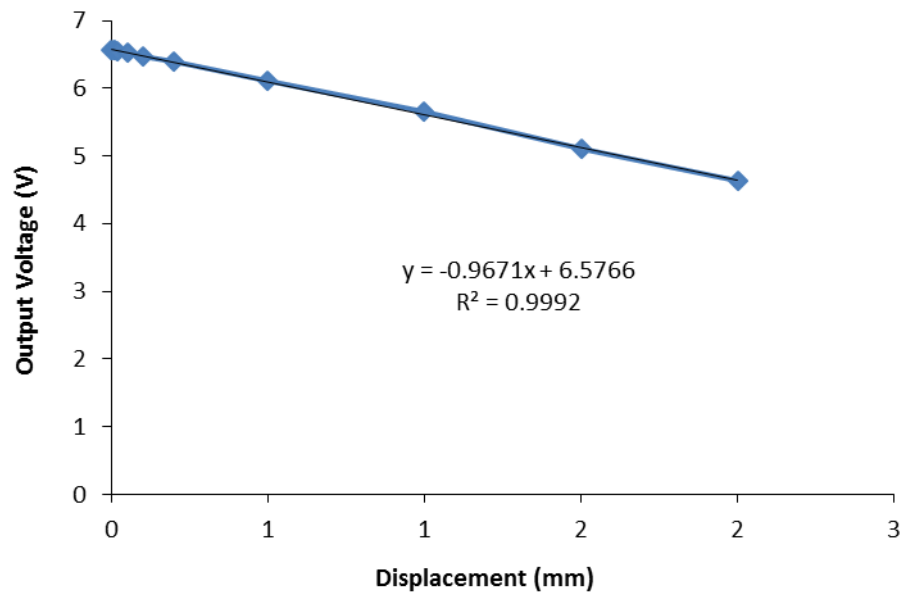


Fig 2.1: Voltage against slip disc height calibration plot.

To calibrate the force transducer, the voltage was recorded over incremental increases of known mass. This again, was plotted as a graph and the equation of the trend line used to convert voltage to Newtons (Fig 2.2).

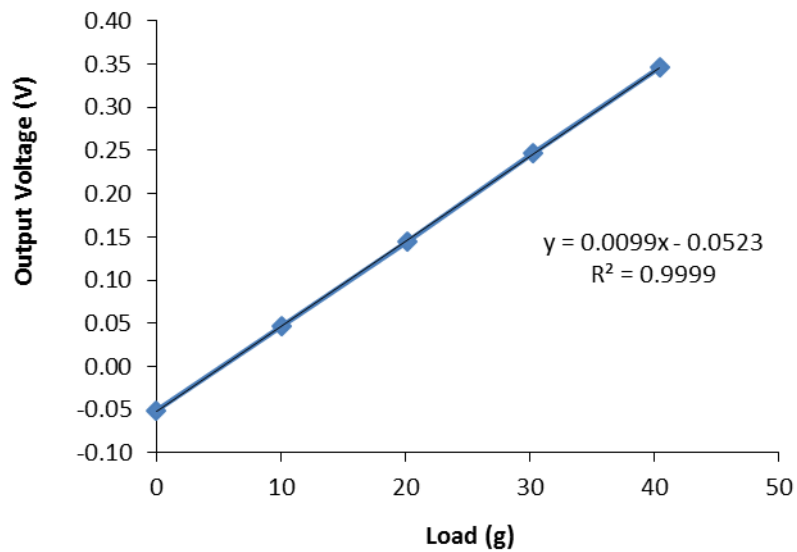


Fig 2.2: Voltage against slip disc weight calibration plot.

2.6.3 Needle indentation for cartilage thickness measurement

The thickness of cartilage was measured in order to normalise deformation data for each cartilage thickness of the condyles so that the percentage deformation could be presented and the material properties could be derived. Cartilage thickness was assessed using needle indentation. An Instron material testing machine (Instron 3365, Bucks, UK) was used for this purpose. A needle attached to the instron arm was manually positioned ~1 mm above the cartilage surface. During testing the arm was controlled via a PC graphic user interface and lowered at a rate of 4.5 mm.min⁻¹. The resistance to motion was measured using a 500 N load cell.

Cartilage thickness was defined as the distance between the increase in resistance from initial needle contact with the surface and the steep increase in resistance from needle contacting the much stiffer bone. Each condyle was indented 6 times and the mean thickness calculated.

2.7 Statistical analysis

2.7.1 Confidence limits

Numerical data was analysed using Microsoft Excel (version 2013, Microsoft) and presented as the mean ($n \geq 3$) \pm 95 % confidence level (CL). The 95% confidence intervals ($\alpha = 0.05$) were calculated using the descriptive statistics part of the data analysis package in Microsoft Excel

2.7.2 Statistical analysis

The student's t-test was used to compare groups of two means or a one way analysis of variance (ANOVA) was used when comparing the means of more than two groups. Individual differences between group means were identified by calculating the minimum significant difference (MSD) at $p = 0.05$ using the T-method, or T'-method when comparing groups of unequal sample size (Sokal & Rohlf, 1995).

2.7.3 Arcsin transformation

Where data is presented as a percentage or proportion, values were transformed to arcsin to allow accurate calculation of 95 % CL and statistical analysis. Following analysis, values were transformed back for presentation.

Chapter 3

Synthesis and characterisation of a synthetic peptide-GAG conjugate

As discussed in Chapter 1, the aim of my approach was to prepare a GAG functionalised version of P11-4. The target route employed a late stage functionalisation of a peptide and derivatised GAG using copper catalysed click chemistry.

This approach was originally tested at Leeds by a postdoctoral researcher (Dr Eva Kainmueller) but only on a very small scale which made characterisation inconclusive and so significant optimisation was required in this chapter. The key reactions involved in the peptide synthesis, GAG functionalisation and biorthogonal connection of the two units will firstly be reviewed followed by discussion of the synthesis of the target functionalised peptide.

3.1 Introduction

3.1.1 Peptide chemistry

Peptide synthesis involves creating a covalent amide bond between the amine group of one amino acid molecule and the carboxylic acid group of another amino acid molecule. This chemistry has changed significantly over the past 100 years, from the first recorded dipeptide synthesis by Fischer in 1901 *via* hydrolysis of a glycine diketopiperazine (Fischer and Fourneau, 1901) through to the formation and use of pseudoprolines by two different groups in 1996 (Liu et al., 1996, Wöhr et al., 1996). The major development in the synthesis of longer peptides was the discovery of solid phase peptide synthesis (SPPS) by Merrifield in 1963. This technique involves attachment of the peptide chain to an insoluble polymeric resin on which the chain grows through iterative amino acid additions (Merrifield, 1963), (Carpino et al., 2003, Chandrudu et al., 2013, Nishiuchi et al., 1998). SPPS enables the easy removal of coupling reagents, simpler peptide isolation/purification procedures and consequently the ability to use excess reagents to drive reactions to completion.

There are currently two different principal strategies for SPPS which differ in the protecting groups used on the α -NH₂ and reactive groups on the amino acid side chains. The most commonly employed method use N- α -fluorenylmethyloxycarbonyl (Fmoc)-protected amino acids which can be deprotected using a mild base – piperidine. A range of side chain protecting

groups are used in Fmoc based synthesis which can be cleaved in TFA. A second approach uses N- α *t*-butyloxycarbonyl (Boc)-protected amino acids however as this protecting group uses TFA for removal, more resilient side chain protection is required which requires deprotection with anhydrous hydrogen fluoride (HF) (Anderson and McGregor, 1957, Carpino, 1957, Carpino and Han, 1970). Avoiding the use of hazardous HF has been one of the main reasons that the Fmoc-based route has gained dominance over the Boc-based methods. Fmoc-based synthesis has been automated using relatively inexpensive equipment as early as 1968 (Chandrudu et al., 2013) and many automated synthesisers are now commercially available.

The relatively simple SPPS method requires four steps – loading, deprotection, coupling and cleavage, as illustrated in **Fig 3.1**, where the deprotection and coupling steps are repeated for each subsequent amino acid residue following the attachment of the first amino acid.

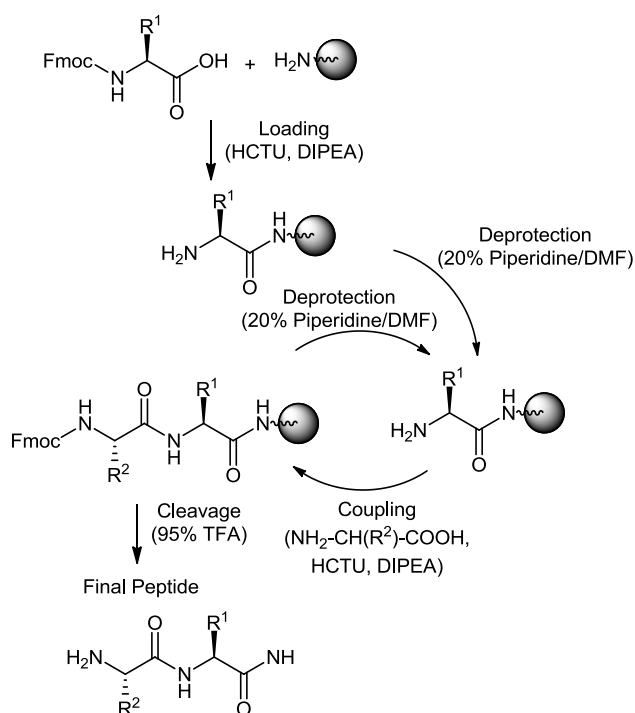


Fig 3.1: A representation of Fmoc-SPPS of a peptide amide where the loading stage uses a resin which has a terminal amino group, with a single synthetic cycle shown.

Whilst the fundamental steps of Fmoc SPPS are simple, different protection and coupling strategies have been developed to optimise the SPPS process. Firstly, both the terminal N^α and the side chain functional group require protection in an orthogonal manner so that chain elongation can be performed without removing the side chain protection (Viola et al., 2003). These lateral protecting groups prevent unwanted side reactions occurring during the coupling reactions. The common side chain protecting groups employed in Fmoc SPPS are illustrated in

Fig 3.2, which include trityl (Trt), pentamethyl-2, 3-dihydrobenzofuran-5-sulfonyl (Pbf), t-butyl (OtBu), and Boc motifs.

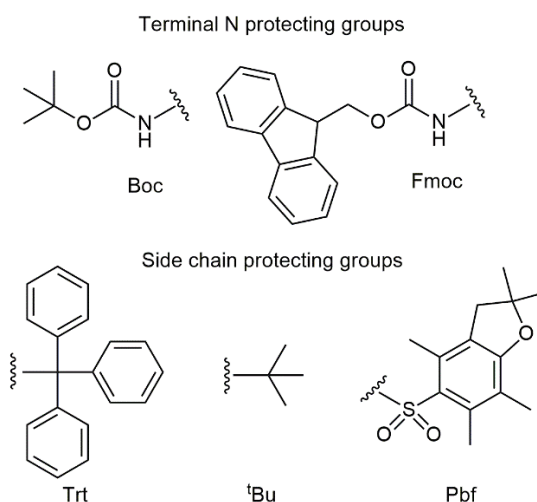


Fig 3.2: Various terminal N and side chain protecting groups.

Another consideration when using SPPS is the coupling method which is used to connect the resin-attached terminal amine to the next amino acid building block. The ideal coupling method should also prevent the potential of racemisation during the coupling (Kokubo et al., 2003). The most commonly used coupling methods are based on using activated esters, frequently of 1-hydroxybenzotriazole (HOBt) or a closely related alternative. These are generated *in situ* using an activating agent such as a carbodiimide (eg DIC) or a uronium reagent such as HATU, or the less allergenic HCTU in the presence of tertiary amine base (Tibbitt and Anseth, 2009). Carbodiimide mediated activation involves *in situ* formation of an *O*-acylisourea intermediate which reacts with HOBt to form the hydroxybenzotriazole ester. The rapid reaction of the HOBt with the intermediate prevents intramolecular cyclisation to form an oxazolone where racemisation can occur (Hutmacher, 2001). The HATU method uses a weak base such as *N,N*-Diisopropylethylamine (DIPEA) to deprotonate the carboxyl group in order to accelerate the coupling reaction but a similar activated ester still results. More recently the observation that HOBt can be explosive under certain conditions has led to alternatives being developed. The most popular is OxymaPure® (Behrendt et al., 2016) which is typically employed with DIC in coupling reactions. The mechanisms of these two methods are shown in **Fig 3.3**.

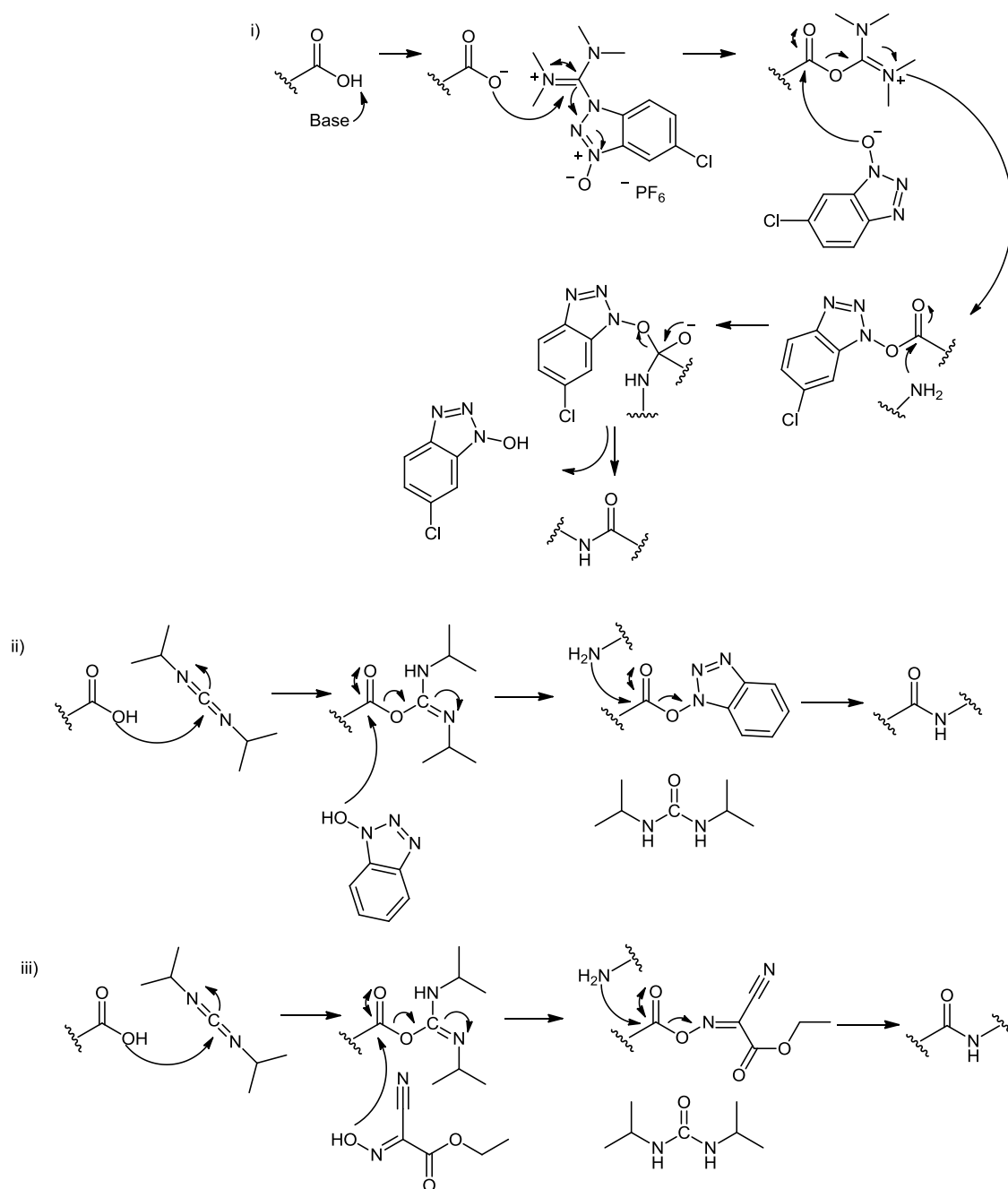


Fig 3.3: i) HATU method mechanism using HCTU, where the base is DIPEA ii) HOBT method mechanism using HOBT and DIC iii) HOBT method mechanism using Oxyma Pure® and DIC.

The final consideration in designing SPPS is the choice of resin and linker where a range of different base resins have been developed with different loading and swelling properties which can affect the yields of peptides, particularly with difficult sequences. A range of linkers can also be used to attach the first amino acid to the resin that produce different C-terminal functions on the peptide (Elashal et al., 2016) and which cleave from the resin under different conditions.

3.1.2 Carbohydrates

Carbohydrates, and especially polysaccharides, have been extensively investigated in the field of biomaterials/regenerative medicine. These naturally occurring polymeric chains comprise various saccharide building blocks connected in linear and sometimes branched arrays. The main focus of attention for biomaterials research ranges from polysaccharides that are found within nature but not the human body – such as chitosan (Bertoldo et al., 2011, Ifuku et al., 2011, Lallana et al., 2009), through to those found in great abundance within the human body – such as hyaluronic acid or chondroitin sulfate (Hu et al., 2011, Upadhyay et al., 2009, Yamaguchi et al., 2010, Yamaguchi et al., 2006) The structures of these polysaccharides is shown in **Fig 3.4**.

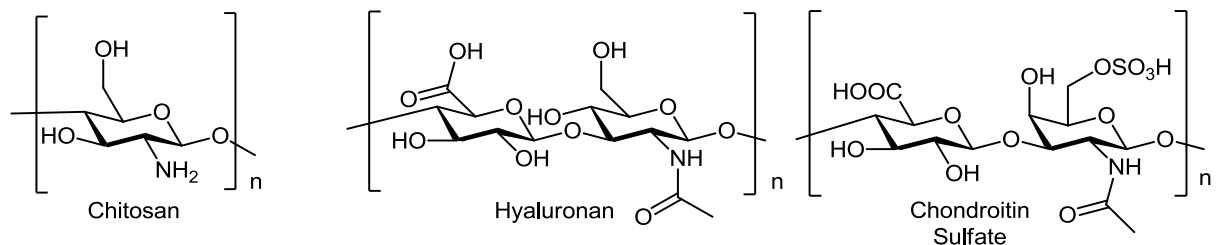


Fig 3.4: Different natural polysaccharides, where chitosan consists of a single repeating uncharged saccharide unit (β -(1-4)- linked D-glucosamine with random glucosamine residues being acetylated), whilst hyaluronic acid (alternating β -(1-3) and β -(1-4)-linked D- glucuronic acid and D-N-acetylglucosamine) and chondroitin sulfate (D-glucuronic acid and D-N-acetylgalactosamine with random sulfation of hydroxyl groups) consist of a repeating anionic disaccharide unit.

Hyaluronic acid and chondroitin sulfate are known as glycosaminoglycans, and are found within many different tissues within the human body but the main tissue where these two GAGs work in synergy is articular cartilage. These GAGs, along with other similar GAGs such as dermatan sulfate and heparin sulfate, associate with one another through linker proteins along a central backbone to form a family of macromolecules called proteoglycans. The most abundant proteoglycan found within the human body is aggrecan, which consists of a hyaluronic acid backbone to which linker proteins connect at random sites. A core protein – ACAN is connected to the linker protein which is highly modified with chondroitin sulfate and dermatan sulfate which project outwards to produce a “brush-like” structure, as illustrated in **Fig 3.5**.

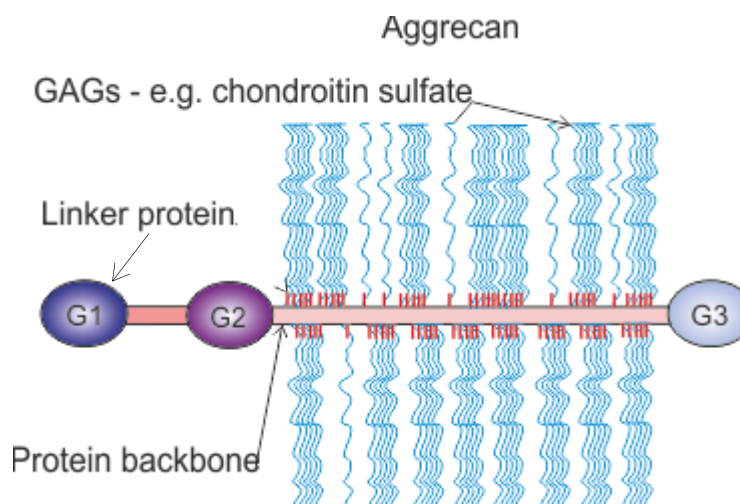


Fig 3.5: A representation of aggrecan, with the GAG chains arranged in a brush-like structure around a protein backbone. A more detailed description can be found in Chapter 1.

These polysaccharides can consist of up to 1000 repeating units of the structures shown in **Fig 3.5** which, when combined with the random modifications through enzymatic processes – such as acetylation in the case of chitosan and hyaluronic acid or sulfation for chondroitin sulfate make direct chemical synthesis of these species impractical. Consequently the GAGs that will be incorporated into materials in this project will need to be derived from natural sources and then selectively derivatised to enable attachment to peptides. Selective derivatisation of GAGs is however challenging resulting from the multiple reactivity of the monomeric building blocks and the length and polydispersity of the polysaccharides which makes controlling stoichiometry and subsequent analysis highly challenging. Various strategies have been employed to modify these high molecular weight structures such as azidation, esterification, amidation and reductive amination (Elchinger et al., 2011). With the exception of reductive amination, these strategies mainly involve modifying the hydroxyl or amino groups on saccharide units. Reductive amination can be carried out selectively on the reducing end of a saccharide due to the equilibrium between the cyclic hemiacetal and the open chain aldehyde forms at this position as shown in **Fig 3.6**. Reductive amination hence selectively functionalises a single position in the saccharide and was the reaction employed in this project.

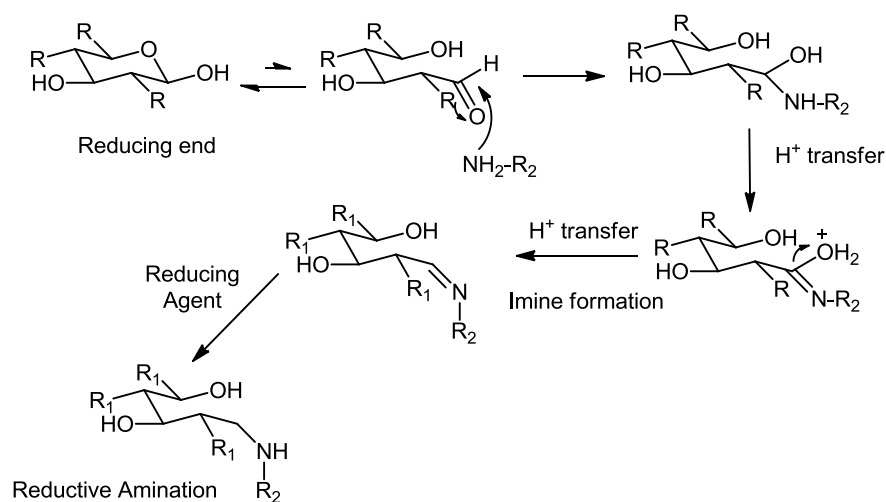


Fig 3.6: The equilibrium state of the reducing end of a saccharide and reductive amination *via* the formation of an imine.

3.1.3 Click chemistry

Once the peptide sequence has been successfully assembled, the terminal nitrogen can either be derivatised with additional functionality. The P₁₁-X series of peptides are acetylated to prevent the N-termini bearing a positive charge which can be detrimental to self-assembly, with the structure of a typical P₁₁-X peptide and the acetylated group shown in **Fig 3.7**. Alternatively the termini can be modified to enable further functionalisation of the peptide to occur after synthesis and cleavage from the resin. One of the most versatile modifications currently employed, is to arm the peptide chain with functional groups that enable a range of biorthogonal reactions, generically categorised by the term 'click' chemistry, to be utilised to append further groups onto the peptide. This type of post-synthesis functionalisation has become common place in the world of chemical biology, chemical engineering, biomaterials and regenerative medicine.

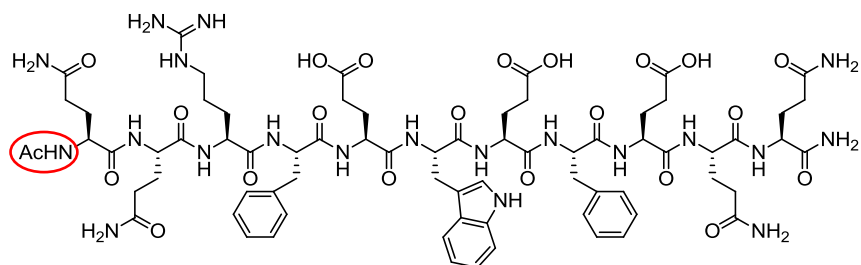


Fig 3.7: An example of a P₁₁-X peptide and the acetylated terminus highlighted.

There are various types of click chemistry currently employed, where the biocompatibility and rate of reaction of the biorthogonal step can differ greatly. One of the most common click chemistries is the azide-alkyne 1, 3 dipolar cycloaddition, first documented by Huisgen in 1963,

where an azide and an internal or terminal alkyne react to form a 1,2,3-triazole (Huisgen, 1963). However, it was not until 2001, when the Sharpless group utilised this reaction in the context of a biological system that the importance of this and other click-type reactions was rediscovered. Since this point groups around the world have developed many different biorthogonal reaction systems (Kolb et al., 2001). These different reactions have varying rate constants (k) ranging from slow ketone condensation reactions with $k \sim 10^{-4} - 10^{-3} \text{ M}^{-1} \text{ s}^{-1}$ (Rideout, 1986, Mahal et al., 1997, Brustad et al., 2008, Chen et al., 2005, Lang and Chin, 2014) through to exceptionally rapid tetrazine-*trans* cyclooctene (TCO) and enzymatic reactions with $k \sim 10^5 \text{ M}^{-1} \text{ s}^{-1}$ (Lang et al., 2012a, Lang et al., 2012b, Seitchik et al., 2012). There are at least eleven different biorthogonal reaction systems that have been developed including a family of systems involving tetrazines (Lang et al., 2012a, Lang et al., 2012b, Seitchik et al., 2012) while another family include strain-promoted alkyne-azide/alkyne-nitrone cycloadditions where the alkyne is usually incorporated into a strain cyclooctyne ring system (Plass et al., 2011, Ning et al., 2010). The most commonly used system though, is based on utilising copper (I) complexes to catalyse the cycloaddition reaction between an alkyne and an azide – this system is called Cu (I)-catalysed alkyne-azide cycloaddition (CuAAC), where the $k \sim 10^2 \text{ M}^{-1} \text{ s}^{-1}$. Typically this reaction is tolerant of a range of pH values and functions in aqueous buffers at a range of concentrations. Example of different biorthogonal click reactions are illustrated in **Fig 3.8**, with the typical k values shown.

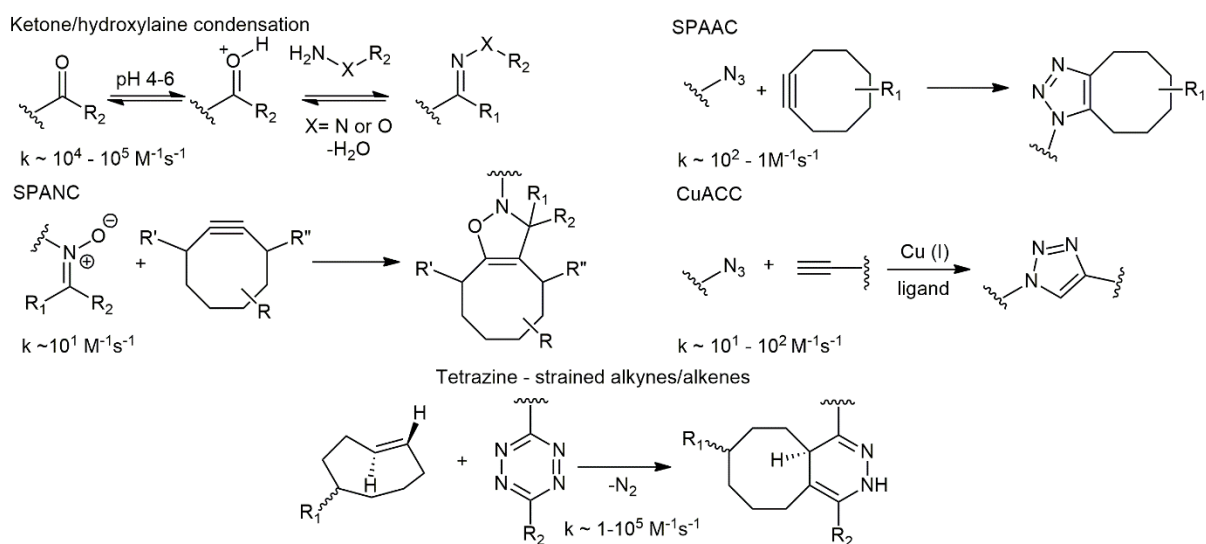


Fig 3.8: Various types of “click” reactions, with the corresponding rate constants shown.

The versatility of this chemistry has opened up the potential for far greater control over constructing complex, multi-domain structures, which, in the field of chemical biology, has allowed labelling of proteins with various diagnostic tools such as fluorophores.

As described in Chapter 1, the general synthetic route will be as shown in **Fig 3.9**.

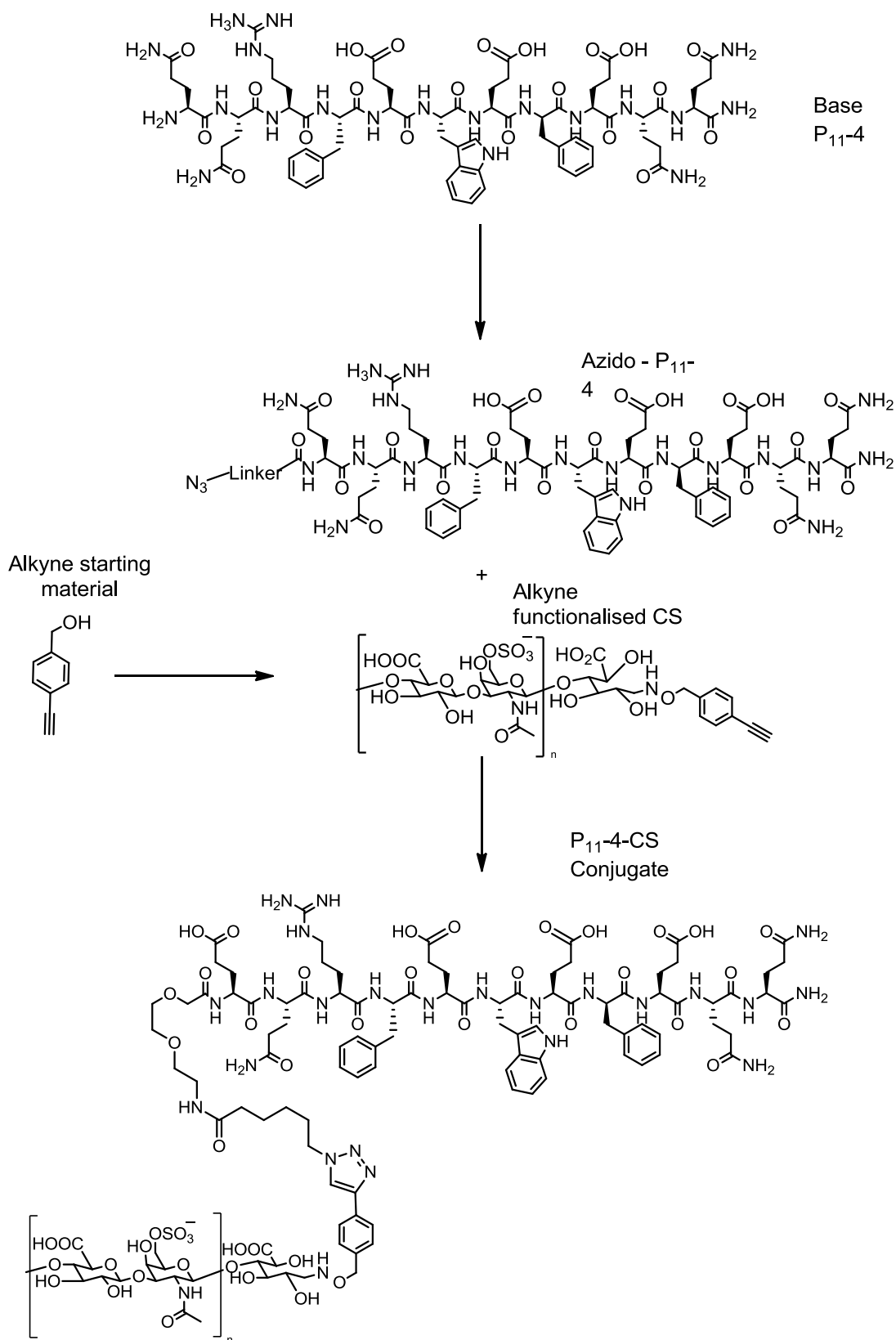


Fig 3.9: The general synthetic strategy for the total synthesis of a peptide-CS conjugate based on synthesizing two fragments: an azide functionalised peptide fragment and a functionalised CS fragment.

3.2 Results

3.2.1 Synthesis of P₁₁₋₄ and P₁₁₋₈ peptide fragments

In order to prepare functionalised peptide building blocks the first step was to prepare the base peptide using manual SPPS. P₁₁₋₄ is acylated at the N-terminus but replacement of this unit can enable the installation of the required functional groups for GAG conjugation. The initial design also envisaged addition of a fluorophore to the peptide chain to enable tracking of the molecule and aid analysis.

The target product bore an N-terminal azido group separated from the peptide by a PEG spacer. A coumarin functionalised lysine residue has been added at the N-terminus of the core P₁₁₋₄ peptide to provide the required fluorescence (**Fig 3.10**).

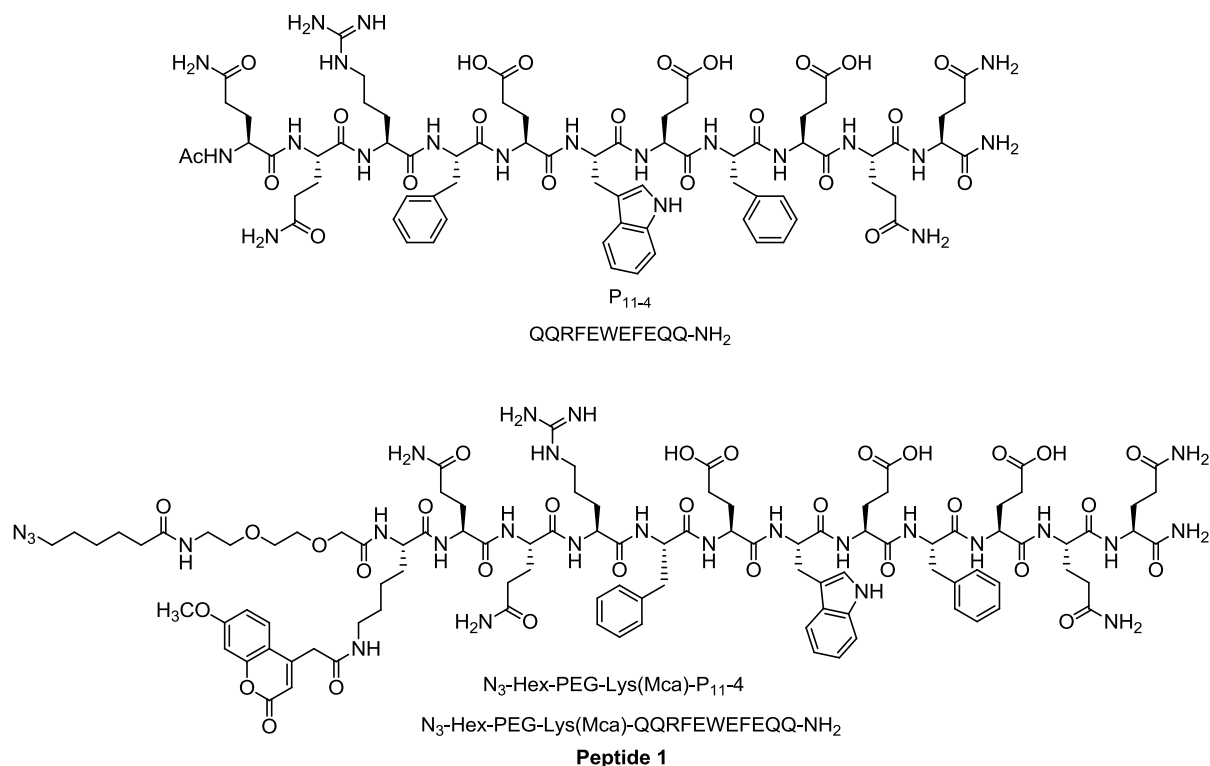


Fig 3.10: Structure of P₁₁₋₄ (top) and peptide 1 - functionalised P₁₁₋₄ (bottom).

This methylcoumarin labelled lysine residue has good photophysical properties with an excitation peak $\sim 360\text{nm}$ which does not overlap with the excitation peak of the tryptophan side chain ($\lambda_{\text{ex}} \sim 284\text{ nm}$), which meant UV detection could be employed to aid in the characterisation of the Pep/GAG conjugate. The appropriate Fmoc protected amino acid building block was also commercially available.

3.2.1.1 P₁₁-4: Unidecamer or Dodecamer

Previous research carried out by the Aggeli group at the University of Leeds, suggested that the optimal number of amino acids in a peptide chain for self-assembly was any odd number as this minimises the entropic penalty and maximises the enthalpic gain during self-assembly (Aggeli *et al.*, 2001). The addition of the coumarin molecule in **peptide 1** extends the formal peptide chain to 12 amino acids due to the coupling of the labelled lysine. In case this disfavoured incorporation of the peptide into a P₁₁-4 array an alternative design was also targeted where the fluorophore was installed after the PEG spacer preserving the length of the self-assembling sequence, as shown in **Fig 3.11 and 3.12**. The alternative would be synthesized in the same manner as the original.

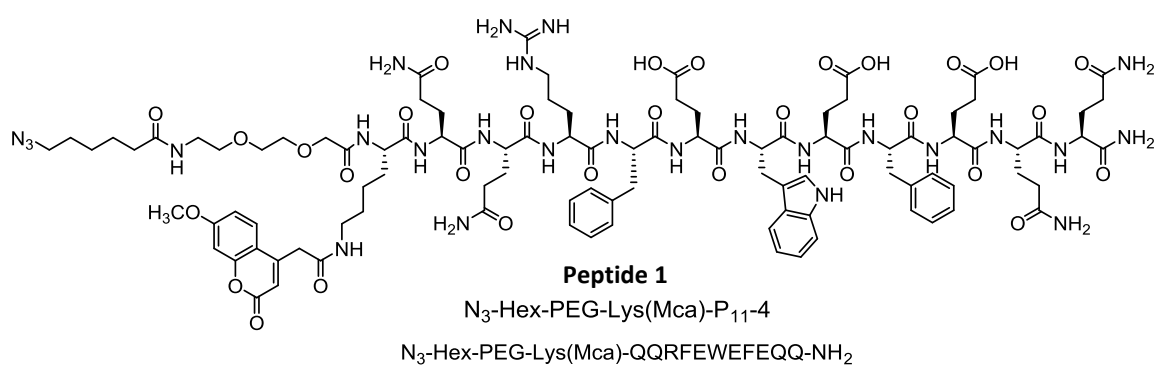


Fig 3.11: Structure of functionalised P₁₁-4 or “P₁₂-4” – dodecamer.

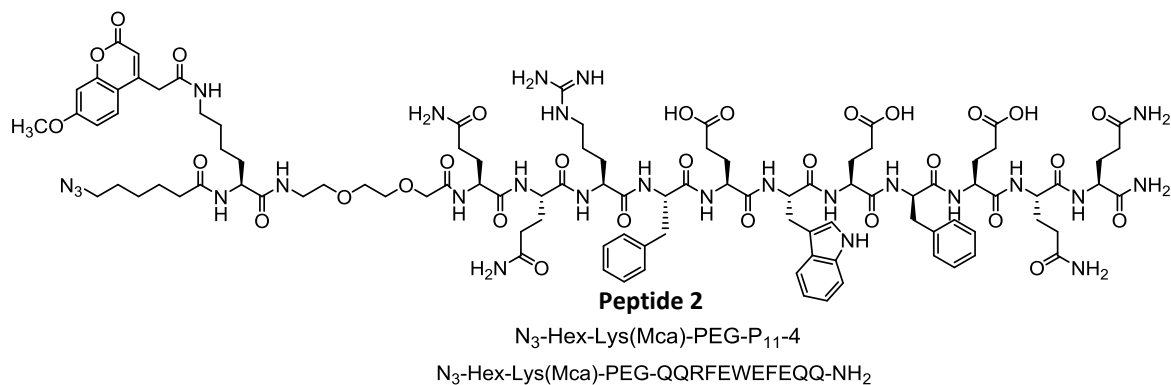


Fig 3.12: Structure of functionalised P₁₁-4 – unidecamer.

Various reaction conditions and reagents were employed to optimise the synthesis of the functionalised P₁₁-4 molecule, and reactions were optimised by synthesising both **peptides 1 and 2** using both manual and automated Fmoc SPPS. The various attempts are summarised in **Table 3.1**.

Reaction N°	Resin	Coupling Reagents	Coupling Time (min)	Manual or Automated	Success	Cleavage Mixture	Comments	Decision for future reactions
1	PEGA Rink Amide	HCTU / DIPEA	180	Manual	×	TFA: Phenol: Ethanediol: Anisole (92.5: 2.5: 2.5: 2.5)	MS-MS analysis showed the presence of P ₁₁ -4 but unsuccessful for functionalised peptide	Reduction of coupling time and change cleavage mixture.
2	PEGA Rink Amide	HCTU / DIPEA	60	Manual	×	TFA: TIPS: DCM (95: 2.5: 2.5)	Unknown reason why synthesis failed – MS showed no peptide species present	Use automated synthesizer, based on research reporting increased success (Collins et al., 2012)
3	PEGA Rink Amide	HCTU / DIPEA	60	Automated (microwave assisted except for R - intramolecular lactam formation - Collins et al., 2012)	×	TFA: TIPS: DCM (95: 2.5: 2.5)	Deletions of amino acids was detected in MS of crude product, as shown in Fig 37	Investigation into loading success testing
4	Novagel Rink Amide	Oxyrna Pure / DIC	60	Automated (base P ₁₁ -4 sequence) / Manual (functionalisation steps)	✓	TFA: TIPS: DCM (95: 2.5: 2.5)	Successful – LC-MS as clean as the previous method but complete synthesis	N/A
5	NovaSyn® TG Sieber	Oxyrna Pure / DIC	60	Automated (base P ₁₁ -4 sequence) / Manual (functionalisation steps)	✓	TFA: TIPS: DCM (95: 2.5: 2.5)	Successful but yield was low – 11 mg – 2.4%	N/A

Table 3.1: A summary of the various methods and conditions employed in the attempt to successfully synthesize the peptide fragment – other than method 5, all methods were employed for peptides 2 and 3.

As noted in **Table 3.1** for reaction 3, the synthesis was partially successful, showing the presence P₁₁-4 and a rather clean mass spectrum probably due to the increased purity achieved by the automated approach. The cleaner mass spectrum allowed further analysis to be carried out which showed the presence of 3 additional peptides besides P₁₁-4 which were shorter than P₁₁-4. Each shorter peptide was missing a C-terminal section indicating incomplete loading of the resin with the first amino acid – Fmoc-Gln (Trt)-OH. The mass spectrum is shown in **Fig 3.13**. This was the consequence of incomplete loading of the resin and not blocking the unreacted groups thus resulting in multiple C-terminal amino acids.

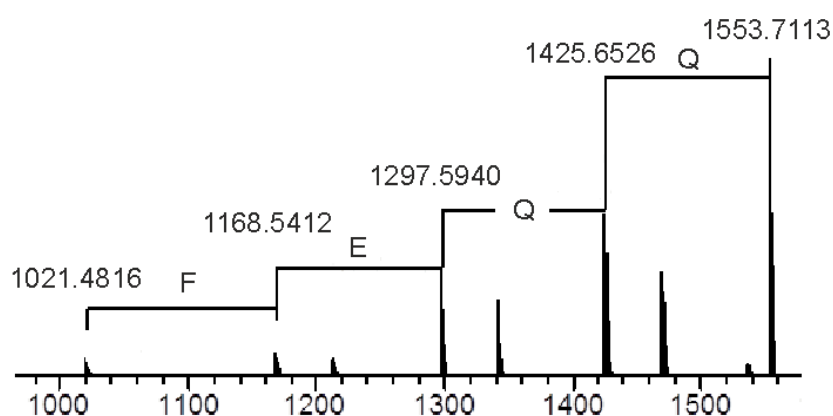


Fig 3.13: Mass spectrum analysis indicating that sequential deletion of amino acids during the P₁₁-4 synthesis which resulted from incomplete loading of the resin with the initial amino acid – Gln.

This observation led to investigation of alternative loading conditions resins and coupling reagents, where the different resins used are shown in **Fig 3.14**. When loading tests were carried out using PEGA Rink Amide Resin and HCTU/DIPEA, with each completed loading cycle monitored by a Kaiser test, the average number of loading cycles required for complete loading was 5 ± 1 .

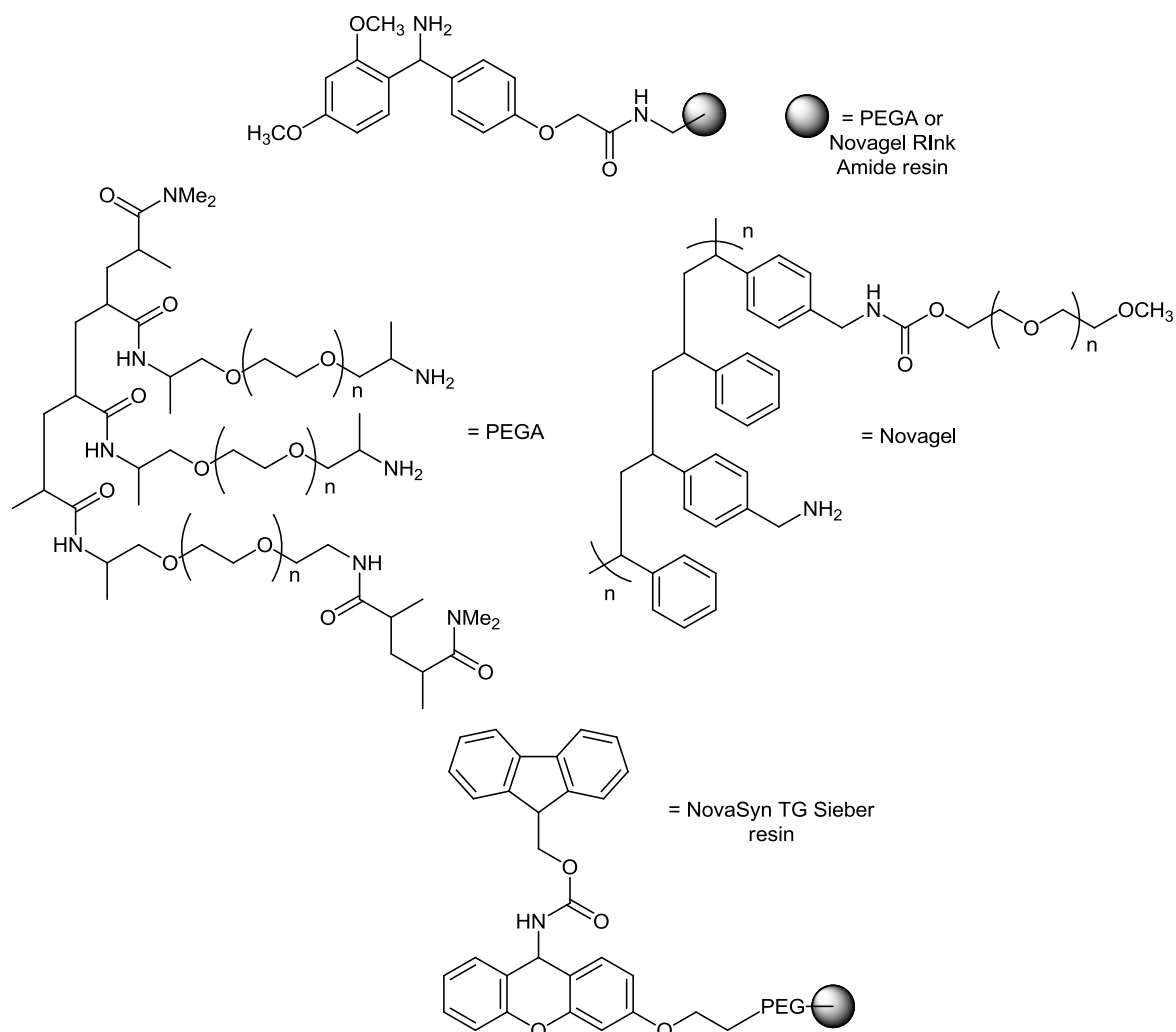


Fig 3.14: The structures of the two different resins mainly employed – PEGA Rink Amide and Novagel® Rink Amide resins.

An alternative resin –Novagel Rink Amide, was chosen which had a larger loading capacity (0.65 mMol/g) than the PEGA Rink Amide (0.2-0.5 mMol/g) and did not require activation but came in a dry form which made accurate weighing out and preparation i.e. swelling easier. As illustrated in **Fig 3.14**, the linker in each type of resin was the same but the solid polymeric support was different. The average number of loading cycles when the same test as above was carried out was 4 ± 1 . Whilst this was an obvious improvement it still meant the loading period was ≥ 2 days so alternative coupling reagents were investigated.

The results of these alternatives – HOBt.nH₂O/DIC and Oxyma Pure/DIC and the results above are summarised in **Table 3.2** below.

Resin	Reagents	N° Loading Cycles
PEGA Rink Amide	HCTU/DIPEA	5 ± 1
Novagel Rink Amide	HCTU/DIPEA	4 ± 1
Novagel Rink Amide	HOBt.nH ₂ O/DIC	4 ± 1
Novagel Rink Amide	Oxyma Pure/DIC	2 ± 0

Table 3.2: Average loading cycles required to achieve complete loading for different combinations of resins and coupling reagents.

On the basis of these results Rink Amide Novagel was employed in future reactions and loaded using DIC/ OxymaPure as activating agent. Using these conditions for loading both functionalised **peptides 1** and **2** were successfully assembled and cleaved from the resin, although in modest yield (4.3 % and 3.9 % respectively)

Mass spectrometry and LC-MS analysis indicated functionalization was successful so the functionalised peptides was cleaved and taken forward to purification *via* HPLC, where the mass spectra are shown in **Fig 3.15**. In the figure below, the highlighted species are the doubly charged species. The carboxylated species was due to the incomplete deprotection of the Boc group from the Trp residue, as illustrated in the figure below.

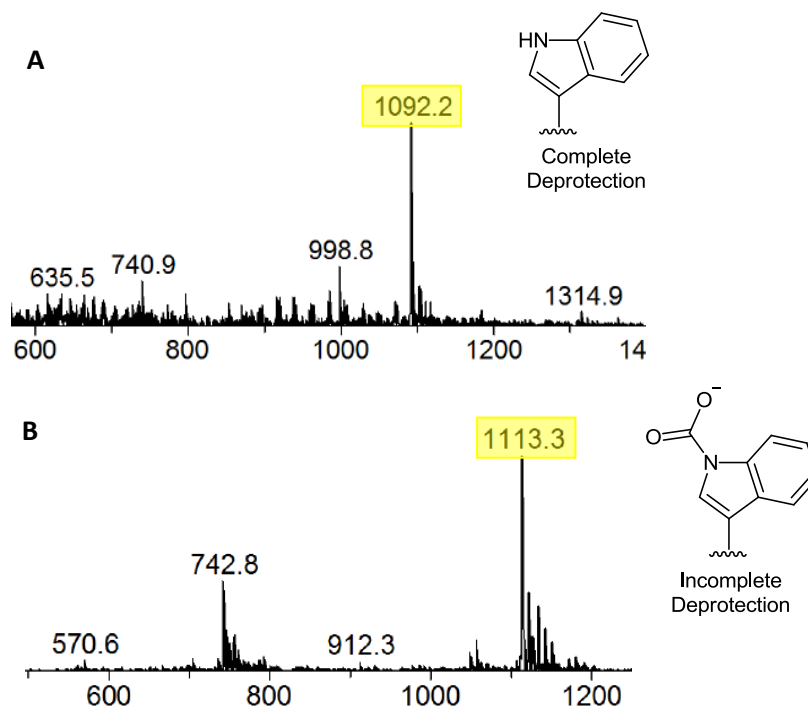


Fig 3.15: Mass spectra of both functionalised P₁₁-4 in crude form, A – P₁₁-4 and B – “P₁₂-4” where the highlighted peptide peak in B had the Trp residue carboxylated. This residual CO₂ group was removed by treatment with AcOH and lyophilisation.

UV-directed reverse phase HPLC was employed to purify the crude peptide with a C18 peptide column and a gradient of 10-30% 0.1% NH₃ aqueous solution (to keep the peptide from self-assembling) as solvent A and CH₃CN as solvent B and fractions detected at 254nm and 280nm (absorbance of the tryptophan side chain). On a test run, a UV absorption peak at 17.4min was collected and analysed by LC-MS which indicated the presence of the functionalised P₁₁-4, with the UV trace and LC-MS spectrum shown in **Fig 3.16**. On full scale purification, the collected fraction showed little during LC-MS analysis. This was predicted to be because of the DMSO added to aid dissolution of the crude peptide for HPLC as 254nm is the absorption peak for DMSO. This issue of solubility of the crude product was reinforced when inspection of the vials of the crude mixture showed the formation of a colourless precipitate, which analysis by LC-MS showed to be functionalised P₁₁-4.

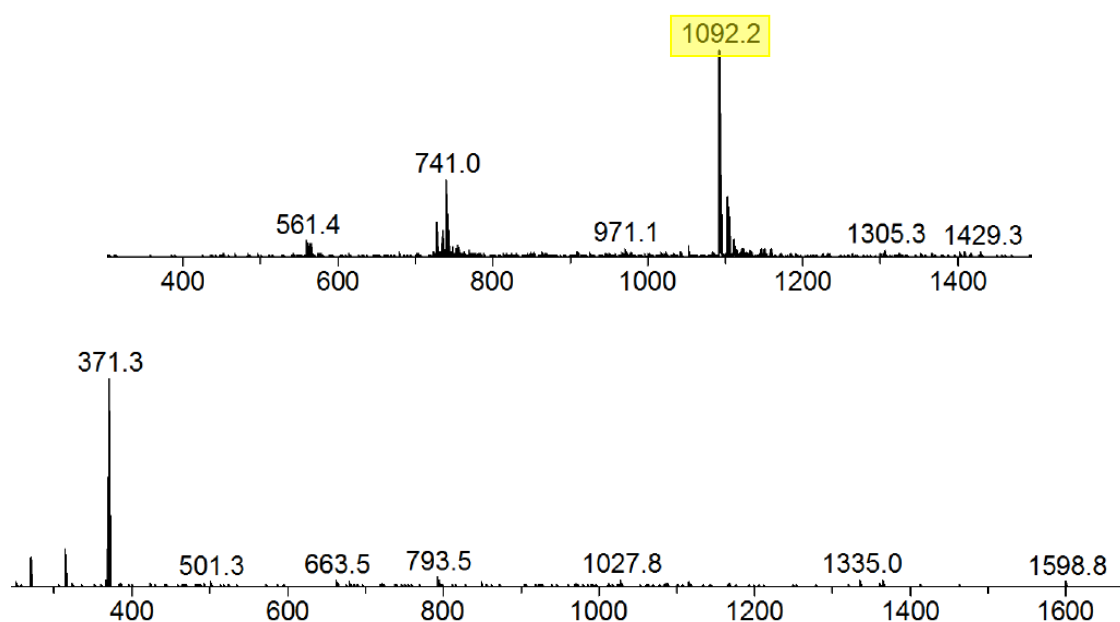


Fig 3.16: Mass spectra showing the test scale (top) and full scale (bottom) purification attempts of the functionalised P₁₁-4 peptides *via* UV directed RP HPLC.

Given the loss of material on HPLC, an alternative system was used. A UV-directed Biotage Isolera One system was employed using a RediSep Rf High Performance GOLD HP C18 50g column. This column also separates by reverse phase interactions but with this system manual loading of the column can be carried out ensuring the full dissolution of the crude peptide and its addition to the column. LC-MS analysis of the collected fractions, shown in **Fig 3.17**, indicated relatively clean purification of the crude peptide which was sufficiently pure to use in further investigations.

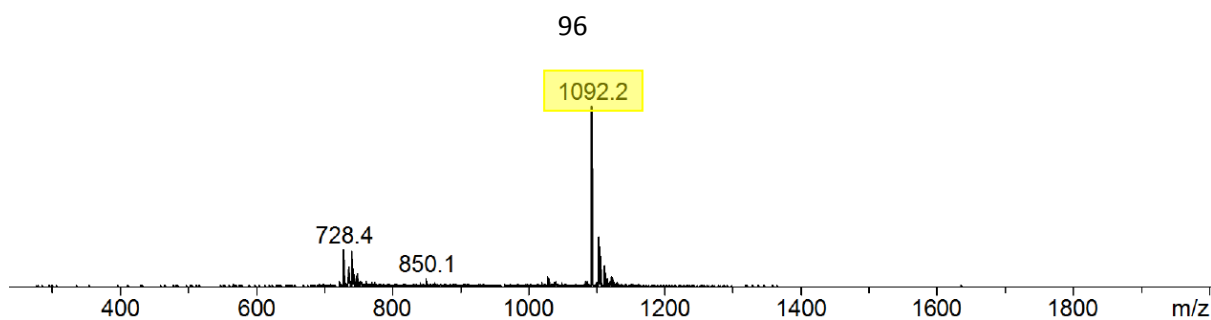


Fig 3.17: Mass spectrum of the purification attempt of functionalised P₁₁₋₄ via chromatography on a UV-directed Biotage instrument, where the peptide peak is highlighted.

3.2.1.2 Effects on self-assembly and morphology

Both P₁₁₋₄ variants – **peptides 1 and 2**, were tested to investigate the effect of having an odd or even consecutive amino acid sequence on the self-assembly. Both variants were tested under different conditions which mimicked physiological conditions: – 1) two different buffer solutions with varying concentrations of various salts, mainly Na⁺ - 130 mM to 230 mM which mimic the limits of Na⁺ content found within articular cartilage (Urban, 1994), 2) two different molar ratios to dope base P₁₁₋₄ - 64:1 and 32:1 (P₁₁₋₄: Variant) which were based on calculations of fibril dimensions and concentrations and the dimensions of native aggrecan from AFM measurements (Ng, 2003).

The effect on morphology was investigated through dimensional analysis of electron micrographs, examples of which are shown in **Fig 3.18**. The width and length of individual fibrils were measured from electron micrographs using image analysis software – ImageJ. The dimensions are shown in **Fig 3.19** for various conditions.

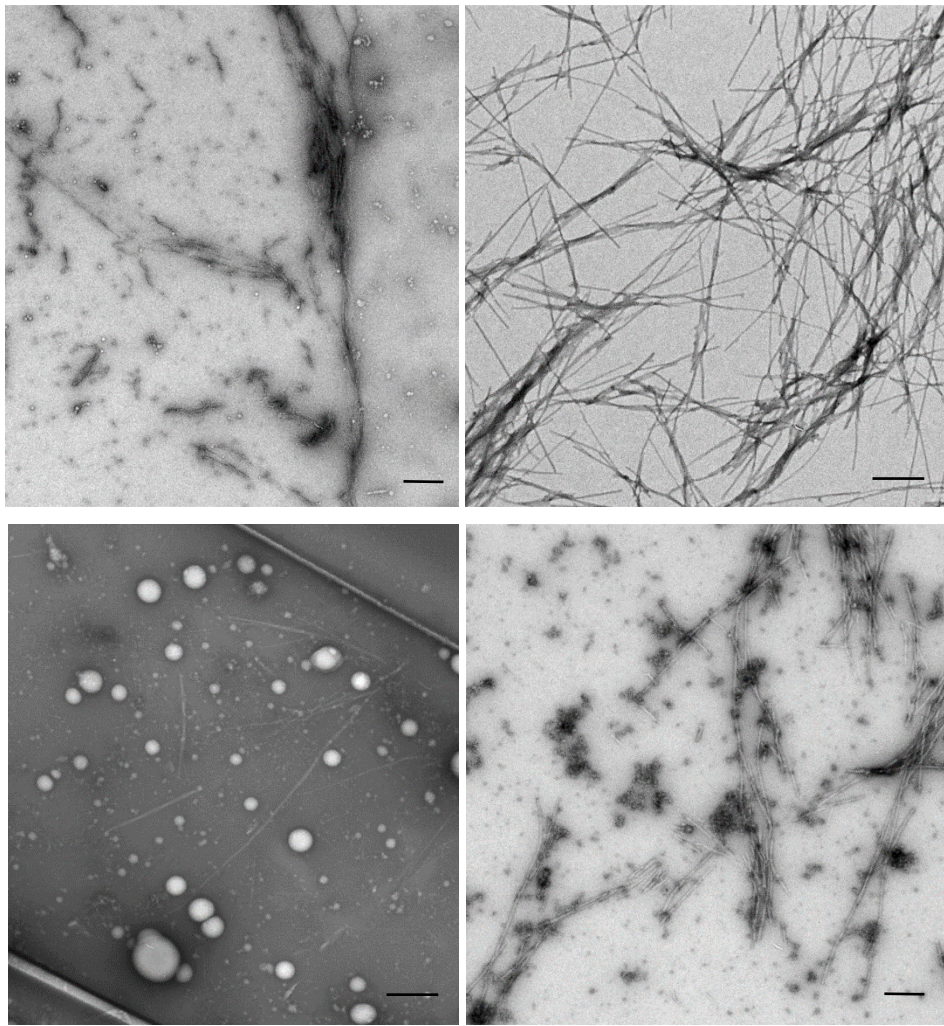


Fig 3.18: TEM Micrographs of two different isomers of P_{11-4} -CS at different molar ratios within P_{11-4} hydrogels (~6 mM). A) P_{11-4} + P_{11-4} -PEG-Lys (Mca)-Hex-CS 32-1 Ratio 230 mM Na^+ buffer, 4000x magnification B) P_{11-4} + P_{11-4} -4-PEG-Lys (Mca)-Hex-CS 64-1 Ratio 230 mM Na^+ buffer, 6000x magnification C) P_{11-4} + P_{11-4} -Lys (Mca)-PEG-Hex-CS 32-1 Ratio 230 mM Na^+ buffer, 5000x magnification c) P_{11-4} + P_{11-4} -Lys (Mca)-PEG-Hex-CS 64-1 Ratio 230 mM Na^+ buffer, 4000x magnification, scale bar – 500 nm.

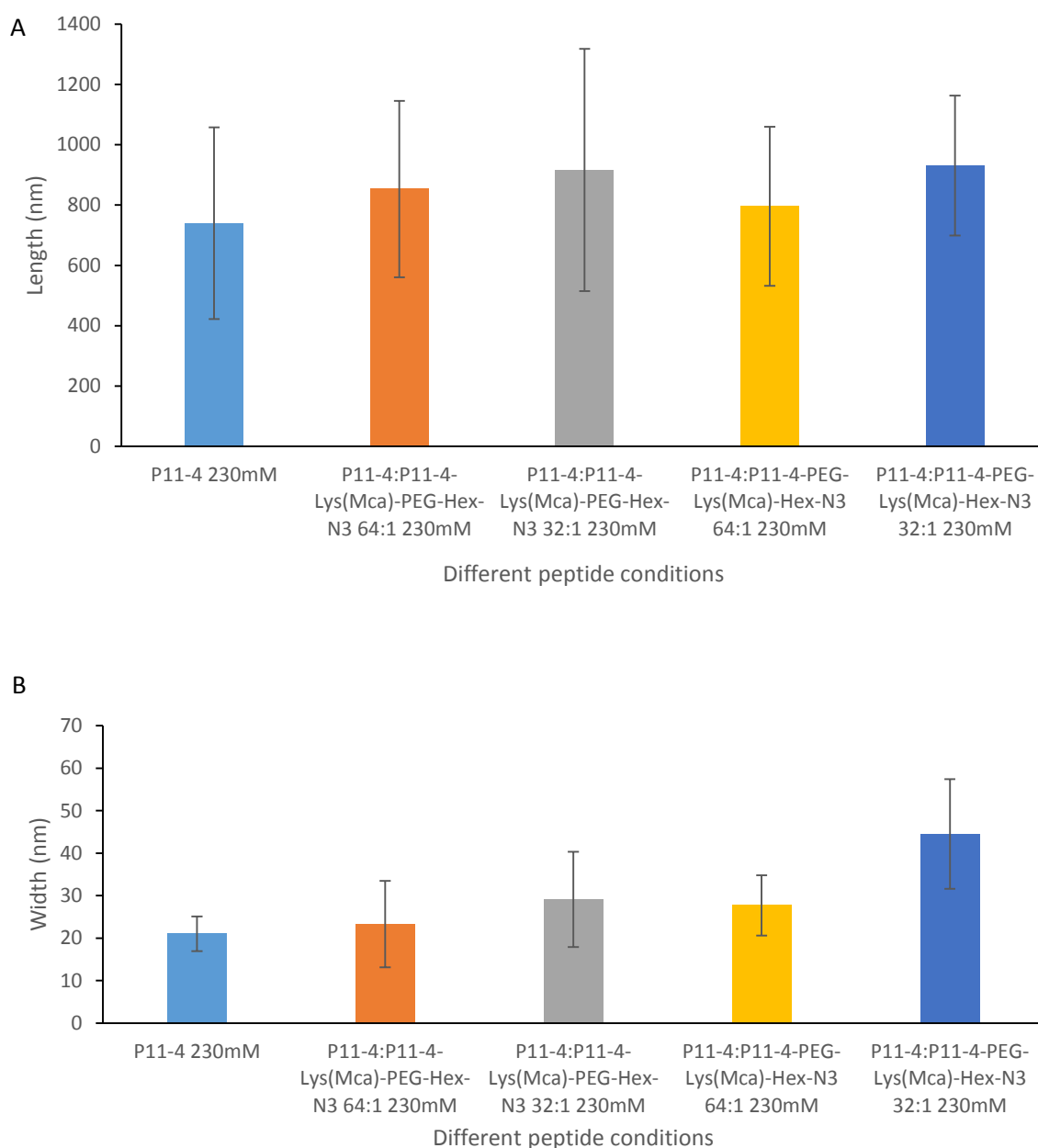


Fig 3.19: The different fibril dimensions, A) effect on fibril length for the different variants at 130 mM and 230 mM Na⁺ concentrations, B) effect on fibril width for different variants at 130 mM and 230 mM Na⁺ concentrations. Error bars: \pm standard deviation, n = 100.

The measured lengths and widths showed no significant differences between the control – P₁₁-4 230 mM Na⁺ and the various alternative conditions when analyzed by a one-way ANOVA statistical test ($\alpha = 0.95$).

The lack of significant difference in terms of morphological dimensions and ability to self-assemble, led to the decision to follow historical research and use the undecameric – **peptide 1** structure. During this work it was also discovered that the addition of the coumarin moiety

significantly complicated the synthesis as well as making the material much more expensive to produce with little benefit in overall analysis. The target peptide was hence redesigned.

3.2.1.3 Final peptide structure

The new structure of the intended peptide –**peptide 3**, is shown in **Fig 3.20**.

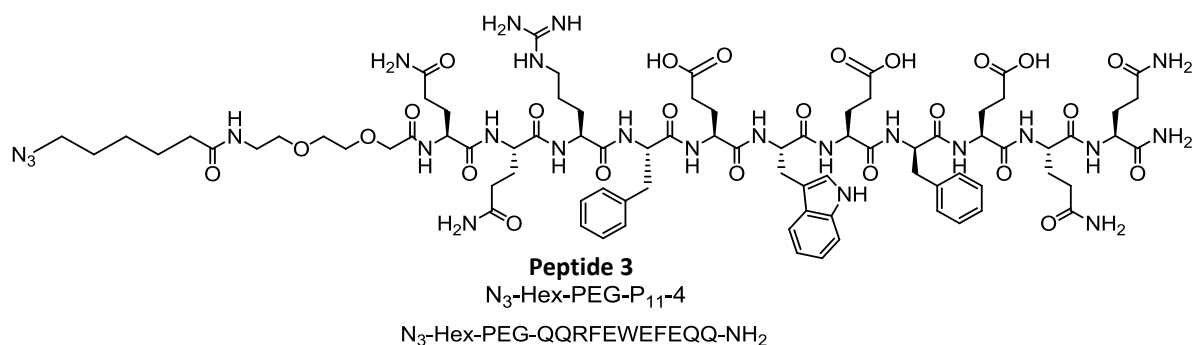
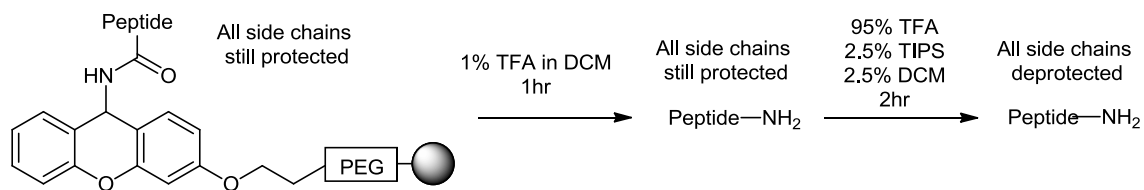


Fig 3.20: Structure of P₁₁-4-PEG-Hex-N₃.

In order to increase the yield of product, a different resin was used – NovaSyn[®] TG Sieber resin which is more acid labile and enables a two-step cleavage process. This enabled release of the peptide from the support before cleavage of the side chain protecting groups. This can prevent self-assembly of the peptide within the resin matrix during the cleavage which can dramatically decrease the yield of product. The different cleavage procedure for the Sieber resin compared to the Rink Amide resins is shown in **Fig 3.21**.

TG Sieber Resin Cleavage



PEGA and Novagel Resin Cleavage

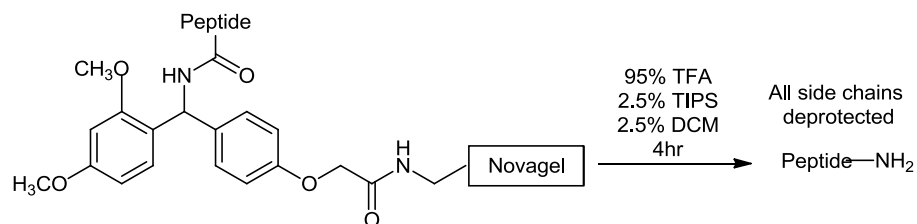


Fig 3.21: The differences between the two types of resin: (top) requires low TFA content to cleave the peptide from the solid support whilst leaving the side groups protected (bottom) high TFA content to cleave the peptide causes the side groups to be deprotected as well as cleaving the solid support.

An analytical HPLC trace and accurate mass MS trace was obtained to check the purity of the functionalized peptide which is shown in **Fig 3.22**.

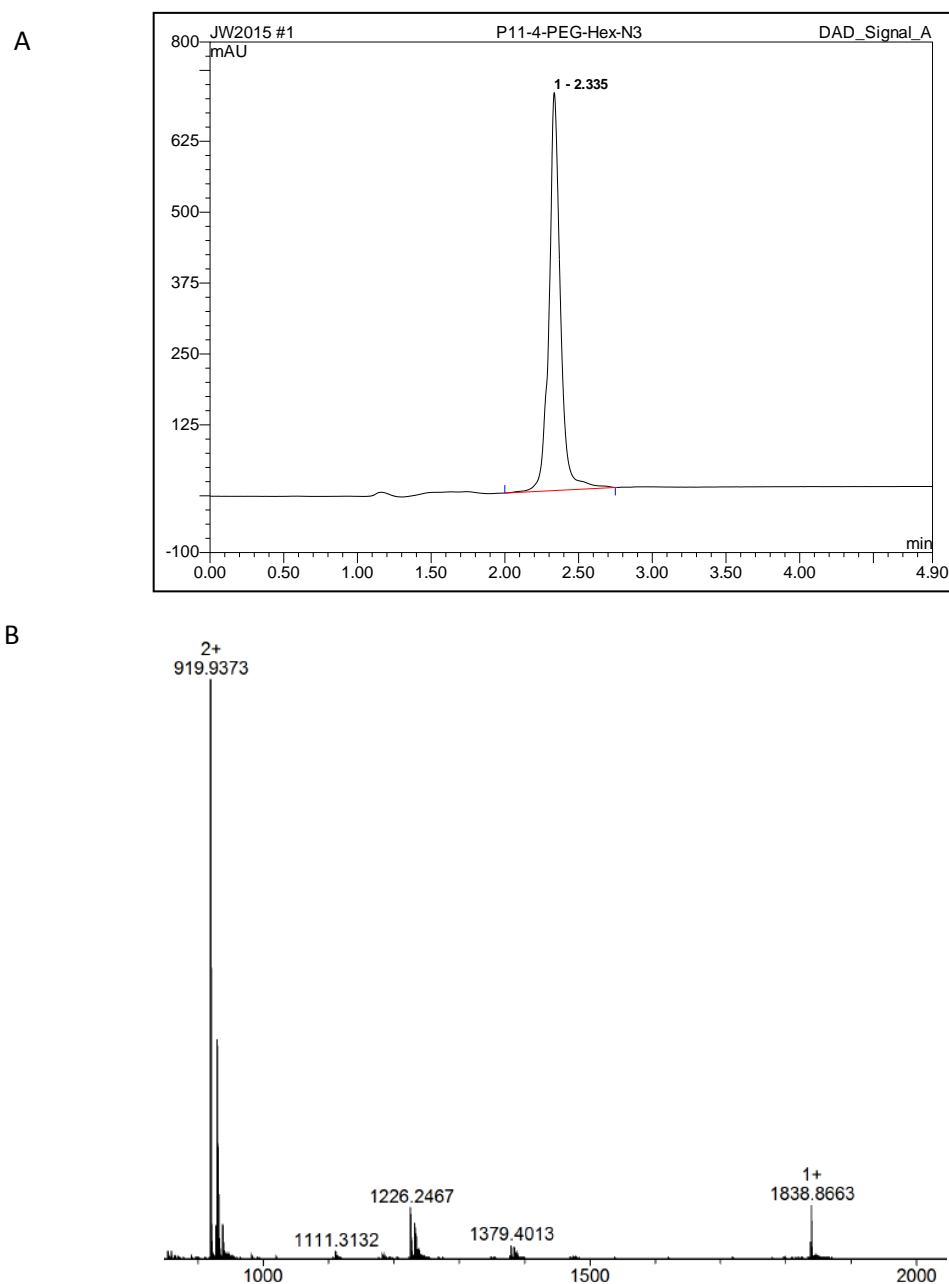


Fig 3.22: A) Analytical HPLC trace B) Accurate mass MS trace for synthesized peptide 3 (P₁₁-4-PEG-Hex-N₃), with the 1+ and 2+ species shown.

The successful synthesis and purification of the **peptide 3** (P₁₁-4-PEG-Hex-N₃) meant an alternative peptide – **peptide 4**, was synthesized using a similar approach with an alternative net charge – P₁₁-8-PEG-Hex-N₃ (+2 net charge), shown in **Fig 3.23** with the analytical HPLC and accurate mass MS trace shown in **Fig 3.24**.

With successful routes to the peptide established large scale synthesis was still challenging and so the decision was made to outsource the bulk synthesis of these materials to Cambridge Bioscience who provided 300 mg of each of the two conjugates.

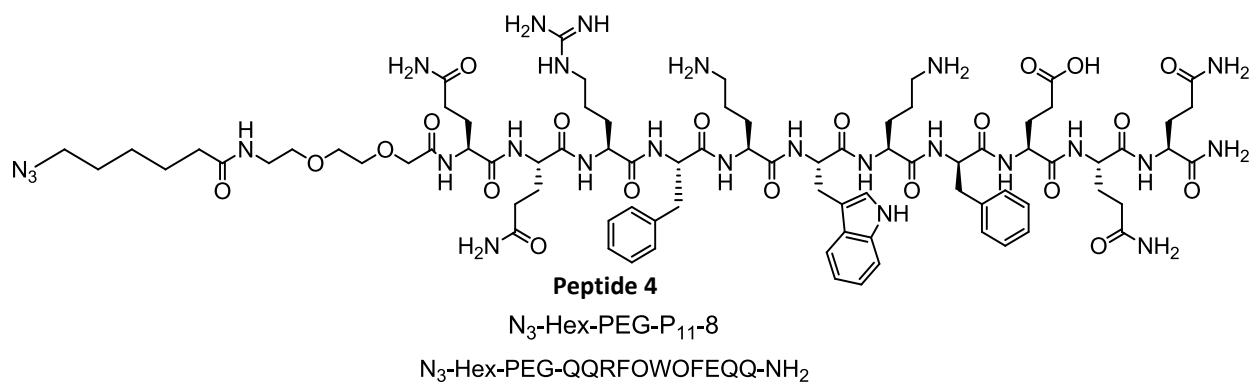


Fig 3.23: Structure of synthesized peptide 4 (P_{11-8} -PEG-Hex- N_3).

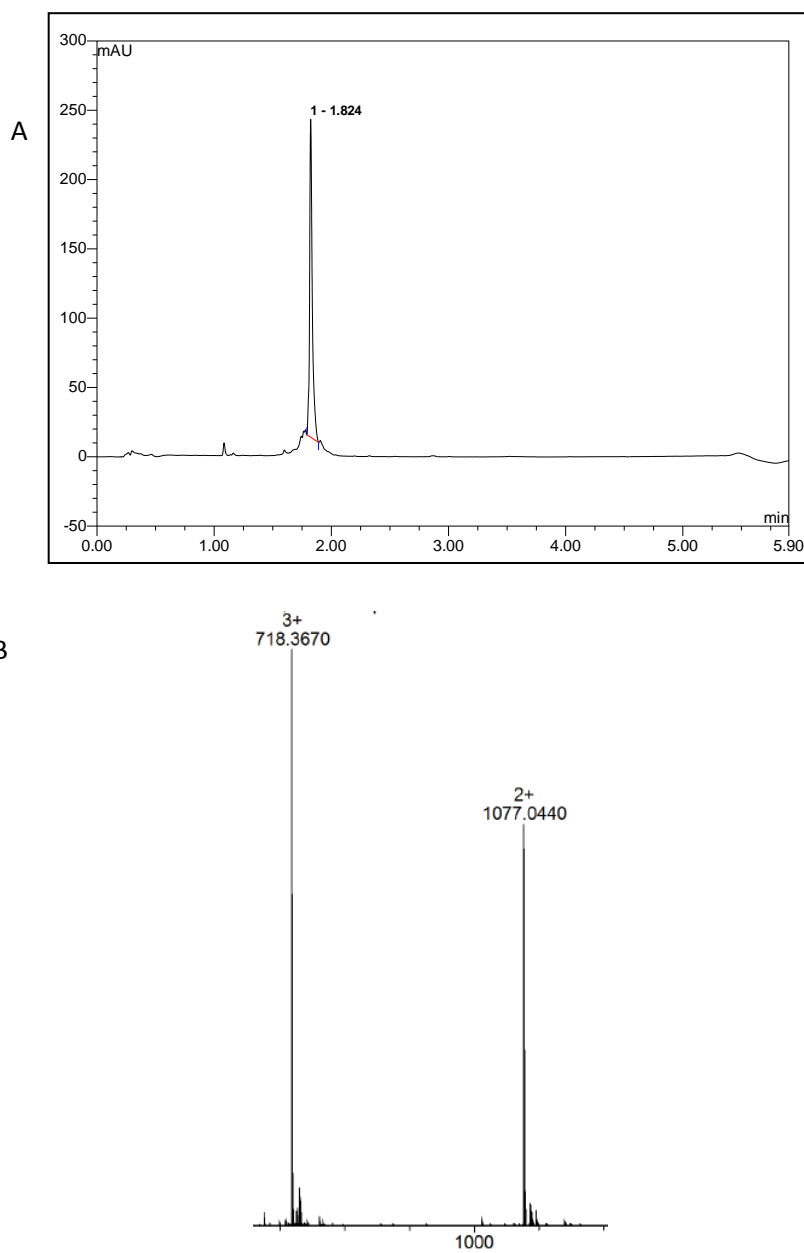


Fig 3.24: Structural determination of peptide 4 (P_{11-8} -PEG-Hex- N_3) with A) Analytical HPLC trace B) Accurate mass MS trace.

3.2.2 Chondroitin Sulfate conjugate synthesis

3.2.2.1 Reductive amination method

The synthetic pathway, shown in **Fig 3.25**, was used to synthesize a linker which could be used to functionalize chondroitin sulfate to arm it for click conjugation to the peptide. 4-Ethynylbenzylalcohol **1** was reacted with N-hydroxyphthalimide **2** under Mitsunobu conditions to form the substituted phthalimide **3**. Cleavage of the phthalimide with hydrazine gave the desired alkynyl substituted hydroxylamine which was isolated as the hydrochloride salt **4**

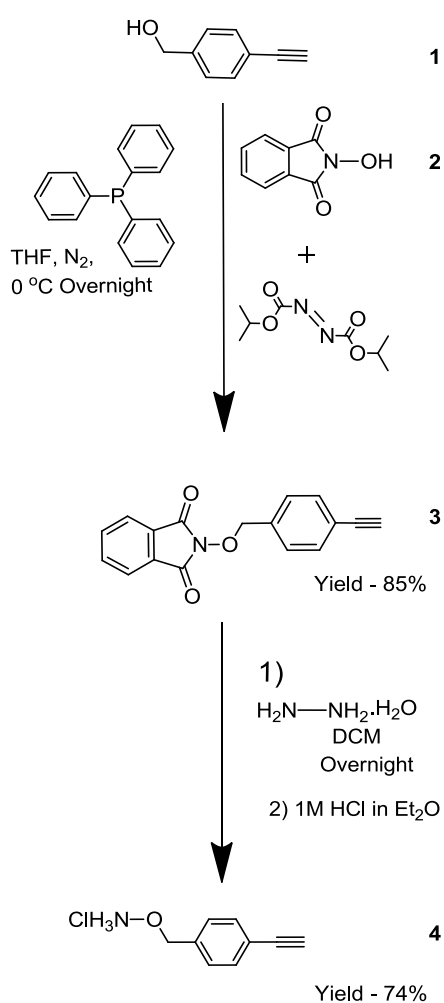


Fig 3.25: Synthetic pathway of alkynyl substituted hydroxylamine linker as hydrochloride salt.

Reductive amination reactions were attempted under a variety of conditions with the general synthetic scheme shown in **Fig 3.26**.

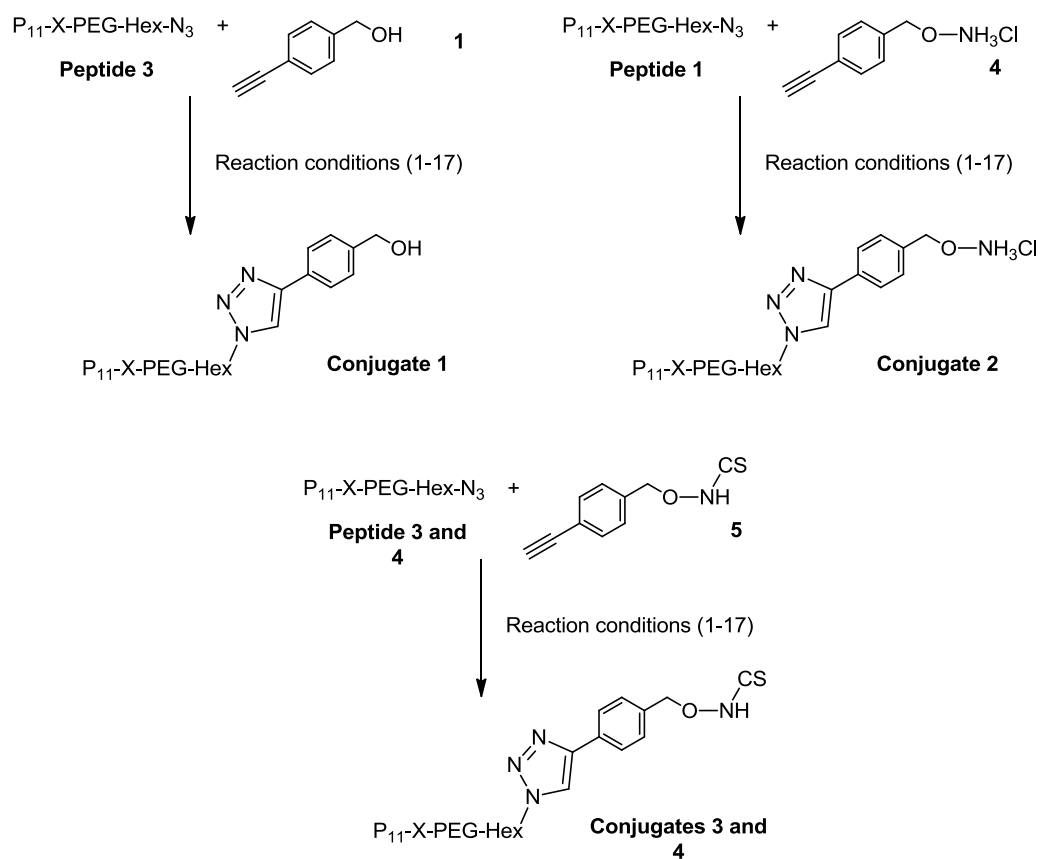


Fig 3.28: Generic reaction scheme of CuAAC reaction linking functionalized peptide with either 4-Ethynylbenzylalcohol 1, aminooxy 4 or functionalized CS 5 under various conditions.

Attempt	Solvent	pH	[Pep]	[Benzyl]	[TCEP]	[TBTA]	[CuSO ₄]	[Na-ascorbate]	Time (hr)	Other	Success
1	H ₂ O	7	0.3 mM	0.15 mM	-	-	1 mM	10 mM	90	Order of addition was: 1) Benzyl, 2) Pep, 3) CuSO ₄ then 4) Na-ascorbate	Yes (~20%)
2	H ₂ O	7	0.3 mM	0.15 mM	-	-	0.03 mM	0.3 mM	24	Order of addition was: 1) Benzyl, 2) Pep, 3) CuSO ₄ then 4) Na-ascorbate	No
3	H ₂ O	7	0.3 mM	0.15 mM	-	-	0.045 mM	0.45 mM	24	Order of addition was: 1) Benzyl, 2) Pep, 3) CuSO ₄ then 4) Na-ascorbate	No
4	H ₂ O	7	0.3 mM	0.15 mM	-	-	0.06 mM	0.6 mM	24	Order of addition was: 1) Benzyl, 2) Pep, 3) CuSO ₄ then 4) Na-ascorbate	No
5	H ₂ O	7	0.3 mM	0.15 mM	-	-	0.075 mM	0.75 mM	24	Order of addition was: 1) Benzyl, 2) Pep, 3) CuSO ₄ then 4) Na-ascorbate	No

Table 3.3: Various conditions investigated for the CuAAC reaction between P₁₁-X-PEG-Hex-N₃ and alkyne-CS fragments.

6	H ₂ O	7	0.3 mM	0.15 mM	-	-	0.15 mM	15 mM	24	Order of addition was: 1) Benzyl, 2) Pep, 3) CuSO ₄ then 4) Na-ascorbate	No
7	H ₂ O	7	20 μM	30 μM	1 mM	100 μM	1 mM	-	-	-	No
8	H ₂ O	7	20 μM	30 μM	1 mM	100 μM	1 mM	-	1	Order of addition was: 1) Pep, 2) TCEP, 3) CuSO ₄ (wait 2min), 4) TBTA then 5) Benzyl	No
9	H ₂ O	7	1 mM	1 mM	1 mM	1 mM	1 mM	-	1	Order of addition was: 1) Pep, 2) TCEP, 3) CuSO ₄ (wait 2min), 4) TBTA then 5) Benzyl	No
10	PBS	7.4	1 mM	1 mM	1 mM	1 mM	1 mM	-	1	Order of addition was: 1) Pep, 2) TCEP, 3) CuSO ₄ (wait 2min), 4) TBTA then 5) Benzyl	Yes (~40-50 %)
11	10 mM NaPO ₄ buffer	7.4	1 mM	1 mM	1 mM	1 mM	1 mM	-	1	Order of addition was: 1) Pep, 2) TCEP, 3) CuSO ₄	Yes (~40 %)

Table 3.3: Various conditions investigated for the CuAAC reaction between P₁₁-X-PEG-Hex-N₃ and alkyne-CS fragments.

										(wait 2min), 4) TBTA then 5) Benzyl	
12	100 mM NaPO ₄ buffer	7.4	1 mM	-	1	Order of addition was: 1) Pep, 2) TCEP, 3) CuSO ₄ (wait 2min), 4) TBTA then 5) Benzyl	Yes (~60 %)				
13	100 mM NaPO ₄ buffer	7.4	1 mM	5 mM	1 mM	1 mM	1 mM	-	1	Order of addition was: 1) Pep, 2) TCEP, 3) CuSO ₄ (wait 2min), 4) TBTA then 5) Benzyl	Yes (~80 %)
14	100 mM NaPO ₄ buffer	7.4	0.5 mM	-	1	Order of addition was: 1) Pep, 2) TCEP, 3) CuSO ₄ (wait 2min), 4) TBTA then 5) Benzyl	Yes (~10 %)				
15	100 mM NaPO ₄ buffer	7.4	1 mM	1 mM	2 mM	2 mM	2 mM	-	1	Order of addition was: 1) Pep, 2) TCEP, 3) CuSO ₄ (wait 2min), 4) TBTA then 5) Benzyl	Yes (~30 %)

Table 3.3: Various conditions investigated for the CuAAC reaction between P₁₁-X-PEG-Hex-N₃ and alkyne-CS fragments.

16	100 mM NaPO ₄ buffer	7.4	1 mM	5 mM	2 x 2 mM	2 x 2 mM	2 x 2 mM	-	1	Order of addition was: 1) Pep, 2) TCEP, 3) CuSO ₄ (wait 2min), 4) TBTA then 5) Benzyl	Yes (~80 %)
17	100 mM NaPO ₄ buffer	7.4	1 mM	1 mM	-	1 mM	1 mM	1 mM	1	Order of addition was: 1) Pep; 2) Alkyne, 3) Na- ascorbate; 4) TBTA then 5) CuSO ₄	Yes (~80- 90 %)

Table 3.3: Various conditions investigated for the CuAAC reaction between P₁₁-X-PEG-Hex-N₃ and alkyne-CS fragments.

The simple analogue allowed monitoring of the reaction through LC-MS and ^1H NMR with the success being judged by the relative percentage of product vs the alkyne and azide starting materials. The product triazole was small enough that the product could be clearly seen on the LC-MS trace. In **Fig 3.29**, the LC-MS trace for the most successful conditions are shown – 2 equivalents of alkyne, 1 equivalent of peptide, TBTA as ligand for the copper, TCEP as reducing agent and $\text{CuSO}_4 \cdot 5\text{H}_2\text{O}$ as the copper source. The increase in mass on triazole formation is clearly visible. One issue which arose using the TBTA: TCEP system was the short lifetime of activity the *in situ* Cu (I) species had of $\sim 1\text{hr}$, where the issue was exacerbated by the limited solubility of the system as well where after $\sim 2\text{hrs}$ a white precipitate formed which on investigation turned out to be TBTA which had precipitated over time.

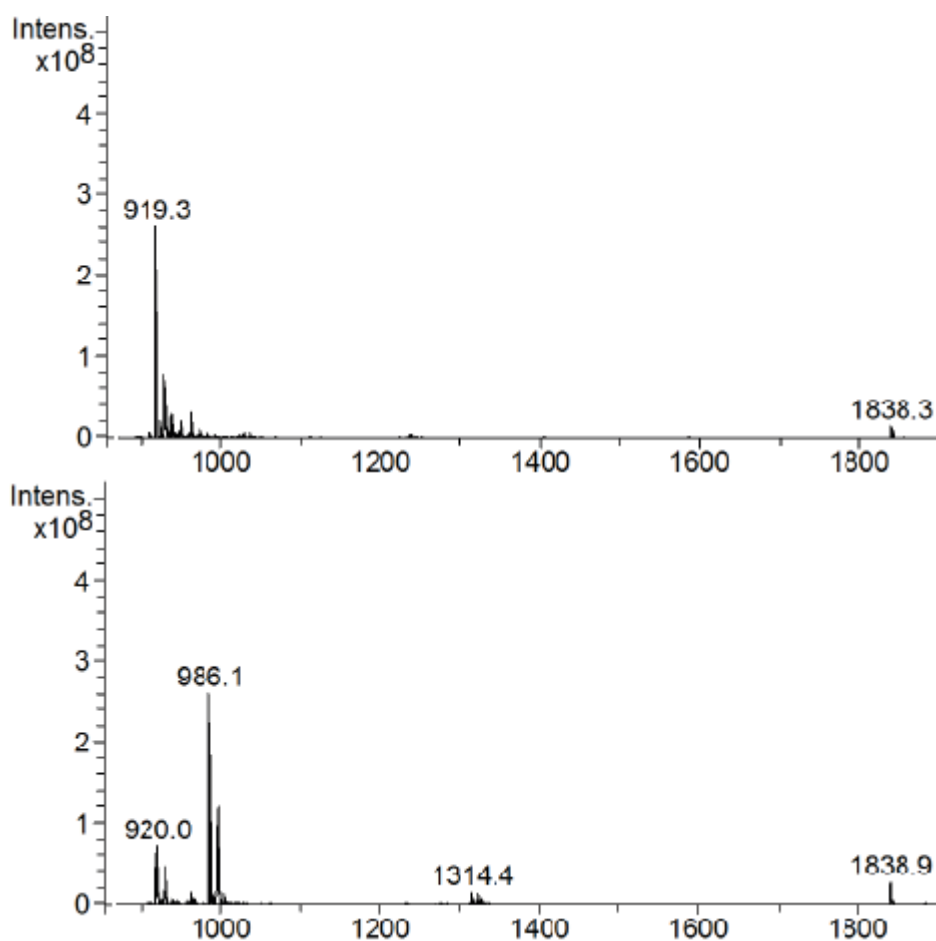


Fig 3.29: Mass spectra for starting peptide 3 (P₁₁-4-PEG-Hex-N₃) material (top) and click reaction product conjugate 1 with ethynyl benzyl alcohol (bottom) under reaction 13 conditions.

As an alternative method of monitoring, ^1H NMR was used to monitor the formation of the characteristic triazole proton at $\sim 8\text{ppm}$. The spectrum of a test reaction is shown in **Fig 3.30**.

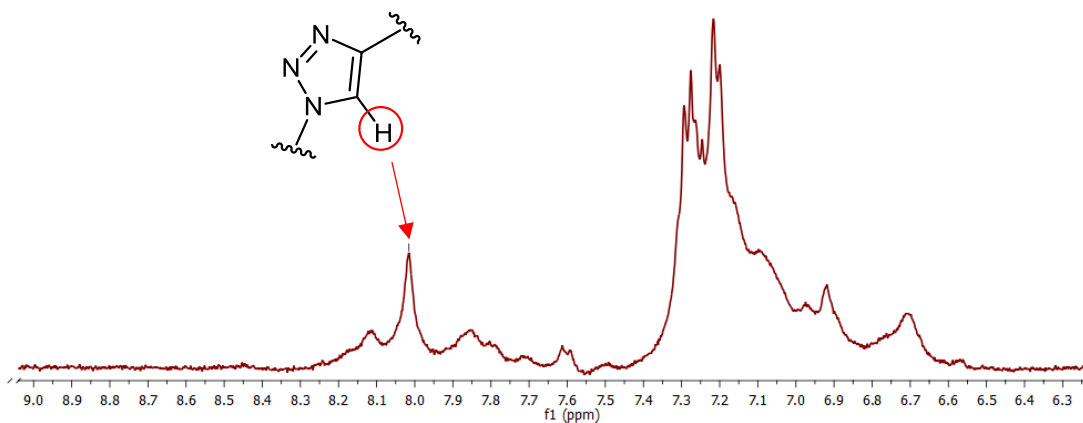


Fig 3.30: The ¹H NMR spectrum of the product of an ethynyl benzyl alcohol – P₁₁-4-PEG-Hex-N₃ click reaction – conjugate 1 using reaction 13 conditions. The characteristic triazole proton peak is ~8 ppm.

Using the optimal conditions the aminoxy alkyne **4**, also reacted successfully. Key spectra from the LC-MS analysis are shown in **Fig 3.31**.

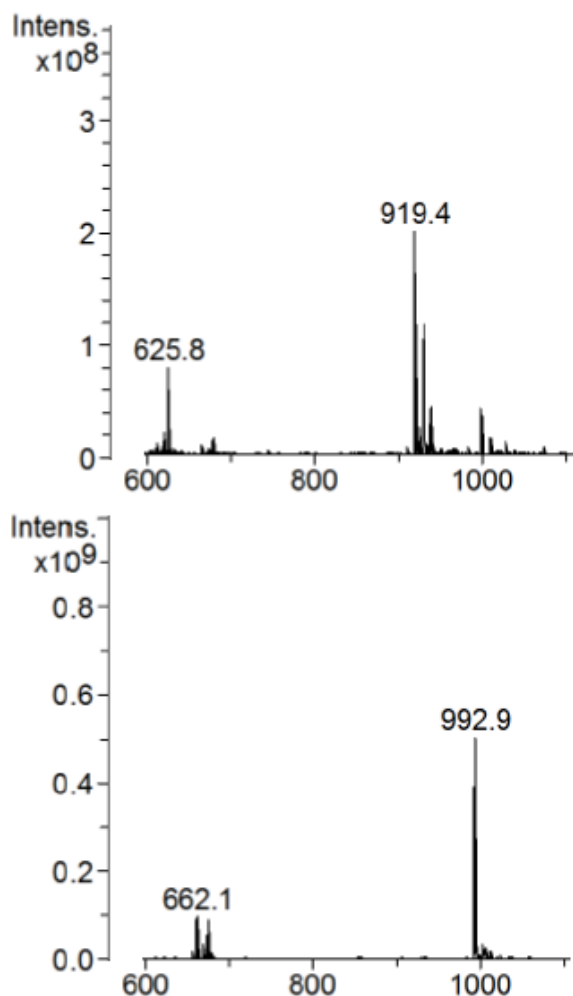


Fig 3.31: Mass spectra for starting peptide 3 (P_{11} -4-PEG-Hex- N_3) material (top) and click reaction product conjugate 3 with aminoxy intermediate 4 (bottom) under reaction 13 conditions.

The same conditions worked for the aminoxy intermediate showing $\sim 75\%$ conversion, almost matching the $\sim 80\%$ conversion observed for the benzyl starting material. The final step to investigate was to check whether the click reaction conditions worked for the CS fragment. This reaction was much harder to monitor as the polydisperse and exceedingly large product that would result is not amenable to normal analytical methods. The highly sulfated CS resists electrospray ionization and NMR spectra are extremely complex. A number of different analytical methods were used to infer success. The reaction was monitored in the same manner as previous analogues with the starting **peptide 3** (P_{11} -4-PEG-Hex- N_3) concentration measured by LC-MS. During the reaction all the free **peptide 3** disappeared from the reaction mixture which was consistent with a successful click reaction to form the desired conjugate which was invisible in the LC-MS. The LC-MS trace is shown in **Fig 3.32**. The formation of the triazole proton formation was also analyzed using 1H NMR. The 1H NMR spectrum is shown in **Fig 3.33**.

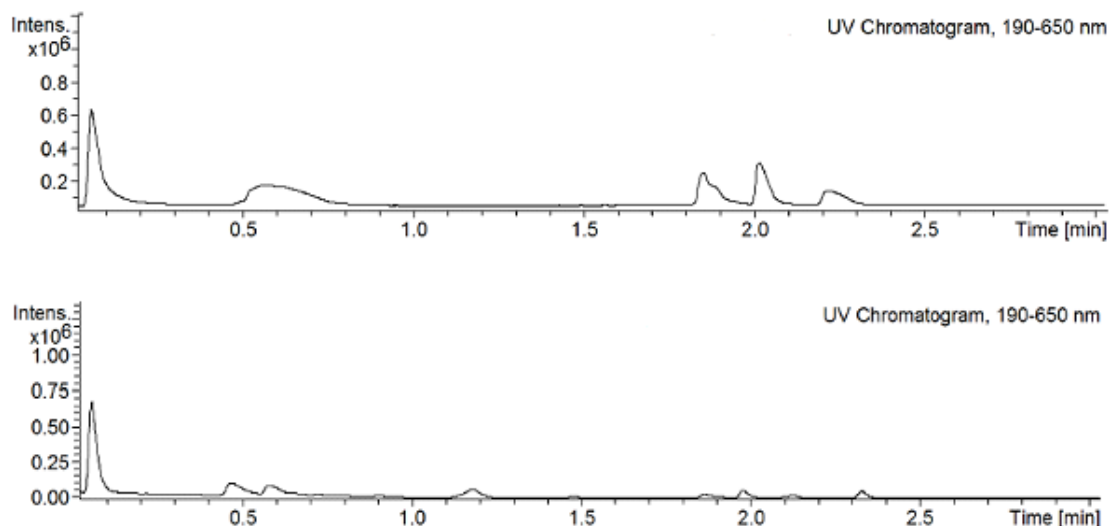


Fig 3.32: UV trace of conjugate 5 (P_{11} -4-PEG-Hex-(triazole)-CS) reaction before (above) and after (bottom) completion. There was no presence of the starting peptide material indicating the reaction has gone to completion with the UV peak at 1.9 min having disappeared.

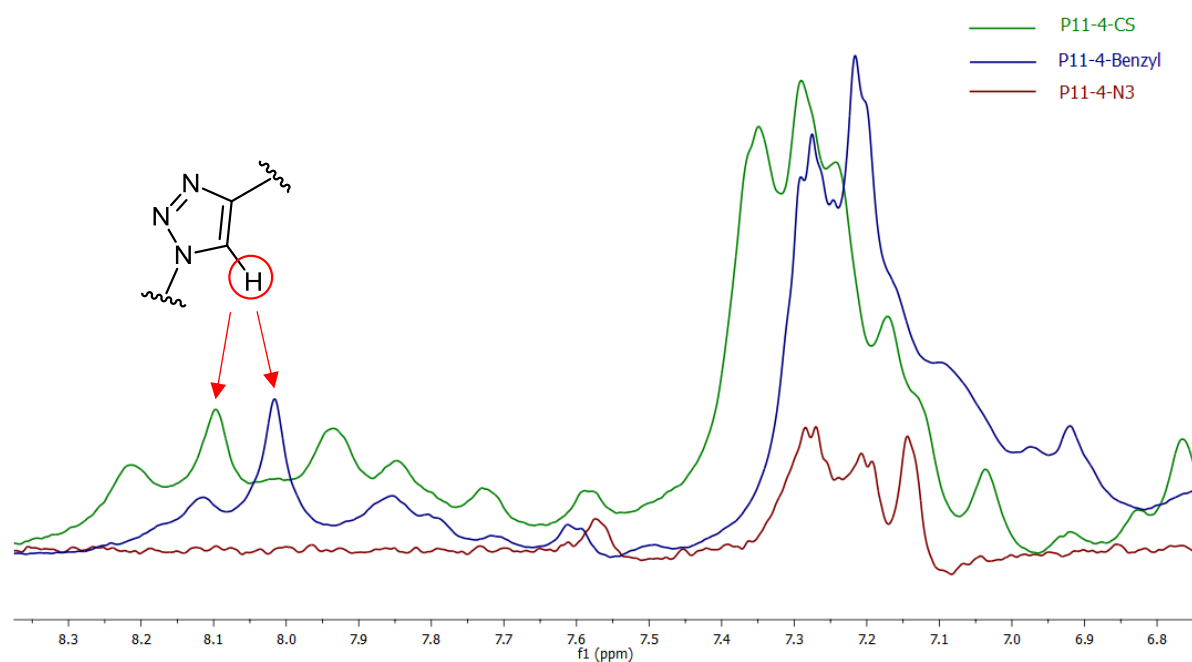


Fig 3.33: ^1H NMR trace comparing peptide 3 (P_{11} -4-PEG-Hex- N_3), conjugate 3 (P_{11} -4-PEG-Hex-Benzyl) and conjugate 5 (P_{11} -4-PEG-Hex-CS), with the characteristic triazole proton ~ 8 ppm.

The low amount of triazole proton compared to the CS protons in the spectra made this analysis challenging but through using a large number of scans it was possible to identify the triazole proton which was apparent in the ^1H NMR spectrum of both **conjugate 1** and **conjugate 5** but not the spectrum of **peptide 3** as highlighted in **Fig 3.33**. The aromatic peaks around 7-7.5 ppm

correspond to the aromatic protons on the peptide from the tryptophan and phenylalanine side groups, as the ^1H NMR spectrum of **peptide 3** shows similar aromatic peaks, but the missing protons seen in the conjugate spectra come from the protons on the benzyl group located within the linker.

The final method of characterization of the click product was to use size-exclusion chromatography with multi angle laser light scattering (SEC-MALLS) to measure the shift in retention time based on different molecular weights. The SEC-MALLS UV and light scattering (LS) trace for CS and **conjugate 5** (P_{11} -4-PEG-Hex-CS) is shown in **Fig 3.34** In both traces a significantly different retention time was observed suggesting that indeed the click reaction has occurred successfully.

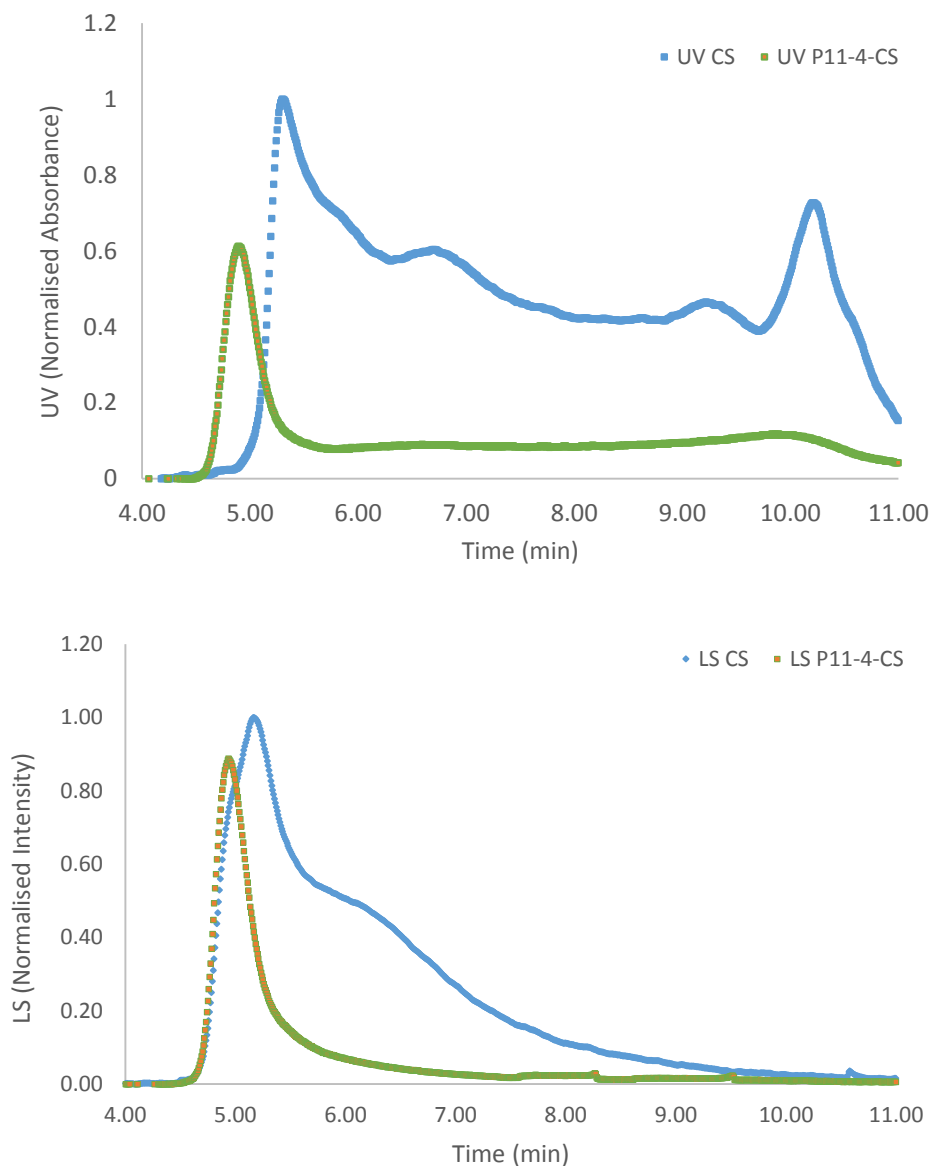


Fig 3.34: SEC-MALLS trace – UV trace (top) and LS trace (bottom) with CS (blue) and conjugate 5 (P₁₁-4-PEG-Hex-CS) (orange).

With the validation and characterization of **conjugate 5** (P₁₁-4-PEG-Hex-CS) the next step was to use the alternative **peptide 4** (P₁₁-8-PEG-Hex-N₃) to create a net positively charged peptide-GAG conjugate. The same conditions were used for the click reaction. LC-MS once again showed complete disappearance of starting peptide and ¹H NMR showed appearance of a proton at the correct chemical shift for a triazole. **Fig 3.35** and **Fig 3.36**.

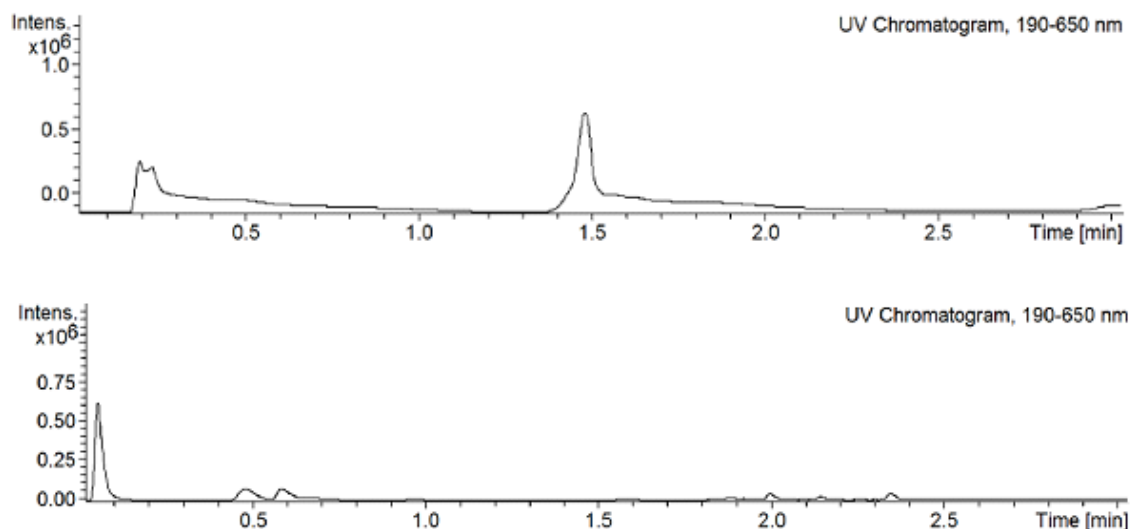


Fig 3.35: UV trace of conjugate 6 (P_{11} -8-PEG-Hex-CS) reaction before (above) and after (bottom) completion. There was no presence of the starting peptide material indicating the reaction has gone to completion with the UV peak at 1.5 min having disappeared.

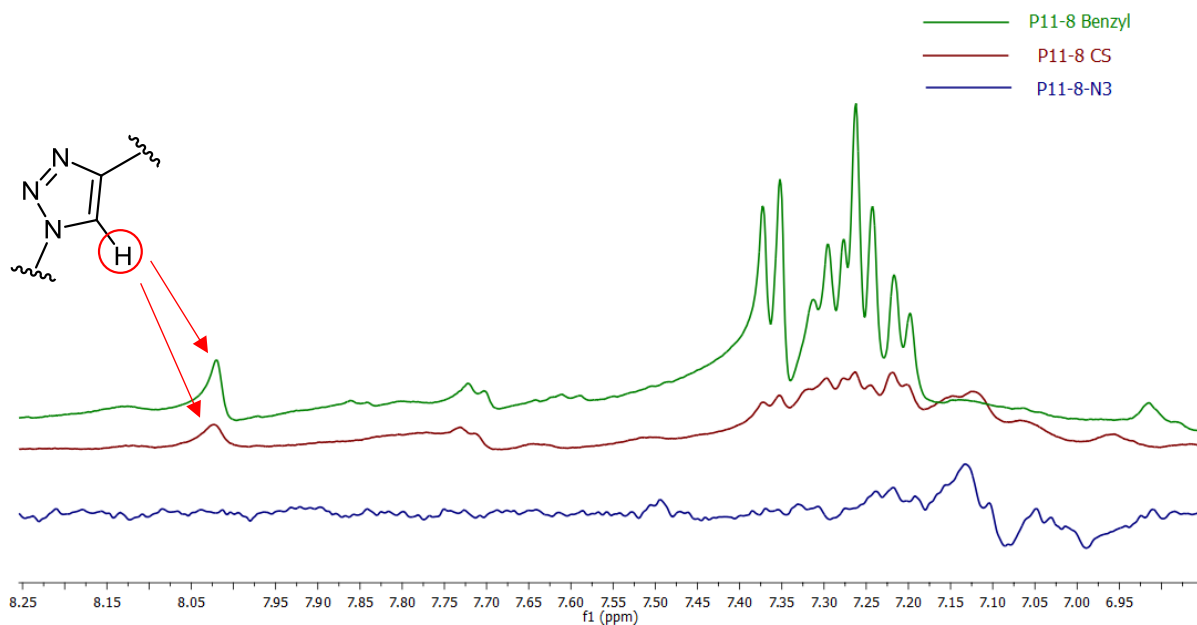


Fig 3.36: ^1H NMR trace comparing peptide 4 (P_{11} -8-PEG-Hex- N_3), conjugate 4 (P_{11} -8-PEG-Hex-Benzyl) and conjugate 6 (P_{11} -8-PEG-Hex-CS), with the characteristic triazole proton $\sim 8\text{ppm}$.

SEC-MALLS was used again to compare the shift in molecular weights of the **conjugate 6** (P_{11} -8-PEG-Hex-CS) and CS to indicate the click reaction was a success. The SEC-MALLS traces for both the UV and LS detectors are shown in **Fig 3.37**.

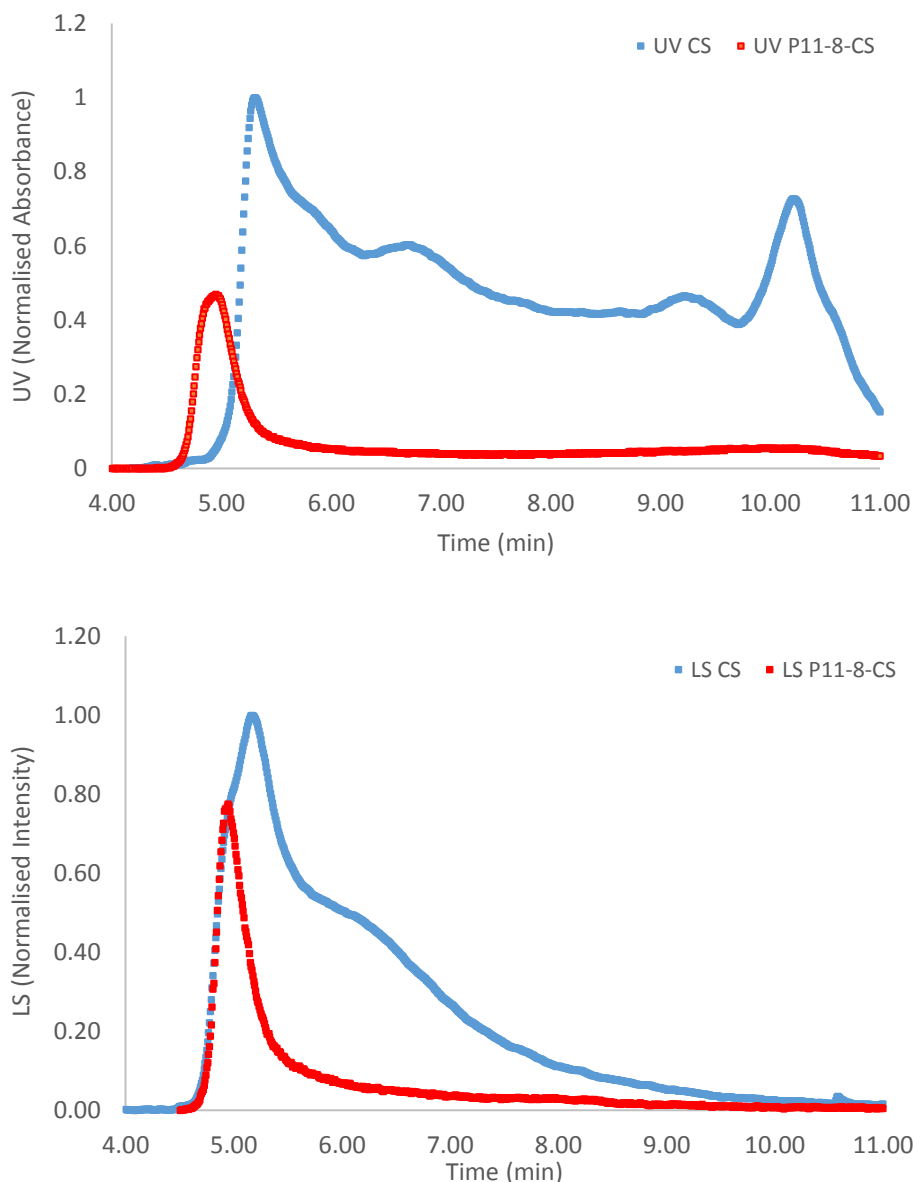


Fig 3.37: SEC-MALLS traces for conjugate 6 (P₁₁-8-PEG-Hex-CS) (red) compared to CS only (blue). UV trace (top) and LS trace (bottom).

3.2.4 Cu cytotoxicity

The one possible issue with using CuAAC for a biomedical applications is the cytotoxicity of any residual Cu (I) and Cu (II) in biological systems if it is not removed during purification. The Cu content of the reaction mixture (for the maximum Cu (II) – CuSO₄ concentration used in the click reaction), subsequent dialysis fluid and final dialysis mixture were measured through flame atomic absorption spectroscopy (FAAS). The system was calibrated based on a calibration gradient from prepared known concentration of CuSO₄ – 0-12 ppm, shown in **Fig 3.38**. The initial concentration of CuSO₄ used in the click reaction was 1 mM with a volume of 1 ml and the final concentration of the product once removed from the dialysis tube (~1 ml) was 0.009 mM, indicating that over 99% of the Cu species had been removed through dialysis.

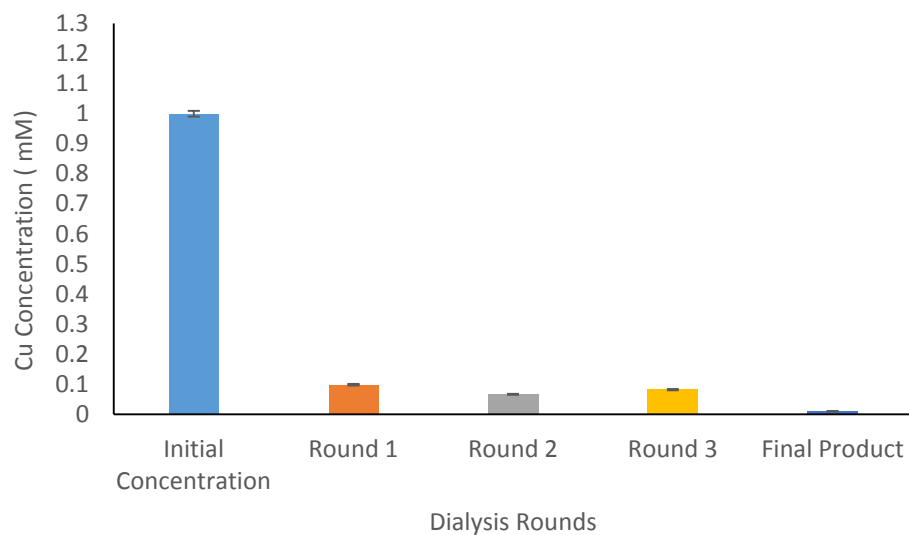
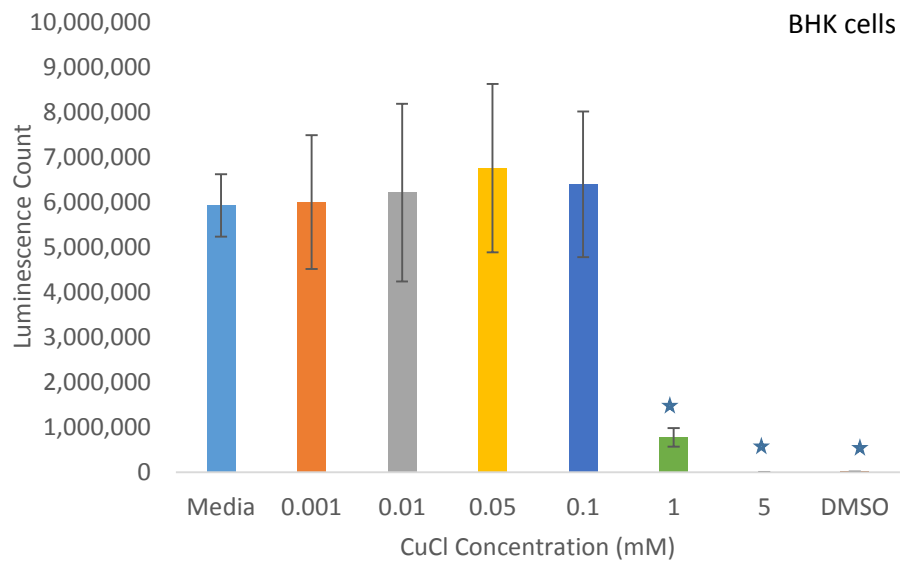
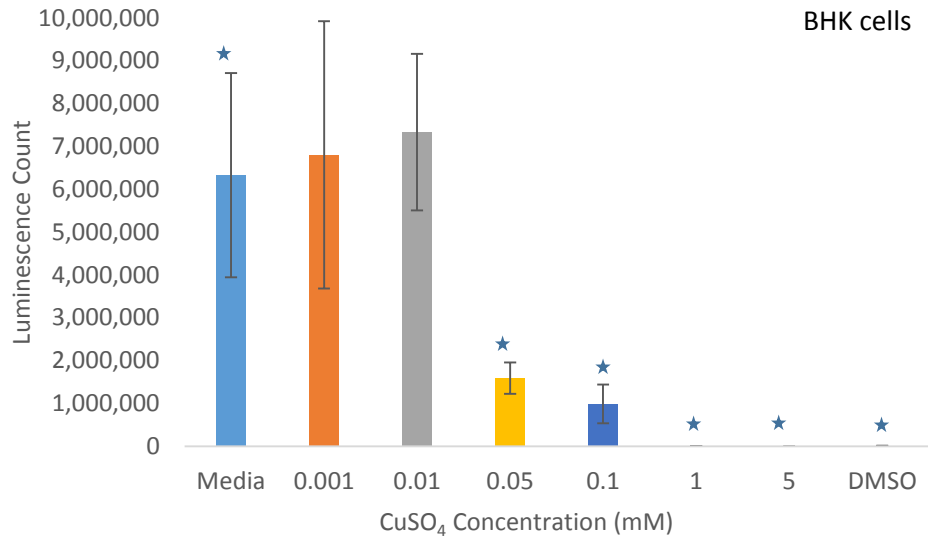


Fig 3.38: Amount of Cu (II) present (mM) in consecutive rounds of dialysis as determined by FAAS using a calibration gradient.

The effect of the residual Cu concentrations were then investigated through an extract cytotoxicity test using 2 cell lines – Baby Hamster Kidney (BHK) cells and murine fibroblast (L929) cells. The copper species selected were CuSO_4 to represent a Cu (II) species and CuCl to represent a Cu (I) species with each species concentration ranging from 0.001 – 5 mM. The cell lines were incubated in the presence of each Cu species for 48 hr and then an ATP-lite assay was performed to measure the cell viability after exposure. The results from the extract cytotoxicity tests are shown in **Fig 3.39**.



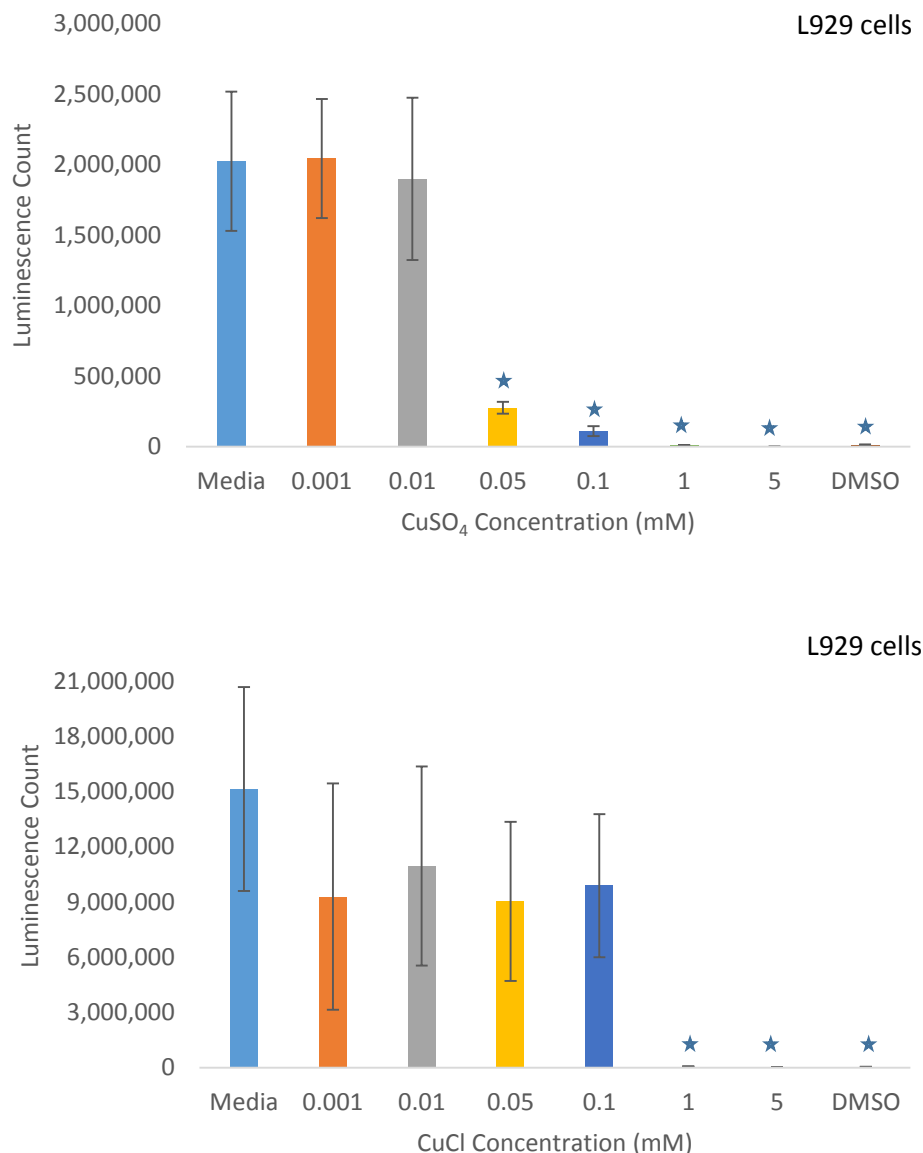


Fig 3.39: Extract cytotoxicity results for residual Cu (I) and Cu (II) concentrations using BHK and L929 cell lines. (Uppermost) BHK cells exposed for 48 hr to CuSO₄ at various concentrations. (Upper middle) BHK cells exposed for 48 hr to CuCl at various concentrations. (Lower middle) L929 cells exposed for 48 hr to CuSO₄ at various concentrations. (Lowermost) L929 cells exposed for 48 hr to CuCl at various concentrations. ★ = Significant difference to negative control (Media) ($\alpha = 0.95$).

The results of the extract cytotoxicity showed that with the maximum residual Cu amount detected with FAAS (0.009 mM) was not cytotoxic to either BHK or L929 cell lines at the maximum potential concentration of CS conjugate that the cell lines could be exposed to, as the amount of product extracted following dialysis was ~50 mg in 1 ml (0.26 μg of Cu or 0.004 mM) which was a greater concentration than the maximum concentration possible for the hydrogels – 30 mg ml^{-1} (0.15 μg of Cu or 0.002 mM). This validated that 3 rounds of dialysis was sufficient to remove an adequate amount of Cu from the click product mixture but to be sure an additional

2 rounds of dialysis were carried out to ensure the amount of residual Cu was definitely below the concentration deemed to be cytotoxic.

3.3 Discussion

3.3.1 Functionalised peptide synthesis

The work presented in this chapter provides methods and evidence for the first reported successful synthesis of a self-assembling peptide-CS conjugate through utilising the reducing end of the polysaccharide. The first aim was to synthesize a peptide containing an azide functionality which also had a propensity to self-assemble under certain conditions such as pH, ionic strength and concentration. The propensity to self-assemble was based around the amino acid sequences chosen: P₁₁-4 – QQRFEWEFEQQ and P₁₁-8 – QQRFOWOFEQQ. These are sequences previously reported by the Aggeli group at the University of Leeds (Bell, 2006, Maude et al., 2011). The difficulties reported in this chapter was both the synthesis of these core peptide sequences, and the post modification of these, in terms of coupling a biocompatible linker and introducing a functional group which could be transformed into the azide motif. The final synthesis of the core peptide sequence arose from difficulties with the initial loading of the resins and sequential coupling reactions from inappropriate coupling reagents. The subsequent modification increased the length of the synthesized peptide chain which may have contributed in conjunction with the peptides self-assembling properties, to make the overall synthesis and purification difficult. These difficulties were overcome by changing the initial resin used from a PEGA Rink Amide resin to a Novagel Rink Amide resin (Pipkorn, 2000, Stetsenko and Gait, 2000). The rationale for this change was to make the preparation and swelling of the resin easier, because it came in a dry form compared to the PEGA Rink Amide resin which came in a swollen form. The LC-MS data indicated this change meant the synthesis was successful according to the LC-MS data for the crude mixture following cleavage from the resin. Further difficulties were encountered purifying the crude products either through mass/UV directed reverse phase HPLC or UV directed Biotage purification which resulted in low recoveries. The problems were believed to be due to the peptides self-assembling during cleavage and aggregating onto the resin beads as well as self-assembling when they were re-solubilised following ether precipitation. Small amounts of **peptide 1 and 2** (P₁₁-4-(PEG-Lys(Mca)/Lys(Mca)-PEG)-Hex-N₃) were produced which allowed the investigation into whether the order of the linker and fluorophore residues made a significant difference to the ability of the peptide to self-assemble. This investigation indicated there was no significance between the two different variants in terms of micro-structure and dimensional measurements or critical concentration for self-assembly using a 1-way ANOVA statistical test ($\alpha=0.05$). As the sequence was not critical and the Mca residue had been of little value in the analysis of the reaction the peptide structure was simplified by removal of the fluorescent residue.

The final resin change from Novagel Rink Amide to the TG Sieber resin was to overcome the difficulties and low yields experienced during purification. The resin had a lower loading capacity (0.1-0.25 mMol/g) with a dual stage cleavage mechanism, where the peptide can be cleaved from the resin using 1% TFA, leaving the side groups protected until it is exposed to a 95% TFA mixture (Sieber, 1987). The lower loading reduced the potential of unfavourable interactions between growing peptide chains within the resin bead by having a lower loading capacity and the side groups still being protected to minimise non-covalent side group interactions. This dual stage process reduced aggregation within the resin matrix. The LC-MS data showed this change allowed purification to be carried out to an acceptable level with multiple milligrams produced. However, with the scale required to continue the project the decision was taken to outsource the peptide synthesis to Cambridge BioScience which guaranteed purity and supply, with the company synthesizing both azido functionalised P₁₁₋₄ and P₁₁₋₈ variants – **peptides 3 and 4** on a 300mg scale.

3.3.2 Modified chondroitin sulfate synthesis

The functionalisation of chondroitin sulfate was based on derivatising the reducing end of the chondroitin polysaccharide chain instead of the more conventional hydroxyl and amino side group functionalisation more commonly employed with GAG functionalisation.

The two different methods (oxime formation and reductive amination) for functionalisation reported in this chapter were based around a similar synthetic route with only the conjugation of the alkyne containing motif with the chondroitin sulfate polymer differing. The reductive amination method used excess amounts of reducing agent to force the reaction, towards the amine product which is a stable bond and resistant chemical cleavage e.g. hydrolysis. The one disadvantage of this method compared to the oxime formation method is the lack of a characteristic proton signal in NMR as with the oxime the imine proton ~7.5-8 ppm can be observed, as reported by Brand *et al.* (Brand *et al.*, 2006). The oxime method was a more expedient method, requiring a maximum reaction time of ~ 24hrs compared to the 144hrs for the reductive amination method. The reaction could be monitored by the formation of the characteristic oxime peak as mentioned above, but the disadvantage this method had was the removal of the aniline or aniline substitute – *P*-phenyldiamine (PPD) which aggregated with the product or readily oxidised respectively (Wendeler *et al.*, 2013, Meyer and Fischer, 2015). All attempts to remove the catalyst through phase separation, extraction, azotropic separation or precipitation failed with excessive amounts of the catalyst still present in the product as determined by LC-MS. This removal issue has been investigated and documented in published work, where it was found that PPD has various oxidation products with varying solubilities and

polarities making extraction difficult (Bai et al., 2010, Aeby et al., 2009, Solis et al., 1976), which was one of the deciding factors in using the reductive amination method for the project, as well as the fact the reductive amination method being able to be scaled up to multi-gram scale (Meyer and Fischer, 2015).

3.3.3 P₁₁-4-CS conjugate: Click reaction optimization

In this chapter, various modifications of the classic CuAAC reaction have been reported, which have been reported previously by many groups. The difference here is the application of the click reaction in terms of covalently linking a relatively small peptide with a propensity to self-assembly with a poly-anionic polysaccharide. The difficulties encountered with optimising the click reaction came down to the massive differences in molecular weight of the two components – peptide ~ 2kDa, CS ~48kDa. The high molecular weight of the CS made monitoring the click reaction difficult so the reaction had to be optimised as much as possible using smaller analogues to check various conditions. This allowed monitoring through LC-MS and NMR techniques but due to the large discrepancies between the analogues and CS molecular weights meant that SEC-MALLS had to be employed to validate the final click reaction as well as the presence of the characteristic triazole proton signal ~8ppm in the ¹H NMR spectrum (Appukkuttan et al., 2004). The various conditions investigated were relatively robust, in terms of the types of aqueous buffers the reaction was successful in, but all of the conditions were pH sensitive with successful reaction only when then pH was ~7-7.4, which matches the observations of various groups that have reported similar difficulties with polysaccharides (Elchinger et al., 2011, Appukkuttan et al., 2004). This may have been due to the peptides inherent self-assembling ability which could have interfered with the reaction by collapsing or aggregating intermolecularly causing the N₃ group to become buried within the aggregate thus inhibiting the click reaction (Kakwere et al., 2011). The stoichiometry of the click reaction catalysts was also important as investigation into reactions with lower amounts of catalytic reagents were unsuccessful. The optimum ratio turned out to be a 1:1:1 for CuSO₄: TBTA: Na-ascorbate, with a 1:1 ratio of peptide: alkyne yielding ~80-90% conversion based on amount of peptide remaining following the click reaction. These conditions were originally described by Cielpla *et al* for their work on covalently linking fluorophores on to human and zebrafish cells (Ciepla et al., 2014). As mentioned previously, one issue with using TBTA was encountered when used in tandem with TCEP, due to the formation of a white precipitate after ~2hrs which was in fact TBTA. This issue with solubility has been noted by other groups using TBTA as a stabilizing ligand for the Cu (I) reactive species. (Lallana et al., 2011, Ciepla et al., 2014). This meant the two vastly different reagents had relatively little time to collide considering both of the propensities to inter and intramolecularly aggregate as well as the loss of the stabilising ligand for the Cu (I)

species, thus killing the catalytic reaction. Compared to this, the Na-ascorbate: TBTA system could be left overnight to go to completion before a precipitate formed \sim 36hrs, which was probably due to the stabilising effect the TBTA had on the *in situ* Cu (I) formation and stability. This greater duration window for the reaction meant the reagents could be scaled up significantly with no major loss of conversion, where the test scale reactions were carried out on 1-5mg while the full scale reactions were carried out on 10-50mg scales with no significant increase in unreacted azido-peptide. The only issue with using Na-ascorbate as the mild reducing agent in the click reaction is the sensitivity to light, where the CuSO₄/Na-ascorbate/TBTA mixture turned a yellow-orange colour but if left exposed to light the mixture turned a cloudy white colour indicating the oxidation of the Na-ascorbate or the Cu (I) species. In order to overcome this issue the reaction was simply carried out in a vessel protected by foil. Over time, as the reaction progressed, the CS product did precipitate from the conjugate trying to self-assemble into fibrillar structures.

3.3.4 Cu cytotoxicity

The main concern with the type of click chemistry reported in this chapter is the presence of Cu (I) and Cu (II) which has previously been reported to be cytotoxic in biological systems. When the rationale for this project was with the aim of being injected into human patients, this meant the presence of excessive residual Cu after the click reaction and purification could be an issue. The results from the FAAS assay showed the residual Cu to be approximately 0.9% of the starting mass of Cu (II) indicating if the starting concentration was 1 mM the residual concentration for the same volume was approximately 9 μ M. This concentration was then used to base the limits to which to expose the two different cell lines to, with the maximum being a huge excess – 5 mM and the minimum being 0.001 mM, equalling the upper limit of the measured amount of residual Cu. The extract cytotoxicity results showed that both L929 and BHK cells survived in concentrations as high as 0.1 mM, so 10x the maximum residual Cu measured, where Lanke *et al.* reported observing a similar concentration being cytotoxic to BHK cells (Lanke *et al.*, 2007). This result showed that the number of rounds of dialysis were sufficient to remove enough Cu from the peptide-CS conjugation product but as mentioned in section 3.2.4, the number of rounds of dialysis was increased to 5 x 1hrs rounds to ensure the residual Cu was not an issue in the future.

3.4 Conclusion

The aim was to synthesize and characterise a self-assembling peptide-CS conjugate through utilising click chemistry to form a covalent bond between peptide and GAG through the

formation of a triazole link. The peptide was based on a previously reported peptide sequence – P₁₁-4 (QQRFEWEFEQQ) (Aggeli, 1997, Aggeli, 2001b, Carrick, 2007a, Carrick et al., 2007, Davies and Aggeli, 2011, Davies et al., 2006, Maude et al., 2012), but further modified to allow Cu catalysed click chemistry to be employed to covalently link it to an alkyne functionalised CS molecule. This is the first reported example of such a conjugate having been synthesized with the propensity to form macromolecular structures. Similar examples include hydrogels formed from crosslinked GAG molecules such as hyaluronate, chondroitin sulfate and gelatin (Hu, 2011) or using different polysaccharides such as chitosan (Tan et al., 2009). These are permanent hydrogels once formed, in contrast to the system reported in this chapter where the mechanism of hydrogel formation is through the reversible, equilibria controlled formation of a fibrillary network based on an anti-parallel β -sheet secondary structure. With these materials in hand the effects of the CS conjugates on peptide self-assembly could be investigated in terms of morphology and mechanical properties to identify the most appropriate gel combination to carry forward to investigate the effect within a tissue model.

Chapter 4

Effect of peptidoglycan content on morphology and mechanical properties of hydrogels

As discussed in Chapter 1, the aim was to investigate the physical properties of undoped and doped peptide hydrogels in terms of the different morphologies different compositions, with and without the synthesized P₁₁-4/8-CS conjugate, formed and the rheological properties of each composition to identify and rationalise the results in terms of the effect that introducing CS into the self-assembling peptide network has upon these different properties.

In this chapter I will identify and analyse the different morphologies through the use of transmission electron microscopy and graphical software. The observations of this will then be used, in conjunction with rheological experiments to measure the hydrogel mechanical properties, to establish and rationalise the “strongest” gels to take forward to *in vitro* testing in a whole condyle porcine osteoarthritic model.

4.1 Introduction

With methods established to prepare chondroitin sulfate functionalised peptides the next stage was to determine how these changes affected the self-assembling properties of the system.

4.1.1 Self-assembling systems

Self-assembly is the spontaneous association of smaller structures into larger, ordered arrays. There are two types of self-assembly: static and dynamic. Most research has been based around static systems whilst dynamic systems still remain poorly understood (Lee et al., 2001, Hosseinkhani et al., 2013). Static self-assembling systems are defined as ones that have reached local or global equilibrium through the process of self-assembly. This process may require energy but once formed the ordered structure is stable leading to a loss of free energy from the system. Dynamic self-assembling systems in contrast are ones that require the system to lose energy during the formation of an ordered structure before the system reaches a state of equilibrium (Lee et al., 2001, Hosseinkhani et al., 2013). This required loss of free energy, from non-covalent, specific interactions makes investigating dynamic systems far more complex than static systems with the amount of energy lost needing to be both controlled yet unconstrained such as controlling the temperature of the system through isothermal parameters e.g. room

temperature which would not limit the potential for self-assembly. These two different types of self-assembly can be further differentiated based on the scale over which self-assembly occurs: - molecular, nanoscale mesoscopic, macroscopic self-assembly can all be observed, with molecular and nanoscale being further classified as intramolecular and intermolecular. Intramolecular self-assembly, the best example of which is the process by which proteins fold in nature, occurs when a complex random structure adopts an ordered conformation. Intermolecular self-assembly occurs when molecules form supramolecular arrays through various associations. The functional properties of the array is dependent on the composition of the independent building blocks (Lee et al., 2001, Hosseinkhani et al., 2013).

This study concerns the self-assembly of peptides, which can be described as a dynamic, intra and intermolecular, molecular/nanoscale system.

4.1.2 Self-assembling peptide hydrogels

Self-assembling peptides are short peptide chains that can undergo spontaneous ordered intramolecular and intermolecular organisation through non-covalent interactions such as hydrogen bonding and π - π interactions as well as the hydrophobic effect (Koutsopoulos, 2016). Such spontaneous organisation can be triggered by simple proximity to other molecules or through exposure to an external stimuli such as a change in pH, temperature or ionic strength.

As previously discussed (Section 1.8), there are two principal types of self-assembling peptidic families based on either α -helical or β secondary structures. Compared to α -helical peptides, β structure forming peptides are quite diverse in the primary peptide sequence and the adopted secondary structure. The differences between the structures and self-assembly at the molecular level lead to different outcomes at the nano- and macro-scales.

4.1.3 Methods of morphological analysis

On the macro-scale β strand based arrays can produce hydrogels with different characteristics such as flocculate formation, nematic fluid or gel as shown in **Fig 4.1** using the P₁₁-X class of β -sheet forming self-assembling peptides developed by the Aggeli group. These hydrogels can also show a range of stiffness and opacity (Aggeli *et al.*, 2001).

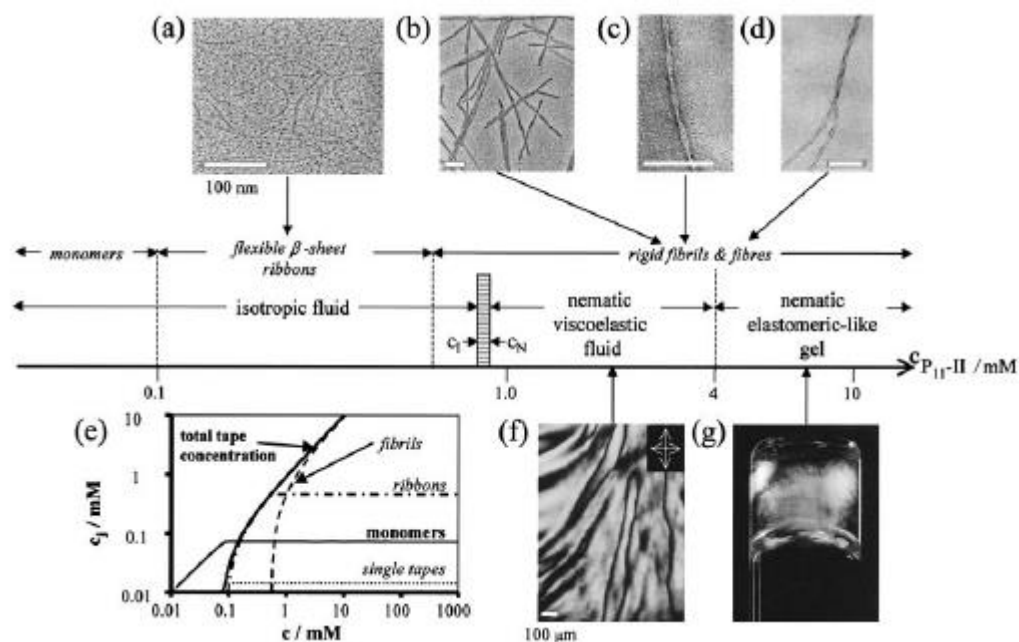


Fig 4.1: Stages of self-assembly and hydrogel formation for P₁₁-X class of self-assembling peptides (Reproduced from Aggeli *et al* with permission from PNAS).

At the nano-scale sequence variation can lead to different fibrillary construction, interconnectivity and dimensions. The study of self-assembling peptides uses a diverse toolkit of techniques to analyse the materials at these different scales including microscopic techniques such as transmission electron microscopy (TEM) and interaction based atomic force microscopy (AFM) through to rheological techniques to measure the physiochemical properties of hydrogels.

Transmission electron microscopy is a microscopic technique enables the imaging of materials through the interaction of an electron beam as it passes through a sample. The sample is usually placed on a copper grid that can have varying mesh sizes to allow different sized spaces for the sample to reside on. For the field of self-assembling peptides, a staining agent is used to help act increase image contrast for the relatively thin nanostructures. The most common staining agent is uranyl acetate, which is very electron dense and scatters the electron beam based on how much stain is absorbed by the sample, which is known as negative staining. This technique allows intricate imaging of the fine, twisted, nanostructure which can be then used to measure dimensions (e.g. width, length, pitch twist), as well as determine connectivity and branching of the fibrils. A basic schematic of how TEM works is shown in **Fig 4.2**.

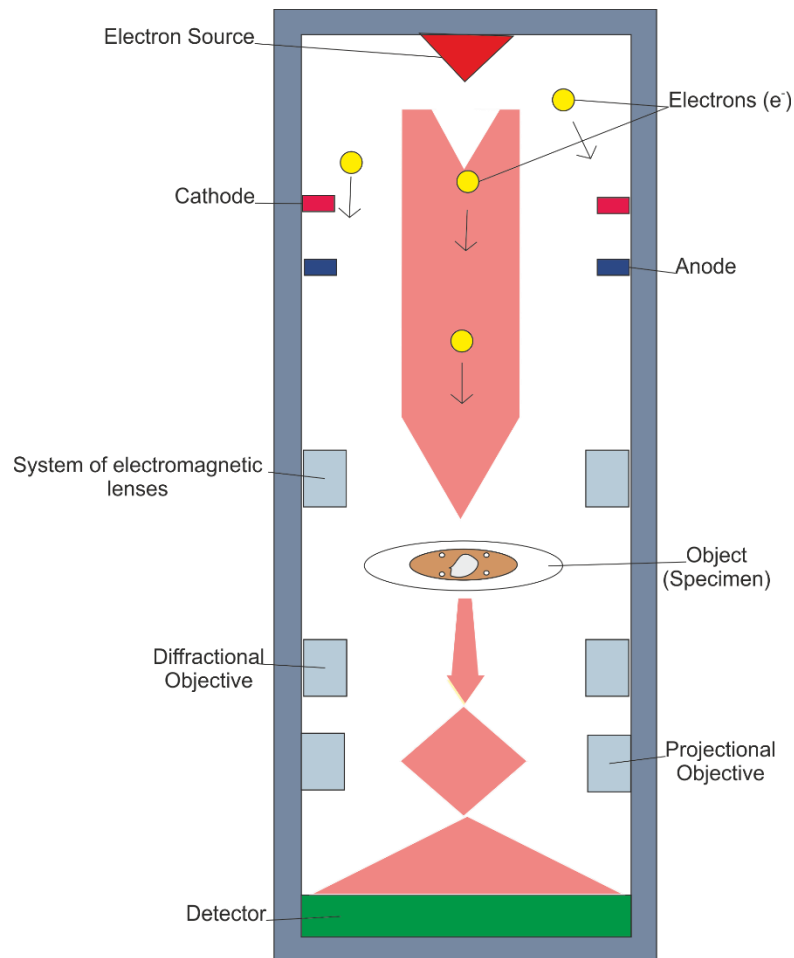


Fig 4.2: A schematic of a typical transmission electron microscope

4.1.4 Physical testing of hydrogels

Hydrogels are defined as compositions of materials that form colloidal suspensions with water as the medium which have varying degrees of phase, opacity and stiffness. These various properties make testing the physical bulk properties of hydrogels a challenge but rheology can be used to measure the liquid and solid component properties both jointly and separately by measuring the storage or elastic modulus (G') and loss or viscous modulus (G''). The storage modulus reflects the “solid component” and the loss modulus the “liquid component” of the system. These two properties, in conjunction, describe the composition of the hydrogel and whether it is more “solid”-like (where it contains more solid particles) or more “liquid”-like (where it contains a greater proportion of water). Rheological experiments can be classified into two types of set ups: strain and stress controlled. In strain controlled experiments, the motor and transducer are independent and operate separately. The motor applies a particular strain to the sample and the sample response is measured as stress through the transducer. An example of this type of setup is shown in **Fig 4.3**.

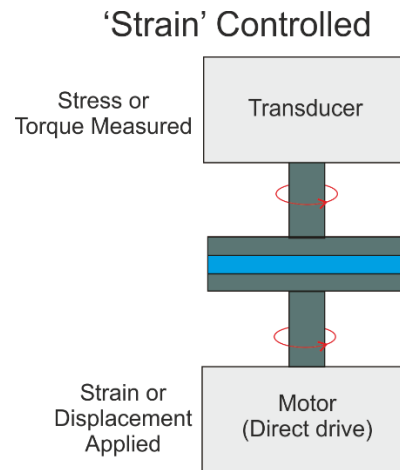


Fig 4.3: A schematic representation of a strain controlled rheological experiment.

In stress controlled experiments, the motor and transducer are linked so operate in a combined manner. The motor applies a set stress or torque to the sample with the displacement measured using a sensor. An example of this type of setup is shown in **Fig 4.4**.

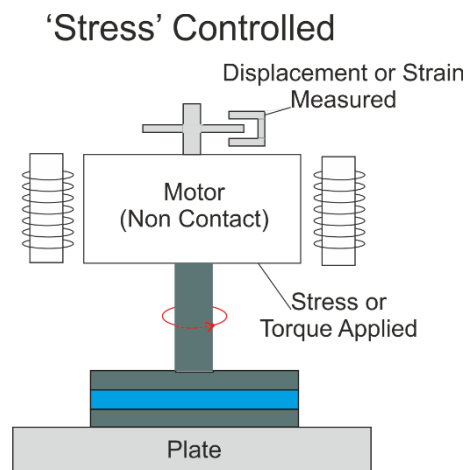


Fig 4.4: A schematic representation of a stress controlled rheological experiment.

Another factor to consider with rheological experiments is the types of plates used to apply the stress or strain to the sample. There are three main types of plate setups: concentric cylinders, cone on plate and plate on plate. Each setup has a different range of viscosity limits so are tailored to certain samples, where plate on plate is the most commonly used for soft hydrogel samples. A simple representation of the three setups is shown in **Fig 4.5**.

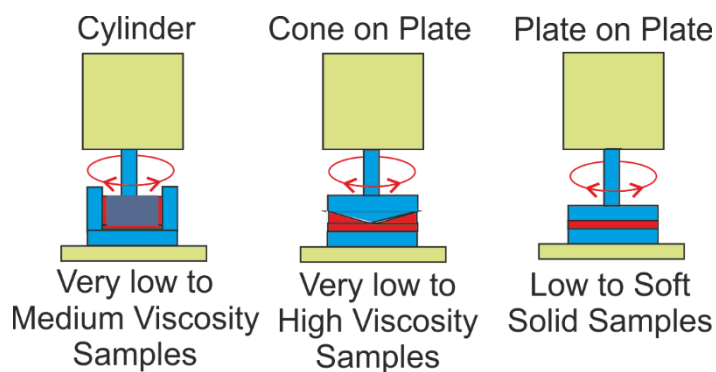


Fig 4.5: The various configurations of measurement interfaces possible with rheological experiments

The techniques mentioned above were utilized to investigate the micro and macroscopic physical properties of gels composing of P₁₁₋₄ and P₁₁₋₈ peptides (and functionalised variants) under a range of conditions. The conditions investigated are summarized below in **Table 4.1**, where the different conditions in terms probed the effects of: 1) molar ratio between the base P_{11-4/8} peptide and either the free CS or covalently linked P_{11-4/8}-CS conjugate, 2) the different ionic buffer solution in which the gels were made up in and, most importantly whether covalent linkage of the CS to the peptide produced a different response to simple mixing of the two materials.

Sample	No	Peptide	CS	Buffer	Molar ratio	[Peptide] mg ml ⁻¹ (~ mM)
P ₁₁ -4 only 230 mM Na ⁺	1	P ₁₁ -4	-	230 mM Na ⁺	-	10 (6)
P ₁₁ -4 only 130 mM Na ⁺	2	P ₁₁ -4	-	130 mM Na ⁺	-	10 (6)
P ₁₁ -4 + CS 32:1 230 mM Na ⁺	3	P ₁₁ -4	Free	230 mM Na ⁺	32:1	10 (6)
P ₁₁ -4 + CS 64:1 230 mM Na ⁺	4	P ₁₁ -4	Free	230 mM Na ⁺	64:1	10 (6)
P ₁₁ -4 + CS 32:1 130 mM Na ⁺	5	P ₁₁ -4	Free	130 mM Na ⁺	32:1	10 (6)
P ₁₁ -4 + CS 64:1 130 mM Na ⁺	6	P ₁₁ -4	Free	130 mM Na ⁺	64:1	10 (6)
P ₁₁ -4 + P ₁₁ -4-CS 32:1 230 mM Na ⁺	7	P ₁₁ -4	Covalently bound	230 mM Na ⁺	32:1	10 (6)
P ₁₁ -4 + P ₁₁ -4-CS 64:1 230 mM Na ⁺	8	P ₁₁ -4	Covalently bound	230 mM Na ⁺	64:1	10 (6)
P ₁₁ -4 + P ₁₁ -4-CS 32:1 130 mM Na ⁺	9	P ₁₁ -4	Covalently bound	130 mM Na ⁺	32:1	10 (6)
P ₁₁ -4 + P ₁₁ -4-CS 64:1 130 mM Na ⁺	10	P ₁₁ -4	Covalently bound	130 mM Na ⁺	64:1	10 (6)
P ₁₁ -8 only 230 mM Na ⁺	11	P ₁₁ -8	-	230 mM Na ⁺	-	10 (6)
P ₁₁ -8 only 130 mM Na ⁺	12	P ₁₁ -8	-	130 mM Na ⁺	-	10 (6)
P ₁₁ -8 + CS 32:1 230 mM Na ⁺	13	P ₁₁ -8	Free	230 mM Na ⁺	32:1	10 (6)
P ₁₁ -8 + CS 64:1 230 mM Na ⁺	14	P ₁₁ -8	Free	230 mM Na ⁺	64:1	10 (6)
P ₁₁ -8 + CS 32:1 130 mM Na ⁺	15	P ₁₁ -8	Free	130 mM Na ⁺	32:1	10 (6)
P ₁₁ -8 + CS 64:1 130 mM Na ⁺	16	P ₁₁ -8	Free	130 mM Na ⁺	64:1	10 (6)
P ₁₁ -8 + P ₁₁ -8-CS 32:1 230 mM Na ⁺	17	P ₁₁ -8	Covalently bound	230 mM Na ⁺	32:1	10 (6)
P ₁₁ -8 + P ₁₁ -8-CS 64:1 230 mM Na ⁺	18	P ₁₁ -8	Covalently bound	230 mM Na ⁺	64:1	10 (6)
P ₁₁ -8 + P ₁₁ -8-CS 32:1 130 mM Na ⁺	19	P ₁₁ -8	Covalently bound	130 mM Na ⁺	32:1	10 (6)
P ₁₁ -8 + P ₁₁ -8-CS 64:1 130 mM Na ⁺	20	P ₁₁ -8	Covalently bound	130 mM Na ⁺	64:1	10 (6)

Table 4.1: Summary of the different samples, peptide type, CS introduction manner, buffer type, molar ratio and peptide concentration.

P₁₁-4/8 only gels composed of only the base peptide at a concentration of 10 mg ml⁻¹, while P₁₁-4/8 + CS gels were gels comprising of the same quantity of base peptide as the previous gels but were doped with free CS at the two mentioned molar ratios. These gels were designed to represent a model where the CS was “suspended” within the gel matrix rather than covalently

linked. The P₁₁-4/8-CS gels were gels again comprising of the same base peptide but doped with the covalently linked P₁₁-4/8-CS conjugate rather than the free CS.

4.2 Results

4.2.1 Morphologies of different P₁₁-4 gels at different ionic strengths

The morphologies of the gels on the microscopic scale were imaged using TEM and the images analysed using ImageJ to measure the fibrillary lengths and widths. An example of how the fibrillary widths and lengths were measured on a micrograph is shown below in **Fig 4.6**.

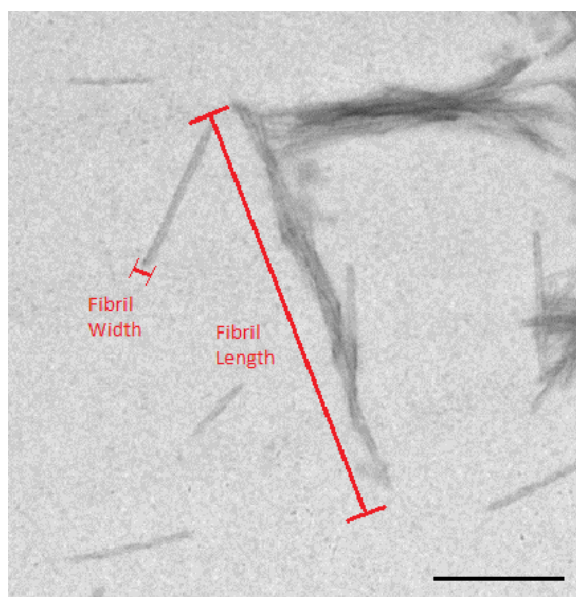


Fig 4.6: An example TEM micrograph to highlight how the fibril lengths and widths were measured – where the length was the persistence length and the width was the width of the fibril at the widest point (to avoid any variation in other unmeasured dimensions such as pitch twist). Scale bar – 500 nm.

4.2.1.1 P₁₁-4 only

The morphology of P₁₁-4 gels formed in the two different ionic strength physiological buffers (130 mM and 230 mM Na⁺) mentioned previously were analysed. A consistent concentration of peptide was used – 10 mg ml⁻¹ (~5.85 mM) with the method of preparation, pH switching and testing standardized as detailed in Section 2. Different TEM micrographs of P₁₁-4 hydrogels are shown in **Fig 4.7**, for each different concentration.

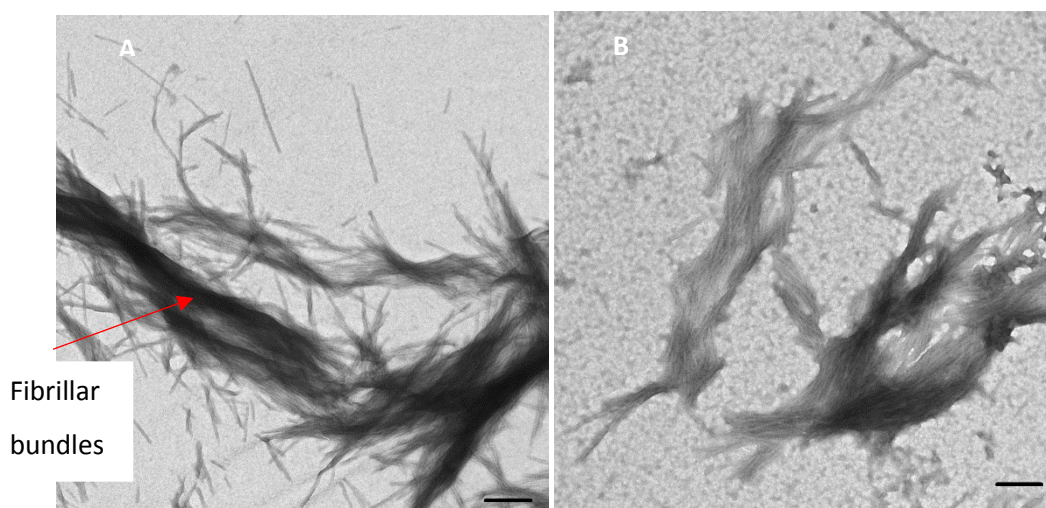


Fig 4.7: TEM images of P₁₁₋₄ (~6 mM) gels in different ionic strength buffers. A) 230 mM Na⁺ buffer, 4000x magnification, scale bar - 500nm. B) 130 mM Na⁺ buffer, 4000x magnification, scale bar – 500nm.

Analysis of the fibrillar lengths and widths of the gels at both buffer strengths (130 mM and 230 mM) yielded the following dimensions presented in **Table 4.2**.

Sample	Length (nm)	Width (nm)
P ₁₁₋₄ only 230 mM Na ⁺	513 ± 105	37 ± 9
P ₁₁₋₄ only 130 mM Na ⁺	423 ± 171	35 ± 10

Table 4.2: The fibrillar lengths and widths for P₁₁₋₄ only samples at two different ionic strength buffers (± S.D).

Statistical analysis ($\alpha = 0.95$) indicated there was no significant difference between the fibrillar dimensions at the two different salt concentrations. Visual analysis of the micrographs of the gel samples on the grids showed that the 230 mM Na⁺ samples were more defined in terms of fibrils rather than more open structured, ribbon like structures. The fibrils were more tightly bound and denser bundles were seen in the 230 mM Na⁺ samples compared to the 130 mM Na⁺ samples. Both gels appeared similar in terms of opacity and stiffness as shown in **Fig 4.8**.



Fig 4.8: Image of P₁₁₋₄ gels only at 230 mM Na⁺ (left) and 130 mM Na⁺ (right)

4.2.1.2 P₁₁₋₄ + CS

The morphology of P₁₁₋₄ was examined in the presence of CS at the same conditions as the previous samples. The same concentration of peptide was used – 10mgml⁻¹ (~5.85mM) but two molar ratios of peptide to CS were employed (Pep: CS 32:1 and 64:1). Different TEM micrographs of P₁₁₋₄ + CS hydrogels are shown in **Fig 4.9**, for each different concentration and molar ratio.

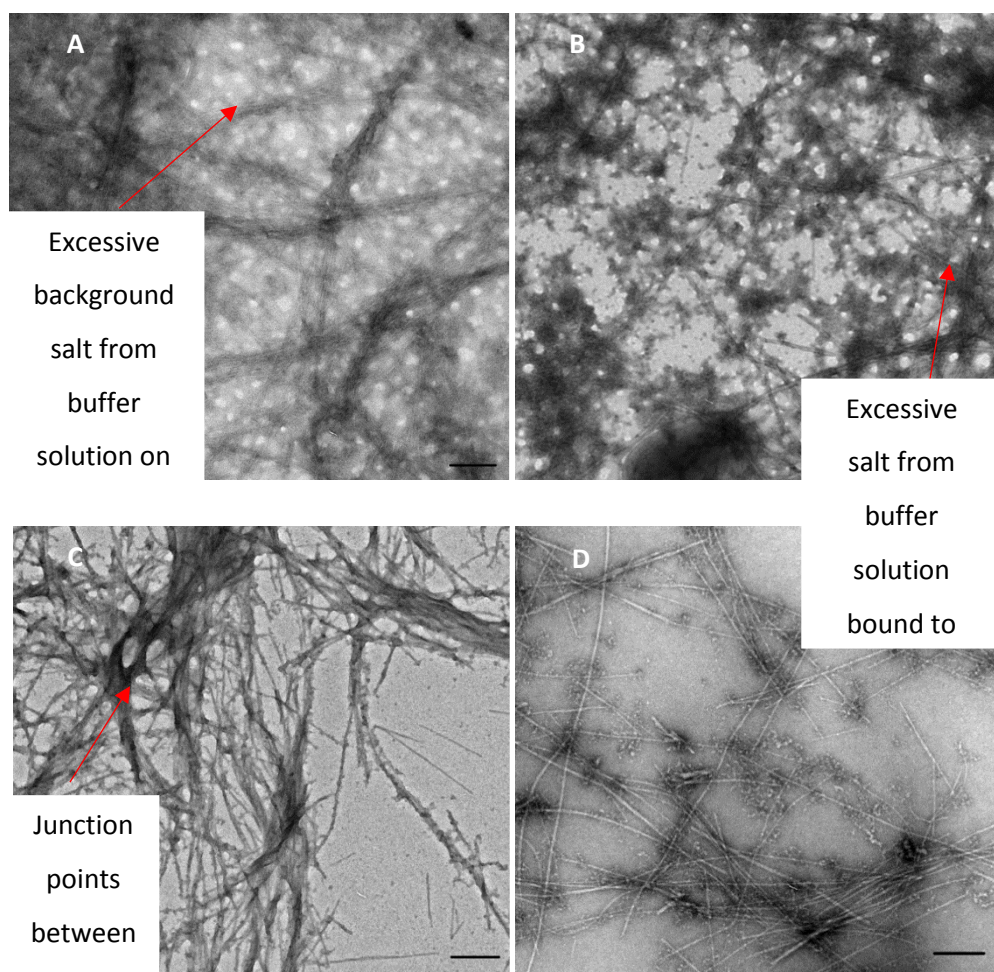


Fig 4.9: TEM images of P₁₁₋₄ + CS (~5.85mM) gels in different ionic strength buffers. A) P₁₁₋₄ + CS 32-1 Ratio 230 mM Na⁺ buffer, 4000x magnification, scale bar - 500nm. B) P₁₁₋₄ + CS 64-1 Ratio 230 mM Na⁺ buffer, 4000x magnification, scale bar - 500nm. C) P₁₁₋₄ + CS 32-1 130 mM Na⁺ buffer, 4000x magnification, scale bar – 500nm. D) P₁₁₋₄ + CS 64-1 130 mM Na⁺ buffer, 4000x magnification, scale bar – 500nm.

Analysis of the fibrillar lengths and widths of the gels at both molar ratios of CS (32:1 and 64:1 (P₁₁₋₄: CS) at both buffer strengths (130 mM and 230 mM) yielded the following dimensions presented in **Table 4.3**.

Sample	Length (nm)	Width (nm)
P ₁₁ -4+ CS 230 mM Na ⁺ 32:1	694 ± 88	35 ± 7
P ₁₁ -4 + CS 230 mM Na ⁺ 64:1	731 ± 93	37 ± 7
P ₁₁ -4+ CS 130 mM Na ⁺ 32:1	881 ± 178	37 ± 9
P ₁₁ -4+ CS 130 mM Na ⁺ 64:1	739 ± 130	34 ± 8

Table 4.3: The fibrillar lengths and widths for P₁₁-4 +CS samples at two different molar ratios and ionic strength buffers (± S.D).

Again, statistical analysis ($\alpha=0.95$) indicated there was no significant difference between the fibrillar dimensions at the two different concentrations. Visual analysis of the images of the gel samples showed that in the presence of the higher 230 mM Na⁺ buffer, the fibrillary network appeared to have more junction points as well as greater salt precipitation in and around the fibrils, which may be a result of the relatively high concentration of salt in the buffer from reduced solubility of the solution from the presence of the CS molecules which have a low solubility inherently due to the high molecular weight, the evidence for this hypothesis was the greater salt precipitation present in the higher CS ratio samples (32:1). The fibrils appeared defined and rigid in shape being relatively straight and consistent in thickness throughout the fibrillary length. In comparison, in the presence of the lower 130 mM Na⁺ buffer the fibrils appeared to be more defined but this could be due to the absence of salt precipitation making the image less blurred. When comparing all four samples, there was no significant difference between each in terms of fibrillary length showing that the variation of CS content and salt concentration do not affect the ability of the non-covalent mixture of P₁₁-4 and CS to self-assemble into fibrillary networks. However when the samples in this group are compared to the controls – P₁₁-4 only in both buffers, there is a significant difference in terms of fibrillar length, with the introduction of CS into the network seeming to cause the fibrils to elongate. The fibrillar widths in contrast have remained unchanged. Both gels appeared similar in terms of opacity as shown in **Fig 4.10**.

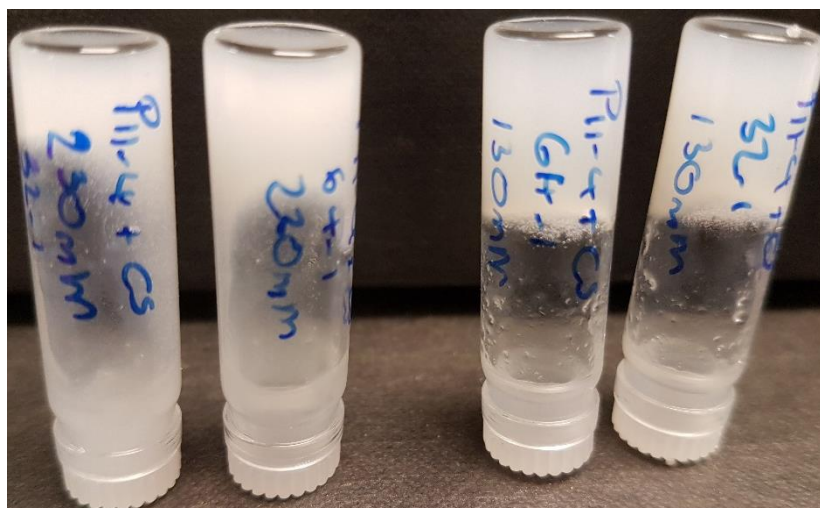


Fig 4.10: Image of P₁₁₋₄ + CS gels at 230 mM Na⁺ at both 32:1 (far left), 64:1 (left) molar ratios and 130 mM Na⁺ at both 32:1 (far right), 64:1 (right) molar ratios.

4.2.1.3 P₁₁₋₄ + P₁₁₋₄-PEG-Hex-CS

The morphology of P₁₁₋₄ + P₁₁₋₄-PEG-Hex-CS in which the CS is covalently linked to the P11-4 molecule was studied in a similar way. Different TEM micrographs of P₁₁₋₄ + P₁₁₋₄-PEG-Hex-CS hydrogels are shown in **Fig 4.11**, for each different concentration and molar ratio.

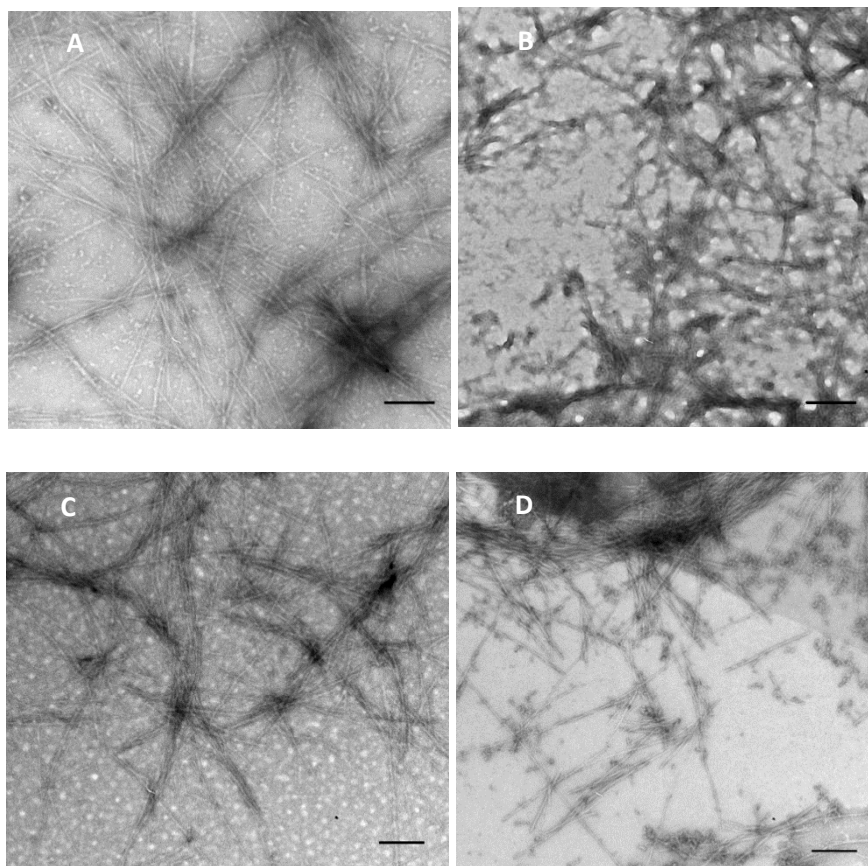


Fig 4.11: TEM images of P₁₁-4 + P₁₁-4-CS (~5.85mM) gels in different ionic strength buffers. A) P₁₁-4 + P₁₁-4-CS 32-1 Ratio 230 mM Na⁺ buffer, 4000x magnification, scale bar - 500nm. B) P₁₁-4 + P₁₁-4-CS 64-1 Ratio 230 mM Na⁺ buffer, 4000x magnification, scale bar - 500nm. C) P₁₁-4 + P₁₁-4-CS 32-1 130 mM Na⁺ buffer, 4000x magnification, scale bar – 500nm. D) P₁₁-4 + P₁₁-4-CS 64-1 130 mM Na⁺ buffer, 4000x magnification, scale bar – 500nm.

Analysis of the fibrillar lengths and widths of the gels at both molar ratios (32:1 and 64:1 (P₁₁-4: P₁₁-4-PEG-Hex-CS) at both buffer strengths (130 mM and 230 mM) yielded the following dimensions presented in **Table 4.4**.

Sample	Length (nm)	Width (nm)
P ₁₁ -4+ P ₁₁ -4-CS 230 mM Na ⁺ 32:1	1083 ± 109	70 ± 13
P ₁₁ -4+ P ₁₁ -4-CS 230 mM Na ⁺ 64:1	931 ± 65	66 ± 13
P ₁₁ -4+ P ₁₁ -4-CS 130 mM Na ⁺ 32:1	941 ± 134	60 ± 12
P ₁₁ -4+ P ₁₁ -4-CS 130 mM Na ⁺ 64:1	945 ± 137	61 ± 6

Table 4.4: The fibrillar lengths and widths for P₁₁-4 + P₁₁-4-CS samples at two different molar ratios and ionic strength buffers (± S.D).

ANOVA analysis again ($\alpha = 0.95$) indicated there was no significant difference between the fibrillary dimensions under the different conditions concentrations. Visual analysis of the TEM images once again showed that with the higher buffer concentration the images were partially

masked by background salt precipitation but that again there appears to be more junction points and more closely packed fibrils in the network compared to samples formed at the lower buffer concentration. The major difference compared to the previous sample group (P11-4 with added CS) is a significant change ($\alpha = 0.05$) in fibrillary width. This could be due to the fact the CS chains are now covalently bound to the fibrils but rather than project outwards from the central fibrillary core, the chains could be collapsing and wrapping around the fibrils, making the widths thicker. All the gels appeared similar in terms of opacity as shown in **Fig 4.12**.

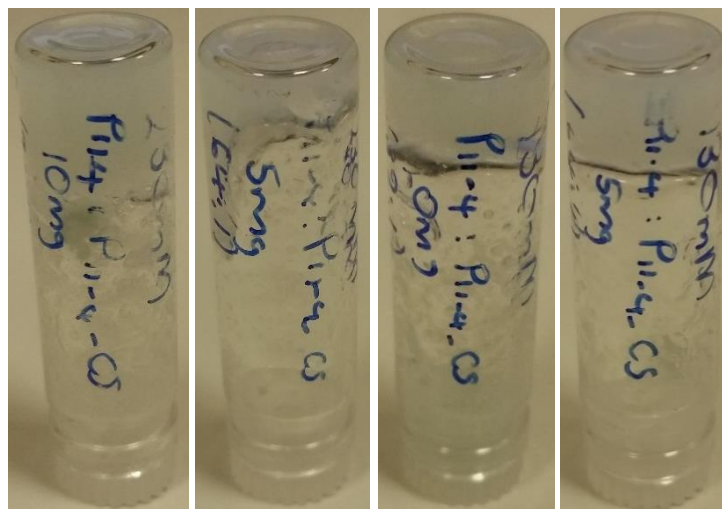


Fig 4.12: Images of P₁₁-4 + P₁₁-4-CS gels at 230 mM Na⁺ at both 32:1 (far left), 64:1 (left) molar ratios and 130 mM Na⁺ at both 32:1 (right), 64:1 (far right) molar ratios.

A comparison of the different fibrillary lengths and widths of each sample reveal distinct differences between the different samples and between groups. The data is shown below in **Fig 4.13**.

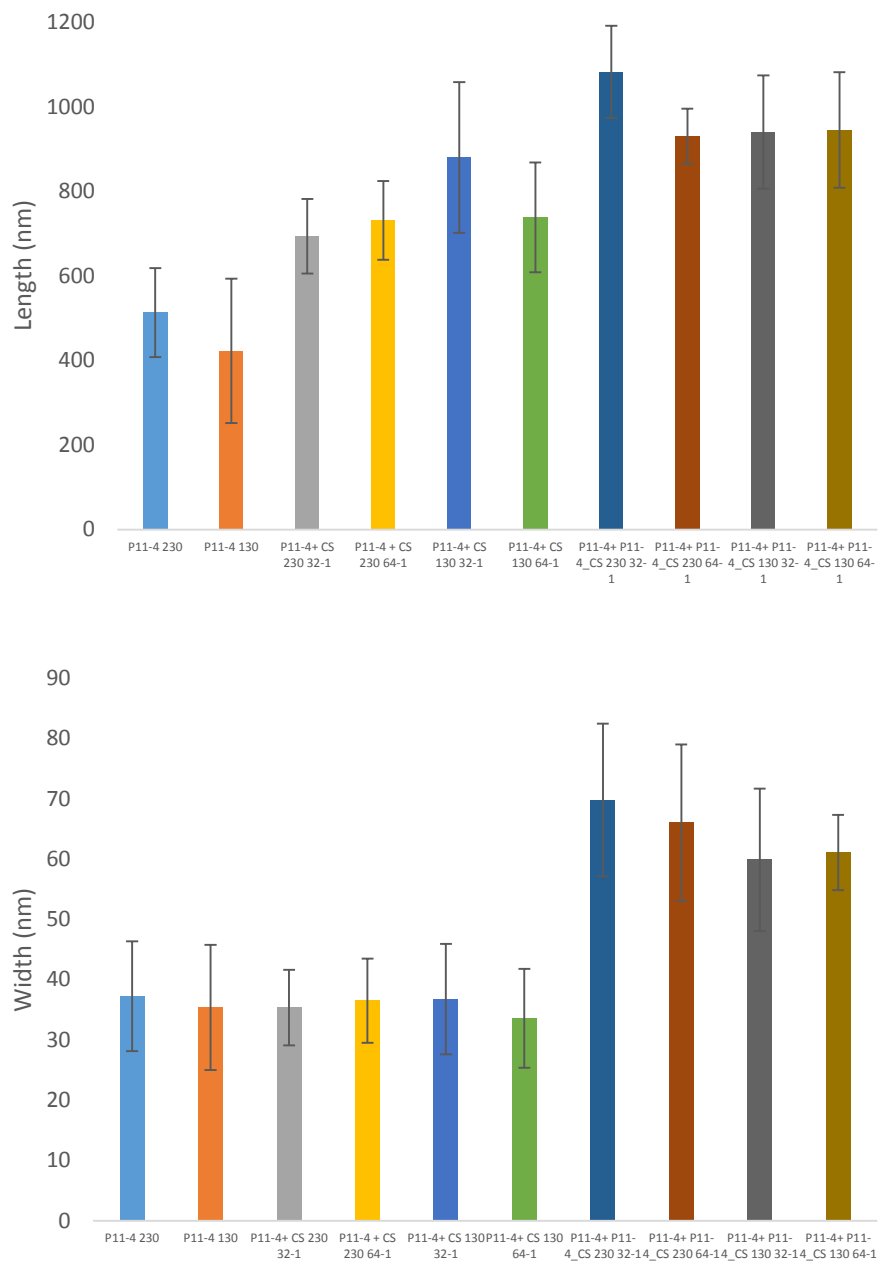


Fig 4.13: Comparison of the different fibrillar lengths and widths for each different P₁₁₋₄ sample. A) Fibrillar lengths of each P₁₁₋₄ sample. B) Fibrillar widths of each P₁₁₋₄ sample. (Error bars = ± S.D).

4.2.2 Morphologies of different P₁₁-8 gels at different ionic strengths

The morphology of the P₁₁-8 gels, including the suspension and integration manner incorporation of CS groups, were tested at the same conditions and concentrations as those with P₁₁-4 gels.

4.2.2.1 P₁₁-8 only

Different TEM micrographs of P₁₁-8 hydrogels are shown in **Fig 4.14**, shown for each different concentration.

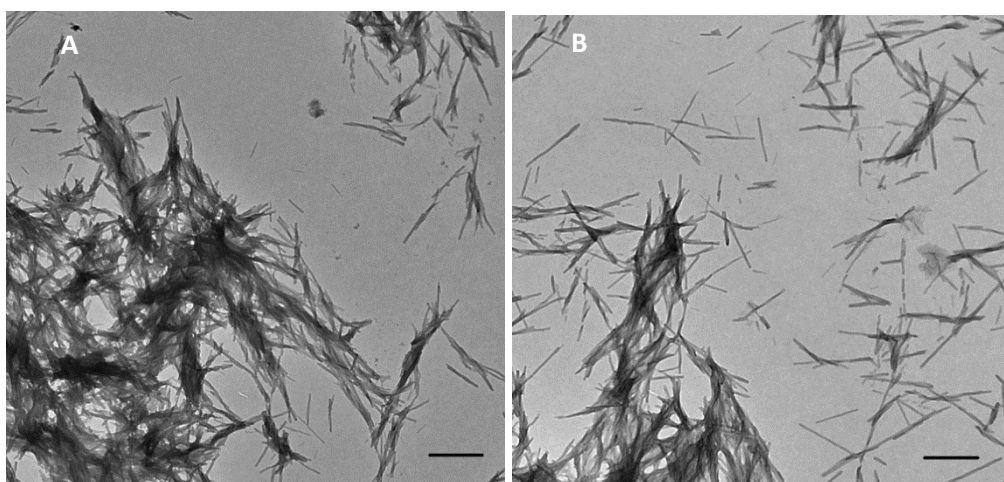


Fig 4.14: TEM images of P₁₁-8 (~5.85mM) gels in different ionic strength buffers. A) 230 mM Na⁺ buffer, 4000x magnification, scale bar - 500nm. B) 130 mM Na⁺ buffer, 4000x magnification, scale bar – 500nm.

Analysis of the fibrillar lengths and widths of the gels at the two respective ionic concentrations (130 mM and 230 mM Na⁺) yielded the following results shown in **Table 4.5**.

Sample	Length (nm)	Width (nm)
P ₁₁ -8 230 mM Na ⁺	611 ± 148	34 ± 11
P ₁₁ -8 130 mM Na ⁺	606 ± 83	35 ± 7

Table 4.5: The fibrillar lengths and widths for P₁₁-8 only samples at two different ionic strength buffers (± S.D).

One-way ANOVA analysis ($\alpha = 0.05$) indicated there was no significant difference between the fibrillar dimensions at the two different concentrations. The showed very little difference between the two different buffer concentrations with the fibrils looking similar in terms of definition, packing and propensity to form junction points. This net positively charged peptide seems to form slightly longer fibrils compared to the negatively charged P₁₁-4 peptide gels. There was no significant difference between the two buffer concentrations in fibrillary length and width. Both gels appeared similar in terms of opacity as shown in **Fig 4.15**.



Fig 4.15: Image of P₁₁₋₈ gels only at 230 mM Na⁺ (left) and 130 mM Na⁺ (right)

4.2.2.2 P₁₁₋₈ + CS

Different TEM micrographs of P₁₁₋₈ self-assembled in the presence of CS are shown in Fig 4.16, shown for each different concentration and molar ratio.

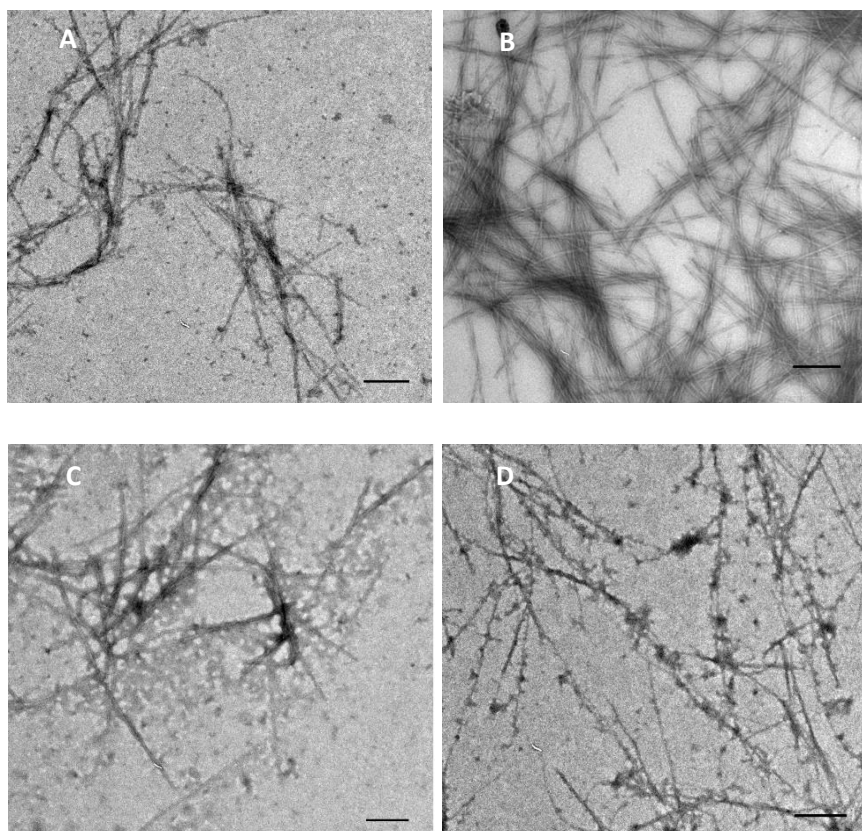


Fig 4.16: TEM images of P₁₁₋₈ + CS (~5.85mM) gels in different ionic strength buffers. A) P₁₁₋₈ + CS 32-1 Ratio 230 mM Na⁺ buffer, 4000x magnification, scale bar - 500nm. B) P₁₁₋₈ + CS 64-1 Ratio 230 mM Na⁺ buffer, 4000x magnification, scale bar - 500nm. C) P₁₁₋₈ + CS 32-1 130 mM Na⁺ buffer, 4000x magnification, scale bar - 500nm. D) P₁₁₋₈ + CS 64-1 130 mM Na⁺ buffer, 4000x magnification, scale bar - 500nm.

Analysis of the fibrillar lengths and widths of the gels at the two respective ionic concentrations (130 mM and 230 mM Na⁺) and two different molar ratios (32:1 and 64:1) resulted in the following fibrillary lengths and widths shown below in **Table 4.6**.

Sample	Length (nm)	Width (nm)
P ₁₁ -8 + CS 230 mM Na ⁺ 32:1	652 ± 182	49 ± 11
P ₁₁ -8 + CS 230 mM Na ⁺ 64:1	574 ± 166	34 ± 10
P ₁₁ -8 + CS 130 mM Na ⁺ 32:1	610 ± 116	46 ± 14
P ₁₁ -8 + CS 130 mM Na ⁺ 64:1	654 ± 100	41 ± 11

Table 4.6: The fibrillar lengths and widths for P₁₁-8 +CS samples at two different molar ratios and ionic strength buffers (± S.D).

One-way ANOVA analysis ($\alpha = 0.05$) indicated there was no significant difference between the fibrillar dimensions at the two different buffer concentrations. Visually, the images no significant difference in terms of definition, rigidity and propensity to form junction points. There was also no significant between the different samples in terms of fibrillar length and width, and there was also no significant difference between this sample group – P₁₁-8 + CS and the control group – P₁₁-8 only. All gels appeared similar in terms of opacity and ability to form self-supporting gels, as shown in **Fig 4.17**.



Fig 4.17: Image of P₁₁-8 + CS gels at 230 mM Na⁺ at both 32:1 (far left), 64:1 (left) molar ratios and 130 mM Na⁺ at both 32:1 (right), 64:1 (far right) molar ratios.

4.2.2.3 P₁₁-8 + P₁₁-8-PEG-Hex-CS

The influence of covalently linking the CS to the P₁₁-8 molecule was then investigated. Different TEM micrographs of P₁₁-8 + P₁₁-8-PEG-Hex-CS hydrogels are shown in **Fig 4.18**, shown for each different concentration and molar ratio.

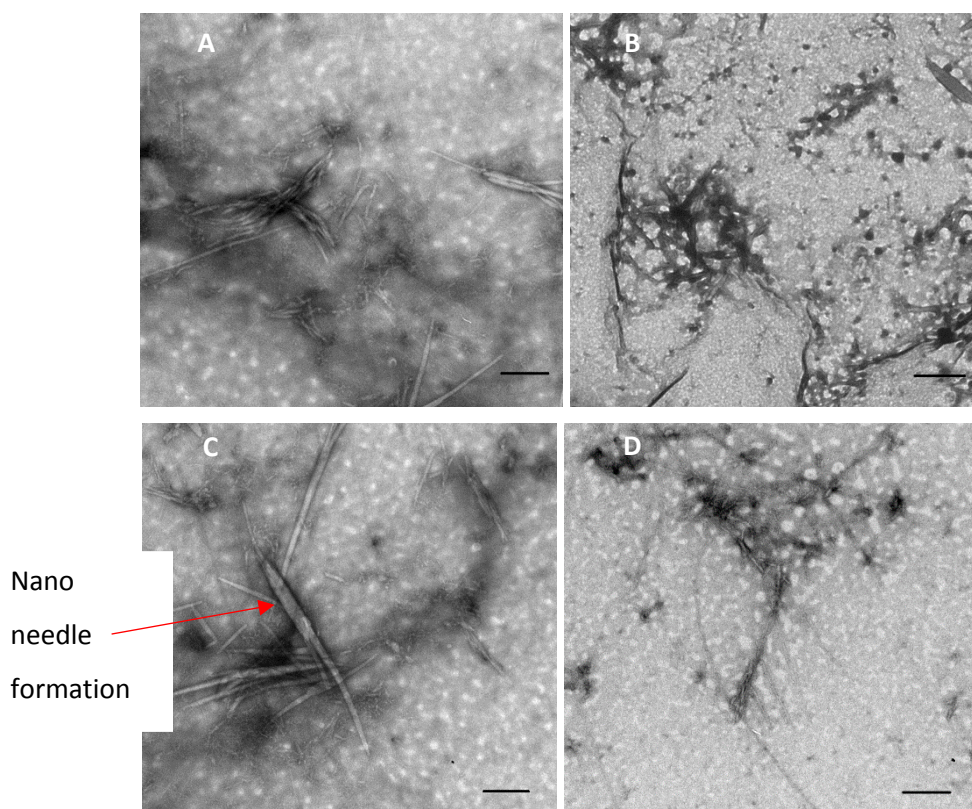


Fig 4.18: TEM images of P₁₁-8 + P₁₁-8-CS (~5.85mM) gels in different ionic strength buffers. A) P₁₁-8 + P₁₁-8-CS 32-1 Ratio 230 mM Na⁺ buffer, 4000x magnification, scale bar - 500nm. B) P₁₁-8 + P₁₁-8-CS 64-1 Ratio 230 mM Na⁺ buffer, 4000x magnification, scale bar - 500nm. C) P₁₁-8 + P₁₁-8-CS 32-1 130 mM Na⁺ buffer, 4000x magnification, scale bar - 500nm. D) P₁₁-8 + P₁₁-8-CS 64-1 130 mM Na⁺ buffer, 4000x magnification, scale bar - 500nm.

Analysis of the fibrillar lengths and widths of the gels at the two respective ionic concentrations (130 mM and 230 mM Na⁺) and two different molar ratios (32:1 and 64:1) revealed the fibrillary lengths and widths shown below in **Table 4.7**.

Sample	Length (nm)	Width (nm)
P ₁₁ -8 + P ₁₁ -8-CS 230 mM Na ⁺ 32:1	642 ± 94	55 ± 8
P ₁₁ -8 + P ₁₁ -8-CS 230 mM Na ⁺ 64:1	633 ± 171	79 ± 19
P ₁₁ -8 + P ₁₁ -8-CS 130 mM Na ⁺ 32:1	690 ± 170	62 ± 13
P ₁₁ -8 + P ₁₁ -8-CS 130 mM Na ⁺ 64:1	653 ± 104	64 ± 12

Table 4.7: The fibrillar lengths and widths for P₁₁-8 + P₁₁-8-CS samples at two different molar ratios and ionic strength buffers (± S.D).

Statistical analysis ($\alpha = 0.95$) showed no significant differences within the sample group, indicating the different self-assembly conditions (CS doping ratio and salt concentration) had no significant effect on the morphology of the fibrils formed when each different condition was compared with one another. Visual analysis of the micrographs showed the presence of

excessive salt as seen in previous sample containing CS. There were indications of other nanostructures, such as nano needles, being formed as well as fibrils. The fibrils were less rigid than observed in the P₁₁₋₄ series of gel samples, but rather than the formation of junction points the fibrils seemed to aggregate through lateral association rather than entwinement. All gels appeared cloudy and opaque in physical appearance and were self-supporting, indicating the formation of nematic gels as shown in **Fig 4.19**.

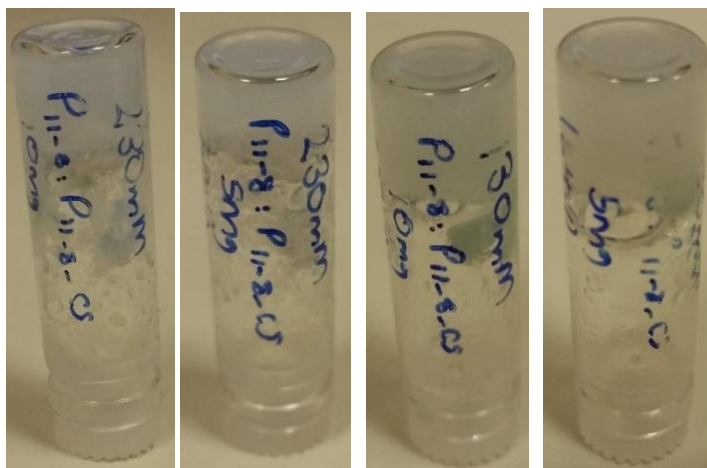


Fig 4.19: Images of P₁₁₋₈ + P₁₁₋₈-CS gels at 230 mM Na⁺ at both 32:1 (far left), 64:1 (left) molar ratios and 130 mM Na⁺ at both 32:1 (right), 64:1 (far right) molar ratios.

The comparison of the different self-assembly conditions and samples is shown below in **Fig 4.20**. This highlights the differences between the fibrillar lengths and widths of the groups and samples.

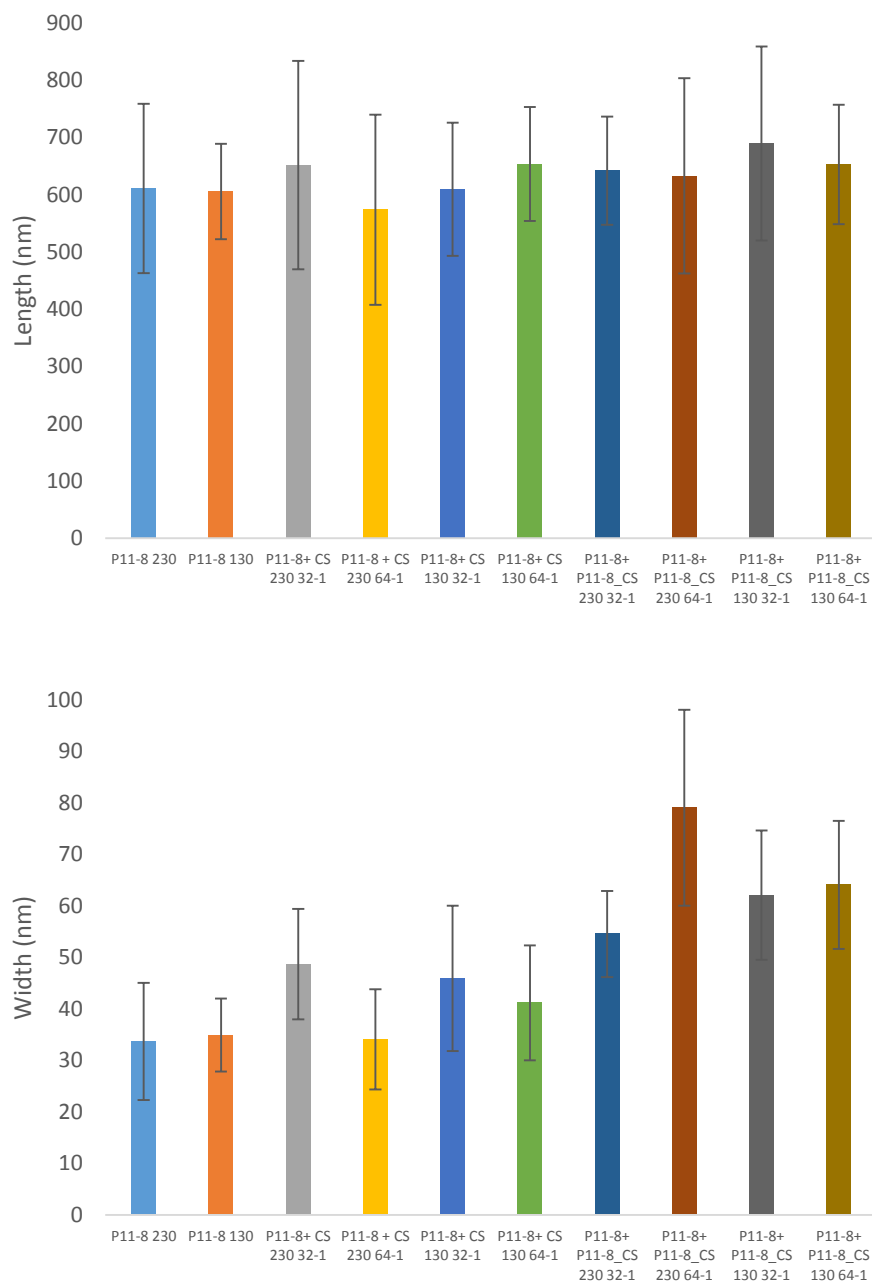


Fig 4.20: Comparison of the different fibrillar lengths and widths for each different P₁₁₋₈ sample. A) Fibrillar lengths of each P₁₁₋₈ sample. B) Fibrillar widths of each P₁₁₋₈ sample. (Error bars = \pm S.D).

The fibrillar length and widths of each group are summarised in **Table 4.8** below, where significant differences are highlighted ($\alpha = 0.95$).

Sample	Length (nm)	Width (nm)
P ₁₁ -4 only 230 mM Na ⁺	513 ± 105	37 ± 9
P ₁₁ -4 only 130 mM Na ⁺	423 ± 171	35 ± 10
P ₁₁ -4+ CS 230 mM Na ⁺ 32:1	694 ± 88	35 ± 7
P ₁₁ -4 + CS 230 mM Na ⁺ 64:1	731 ± 93	37 ± 7
P ₁₁ -4+ CS 130 mM Na ⁺ 32:1	881 ± 178	37 ± 9
P ₁₁ -4+ CS 130 mM Na ⁺ 64:1	739 ± 130	34 ± 8
P ₁₁ -4+ P ₁₁ -4-CS 230 mM Na ⁺ 32:1	1083 ± 109	70 ± 13
P ₁₁ -4+ P ₁₁ -4-CS 230 mM Na ⁺ 64:1	931 ± 65	66 ± 13
P ₁₁ -4+ P ₁₁ -4-CS 130 mM Na ⁺ 32:1	941 ± 134	60 ± 12
P ₁₁ -4+ P ₁₁ -4-CS 130 mM Na ⁺ 64:1	945 ± 137	61 ± 6
P ₁₁ -8 230 mM Na ⁺	611 ± 148	34 ± 11
P ₁₁ -8 130 mM Na ⁺	606 ± 83	35 ± 7
P ₁₁ -8 + CS 230 mM Na ⁺ 32:1	652 ± 182	49 ± 11
P ₁₁ -8 + CS 230 mM Na ⁺ 64:1	574 ± 166	34 ± 10
P ₁₁ -8 + CS 130 mM Na ⁺ 32:1	610 ± 116	46 ± 14
P ₁₁ -8 + CS 130 mM Na ⁺ 64:1	654 ± 100	41 ± 11
P ₁₁ -8 + P ₁₁ -8-CS 230 mM Na ⁺ 32:1	642 ± 94	55 ± 8
P ₁₁ -8 + P ₁₁ -8-CS 230 mM Na ⁺ 64:1	633 ± 171	79 ± 19
P ₁₁ -8 + P ₁₁ -8-CS 130 mM Na ⁺ 32:1	690 ± 170	62 ± 13
P ₁₁ -8 + P ₁₁ -8-CS 130 mM Na ⁺ 64:1	653 ± 104	64 ± 12

Table 4.8: Summary of the different fibrillar lengths and widths (nm) for each different peptide sample from both the P₁₁-4 and P₁₁-8 series (± S.D).

4.2.3 Mechanical properties of P₁₁₋₄ gels at different ionic concentrations

The mechanical properties of the gels was measured using rheology in terms of G' (elastic modulus) and G'' (viscous modulus) through firstly measuring and identifying the linear viscoelastic region (LVER) of the sample by carrying out a strain-controlled amplitude sweep from 0-100% shear strain at two different frequencies – 1Hz and 20Hz. The LVER strain rate was then used to carry out a strain controlled frequency sweep from 1-20Hz to measure the G' and G'' of each sample.

An illustrated example using P₁₁₋₄ only 230 mM Na⁺ is shown in **Fig 4.21** which illustrates the analysis of the amplitude sweep data in order to choose the LVER region and how the region was similar at both 1 Hz and 20 Hz.

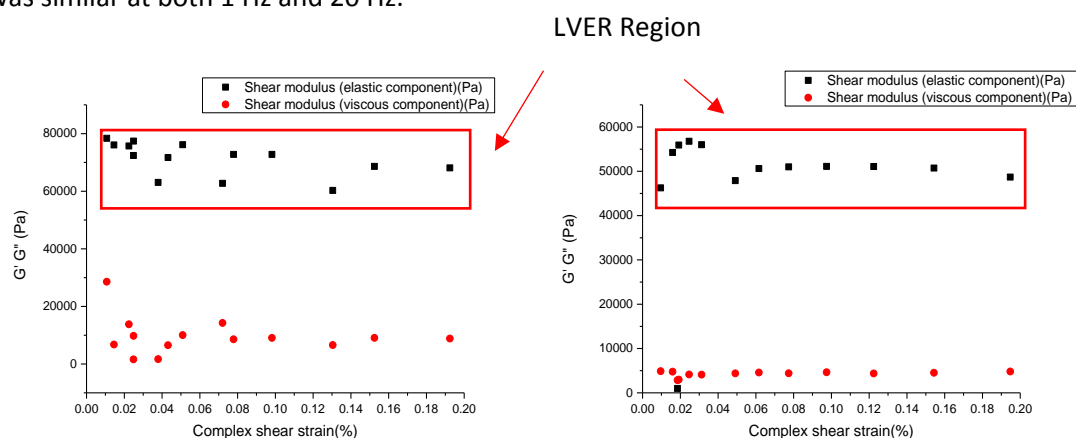


Fig 4.21: An example illustrating the LVER region from two amplitude sweeps: 1 Hz (left) and 20 Hz (right), where the plateau region is apparent.

The two graphs above: 1 Hz (left) and 20 Hz (right) amplitude sweeps were carried out to identify the LVER as mentioned above. This is the region where the gel behaves as both a viscous and elastic substance but the two components can be separated sufficiently to measure the individual moduli. The LVER region is identifiable by a region when in a stress-controlled experiment the sample exhibits a resistance to strain, or a plateau region is observed, up to a certain limit. Once this limit has been reached, either the viscous or elastic component becomes more dominant upon which the plateau region is no longer observed due to the strain response becoming non-linear.

In this sample, the LVER region has been highlighted to reside between 0-0.2% shear strains, so 0.15% shear strain was selected at which to carry out a frequency sweep to measure the viscoelastic properties or G' and G'' as mentioned above, of the sample. The frequency sweep between 1-20 Hz is shown below for P₁₁₋₄ only 230 mM Na⁺ in **Fig 4.22**, where the shear strain was controlled at 0.15%.

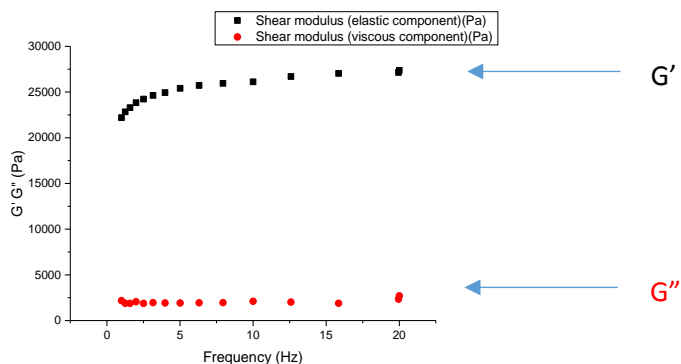


Fig 4.22: An example of which value indicates the G' and G'' moduli, which are obtained from the frequency sweeps at the selected strain chosen from the amplitude sweeps for the LVER region of the sample.

The relatively linear response to the change in frequency indicated that the LVER region was selected correctly due to the equal response in both the G' and G'' moduli and no crossover of these moduli indicating again the LVER was correctly selected. The G' and G'' moduli values can be taken directly from the graph, which were $G' - 25.2 \pm 7.3$ kPa, $G'' - 2.0 \pm 0.7$ kPa.

The rheological analysis was performed for each combination of peptide, CS additive and salt concentration discussed above (**Table 4.1**) For each sample the corresponding shear strain regions were different and the selected shear strain for the frequency sweeps were different. The various parameters and results are summarised in **Table 4.9** below. Raw data is available in Appendix 3.

Sample	LVER Region (%)	Shear Strain (%)	G' (kPa)	G'' (kPa)
P ₁₁ -4 only 230 mM Na ⁺	0 – 0.2	0.15	25.2 ± 7.3	2.0 ± 0.7
P ₁₁ -4 only 130 mM Na ⁺	0 - 0.2	0.15	15.4 ± 3.1	1.4 ± 0.3
P ₁₁ -4 + CS 32:1 230 mM Na ⁺	0.05 - 0.2	0.15	19.2 ± 0.6	1.8 ± 0.2
P ₁₁ -4 + CS 64:1 230 mM Na ⁺	0.05 - 0.1	0.08	7.3 ± 1.8	0.9 ± 0.2
P ₁₁ -4 + CS 32:1 130 mM Na ⁺	0.05 - 0.3	0.25	11.6 ± 6.3	1.8 ± 0.9
P ₁₁ -4 + CS 64:1 130 mM Na ⁺	0.05 - 0.2	0.15	5.9 ± 3.8	0.7 ± 0.3
P ₁₁ -4 + P ₁₁ -4-CS 32:1 230 mM Na ⁺	0.05 - 0.3	0.23	234.8 ± 12.6	25.9 ± 3.0
P ₁₁ -4 + P ₁₁ -4-CS 64:1 230 mM Na ⁺	0.05 - 0.3	0.23	63.1 ± 34.3	7.6 ± 3.9
P ₁₁ -4 + P ₁₁ -4-CS 32:1 130 mM Na ⁺	0.05 - 0.3	0.27	277.5 ± 8.1	36.1 ± 3.2
P ₁₁ -4 + P ₁₁ -4-CS 64:1 130 mM Na ⁺	0.05 - 0.2	0.15	95.0 ± 6.8	12.2 ± 0.8

Table 4.9: Summary of the G' and G'' values of the P₁₁-4 series of hydrogels, along with the parameters used to obtain the values from the frequency sweep.

4.2.3.4 P₁₁-4 series comparison

A comparison of the G' and G'' values obtained for each sample indicated a significant increase in gel strength when the CS was introduced by covalent conjugation to the peptide, with the results shown in **Fig 4.23** below.

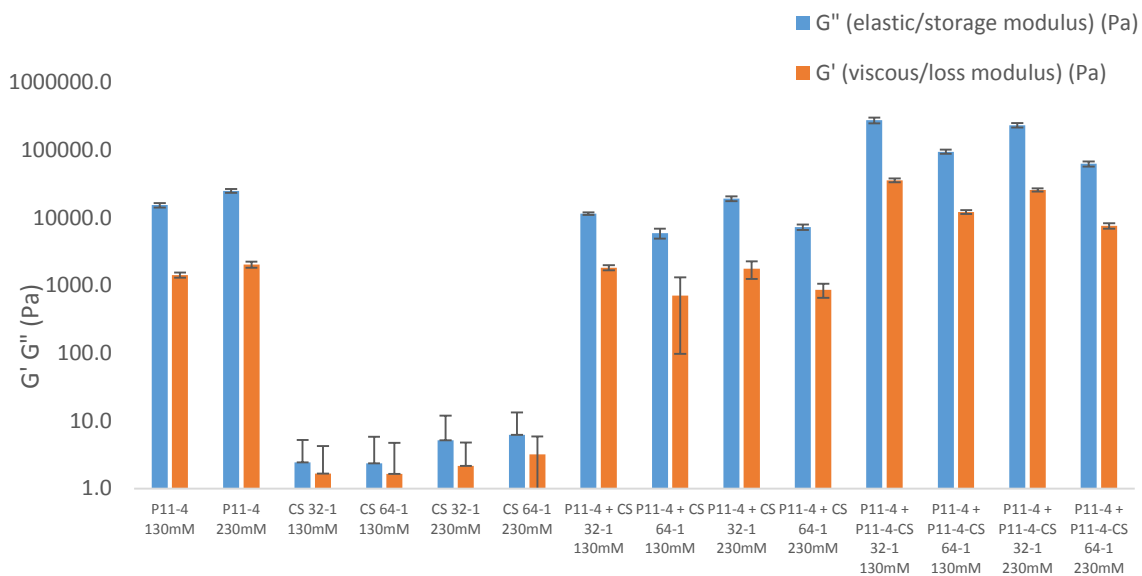


Fig 4.23: A comparison of the G' and G'' values for each of the P₁₁₋₄ samples, with the moduli axis in a log scale to show the relative magnitudes.

4.2.4 Mechanical properties of P₁₁₋₈ gels at different ionic concentrations

The physical mechanical properties of the P₁₁₋₈ gels were tested in the same manner as the P₁₁₋₄ gels were. The different parameters and results are summarised in **Table 4.10** below.

Sample	LVER Region (%)	Shear Strain (%)	G' (Pa)	G'' (Pa)
P ₁₁ -8 only 230 mM Na ⁺	0.05 – 0.2	0.15	100.4 ± 7.4	9.4 ± 1.0
P ₁₁ -8 only 130 mM Na ⁺	0.05 – 0.2	0.1	100.1 ± 7.7	10.1 ± 0.8
P ₁₁ -8 + CS 32:1 230 mM Na ⁺	0.05 – 0.35	0.3	20.4 ± 1.0	2.2 ± 0.2
P ₁₁ -8 + CS 64:1 230 mM Na ⁺	0.05 – 0.35	0.3	15.2 ± 1.3	1.8 ± 0.1
P ₁₁ -8 + CS 32:1 130 mM Na ⁺	0.05 – 0.35	0.3	30.4 ± 2.2	3.6 ± 0.3
P ₁₁ -8 + CS 64:1 130 mM Na ⁺	0.05 – 0.35	0.3	15.9 ± 0.9	1.6 ± 0.1
P ₁₁ -8 + P ₁₁ -8-CS 32:1 230 mM Na ⁺	0.05 – 0.25	0.22	153.7 ± 15.4	21.9 ± 1.0
P ₁₁ -8 + P ₁₁ -8-CS 64:1 230 mM Na ⁺	0.05 – 0.3	0.25	140.8 ± 9.5	16.3 ± 1.9
P ₁₁ -8 + P ₁₁ -8-CS 32:1 130 mM Na ⁺	0.05 – 0.3	0.24	54.2 ± 4.1	5.7 ± 0.4
P ₁₁ -8+ P ₁₁ -8-CS 64:1 130 mM Na ⁺	0.05 – 0.3	0.24	43.7 ± 4.7	5.4 ± 0.9

Table 4.10: Summary of the G' and G'' values of the P₁₁-8 series of hydrogels at 10 mg ml⁻¹, along with the parameters used to obtain the values from the frequency sweep.

4.2.4.4 P₁₁-8 series comparison

A comparison of the different samples in the P₁₁-8 series showed a significant decrease in gel strength when the CS was introduced through the non-covalent manner, and no significant change when introduced in the covalent manner, where the results are shown below in **Fig 4.24** below.

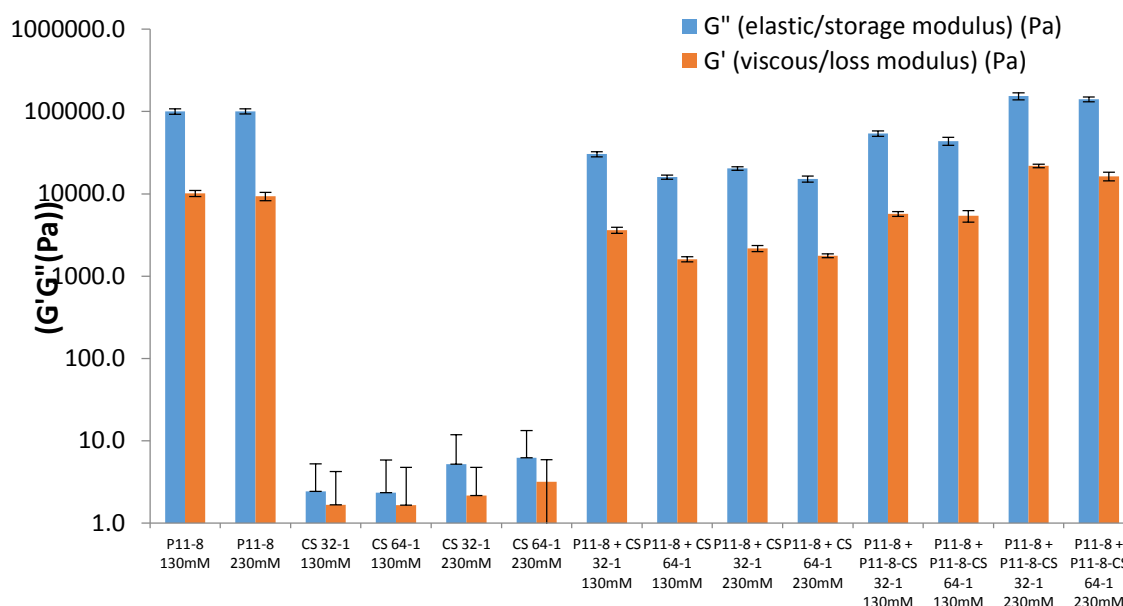


Fig 4.24: A comparison of the G' and G'' values for each of the P₁₁-8 samples, with the moduli axis (y-axis) in a log scale to show the relative magnitudes.

4.2.5 P₁₁-4 Series at an increased concentration (30 mg ml⁻¹ or ~18mM)

The results reported above were at a peptide concentration of ~5.8mM or 10 mg ml⁻¹, which was just above the concentration reported by the Aggeli group at which P₁₁-4 formed a self-supporting nematic gel ~4mM. At the lower end of this region of macroscopic states, subtle changes in environment or conditions could cause phase separation to occur overtime which was not desirable for the application of the project so the mechanical properties at the higher end of the concentration region was also explored by using 30 mg ml⁻¹ ~ 18mM peptides. The results from increasing the peptide concentration from ~6 -18 mM is illustrated below in **Table 4.11**.

Sample	LVER Region (%)	Shear Strain (%)	G' (Pa)	G'' (Pa)
P ₁₁ -4 only 130 mM Na ⁺ (30 mg ml ⁻¹)	0.05 - 3	0.27	143.5 ± 21.9	20.6 ± 2.9
P ₁₁ -4 + CS 32:1 130 mM Na ⁺ (30 mg ml ⁻¹)	0.05 – 0.3	0.28	207.0 ± 13.7	20.2 ± 2.2
P ₁₁ -4 + P ₁₁ -4-CS 32:1 130 mM Na ⁺ (30 mg ml ⁻¹)	0.05 – 0.35	0.31	434.6 ± 51.3	58.7 ± 10.2

Table 4.11: Summary of the G' and G'' values of the P₁₁-4 series of hydrogels at 30 mg ml⁻¹, along with the parameters used to obtain the values from the frequency sweep.

4.2.5.4 P₁₁₋₄ series comparison including 30 mg ml⁻¹ samples

The increased peptide content samples were included in the previous comparative graph for the G' and G'' values where a significant increase across all three "groups" was observed compared to the relative 10 mg ml⁻¹ samples in each group. The pattern though, was that the introduction of CS into the P₁₁₋₄ system showed a significant increase each time, where the non-covalent introduction of CS gave a gel that was significantly stronger than just P₁₁₋₄ only at 30 mg ml⁻¹ and the covalent introduction of CS gave even further significant increase in gel strength. The results of the comparison are shown below in Fig 4.25.

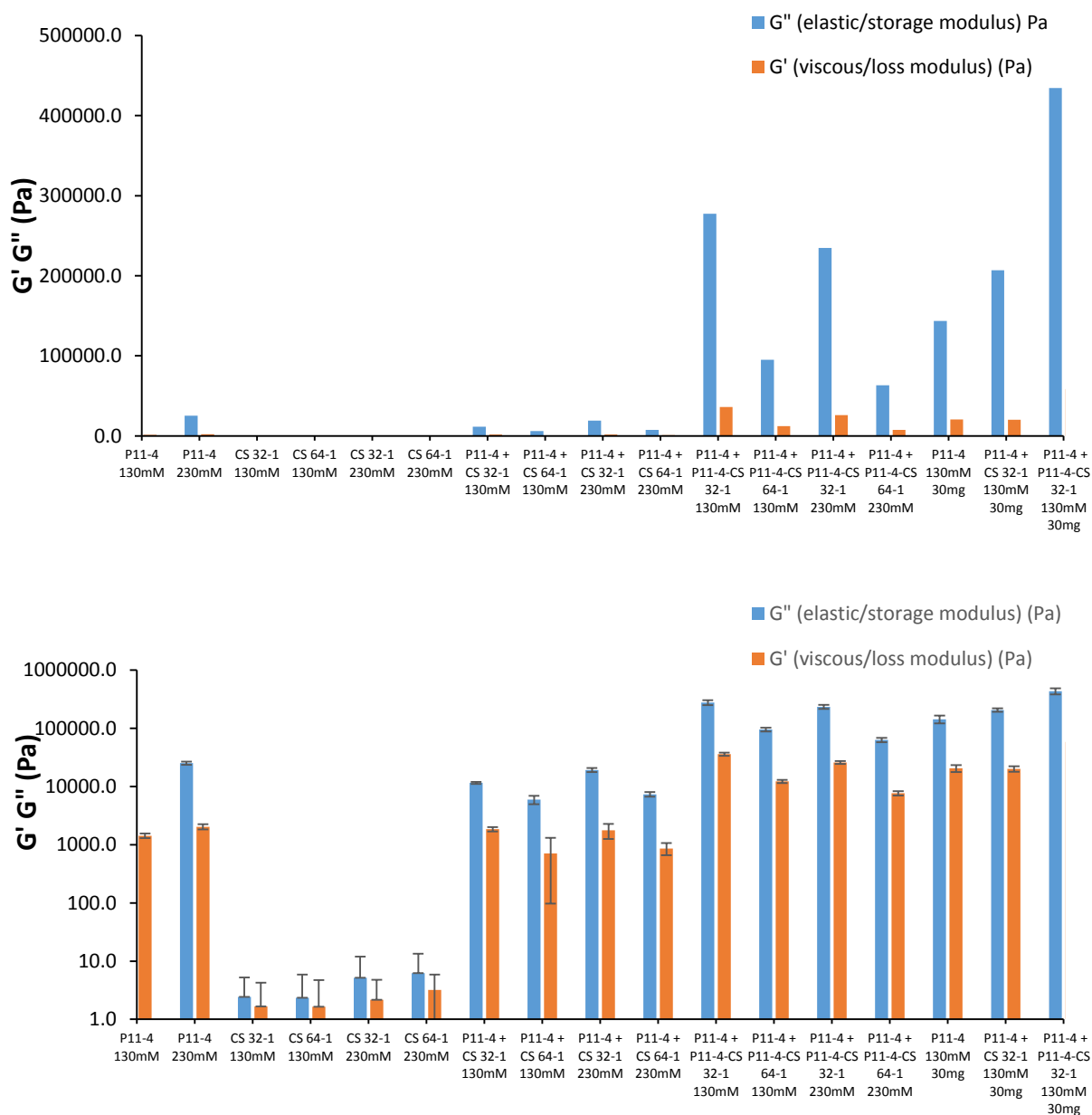


Fig 4.25: A comparison of the G' and G'' values for each of the P₁₁₋₄ samples including the 30 mg ml⁻¹ samples, A) the moduli axis in a numerical scale, B) with the moduli axis in a log scale to show the relative magnitudes.

4.2.6 P₁₁-8 Series at an increased concentration (30 mg ml⁻¹ or ~18mM)

Similarly, the P₁₁-8 series was investigated at the 30 mg ml⁻¹ concentration regime to investigate whether the increased peptide content altered the mechanical properties of the subsequent gels. Again, these results are summarised and reported in **Table 4.12** below.

Sample	LVER Region (%)	Shear Strain (%)	G' (Pa)	G'' (Pa)
P ₁₁ -8 only 130 mM Na ⁺ (30 mg ml ⁻¹)	0.05 - 35	0.3	205.1 ± 14.6	23.3 ± 1.1
P ₁₁ -8 + CS 32:1 130 mM Na ⁺ (30 mg ml ⁻¹)	0.05 – 0.4	0.35	207.8 ± 19.9	31.5 ± 2.3
P ₁₁ -8 + P ₁₁ -8-CS 32:1 130 mM Na ⁺ (30 mg ml ⁻¹)	0.05 – 0.35	0.3	101.6 ± 8.5	13.5 ± 0.9

Table 4.12: Summary of the G' and G'' values of the P₁₁-8 series of hydrogels at 30 mg ml⁻¹, along with the parameters used to obtain the values from the frequency sweep.

4.2.6.4 P₁₁-8 series comparison including 30 mg ml⁻¹ samples

The increased peptide content samples were included with the previous data for the G' and G'' values where a significant increase across all three “groups” was observed compared to the relative 10 mg ml⁻¹ samples in each group. However, compared to the P₁₁-4 series, there was no pattern in terms of changing gel strengths. The peptide only and non-covalent CS introduction samples were not significantly different, and the covalent introduction of CS showed a significant decrease compared to the peptide only sample (**Fig 4.26**).

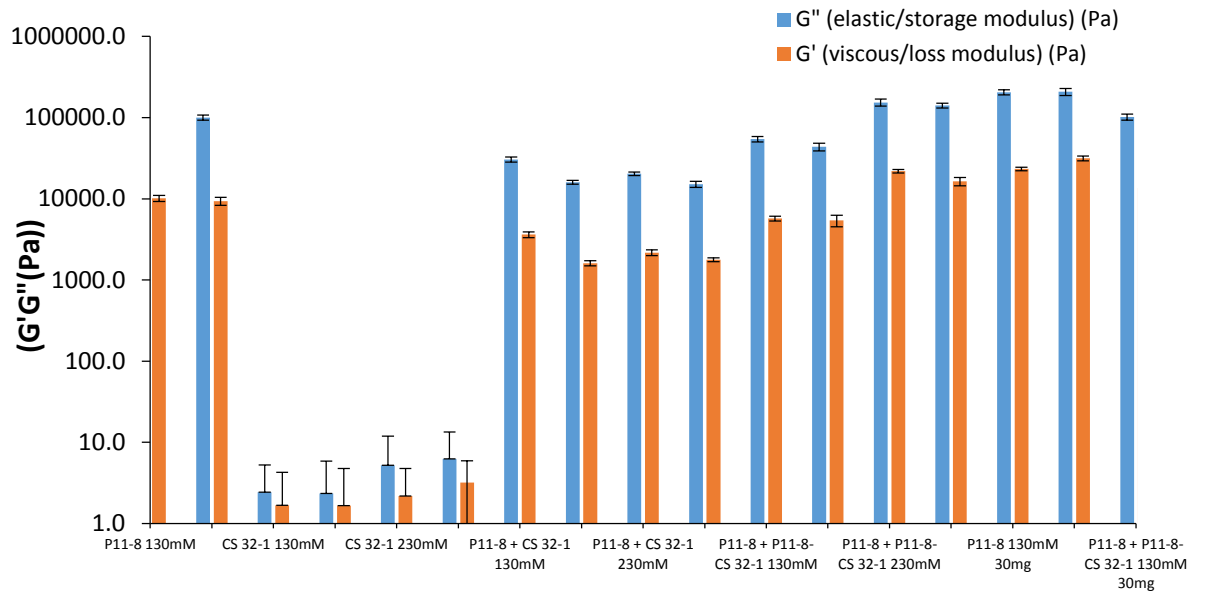
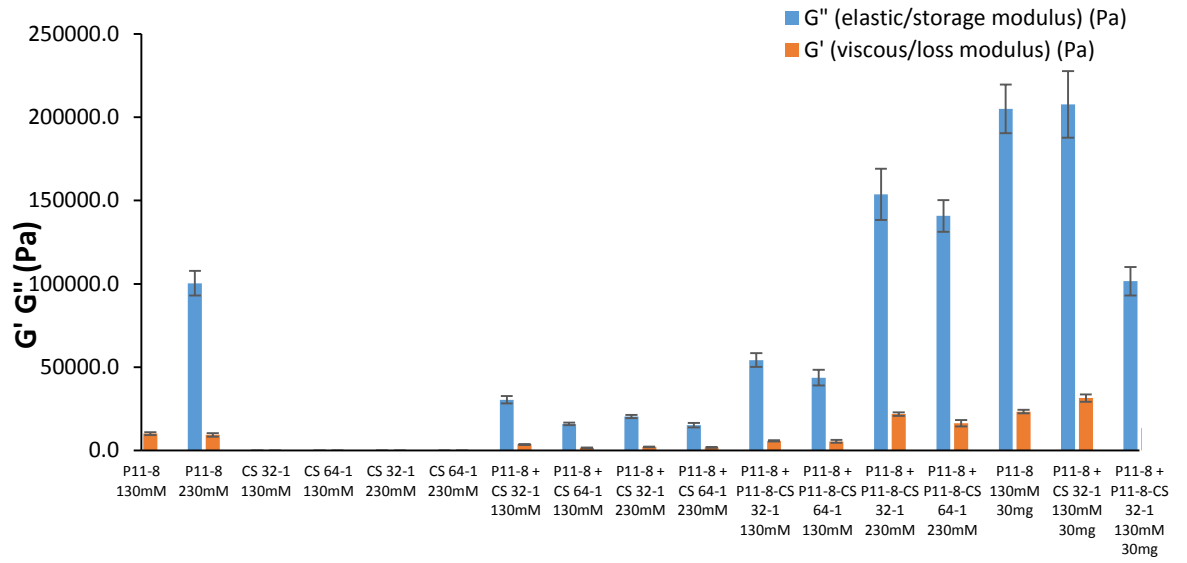


Fig 4.26: A comparison of the G' and G'' values for each of the P_{11-8} samples including the 30 mg ml⁻¹ samples, A) the moduli axis in a numerical scale, B) with the moduli axis in a log scale to show the relative magnitudes.

4.3 Discussion and Conclusion

4.3.1 Morphologies of different P₁₁₋₄ gels at different ionic concentrations

Analysis of the different morphologies of the P₁₁₋₄ series of gels produced under different conditions gave interesting results. The fibrillary widths and lengths of P₁₁₋₄ in the two different buffer strengths showed no significant difference but compared to the fibrils produced in the presence of CS the fibrils were small, up to ~ 50% smaller when compared to the conjugate doped samples (P₁₁₋₄: P₁₁₋₄-CS). When CS was introduced into the system, firstly in a non-covalent, suspension manner (P₁₁₋₄ + CS) and secondly the covalently bound conjugate manner (P₁₁₋₄: P₁₁₋₄-CS), a trend was observed in terms of fibrillar length and width. The introduction *via* in a non-covalent fashion caused the formation of longer fibrils when compared to the P₁₁₋₄ only controls but the fibrillary widths were not significantly different, indicating the presence of CS in the system promoted self-assembly through the formation of longer tape and in turn ribbon structures rather than the formation of fibres. This hypothesis was based on the mechanism of 1-D hierarchical self-assembly, where the fibrillary length is dependent on ribbon length whilst fibrillary width is dependent on the inter-ribbon spacing. The presence of a polyanionic species, such as CS, is probably acting as a template along which the β -strands can align through electrostatic and non-covalent interactions which could be lowering the ϵ_{tape} energy as represented in **Eq 1**.

$$\text{(Eq 1)} \quad \epsilon_{\text{tape}} = \epsilon_c k_B T + \epsilon_\beta k_B T$$

Eq 1: The equation for the energetics behind tape formation, where $\epsilon_c k_B T$ represents the tape scission energy and $\epsilon_\beta k_B T$ represents the β -sheet tape formation energy, at $k_B T$.

The large, undefined lengths of the CS molecules could allow simultaneous promotion of the formation of multiple tapes which are then stabilised during ribbon formation through non-covalent and coulombic interactions by the CS molecules as well. This promotion of tape formation would cause the lengthening of the tapes, hence eventually through 1-D hierarchical self-assembly the lengthening of the fibrils (PNAS, Aggeli, 2001) (Nyrkova, Eur Phys J B, 2000). The introduction of CS *via* the covalently bound method caused the formation of longer and thicker fibrils when compared to both the P₁₁₋₄ only controls and the non-covalent group (P₁₁₋₄ + CS). The fibrils were nearly twice as long and thick as the peptide only controls while 20% longer and 200% thicker as the non-covalent group samples. These data indicated that the permanent incorporation of the CS molecules into the fibrillar network through the triazole linker, had a stabilising effect on the self-assembly. There was probably a negative repulsive effect of incorporating the CS into the fibrillar structure which may have resulted from the

similar net charges on both the CS and P₁₁-4 molecules. The repulsive forces between the two molecules probably lead to a greater inter-ribbon spacing distance but the net positive effect of the dense negative charge of the sulfate groups on each CS molecule drew counter-ions such as Na⁺ and Ca²⁺ present in the buffer. These counter-ions screened the negative charge of the sulfate groups through coulombic interactions which led to minimising excessive repulsion between CS – P₁₁-4 and P₁₁-4 – P₁₁-4 molecules. The net effect of this screening could be thicker fibrils through the greater inter-ribbon spacing occurring but no detriment to the ability to form fibrils, in conjunction with the templated promotion of tape formation as hypothesized above could explain the thicker and longer fibrils observed in the conjugate doped system samples (Aggeli et al., 2001, Carrick, 2007a, Nyrkova et al., 2000).

The presence of GAGs – including CS has been previously reported by various researchers investigating amyloid studies to promote fibril formation (Cai et al., 1993, Citron et al., 1994, Fraser et al., 1992, Hilbich et al., 1991, Jarrett et al., 1993, Jarrett and Lansbury, 1993, Lomakin et al., 1996, McLaurin and Chakrabartty, 1996, McLaurin et al., 1998, McLaurin et al., 1999, Terzi et al., 1995). The P₁₁-X family of peptide are classed as “amyloid like” due to the cross β structure of the fibril and so similar effects could well occur in this synthetic system. McLaurin *et al* reported that in the presence of CS, the amyloid peptide A β 40 formed fibrils which showed lateral aggregation but in the absence of CS no aggregation was observed beyond forming short thin fibrils. This was reinforced by the observation that a similar peptide - A β 42, the elongated version of A β 40, showed fibril thickening in the presence of GAGs (Castillo et al., 1999, McLaurin et al., 1999). McLaurin *et al* hypothesised that the GAGs act as a scaffold for fibril formation through enhancing β -sheet conformer formation and stabilising fibrils through lateral association in the latter stages of self-assembly. Furthermore, the group also reported that the presence of sulfate groups may be involved with promoting fibril formation by observing decreased fibril formation in the presence on desulfated GAGs (Castillo *et al.*, 1999, McLaurin *et al.*, 1999). Further evidence to support the hypothesis of CS promoting fibril formation in the P₁₁-4 system was the observation by McLaurin *et al* that CS was the most effective GAG at promoting nucleation and lateral association of A β fibrils which they theorise may be due to CS having sulfate groups on only one face and having the ideal distribution of sulfate groups to promote fibril formation (McLaurin et al., 1999).

4.3.2 Morphologies of different P₁₁-8 gels at different ionic concentrations

In comparison to P₁₁-4, no similar trend was observed in the P₁₁-8 series in terms of the sequential growth of the fibrils through the differing introduction of CS into the system. All three groups: - P₁₁-8 only controls, non-covalent samples – P₁₁-8 + CS and covalently bound samples –

P₁₁₋₈ + P₁₁₋₈-CS, showed no significant difference in terms of fibrillar length and width as observed with the P₁₁₋₄ series. This could be possibly due to the opposite net charges between the polyanionic CS and the net positive charged P₁₁₋₈ peptide, resulting in an electrostatic attraction which may not promote and/or stabilise further self-assembly from β -strands to tapes. There is obviously no detrimental effect on self-assembly as the lengths and widths are not significantly different in the presence of CS.

4.3.3 Mechanical properties of different P₁₁₋₄ gels at different ionic concentrations

The measured mechanical properties of the P₁₁₋₄ gels as obtained through rheological experiments correlated well with the dimensional analysis of TEM micrographs. The presence of CS within P₁₁₋₄ samples in simply a non-covalent suspension manner had no significant effect on the G' and G'' of the samples compared to the peptide only samples indicating the CS did not cause any significant increase in gel strength. There was no significant difference in regards to the ratio of G'' to G' again indicating the composition of the different gels (in terms of being more solid or liquid like) are not significantly different. These data indicate that while the presence of CS in the system caused the formation of longer fibrils, this did not translate into an effect on gel strength and composition.

When compared to the covalently conjugated samples, there was a significant change in gel strength. The G'' and G' measurements for each of the covalent samples were significantly higher than any of the other samples. This indicated the covalent gels were significantly stronger, although the ratio of G'' to G' was similar to the P₁₁₋₄ only and P₁₁₋₄ + CS samples and hence the composition of the covalent gels were comparable in terms of solid and liquid like behaviour. These comparable properties indicate the only possible explanation for the higher G'' and G' values was due to the effect of the covalently introducing CS into the fibrillar network. This observation was backed up from the TEM analysis where longer, thicker fibrils were observed in the covalently incorporated CS gels. The increased dimensions signified the formation of stronger networks. CS only controls demonstrated that with the lack of the self-assembling peptide network, a CS solution at either molar ratio or buffer concentration behaved like a pure liquid with very low G'' and G' values but the ratio of G'' to G' was far smaller again reinforcing the liquid like behaviour observed.

4.3.4 Mechanical properties of different P₁₁₋₈ gels at different ionic concentrations

Similarly, in the P₁₁₋₈ series, covalently incorporating CS into the fibrillar network gave rise to greater G'' and G' values but significant difference between peptide only and P₁₁₋₈-CS were only observed when the 230 mM Na⁺ buffer was used to make up the gel samples. The hypothesis

for this was the increased sodium content screened the electrostatic interaction between the negatively charged CS and positively charged P₁₁₋₈. This was the opposite behaviour to that observed with the P₁₁₋₄ series where the increased ionic strength of the buffer probably screened the electrostatic repulsion between the like charged CS and P₁₁₋₄ molecules. Unlike the P₁₁₋₄ series, where every covalent system sample showed significant difference to the peptide only control group, only the covalent samples with 230 mM Na⁺ buffer showed significant difference, indicating the introduction of the CS covalently into the fibrillar network maybe not as favourable with the oppositely charged species of P₁₁₋₈ and CS which could be due to the longer range of electrostatic attraction compared to the shorter range of electrostatic repulsion which could have led to greater disruption of the fibrillar network.

4.3.5 Mechanical properties of different P₁₁₋₄ gels at different ionic concentrations at 30 mg ml⁻¹

The increased peptide content caused an increase in the measured G' and G'' values for P₁₁₋₄ only samples, causing an increase by nearly an order of magnitude – 9.2x. This observed increase in gel strength is explained by previously reported data on P₁₁₋₄ by the Aggeli group, where due to the concentration dependent mechanism of self-assembly, the increased peptide content causes the formation of thicker fibrils/fibres which promotes the gel to become more “solid-like” thus having increased elastic and viscous moduli. Interestingly, unlike in the 10 mg ml⁻¹ regime, the presence of CS caused an even greater increase in gel strength – a further 1.4x. This observation further reinforces the hypothesis that the CS acts and stabilises fibril nucleation and growth as observed with amyloid fibrils. But the most interesting observation, was the further enhancement of gel strength of the covalent P₁₁₋₄: P₁₁₋₄-CS samples when in the 30 mg ml⁻¹ regime. At 10 mg ml⁻¹, the measured G' and G'' values were already larger than any measured value indicating these were the strongest gels but at 30 mg ml⁻¹ the gels are even stronger with a further 2.1x increase on the P₁₁₋₄ + CS sample mentioned above, or a 1.8x increase on the 10 mg ml⁻¹ covalent sample.

These measured gel moduli have never been reported for a reversible system incorporating biopolymeric materials, and are higher than some reported permanently cross-linked synthetic polymeric materials such as acrylamide or poly-vinyl alcohol (PVA) where Oyen (Oyen, 2014) and Pal *et al.* (Pal *et al.*, 2009) reported dynamic moduli were in the order of 10⁴ Pa (Pal *et al.*, 2009). Biopolymer hydrogels such as agrose and gelatin hydrogels were investigated by Zuidema *et al.*, where the dynamic moduli reported there were in the order of 10³ Pa (Zuidema *et al.*, 2014). The reported dynamic moduli for the covalent peptide: peptide-CS gels are 1-2 orders of magnitude larger than these covalently cross-linked hydrogels indicating the incorporation of

the CS permanently into the fibrillar network has a significant stabilising effect on the hydrogel structure.

4.3.6 Mechanical properties of different P₁₁-8 gels at different ionic concentrations at 30 mg ml⁻¹

When the P₁₁-8 samples were increased to 30 mg ml⁻¹, there was a significant increase in dynamic moduli between the P₁₁-8 only at 10 mg ml⁻¹ and 30 mg ml⁻¹. This again matches previously reported data by the Aggeli group, where increasing the peptide content, the fibrillar structure becomes more rigid and thicker thus increasing the gel strength. The influence of doping the gel with CS showed an increase in dynamic moduli but it was not a significant increase, but the influence of doping the gel with the covalently bound CS-peptide conjugate did show a significant effect, but the opposite to that observed for P₁₁-4, the dynamic moduli decreased to a similar value measured for the base P₁₁-8 only gels at 10 mg ml⁻¹.

4.3.7 Conclusion

The effect of introducing CS into two different peptide systems in two different fashions showed stark differences. In the similarly charged system of P₁₁-4 and CS at 10 mg ml⁻¹ or ~ 6mM, introducing the CS non-covalently resulted in a significant change in the fibrillar length but no significant change in fibrillar width compared to the peptide only samples and the gels showed no significant change in dynamic moduli at any molar ratio or buffer strength. However, when CS was incorporated by using a covalently linked peptide-CS conjugate, a significant change in both fibrillar length and width was observed alongside large changes in the dynamic moduli of the hydrogels which increased significantly across all molar ratios and buffer strengths. When the peptide content was increased to 30 mg ml⁻¹, a significant increase of dynamic moduli was observed for the base peptide only, whilst introducing the CS in non-covalently at this concentration gave a significant increase in dynamic moduli compared to the peptide alone, again, the covalent manner of introduction gave further significant increases above every other measured gel yield a hydrogel with an elastic modulus measured at 0.48MPa.

In the oppositely charged system of P₁₁-8 and CS at 10 mg ml⁻¹ or ~ 6mM, introducing the CS in both the non-covalent and covalently bound manner resulted in no significant change in either the fibrillar length or width and it caused a significant decrease in the dynamic moduli indicating a destabilising effect on the fibrillar network. In comparison, the covalently introduced CS manner caused a significant increase in dynamic moduli in the 230 mM Na⁺ buffer samples for both molar ratios indicating the increased sodium content screened and overcame the destabilising effect of the opposite charges of the P₁₁-8 and CS, probably caused by electrostatic

attraction. When the peptide content was increased to 30 mg ml^{-1} , significant increases in dynamic moduli for the P₁₁-8 only and non-covalent P₁₁-8 + CS samples were observed but for the covalent sample a significant decrease occurred compared to the other 30 mg ml^{-1} samples. This indicated the increase P₁₁-8 content had some stabilising effect on the gel but it was countered by the increased P₁₁-8-CS conjugate to some degree.

Chapter 5

Assessment of functionalised self-assembling peptides in a GAG depleted cartilage model

Following the characterisation of the self-assembling peptide gels, their ability to restore the resistance to deformation properties of an early stage GAG depleted osteoarthritic cartilage model was investigated through qualitative and quantitative measurement of the resistance to deformation properties of both native and GAG depleted tissue through indentation and material testing, while confirmation of self-assembly within the tissue was achieved through the use of confocal microscopy.

5.1 Introduction

5.1.1 Osteoarthritic cartilage models

5.1.1.1 Choice of animal model

Within the field of tissue engineering and regenerative medicine, it is necessary to have models of tissue exhibiting the biomechanics and biology of the affected tissue being investigated. In research directed towards understanding and developing treatments for osteoarthritis there is a requirement for various models, depending on the hypothesis being evaluated and in which to test treatments *in vitro* and *in vivo*. Various animals have been used for *in vivo* testing and their (osteo)chondral tissues used *in vitro*. Commonly murine, laprine, and canine models are used, but when the experiment requires testing intervention under appropriate physiological loads, i.e. loads suitable for human anatomy, larger species are employed and ovine, porcine, caprine, bovine and equine as well human tissue are usually employed (Ahern et al., 2009, Fermor et al., 2015a, Fermor et al., 2015b, Wayne et al., 1998).

The rationale for the use of larger species of animal for physiological loading is mainly due to the thickness of the cartilage, the maximum load capacity of the skeletal structure, abundance of the tissue and the ethical considerations behind using the species. When live animal models are required other factors come into play, such as cost of housing, feeding and medical care for the subjects. In this chapter only *in vitro* animal tissue models will be employed. The pros and cons of the animal tissue used *in vitro* is summarised in **Table 5.1** below.

Species	Pros	Cons
Ovine	Large availability and low cost of sourcing tissue	Variability in cartilage thickness makes modelling difficult. Slow rate of skeletal maturation
Porcine	Large availability and low cost of sourcing tissue. Similar anatomy of the knee joint to the human knee	Slightly thinner cartilage than human cartilage
Bovine	Large availability and low cost of sourcing tissue	Different collagen orientation within cartilage compared to human cartilage. Significantly thinner cartilage layer

Table 5.1: Pros and cons of tissue types commonly used in *in vitro* testing. The pros and cons of each different tissue is summarised in terms of practicality and cost effectiveness.

The three larger animal species (bovine, porcine, ovine, caprine) each have their benefits depending on the intended design of the *in vitro* experiment. Sheep is a commonly used species for cartilage animal models due to the availability and low cost of sourcing tissue. The disadvantage of this tissue is the variability in cartilage thickness which often has grade III/IV (ICRS) lesions extending into the subchondral bone. The rate of skeletal maturity is relatively slow which in conjunction to the other disadvantages causes some limitations when the tissue is used as a model. The goat is another commonly used species for cartilage models which is similar in terms of cost and availability and has a less variable cartilage thickness which makes it suitable for small defect modelling. Pigs are not as commonly used as sheep and goats but due to having a larger thickness of cartilage, porcine tissue can be utilized for large to full thickness defect research due to having a similar defect composition to that observed in human tissue in terms of proportions of damage to the cartilage and subchondral layers respectively. A larger proportion of damage is observed in the subchondral region in sheep and goat tissue. Cows are also used for cartilage models due to having a similar availability as to the others and show a similar cartilage thickness as porcine tissue (Ahern et al., 2009, Fermor et al., 2015b, Fermor et al., 2015a).

Whilst the thicknesses of porcine and bovine tissue most closely match that of human tissue, Rieppo *et al* reported huge differences between the cartilage histologies in terms of composition and striations throughout the cartilage regions. The superficial zone thickness was similar across the three species but the organisation and content of the collagen throughout each species differed. In human tissue, birefringence measurements showed a significantly higher level of

collagen in the superficial and deep zones as compared to porcine and bovine tissue. The collagen levels increase linearly throughout the deep zone reaching a maximum close to the cartilage-bone interface whilst in porcine and bovine tissue a plateau region is observed at half-thickness. In both porcine and bovine tissue, a lower anisotropy level was observed at the cartilage-bone interface indicating less organisation compared to human tissue, whereas in the middle or translational zone a higher thickness with a higher anisotropy was noticed in porcine tissue compared to human and bovine tissue which had similar appearances. Besides differences in histology, differences in proteoglycan content are observed between the three tissues, where a lower content was observed in the superficial zone of human tissue compared to bovine and porcine samples. The increase in proteoglycan content throughout the total cartilage thickness differs between the different tissues. In porcine tissue the maximum content occurs approximately one sixth through the total depth whilst in human and bovine tissue a monotonic increase occurs when the animal is skeletally mature. The proteoglycan content increases as the animal matures thus a compromise has to be made between maximum proteoglycan content and maturation time. A small decrease in proteoglycan content, as well as other maturation of structurally important materials such as collagen, can cause changes in the properties of the tissue such as resistance to compression.

These differences highlight the limitations of using animal models to predict how human tissue functions when osteoarthritic, but also the different choices that have to be made when considering which tissue/species to use to base the model on in the first place.

5.1.1.2 Model development and disease simulation

Another consideration when using animal models is how to samples which can mimic the human diseased state, as trying to obtain tissue already in the diseased state of interest is exceedingly difficult. For osteoarthritic models, various methods to create a diseased state have been employed ranging from use of enzymatic digestion (with enzymes such as chondroitinases and proteases such as papain) through to techniques such as ultrasound or mechanical degradation (Grenier et al., 2014, Benam et al., 2015, Johnson et al., 2016). These different methods have been used to create different levels of degradation and defects throughout the tissue, as each technique has a different level of intensity and penetration.

As described in Chapter 1, there are differing severities of disease progression and damage observed in osteoarthritic cartilage, so the method employed to simulate the disease state is also dependent on the severity of damage required due to aforementioned differing levels of intensity and penetration.

In this chapter, the animal model of choice was porcine tissue due to the ease of obtaining samples and the similarities in mechanical strengths of the articular cartilage region on the knee between human and porcine tissue. Whilst the thickness of cartilage in porcine tissue is slightly thinner compared to human cartilage (1.5 mm compared to 2.35 mm average thickness), the only animal tissue with a thicker cartilage layer is equine tissue at 1.75 mm, but porcine tissue is far more abundant and cost effective (Ahern et al., 2009). This is hence one of the reasons behind choosing this tissue for the model of osteoarthritic knee developed by Andres Barco (Barco, 2017). The average GAG content of porcine tissue in the femoral condyles is higher than that found within humans but because the aim of the experiment was to deplete the GAGs from the tissue this increased content was not an issue in choosing porcine tissue for the model (Hosseinia et al., 2013, Fermor et al., 2015a).

5.2 Results

5.2.1 Severe osteoarthritic model validation

An early stage osteoarthritic model with total loss of GAGs was chosen for the testing reported in this chapter. The model was developed by Andres Barco of the Ingham group using a series a process summarised in **Fig 5.1**.

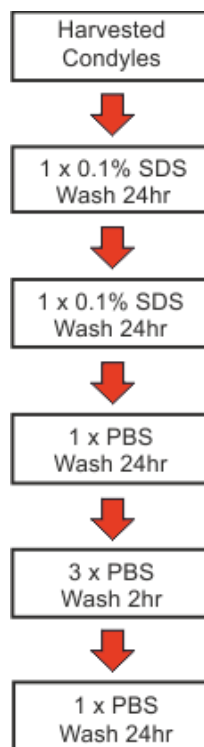


Fig 5.1: Flowchart illustrating the GAG depleting procedure. The procedure involved SDS and PBS washes at varying lengths, whilst being agitated at 240 rpm, 37 °C.

The rationale behind using this model was that while in an early stage osteoarthritic model the level of GAGs are barely diminished and that the total loss of GAGs within cartilage is associated with severe late stage OA, the minimal loss of GAGs would have meant any measurement of changes in biomechanics would have been inaccurate and difficult to measure to any degree of precision so by totally depleting the GAG concentration of an otherwise early stage OA model meant any change in the biomechanics of the tissue could be measured with precision and accuracy with an acceptable level of sensitivity. Histological and immunohistochemical analysis was carried out to confirm that a total GAG depleted tissue model was produced in accordance with the previously developed method.

5.2.1.1 Histological validation of GAG depleted cartilage model

Safranin O Fast Green, selectively reveals the location of proteoglycans within tissue by staining them red while proteoglycan depleted tissue appears green. Staining of paraffin embedded native and GAG depleted cartilage tissue sections shows that treatment with 0.1 % (w/v) SDS effectively removes all proteoglycans from the tissue (**Fig 5.2**).

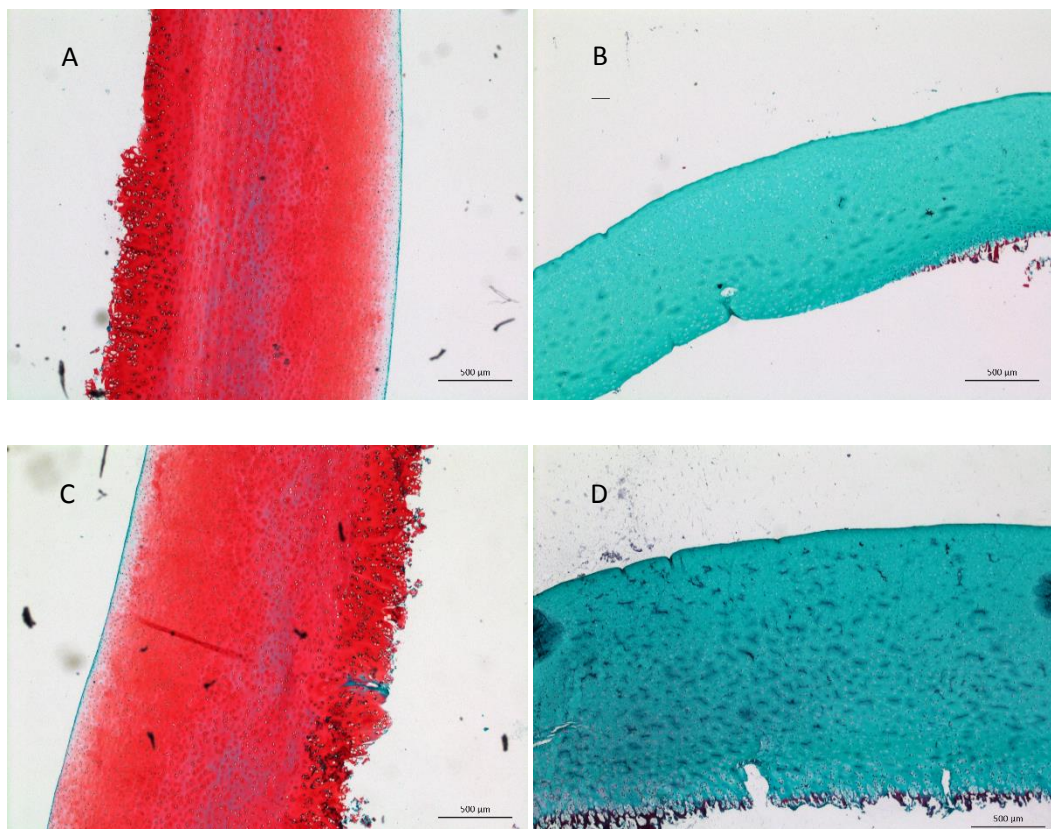


Fig 5.2: Safranin O and fast green stained sections of native and GAG depleted porcine cartilage. Top left (A) – native healthy medial cartilage. Top right (B) – GAG depleted medial cartilage. Bottom left (C) – native healthy lateral cartilage. Bottom right (D) – GAG depleted lateral cartilage. Scale bar = 500 µm.

The micrographs indicated the successful generation of a GAG depleted porcine cartilage model with the total absence of GAGs following the SDS and PBS washes. The 5-10 μm layer of blue at the cartilage surface in the native micrographs are probably due to the various washes carried out during the staining protocol. The superficial zone surface of the GAG depleted samples are defined and little damaged compared to the native healthy samples indicating the process did not damage the cartilage sample during the various agitation steps which had to be relatively rigorous to ensure full penetration of the SDS and PBS washes and sufficient movement of the solutions to wash out any GAGs from the tissue samples.

5.2.1.2 Immunohistochemical validation of GAG depleted cartilage model

Immunohistochemical analysis of both native healthy and GAG depleted tissue was carried out as described in section 2. The procedure employed a CS selective antibody and results in a brown staining of the tissue when CS is present. The micrographs, shown below in **Fig 5.3**, indicated near total loss of CS selectively in the GAG depleted sample (right hand images, B and D, in **Fig 5.3**) compared to the native tissue (left hand images, A and C, in **Fig 5.3**). This reinforced the data from the histology images also showing that the treatment of the tissue with 0.1 % SDS (w/v) and PBS washes removed the majority of the GAGs from the tissue, including CS.

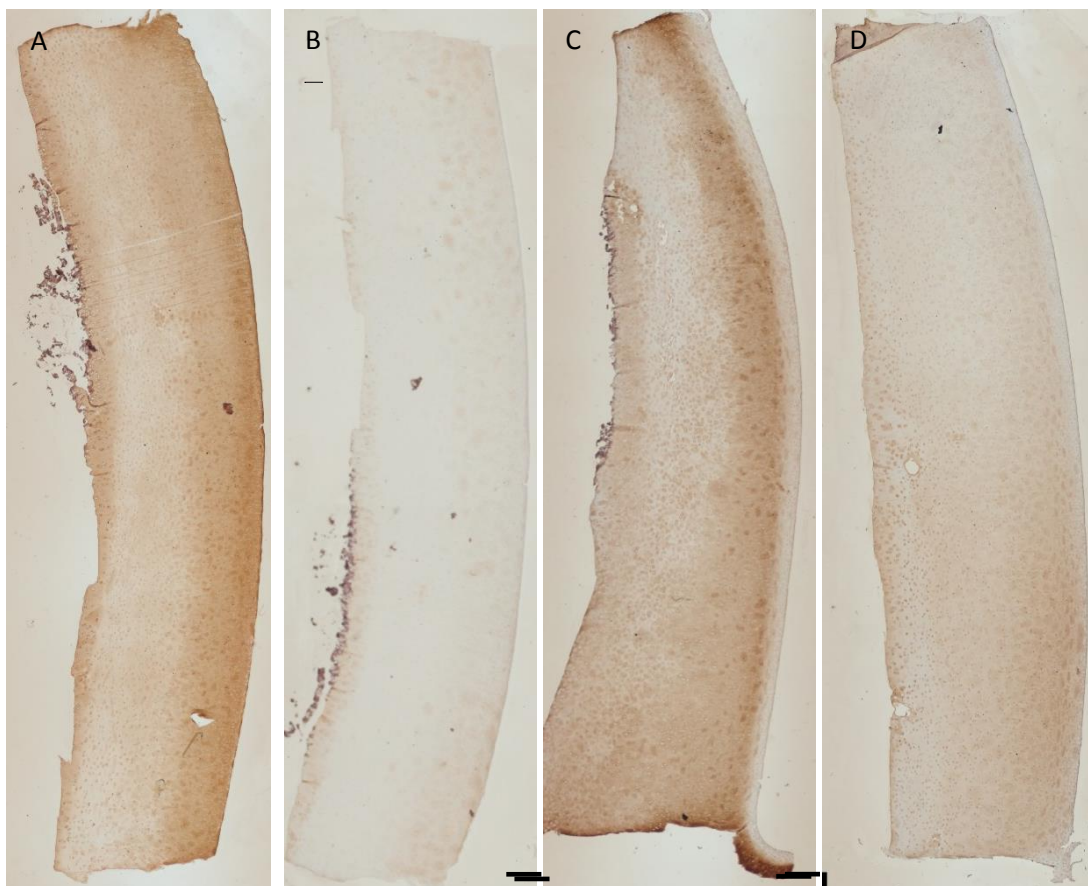


Fig 5.3 : Immunohistochemical micrographs of native and GAG depleted cartilage. CS selective staining for native and GAG depleted samples indicating the presence of CS where the dense brown colouration is located. A) Native medial sample. B) GAG depleted medial sample. C) Native lateral sample. D) GAG depleted lateral sample. Scale bar = 500 μm .

5.2.1.3 Quantitative validation of GAG depleted cartilage model

One issue with histological and immunohistochemical testing is that it does not give truly quantitative results as these tests only provide qualitative images of the tissue. Biochemical assays can be used to quantify the amounts of materials such as chondroitin sulfate using sulphate in the dimethylmethylene blue (DMMB) colorimetric assay. In the DMMB assay example the dye binds to sulphate groups in the molecule causing and produces a change in emission, shifting the wavelength towards a maximum at 525 nm. The assays were performed on desiccated tissue as detailed in Chapter 2. The average GAG content (n=3) measured for native tissue was $267.8 \pm 13.4 \mu\text{g mg}^{-1}$ whilst the SDS depleted tissue had a measured average GAG content (n=3) of $63.9 \pm 3.2 \mu\text{g mg}^{-1}$, indicating a 76% decrease in GAG content following SDS treatment. The reduction in GAG content was significant ($p < 0.05$, Students T-Test) as shown in **Fig 5.4** below.

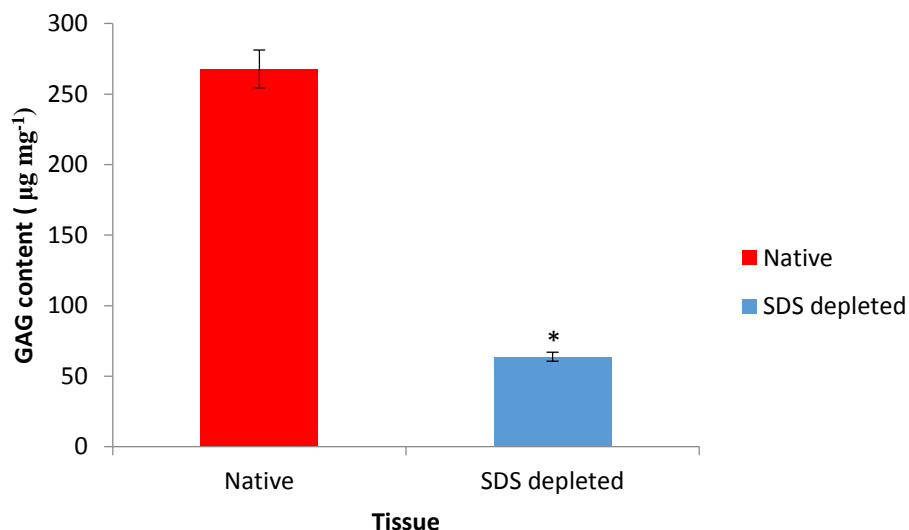


Fig 5.4: Quantification of GAG content of native and GAG depleted cartilage. Data is shown as the mean (n=6) ± 95% CL. * indicates significant (p<0.05, Students T-test).

5.2.1.4 Detection of residual SDS using a Stains-All assay

To assess whether there was any residual SDS present in the GAG depleted model cartilage, a photometric assay was carried out using a carbocyanine based dye which had the commercial name Stains-All, illustrated in **Fig 5.5**.

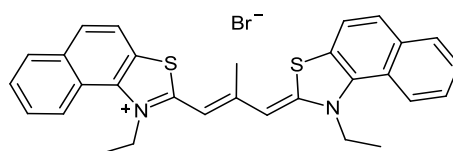


Fig 5.5: Structure of Stains-All dye.

The results are shown in **Fig 5.6** with the medial and lateral samples separated.

Quantitative analysis of SDS in each wash showed that no additional SDS could be detected following PBS wash 4 (**Fig 5.6**). This suggested that SDS was sufficiently removed from the treated cartilage during the processing to not be regarded as an issue with future testing.

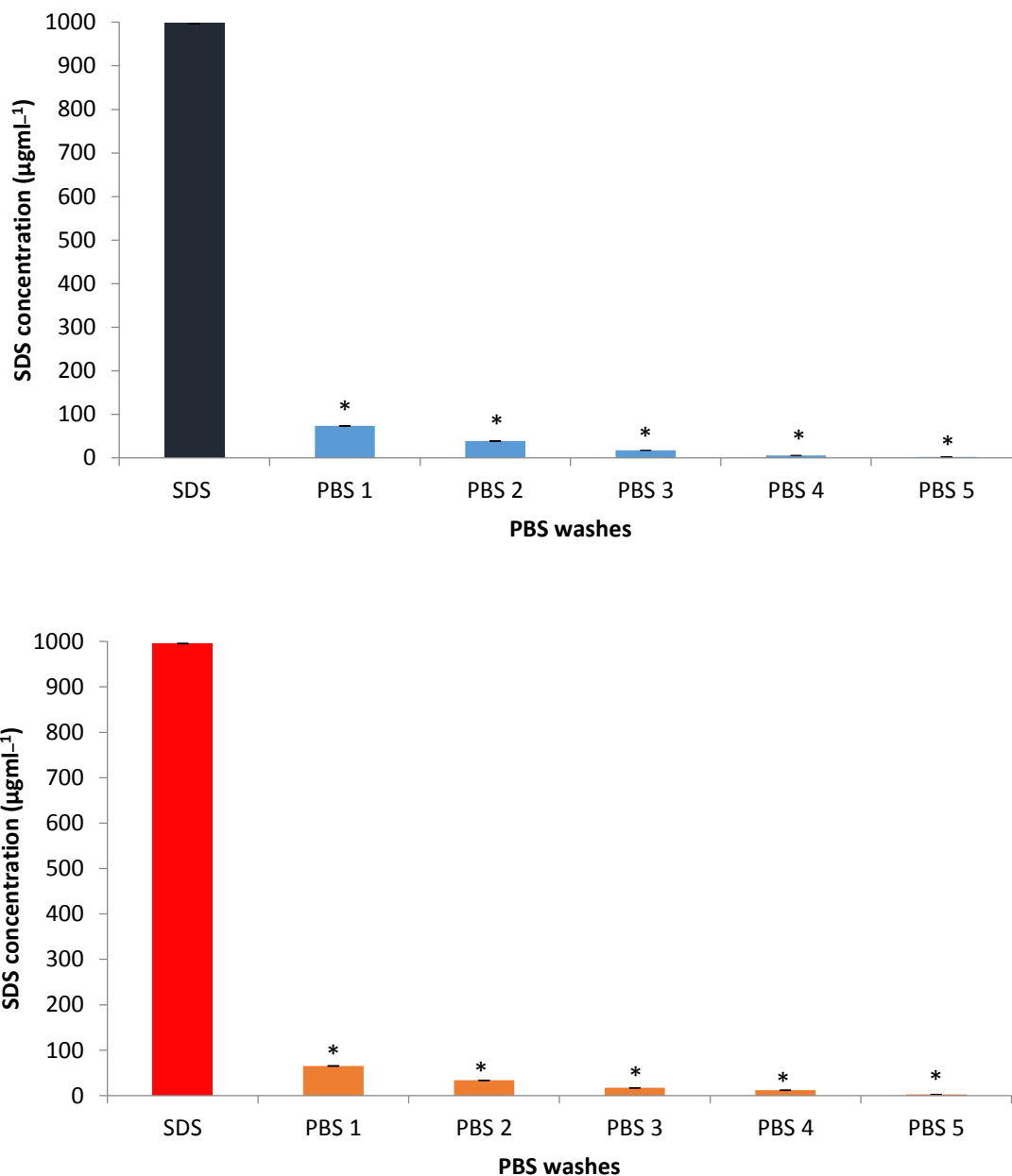


Fig 5.6: Quantitative measurements of average SDS levels in various washes of medial (Top) and lateral (Bottom) tissue samples (n=3). Wavelength read at 447nm. Results are the mean readings (n=3) \pm 95 % CL, where significance ($p < 0.05$) is indicated by *.

The data presented indicated that in the medial samples on average over $99.8 \pm 0.17\%$ of SDS was removed by the final PBS wash, while the lateral samples had over $99.7 \pm 0.14\%$ removed by the final wash. A peptide hydrogel was prepared, as previously described for hydrogels in Chapter 4 except using 0.1% SDS solution instead of the sodium buffers, to investigate whether these levels of residual SDS would interfere with self-assembly, but as shown in **Fig 5.7**, a hydrogel formed in the presence the residual SDS.



Fig 5.7: Images of P₁₁₋₄ only hydrogels (10mgml⁻¹) in the presence of SDS at 0.1 % starting SDS concentration.

These results, as well as the physical formation of a gel at the measured concentrations, indicated the removal steps during the GAG depletion process were sufficient.

The next step was to confirm whether the monomeric peptide solutions firstly penetrated the tissue following injection and secondly whether the self-assembling peptides formed hydrogels *in situ*.

5.2.3 Confirming self-assembly in the tissue

Confirmation as to whether the injected peptide gels had self-assembled within the tissue was required to be able to definitively associate any changes in bio-mechanical properties with the presence of the gels rather than some interaction between the tissue and the monomeric solutions. The challenge was to image the self-assembled gels within the tissue without disrupting the self-assembly. In order to image the materials various fluorescently labelled molecules were employed. For example small quantities of fluorescently labelled peptide could be doped into the self- assembling mixture and employed to visualise the location of the peptide within the tissue. Unfortunately direct fluorescence microscopy was unsuccessful due to artificial creation of fibril like structures which were indiscernible from folds within the tissue section that caused increased fluorescence to be observed, as shown in **Fig 5.8**.

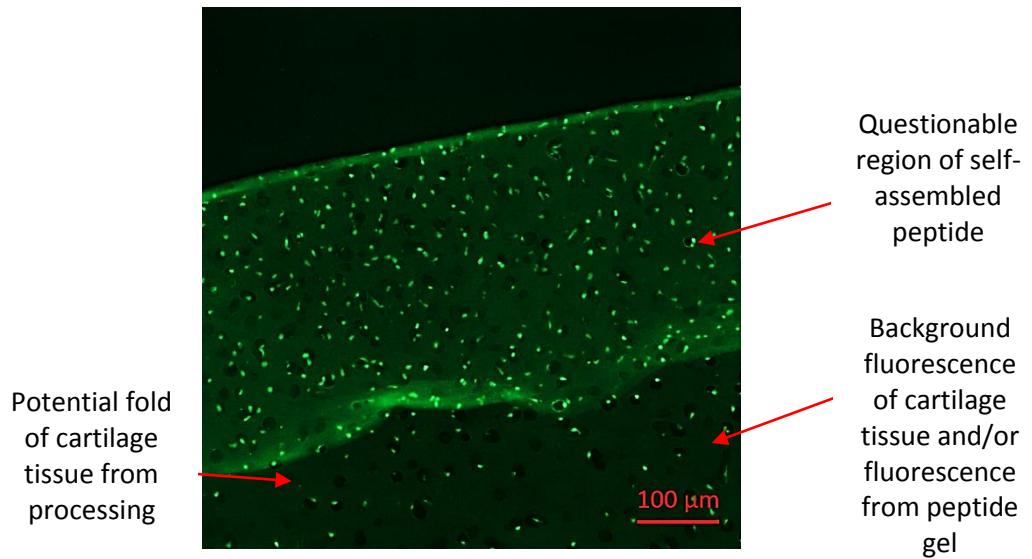


Fig 5.8: Fluorescence micrograph of peptide injected tissue. Gel was P₁₁-4:P₁₁-4-CS 32:1 (P₁₁-4-Fluorescein doped 150:1) injected GAG depleted tissue.

The advantage of having doped the gels with fluorescent molecules was being able to use confocal microscopy which enabled larger sections to be cut and z stacking performed to show the penetration of the fluorescent material throughout the cartilage tissue. However, the greatest advantage confocal microscopy had over other techniques was being able to carry out a fluorescence recovery after photo bleaching (FRAP) type experiments to indicate the diffusion rate of the fluorophore within the tissue.

5.2.3.1 Confocal imaging

In order to show the diffusion rate of a small molecule, a solution of free fluorescein was injected into the tissue and FRAP experiments performed. Selected micrographs are shown below in **Fig 5.9**, with the pre-bleaching, bleached and post bleaching points highlighted.

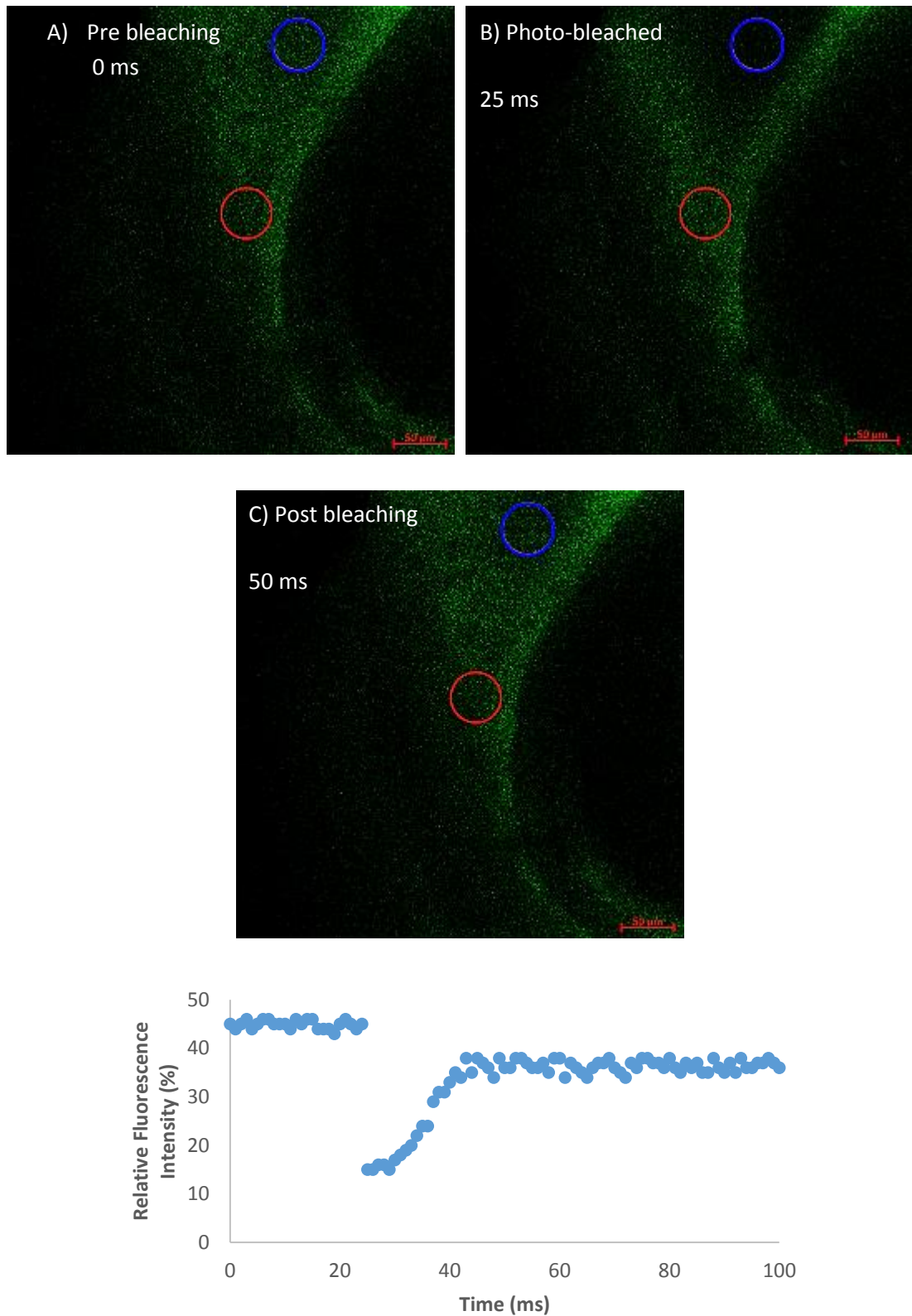


Fig 5.9: Confocal images of fluorescein only control within articular porcine cartilage and FRAP recovery data. A) Pre-bleaching micrograph with the positive control circled in blue, while the negative control circled in red. B) Positive control area has been photo-bleaching using 100% power for 488nm laser. C) Post-bleaching shows recovery of fluorescence after ~50 ms. Graph represents fluorescence recovery rate of over 100 ms following photo bleaching of control area. Scale bar = 50 μ m.

The images showed that the fluorescein was rapidly able to diffuse (25 ms) from the non-bleached tissue surrounding the positive control area, thus restoring fluorescence within the control area by 76 %. This recovery rate represented a non-self-assembled state and showed rapid diffusion of a small molecule through the tissue. This ability to recover was used as the negative control for the peptide samples to indicate whether gels had formed or the peptides were still in a monomeric solution.

The P₁₁₋₄ only sample, doped with fluorescein labelled P₁₁₋₄ (**Fig 5.10**) doped in a ratio of 1:150 fluorescein-P₁₁₋₄:P₁₁₋₄, showed no recovery when FRAP was carried out, indicating a self-assembled state within the tissue. The images below in **Fig 5.11** highlight the lack of recovery in the bleached area.

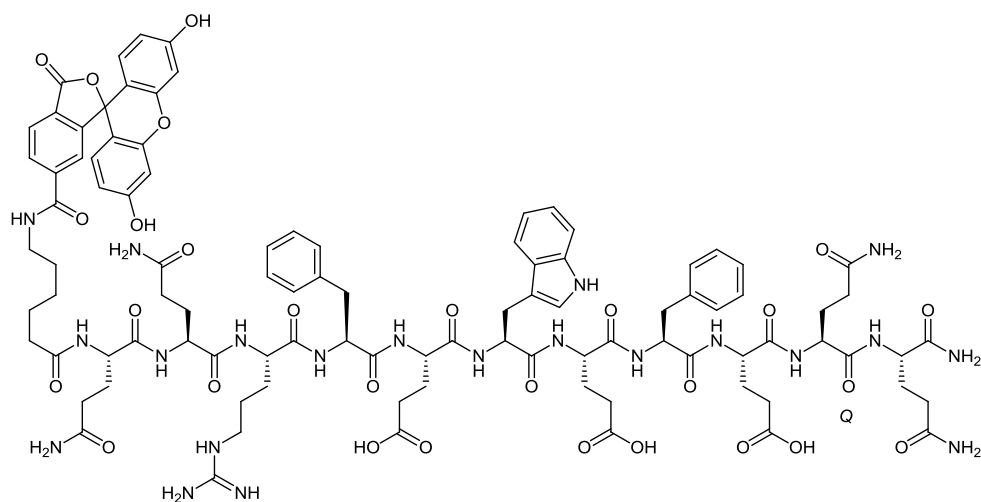


Fig 5.10: Structure of fluorescein labelled P₁₁₋₄ used in the FRAP experiments.

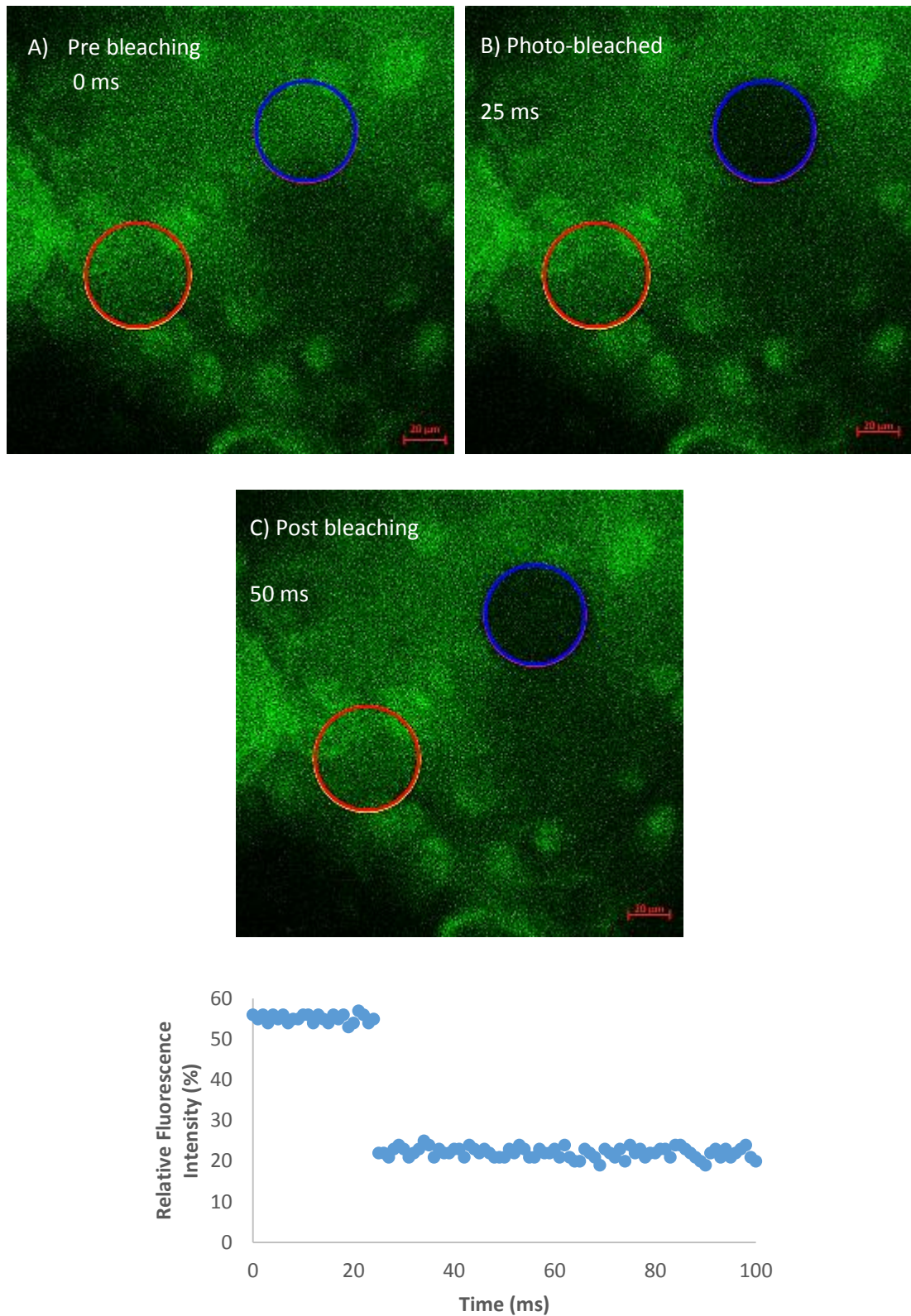


Fig 5.11: Confocal micrographs of P₁₁₋₄ only controls injected within articular porcine cartilage and FRAP recovery data. A) Pre-bleaching micrograph with the positive control circled in blue, while the negative control circled in red. B) Positive control area has been photo-bleaching using 100% power for 488nm laser. C) Post-bleaching shows some recovery of fluorescence after ~50 ms. Graph represents fluorescence recovery rate of over 100 ms following photo bleaching of control area. Scale bar = 20 μm.

The lack of recovery in the P₁₁-4 only sample indicated the peptide bound fluorophore had significantly lower diffusion rates in the tissue which was attributed to the formation of a gel within the tissue. A similar observation was noted in the P₁₁-4-CS sample, when lack of fluorescence recovery was witnessed within the same timescale ~ 50 ms. The micrographs are shown below in **Fig 5.12**, again the negative bleaching control shown to highlight the loss of fluorescence was through control rather than background bleaching of the sample.

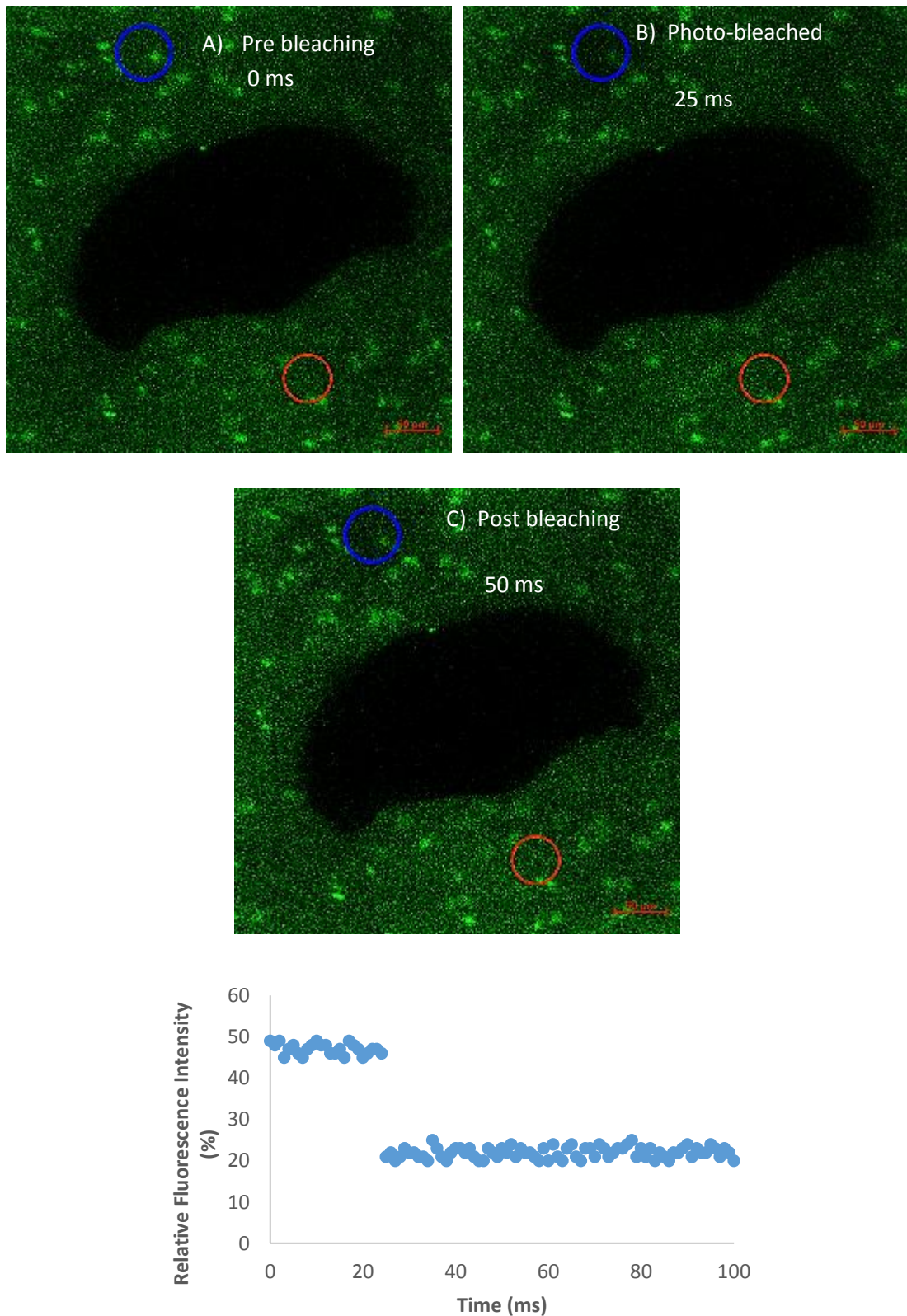


Fig 5.12: Confocal images of P₁₁-4-CS control within articular porcine cartilage and FRAP recovery data. A) Pre-bleaching micrograph with the positive control circled in blue, while the negative control circled in red. B) Positive control area has been photo-bleaching using 100% power for 488nm laser. C) Post-bleaching shows recovery of fluorescence after ~50 ms. Graph represents fluorescence recovery rate of over 100 ms following photo bleaching of control area. Scale bar = 50 μ m.

A fluorescently labelled CS sample, as shown in **Fig 5.13**, was introduced to the tissue to investigate the diffusion rate of the much larger (~48 kDa) material through the tissue.

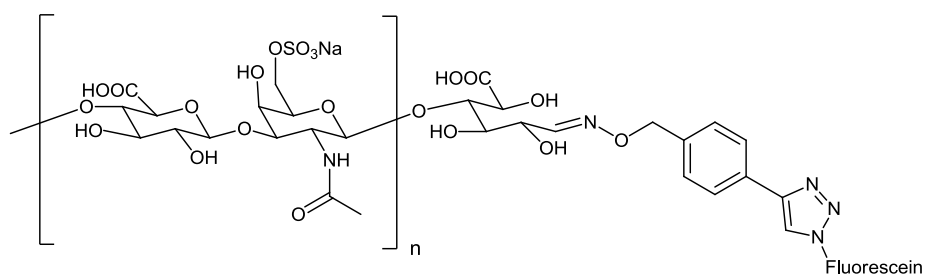


Fig 5.13: Fluorescein labelled CS molecule used in the FRAP experiments.

In comparison to the peptide containing samples, the fluorescently labelled CS only control showed 25 % recovery after 25 ms compared with 1-2 % recovery after 25 ms for the peptide containing samples, as shown in **Fig 5.14**. This observation indicated the CS was not bound in a self-assembled matrix within the tissue but due to the large size of the molecule the recovery time was significantly longer than observed with the fluorescein only control. However the fact that even this large macromolecule diffuses more rapidly than the fluorescently labelled P11-4 demonstrates that the peptide has formed very large self-assembled aggregates within the tissue.

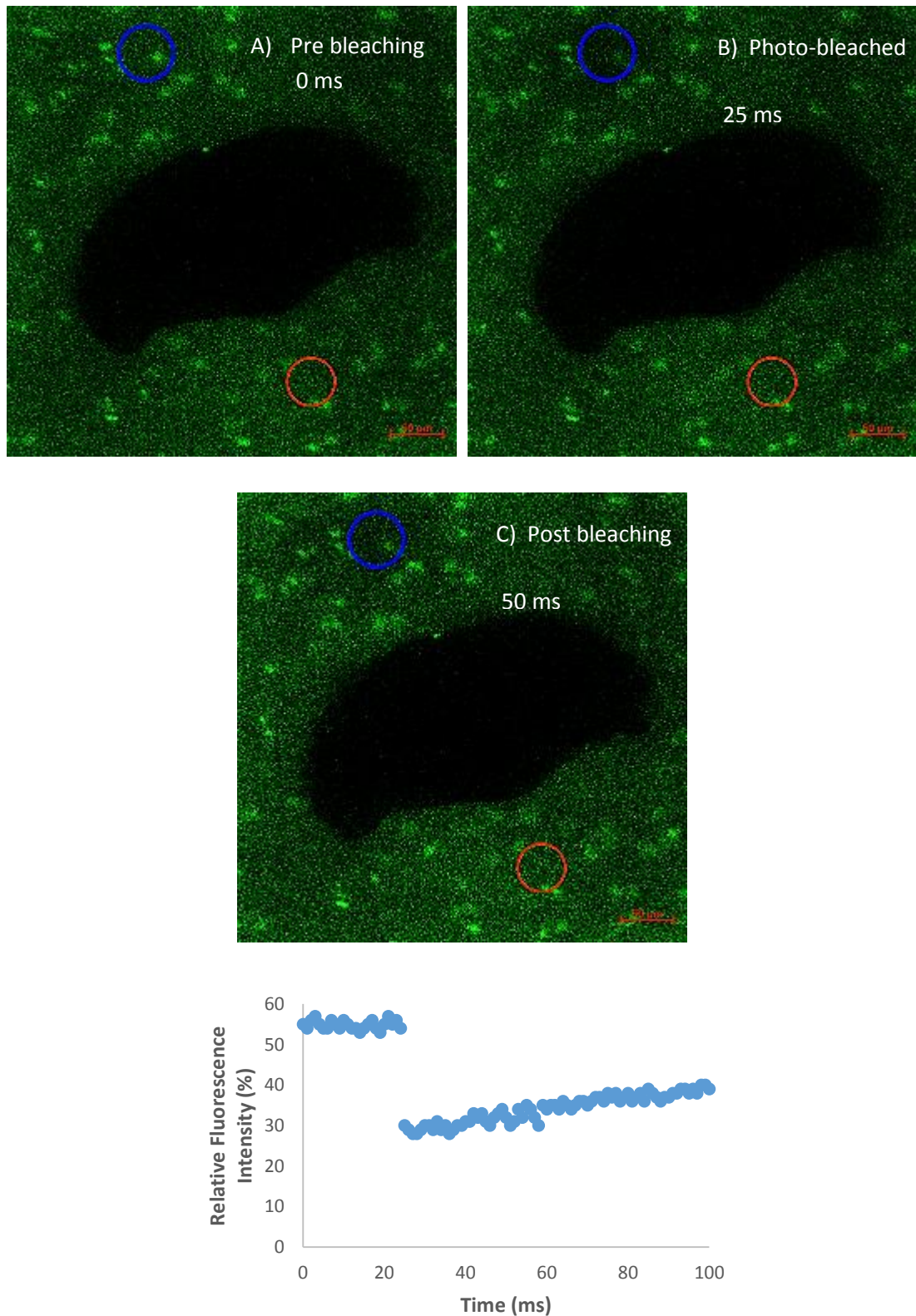


Fig 5.14: Confocal images of fluorescently labelled CS only control within articular porcine cartilage and FRAP recovery data. A) Pre-bleaching micrograph with the positive control circled in blue, while the negative control circled in red. B) Positive control area has been photo-bleaching using 100% power for 488nm laser. C) Post-bleaching shows recovery of fluorescence after ~50 ms. Graph represents fluorescence recovery rate of over 100 ms following photo bleaching of control area. Scale bar = 50 μ m.

5.2.2 Mechanical testing of osteoarthritic tissue model

5.2.2.1 Indentation testing

Once the animal model was validated to be sufficient in terms of mimicking severe osteoarthritic, GAG depleted cartilage and the ability of the peptides to penetrate and self-assemble within the tissue had been confirmed the mechanical properties of the tissue were measured. A range of conditions, as shown in **Table 5.2**, were used in these experiments to provide information about how the different peptides, loading of CS (either conjugated to the peptide or otherwise) and peptide concentration affected the mechanical response.

Tissue Condition	Acronym Used (M/L)	Peptide	Ratio (CS:Peptide)	Buffer	Other
Native (Healthy)	H	-	-	-	-
Native (Healthy)	HN	-	-	-	Needle Only
Native (Healthy)	HS	-	-	130mM Na ⁺ buffer	Sham solution injection
SDS treated – GAG depleted	S	-	-	-	-
SDS treated – GAG depleted	S + CS	-	1:32	130mM Na ⁺ buffer	Fluorescent labelled CS
SDS treated – GAG depleted	S + P	P ₁₁₋₄ (10 mg ml ⁻¹ or ~6mM)	1:32	130mM Na ⁺ buffer	Fluorescent labelled P ₁₁₋₄ (1:150 P _{11-4_F} :P ₁₁₋₄)
SDS treated – GAG depleted	S + P114 30	P ₁₁₋₄ (30 mg ml ⁻¹ or ~18mM)	-	130mM Na ⁺ buffer	Fluorescent labelled P ₁₁₋₄ (1:150 P _{11-4_F} :P ₁₁₋₄)
SDS treated – GAG depleted	S + P11-CS 30	P ₁₁₋₄ (30 mg ml ⁻¹ or ~18mM)	1:32	130mM Na ⁺ buffer	Fluorescent labelled P ₁₁₋₄ (1:150 P _{11-4_F} :P ₁₁₋₄)
SDS treated – GAG depleted	S + P11-8-CS 30	P ₁₁₋₈ (30 mg ml ⁻¹ or ~18mM)	1:32	130mM Na ⁺ buffer	Fluorescent labelled P ₁₁₋₈ (1:150 P _{11-8_F} :P ₁₁₋₈)

Table 5.2: The different control groups tested using the indentation rig to measure the effects of deformation observed within native and depleted cartilage samples.

5.2.2.2 Cartilage thickness measurements

The thickness of the cartilage covering each condyle was measured using a set up as described in Chapter 2, where a needle probe was inserted into the cartilage surface and the compressive load was measured against the relative displacement of the probe. By analysing the compressive

load as the probe moves through the sample, the regions of transition from air to cartilage and cartilage to subchondral bone can be observed and from this the thickness of the cartilage can be determined.

The thickness was calculated from the intersection point of the two linear fits which represented the resistance forces for the cartilage and bone resistances. A representation of the data analysis corresponding to the different regions of the cartilage during the experiment is shown in **Fig 5.15**.

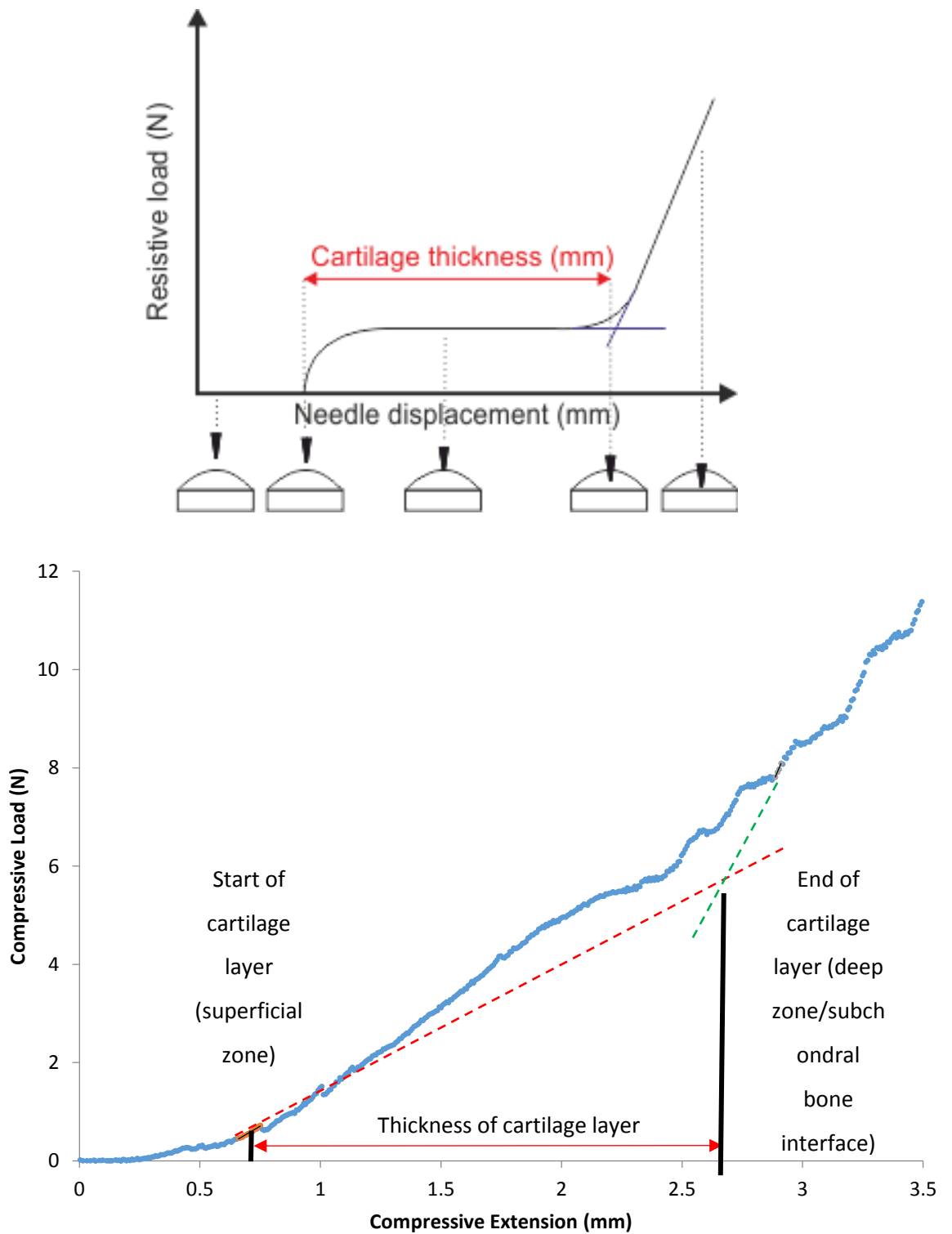


Fig 5.15: Typical schematic of cartilage thickness measurement (Top) and real data interpretation (Bottom). A representation of the data analysis and the corresponding regions of the cartilage sample (top). The thickness of the cartilage layer is calculated from the interception point from the gradients chosen where the boundaries of the cartilage are – the example shown is for a medial sample where the calculated cartilage thickness = 2.01 mm.

The data differed from the idealised model shown in the schematic but with experience the curves could be analysed through by the method shown in the real data graph.

The measured thickness for both the medial and lateral condyles, for both the native and SDS treated samples can be seen below in **Table 5.3** along with literature values for the different regions.

Sample	Region	Measured (mm)	Literature (mm)	Reference
Native	Medial	1.97 ± 0.11	2.00 ± 0.25	(Fermor et al., 2015a)
Native	Lateral	1.67 ± 0.39	1.57 ± 0.43	(Ahern et al., 2009, Wayne et al., 1998, Fermor et al., 2015a)
SDS treated	Medial	2.05 ± 0.14	N/A	N/A
SDS treated	Lateral	1.76 ± 0.35	N/A	N/A

Table 5.3: The measured and literature values for both medial and lateral cartilage thicknesses, with SDS treated measured samples also shown (n=12) where the results are presented as the mean ± 95% CL (p<0.05 student T-test)

The measured thicknesses for the native tissue matched previous measurements from literature made by different techniques such as CT scanning, thus validating the measurements, and were not significantly (p<0.05) different from the SDS treated tissue, which were slightly thicker.

5.2.2.3 Deformation during indentation tests

Tissue deformation was measured using an indentation rig. A 20.5 g 2.5 mm diameter circular indenter was used to apply a 0.22 MPa load to the surface of the cartilage sample. As described in section 2.6.2, the relative displacement of the load cell was measured over the period 1hr at a 10Hz scan rate. The data was then plotted as a time course over the hour in seconds to show the total deformation of the tissue for each experimental condition. The data is shown in **Fig 5.16**, where the medial and lateral condyles are shown on separate graphs.

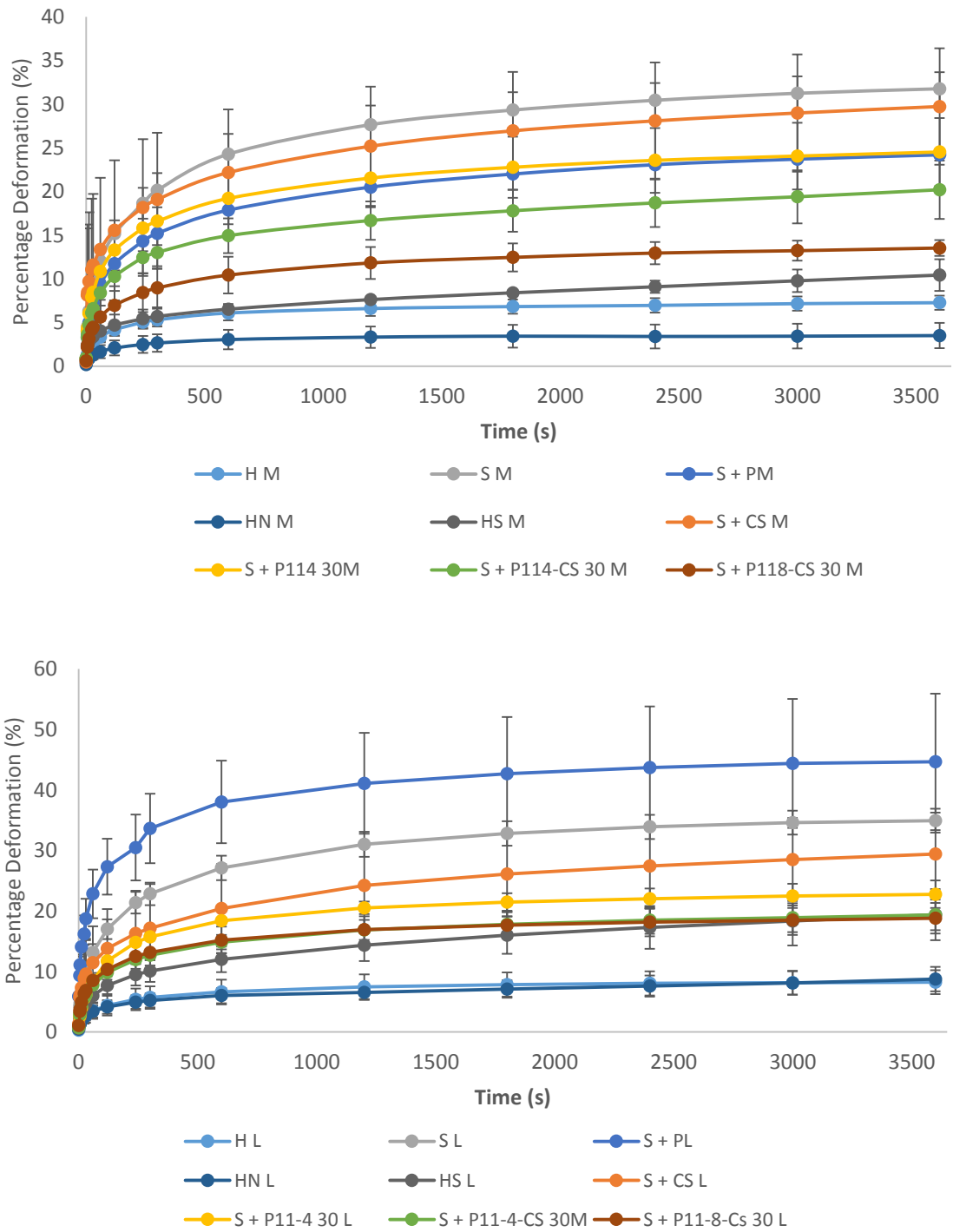


Fig 5.16: Summary of mean deformation data after 1hr. Deformation was shown over 1hr (3600s) for each control group separated for the two condyles – medial samples (top) and lateral samples (bottom) with data representing mean (n=3) ± 95% CL. Labels – M = Medial, L = Lateral, H = Native (Healthy), S = SDS GAG depleted, HN = Native needle only, HS = Native Sham injection, S + P = GAG depleted + P₁₁₋₄-CS 10 mgml⁻¹ injected, S + CS = GAG depleted + CS only injected, S + P₁₁₋₄ 30 = GAG depleted + P₁₁₋₄ 30 mgml⁻¹ only, S + P₁₁₋₄-CS 30 = GAG depleted + P₁₁₋₄-CS 30 mgml⁻¹, S + P₁₁₋₈-CS 30 = GAG depleted + P₁₁₋₈-CS 30 mgml⁻¹.

Upon analysing the rate of deformation by measuring the first and second derivatives of each curve, there were no discernible differences so to better represent the total deformation of each sample as simple bar chart would suffice, as shown in **Fig 5.17**.

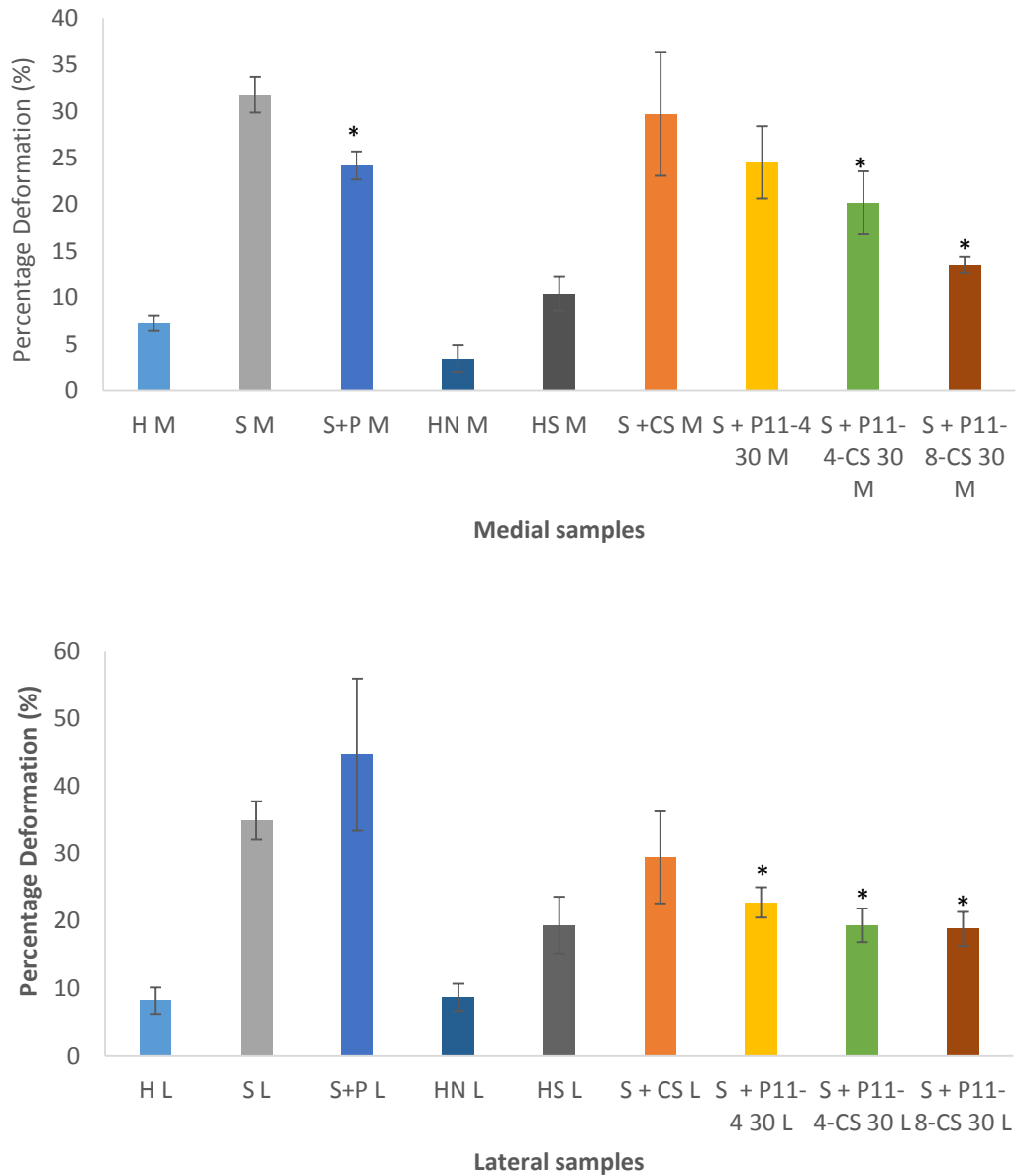


Fig 5.17: Percentage deformation at equilibrium end point. The data shows the percentage deformation once the tissue has reached an equilibrated state ~ 1 hr. The data is split into two data sets, medial (top) and lateral (bottom) samples, with the mean values ($n=3$) \pm 95 % CL shown, where significance ($p < 0.05$, Student T-test) is indicated by *. Labels – M = Medial, L = Lateral, H = Native (Healthy), S = SDS GAG depleted, HN = Native needle only, HS = Native Sham injection, S + P = GAG depleted + P₁₁-4-CS 10 mgml⁻¹ injected, S + CS = GAG depleted + CS only injected, S + P₁₁-4 30 = GAG depleted + P₁₁-4 30 mgml⁻¹ only, S + P₁₁-4-CS 30 = GAG depleted + P₁₁-4-CS 30 mgml⁻¹, S + P₁₁-8-CS 30 = GAG depleted + P₁₁-8-CS 30 mgml⁻¹.

The normalised deformation for the healthy tissue showed that there was no significant difference between the medial and lateral condyles, $7 \pm 1\%$ and $8 \pm 2\%$ respectively which was also observed for the GAG-depleted samples, $32 \pm 2\%$ and $35 \pm 3\%$ respectively. The treated samples though, showed significant differences ($P < 0.05$) in certain groups. The peptide: conjugate (10 mg ml^{-1}) injected samples, the average deformation observed in the medial samples was $\sim 24 \pm 2\%$ whilst in the lateral samples it was $\sim 44 \pm 11\%$. The huge variation in deformation was partially attributed to the larger variation in cartilage thickness observed in lateral samples.

The amount of deformation for each sample indicated the presence of either peptide alone or the peptide: conjugate systems decreased the amount of deformation. The recovery of resistance to deformation, i.e. the percentage reduction in deformation compared to the SDS GAG depleted sample as a maximum and the native sample as the benchmark minimum, was calculated and the results are illustrated in **Table 5.4**.

Medial Sample	Deformation Restoration (%)	Entry Number
SDS + P ₁₁₋₄ -CS M	46.7 ± 1.5	1M
SDS + CS M	29.3 ± 6.7	2M
SDS + P ₁₁₋₄ 30 mg ml ⁻¹ M	45.7 ± 3.9	3M
SDS + P ₁₁₋₄ -CS 30 mg ml ⁻¹ M	59.3 ± 3.4	4M
SDS + P ₁₁₋₈ -CS 30 mg ml ⁻¹ M	80.3 ± 0.9	5M

Lateral Sample	Deformation Restoration (%)	Entry Number
SDS + P ₁₁₋₄ -CS L	-4.3 ± 11.3	1L
SDS + CS L	39.3 ± 6.8	2L
SDS + P ₁₁₋₄ 30 mg ml ⁻¹ L	58.4 ± 2.3	3L
SDS + P ₁₁₋₄ -CS 30 mg ml ⁻¹ L	68.2 ± 2.5	4L
SDS + P ₁₁₋₈ -CS 30 mg ml ⁻¹ L	69.7 ± 2.5	5L

Table 5.4: Summary of restoration of deformation resistance in various controls groups. The data shown is split into two data sets – medial (top) and lateral (bottom) where the data is the mean restoration ($n=3$) \pm 95 % CL.

($p < 0.05$, student T-test)

In both the medial and lateral samples, the presence of chondroitin sulfate (**Table 5.4**, Entry 2M and 2L) alone gave some restoration but when covalently bound to either P₁₁₋₄ (**Table 5.4**, Entry 1M, 4M, and 4L) or P₁₁₋₈ (**Table 5.4**, Entry 5M and 5L) the amount of restoration was significantly higher, except in the case of P₁₁₋₄-CS at 10 mg ml⁻¹ (**Table 5.4**, Entry 1L) when injected into the lateral sample which showed no significant difference compared to the SDS treated degenerated sample. When the concentration of the base peptide was increased from 10 to 30 mg ml⁻¹, a comparable, non-significantly different, rate of restoration was noticed between the P₁₁₋₄ only 30 mg ml⁻¹ (**Table 5.4**, Entry 3M and 3L) and P₁₁₋₄-CS 10 mg ml⁻¹ sample (**Table 5.4**, Entry 1M and 1L). But between the covalently bound P₁₁₋₄-CS and P₁₁₋₈-CS samples there was significantly greater restoration of deformation resistance in both the medial and lateral samples. P₁₁₋₈-CS 30 mg ml⁻¹ (**Table 5.4**, Entry 5M and 5L) performed ~20% better at reducing the amount of deformation in the medial samples compared to P₁₁₋₄-CS 30 mg ml⁻¹ (**Table 5.4**, Entry 4M and 14), whilst in the lateral samples there was no observable difference.

When the amount of deformation was converted to the restoration based on maximum deformation being the measured value for SDS samples then the percentages changed. In the 6 mM P₁₁₋₄: P₁₁₋₄-CS (**Table 5.4**, Entry 1M) in the medial condyle, the percentage restoration was not significantly different from the 18 mM P₁₁₋₄ only (**Table 5.4**, Entry 3M) percentage indicating the presence of the CS covalently bound to the peptide matrix had an equal effect as the stronger peptide only gel but which lacked the osmotic effect from the inclusion of CS. When the concentration was increased for the conjugate sample - P₁₁₋₄: P₁₁₋₄-CS at 18 mM (**Table 5.4**, Entry 3M and 3L), then the percentage restoration significantly increased, with an average restoration of 63% across the whole knee (average between medial and lateral condyles) indicating the stronger gel network as well as the presence of CS within the network had a significant benefit on restoring the biomechanical properties of the tissue. However, the biggest percentage restoration was from the positively charged peptide - P₁₁₋₈: P₁₁₋₈-CS at 18 mM (**Table 5.4**, Entry 5M and 5L), where an average percentage restoration of 75 % was observed, which was significantly higher than that for the P₁₁₋₄ equivalent. This result was not expected based on the rheological data presented in Chapter 4, but one hypothesis for this result was that due to being a slower self-assembling system and “weaker” gel, then the monomeric gel was able to penetrate further into the tissue through an increased lifetime before fully self-assembling to form a gel *in situ*.

5.3 Discussion and conclusion

5.3.1 GAG depleted cartilage model

A GAG depleted porcine cartilage model was produced using 0.1 % SDS followed by PBS washes as previously developed by a PhD student – Andres Barco. The model was validated through histological and immunohistochemical staining as well as photometric assays which showed, the near-complete removal of GAGs in from the depleted cartilage tissue. The chosen model was aimed at cartilage which had damage equivalent to Grade 1 lesions (as rated by ICRS score) where a progressive loss of GAGs has started. This was based on the opinion of the researcher that this was the initial trigger point of degradation of cartilage towards severe osteoarthritis (Matzat et al., 2013, Felson and Hodgson, 2014), rather than trying to mimic the hypothesis that osteoarthritic cartilage formed through damage to the collagen network throughout the extracellular matrix of cartilage (Hosseini et al., 2013, Madry et al., 2016). However the level of GAG loss in these early stage lesions did not have detectable changes in terms of biomechanics when tested with the indentation methodologies so the severely GAG depleted cartilage model allowed changes in biomechanics following the treatment with SAP-GAG conjugates to be detectable and quantifiable.

When each sample was analysed by a DMMB photometric assay, the measured GAG loss was ~ 80% which, whilst less than the visual estimation from the images, matched reported estimates of severe osteoarthritic cartilage by various groups. In order to confirm that all the SDS (which was used to deplete GAGs in the cartilage and may prevent the self-assembly of functionalised peptides in situ) had been removed the level of residual SDS remaining in the cartilage after GAG depletion step was determined. It was confirmed that that over 99% of the SDS had been removed by the PBS washes used in the model generation and that any residual low levels of SDS which may remain within the tissue does not disrupt self-assembly of the peptide. All of these results reinforced that the model was suitable to be taken forward for mechanical testing.

5.3.3 Confirming self-assembly within the tissue

The development of a successful method to show, with good accuracy, whether or not the self-assembling peptides and conjugates actually succeeding in self-assembling within the tissue following injection was an important milestone for the project. This method was not only useful for this area of research into cartilage tissue but could be also be employed for other tissue types where self-assembling peptides have used such as hard tissue like bone or soft tissue such as vascular samples.

The cartilage injected with fluorescein only, or fluorescein covalently bound to chondroitin sulphate showed free diffusing fluorophore when a specific area of cartilage was photo bleached. In contrast, the cartilage injected with fluorescein doped peptide or peptide-CS conjugate showed no recovery of fluorescence in the positive control bleached areas. This indicated that the fluorophore was entrapped within the peptide matrix which could only be possible when the peptide had formed a self-supporting hydrogel within the tissue, thus providing indication that the peptide hydrogels had self-assembled within the GAG depleted cartilage following injection in a monomeric solution.

5.3.2 Mechanical testing of GAG depleted tissue model

Indentation testing indicated that the SDS treatment caused significant ($p < 0.05$) 500 fold increase in the percent deformation of cartilage compared to the native samples. The effect of simply piercing the cartilage with a 30 G needle showed no significant increase in indentation compared to the healthy control, yet when the native tissue was injected with a simple PBS solution, a significant increase in deformation was observed. This may have been due to a disruption of the ionic environment inside the cartilage as well as causing a change in the concentration of GAGs within the injected area. When the concentration of GAGs within the cartilage is altered, there are reported observations of detrimental changes in biomechanical properties (Zhu et al., 1993, Jin and Grodzinsky, 2001, Partington et al., 2013, Griffin et al., 2014). Injection of CS only into the model produced a decreased deformation but it was not significant although ($p < 0.05$) with more sample repeats the significance of the difference may have been confirmed, When any peptide sample was injected at either ~6 or 18 mM, (with the exception of one sample – P₁₁-4: P₁₁-4-CS 6 mM in the lateral condyle), the sample showed significantly reduced percent deformation of the SDS treated tissue. The data from the indentation testing indicated that the conjugation of CS to the peptide produced increased restoration of deformation resistance to the tissue following severe depletion of GAGs from within the tissue. This was in comparison to the peptide and CS only samples which showed a remarkably lower restoration percentage indicating that covalent linkage of the CS to the self-assembling matrix produces a significant beneficial effect. A small difference was noticed between the negatively charged P₁₁-4 and positively charged P₁₁-8 gel samples. As mentioned previously the rheological data presented in chapter 4 predicted that the P₁₁-4-CS samples would produce the greater restoration but from the indentation data it was in fact the P₁₁-8-CS samples that produced the greatest restoration.

In the P₁₁-4 system, the P₁₁-4-CS at 18 mM concentration at 32:1 molar ratio in 130 mM Na⁺ buffer showed the greatest restoration within that series and in the P₁₁-8 system it was P₁₁-8-CS

at 18 mM concentration at 32:1 molar ratio in 130 mM Na⁺ buffer which showed the greatest restoration not just within the P₁₁-8 series but also the whole experiment. These results have shown for the first time significant ($p < 0.05$) restoration of the biomechanical properties of porcine cartilage which was a model for severe GAG depleted osteoarthritic cartilage.

5.3.4 Conclusion

In this chapter, a GAG depleted porcine cartilage model was successfully reproduced and validated. The model was used to assess the efficacy of CS conjugated self-assembling peptide gels to restore the resistance to deformation of articular cartilage. P₁₁-8-CS at 18 mM was the most successful peptide at restoring the resistance to deformation of cartilage following injection. FRAP showed this effect was indeed related to the *in situ* self-assembly of the peptide rather than through some unknown interaction between the tissue matrix, hydrogel matrix and CS polymer. This data suggests that this could be taken forward as a clinical product used during arthroscopy to restore the mechanical behaviour of early OA GAG depleted cartilage.

Chapter 6

Discussion, future work and conclusion

6.1 General Discussion

The hypothesis upon which this study was based was that stable restoration of GAGs into disease depleted tissue would restore its biomechanical properties; however previously reported data suggested that simply injecting a CS solution into cartilage tissue did not show a significant effect probably because the CS is simply pushed out of the material under load. However, it was postulated that if the CS could be entrapped within a matrix that ensured the CS would not be displaced when the tissue was subjected to physiological loading. The beneficial effects of GAG replacement could still be realised. The idea to entrap the CS within a self-assembling peptide matrix meant that the CS could be introduced within a monomeric peptide solution to achieve penetration of the tissue following injection, however simply suspending the CS within the matrix may not be sufficient to entrap the CS following loading. Instead a system was designed which would covalently link the CS to the self-assembling peptide such that an aggrecan like structure would be formed upon self-assembly that could potentially entrap the CS within the matrix in a more permanent manner and prevent any displacement following loading of the tissue as observed in native undamaged cartilage tissue.

The project was divided into three areas as represented by the three results chapters – 1) synthesis of a self-assembling peptide-CS conjugate covalently linked through a triazole motif created using click chemistry, 2) evaluation of the self-assembling properties of hydrogels composed of varying degrees of doping of base self-assembling peptide with the peptide-CS conjugates and subsequent selection of the most appropriate conditions which gave the strongest hydrogels to take forward to further testing *ex vivo* and 3) evaluation the biomechanics of a GAG depleted early stage OA porcine cartilage model and determination of whether injecting the peptide-CS doped hydrogels had an effect on restoring the resistance to deformation of the cartilage tissue. In the synthetic chapter, the issues encountered came from both the propensity of the self-assembling peptide to aggregate whilst still bound to the resin or during purification which had to be solved to enable sufficient material to be produced. The polydispersity and molecular weight of the CS as well as the regioselective approach to functionalising the CS by reductively aminating the reducing end of the polysaccharide also led

to significant synthetic and analytical challenges. The number of amino acid residues in the self-assembling peptide would have usually entailed an easy synthesis for a relatively small peptide but the inherent nature to self-assembly meant that while the synthesis itself was difficult only in terms of ensuring the correct resin and loading/coupling conditions were employed to achieve the highest possible yield, the purification was the main issue to overcome. The difficulty arose from the issues with solubility of the self-assembling peptide following cleavage from the resin and lyophilisation. In order to purify the crude mixture, ideally a small volume with the highest concentration possible would be employed but the self-assembling peptides aggregated and precipitated from solution due to the high local concentration. The use of pH switching the crude mixture as well as addition of DMSO to ensure the peptides stayed in a monomeric state meant that dissolution could be achieved in a reasonable volume but once loaded and run through a reverse phase column the peptides then had nucleation sites to aggregate upon on the C18 functionalised silica within either the HPLC or Biotage columns (Orbach, 2009, Boyle and Woolfson, 2011, Boyle and Woolfson, 2012). Again pH switching the water and acetonitrile used to carrying out the purification meant that the intrinsic nature of the self-assembling peptides to aggregate was overcome sufficiently to actually purify the crude mixtures, but the problem then lay with the final yields which were not high enough for the intended future experiments (Cui, 2010a, Stupp, 2010). This meant the decision to outsource the synthesis to Cambridge Bioscience was taken which ensured a sufficient amount of azido-P₁₁-4/8 was obtained to carry out the click reaction at scales necessary to produce enough material to carry out the self-assembling studies reported in Chapter 4 and the biomechanical studies reported in Chapter 5.

Click chemistry has been employed to selective conjugate small chemical probes or molecules to large biomolecules on a cells surface (Kolb et al., 2001, Binder and Sachsenhofer, 2007, Uttamapinant et al., 2012). However the relatively small functional alkyne group on the CS fragment combined with the azide group on the self-assembling peptide fragment, which could potentially be hidden within the self-assembled structures, meant that the rate of reaction was impeded greatly thus the need for robust click reaction conditions was required. Hence CuAAC was selected rather than a metal free approach such as SPAAC (Elchinger et al., 2011). The relative size and natural origin of the CS, which again was due to the impossibility of synthesizing a CS polymer in the lab, meant that characterising the products of these reactions was difficult. The random sulfation along with the polydispersity of the CS also complicated issues as techniques such as ion exchange chromatography would have potentially led to complex purification mixtures, thus also making analysis *via* this method potentially difficult as well (Cumpstey, 2013, Elchinger et al., 2011). The characteristic proton produced following CuAAC

reactions was identifiable in ^1H NMR following suppression of the water and hydroxyl signals of the CS, which in conjunction with SEC-MALLS to measure the relatively small change in molecular weight of the CS following successful conjugation meant the reaction and production of a self-assembling peptide–CS conjugate could be demonstrated. (Cumpstey, 2013)

The successful production of the CS-peptide conjugate was further reinforced from the results of the self-assembly studies using this material where changes in morphology and rheological properties of the resulting gels were observed. The introduction of covalently linked CS into the self-assembling peptide fibrillar matrix of the negatively charged P₁₁₋₄ peptide system caused a significant increase in fibrillar length and width compared to simply suspending the CS within the peptide matrix in a non-covalent fashion or using undoped peptide. However no significant change was observed for the positively charged P₁₁₋₈ peptide system. These observations could be explained by the electrostatic repulsion between the sulfate and glucuronic acids groups on the CS and the net negative charge on the P₁₁₋₄ peptide leading to less steric hindrance during self-assembly which meant the peptide could integrate into the base fibrillar structure more successfully than the corresponding P₁₁₋₈ system where electrostatic attraction between the positively charged peptide and the poly-anionic CS chain could have led to inhibitory interaction during self-assembly leading to no significant change in fibrillar length and width compared to the other controls. As mentioned in Chapter 4, the effect of CS on fibril formation has been studied but not in the field of tissue engineering but rather amyloid research due to the known propensity of GAGs to promote self-assembly of naturally occurring peptides involved in conditions such as Alzheimer's disease (Fraser et al., 1992, McLaurin et al., 1999).

The incorporation of CS into hydrogels has been previously studied but rather than incorporated into reversible systems such as the one reported in this study, biopolymers such as chitosan or gelatin and other GAGs such as hyaluronic acid (Tan et al., 2009, Hu, 2011, Li et al., 2016) or synthetic polymers like PLLA or PCL (Pal et al., 2009, Zhao et al., 2013, Eslahi et al., 2016) have been investigated. These hydrogels have mainly been employed as scaffolds for cell-based therapies rather than structural supports for cartilage tissue. These routes employed the side chains of the polysaccharides rather than the reducing end of the polymer to form linkage sites for permanent cross-linking of the polymers to occur, thus forming permanent hydrogels, rather than reversible ones such as the ones used in this study. This design meant that non-selective functionalisation occurred meaning no control over the nanostructures formed was achievable. In contrast in this study where the nanostructure is more tightly controlled and is based around forming an aggrecan-like structure.

As mentioned previously, studies have been performed that involved injecting a CS solution into osteoarthritic cartilage with the aim to either 1) restore the biomechanics and osmotic gradient within the tissue (Marshall, 2000, Brief et al., 2001, Oegema et al., 2002, Van Blitterswijk et al., 2003, Kapoor et al., 2016) or 2) act as a lubricant during articulation (Creamer et al., 1994, Basalo et al., 2007b, Ayhan et al., 2014). The issue with both of these hypotheses was the temporary nature of the treatment in terms of clinical applicability. The restoration of the biomechanics and osmotic gradient within the tissue through simply injecting the CS into the tissue is a temporary solution due to the lack of permanent fixation of the CS within the tissue (Bali, 2001). During articulation of the joint, fluid motion throughout the tissue would cause movement of the CS with the potential expulsion of the CS when the tissue is put under physiological loads which are inherently variable. Studies have shown, as mentioned in Chapter 1, that CS is involved in the lubrication of articular joints during motion but other components have also been shown to be involved and the overall effect from CS injection was not significant compared to the effect of other components (Basalo et al., 2007b, Katta et al., 2009). This raises the question whether it is a single component or the cumulative effect of various components that are involved in lubricating the joint during articulation. However, the results from this study have shown that when the CS was incorporated into a hydrogel matrix, formed through the spontaneous assembly of peptide chains, in a covalently linked manner, a restoration of the inherent resistance to deformation of GAG depleted cartilage approaching 75 % in one combination. This approach differs from other techniques showing similar levels of restoration in that it involves the simple injection of a solution under physiological conditions *in situ*. Other techniques include surgical methods, which are damage limitation attempts following the already onset of osteoarthritic damage to the articular cartilage (Sarzi-Puttini et al., 2005, Perera et al., 2012, Thiede et al., 2012, Makris et al., 2015); stem cell based methods which while having shown promise in recent years, complete control of the differentiation of stem cells into the appropriate cell type and encourage the correct production of the complex structures which cartilage contains has still not been achieved to a level to overcome the use of surgical methods. The results reported from this study highlight a potentially cost effective, easy to administer, minimally invasive method that could prevent the onset or further degradation of osteoarthritis within the cartilage tissue. This study is also the first reported attempt at synthesizing a peptide-CS conjugate which has then been studied to evaluate the best candidate to take forward to *ex vivo* testing using an osteoarthritic cartilage model and the effects the corresponding hydrogels had on the biomechanics of the tissue.

[6.2 Detailed approach to future work](#)

The multi-disciplinary nature and requirement for *ex vivo* testing during this project meant that many questions remained uninvestigated. This allows future work to be potentially carried out on this research in terms of understanding the basic science behind the peptide-GAG interaction more specifically to gain an insight into what about the peptide-GAG conjugate causes the changes in morphology and increased gel strength of the hydrogels. Further biocompatibility studies need to be carried out to confirm unequivocally whether any aspect of the peptide-GAG conjugate synthesis is indeed cytotoxic through carrying out a contact cytotoxicity assay using mammalian cell lines as used in the extract cytotoxicity assay reported in this study. Other than creep indentation and needle indentation testing, friction testing should be carried out to investigate whether the incorporation of the peptide-CS conjugate reduces the friction coefficient as reported previously when CS is simply injected into the cartilage tissue as an aqueous solution (Bell, 2006, Katta et al., 2009). A full assessment of the dispersion and penetration of the peptide-CS conjugate prior to self-assembly within the tissue needs to be carried out utilising confocal microscopy to see whether the monomeric solution remains monomeric for a sufficient timescale to penetration into the deep zone of the cartilage tissue. Z stack imaging of the injected tissue should enable this assessment of the penetration and dispersion following some optimisation of the process. The intended structure of the fibrillar assembly after incorporation of the peptide-CS conjugate into a hydrogel was that of native aggrecan found within cartilage tissue. The techniques used in this study did not have sufficient resolution to visualise individual CS chains, but employing atomic force microscopy would give an acceptable resolution to hopefully image individual CS chains and confirm whether the assembly resembles native aggrecan or some other structure.

[6.2.1 Effect of peptide-GAG interaction on self-assembly](#)

Investigating what about the structure of CS causes accelerated fibrillar growth of the P₁₁-X series of peptides would be required to fully understand the interaction the hydrogels is having within the tissue upon injection. The amyloid-like promotion of fibril growth as well as increased gel properties needs to be investigated in terms of whether the effect is based on concentration or length of CS- is there a specific number of subunits of CS that promote the self-assembly or a combination of the length and concentration? This could be achieved through digesting the CS using chondroitinase in a controlled fashion to obtain smaller repeating units of the CS disaccharide and using different concentrations of each subunit, measure the rate of self-assembly, morphology of fibrils produced and the gel properties of the formed hydrogels.

6.2.2 Contact cytotoxicity of peptide-GAG conjugate

Whilst the cytotoxicity of the base peptides have been studied previously in house (Maude et al., 2011), and the cytotoxicity of residual copper resulting from the click reactions used within this study has been investigated in this project, whether the peptide-GAG conjugates are cytotoxic were not investigated within this study so a contact cytotoxicity assay would need to be carried out to confirm the conjugate did not impede cell growth or leached cytotoxic molecules following self-assembly. The same cell lines as used in the extract cytotoxicity test reported in this study – BHK and L929 cell lines, a hydrogel would be formed and visual observation of whether the cells grew up to and on to the hydrogel or an exclusion zone formed around the hydrogel indicating cell death as well as potentially using an ATP-lite® assay to quantitatively measure the number of live cells within the well following incubation of the cells with the hydrogels for 48 h.

6.2.3 Tribological testing

Friction based testing would involve measuring the friction coefficient of a tissue sample by means of using a tribometer where the friction coefficient is measured when the tissue is slid across a surface. The friction coefficient of a tissue sample is specific to the composition and makeup of the tissue along with the intrinsic lubrication mechanism that lowers the friction found within the native environment of the tissue. The measurement of this friction coefficient would evaluate whether the incorporation of CS into the cartilage tissue caused any change in friction coefficient when entrapped, also whether any CS leaked over time modifying the friction coefficient.

6.2.4 Analysis of peptide-GAG conjugate penetration within cartilage tissue

Confirmation of whether the hydrogels actually self-assembled within the cartilage tissue was achieved using FRAP experiments through confocal microscopy, the amount of penetration achieved by the hydrogel when in a monomeric state prior to self-assembly however was not confirmed due to the difficulty in obtaining reliable and full depth z-stack images from confocal microscopy following harvest of the cartilage from the condyles after injection. Simply optimising the harvesting and z-stack imaging of the tissue would allow confirmation of the levels of penetration achieved following injection.

6.2.5 Investigating the structure of the peptide-GAG conjugate upon self-assembly

The intended structure of the peptide-GAG conjugate hydrogels was to resemble that of the aggrecan molecule found within cartilage naturally. TEM did not give sufficient resolution to visualise the CS chains in a brush-like arrangement when incorporated into the fibrillar network.

Atomic force microscopy (AFM) would give the required resolution to visualise the CS chains, as native aggrecan has been visualised previously using AFM, but a functionalised mica surface was required to achieve this imaging. The investigation, optimisation and utilisation of a functionalised mica surface for the peptide-CS conjugate hydrogels and using either contact or tapping mode to investigate whether or not the conjugate does in fact produce an aggrecan-like structure when the CS chains do not collapse into the fibrillar network.

6.3 Conclusion

In conclusion, this study showed the successful restoration of certain biomechanical properties within an animal model which represented an early OA state. The study also represented the first successful example of a synthesized self-assembling peptide-GAG conjugate utilising reductive amination of the reducing end of the GAG and CuAAC to covalently link the peptide and GAG together in a manner that did not disrupt the self-assembly of the base peptide. The challenges encountered in achieving this were the disparity between classic methods of purification for peptide synthesis and that employed for polysaccharide synthesis, which was further compounded by the propensity of the peptides to self-assemble making all purification steps difficult. The incorporation of the conjugate into the matrix demonstrated significant increase in the material properties of the hydrogel in terms of strength, where in certain compositions the observed material properties were more commonly observed in non-reversible covalently cross-linked polymer systems – in the order of MPa rather than kPa. The injection of these hydrogels in a monomeric manner into GAG depleted tissue, along with self-assembly *in situ* showed restoration of resistance to deformation within the tissue – up to 80%, which has not been observed previously with a reversible soft matter system. The characterisation of the interaction between the hydrogel and the cartilage tissue needs to be further investigated however, as well as a more detailed analysis of the interaction between the base peptide and the peptide-CS conjugate in terms of the effect the permanent incorporation has on the self-assembling properties of the peptide. The future work aside, this study demonstrated that the hypothesis to permanently incorporate the CS within the GAG depleted tissue did restore the biomechanics of the tissue, highlighting that the entrapment of CS within the cartilage matrix using self-assembling peptides as a delivery and support system has the potential for an early stage intervention treatment for osteoarthritic cartilage. The success of this work overcame the challenge of delivering CS into the matrix directly and being able to enable the matrix to retain the CS during a loading cycle. The restoration reported in this study indicates there could be significant clinical interest for an intervention as effective, yet minimally

invasive as a simple injection into deteriorated articular cartilage. The advantage this method has over current treatments is the minimal recovery time along with potentially minimal periods of inactivity as well as the ability to repeat the treatment in the future countless times.

Chapter 7

Bibliography

. Available: www.arthritis.org [Accessed 27/06/2014 2014].

Elucidation of Adaptive Lubrication Mechanism with Low Friction and Minimum Wear in Natural Synovial Joints and Development of Artificial Hydrogel Cartilage and Super Lubricity Based on Bionic Design [Online]. Available: <http://bio.mech.kyushu-u.ac.jp/SPR/research-en.html> [Accessed 20/07/2014 2014].

2004. *Functional Tissue Engineering*, Springer.

ABARRATEGI, A., LOPIZ-MORALES, Y., RAMOS, V., CIVANTOS, A., LOPEZ-DURAN, L., MARCO, F. & LOPEZ-LACOMBA, J. L. 2010. Chitosan scaffolds for osteochondral tissue regeneration. *J Biomed Mater Res A*, 95, 1132-41.

AEBY, P., SIEBER, T., BECK, H., GERBERICK, G. F. & GOEBEL, C. 2009. Skin sensitization to p-phenylenediamine: the diverging roles of oxidation and N-acetylation for dendritic cell activation and the immune response. *Journal of Investigative Dermatology*, 129, 99-109.

AGGELI, A. 2001a. Hierarchical self-assembly of chiral rod-like molecules as a model for peptide beta-sheet tapes, ribbons, fibrils and fibers. *PNAS*, 98, 11857-11862.

AGGELI, A., BELL, M., BODEN, N., CARRICK, L. M., STRONG, A. E., 2003a. Self-Assembling Peptide Polyelectrolyte β -Sheet Complexes Form Nematic Hydrogels. *Angewandte Chemie*, 115, 5761-5764.

AGGELI, A., BELL, M., BODEN, N., KEEN, J. N., KNOWLES, P. F., MCLEISH, T. C. B., PITKEATHLY, M., RADFORD, S. E., 1997. Responsive gels formed by spontaneous self-assembly of peptides into polymeric beta-sheet tapes. *Nature*, 386, 259-263.

AGGELI, A., BELL, M., BODEN, N., CARRICK, L. M., STRONG, A. E., 2003b. Self-assembling peptide polyelectrolyte beta-sheet complexes form nematic hydrogels. *Angew Chem Int Ed Engl*, 42, 5603-6.

AGGELI, A., NYRAKOVA, I. A., BELL, M., HARDING, R., CARRICK, L. M., SEMENOV, A. N., BODEN, N., 2001b. Hierarchical self-assembly of chiral rod-like molecules as a model for peptide beta-sheet tapes, ribbons, fibrils, and fibers. *Proc Natl Acad Sci U S A*, 98, 11857-62.

AGGELI, A., NYRKOVA, I. A., BELL, M., HARDING, R., CARRICK, L., MCLEISH, T. C., SEMENOV, A. N. & BODEN, N. 2001. Hierarchical self-assembly of chiral rod-like molecules as a model for peptide beta-sheet tapes, ribbons, fibrils, and fibers. *Proc Natl Acad Sci U S A*, 98, 11857-62.

AHERN, B., PARVIZI, J., BOSTON, R. & SCHAER, T. 2009. Preclinical animal models in single site cartilage defect testing: a systematic review. *Osteoarthritis and cartilage*, 17, 705-713.

AIGNER, J., HUTZLER, P., CAMPOCCIA, D., PAVESIO, A., HAMMER, C., KASTENBAUER, E. AND NAUMANN, A., 1998. Cartilage tissue engineering with novel nonwoven structured biomaterial based on hyaluronic acid benzyl ester. *Journal of Biomedical Materials Research* 42, 172-181.

AIGNER, T., BERTLING, W., STÖSS, H., WESELOH, G. & VON DER MARK, K. 1993. Independent expression of fibril-forming collagens I, II, and III in chondrocytes of human osteoarthritic cartilage. *Journal of Clinical Investigation*, 91, 829.

AMSDEN, B. G., KNIGHT, D. K. AND SHAPKA, S. N., 2007. Methacrylated glycol chitosan as a photopolymerizable biomaterial. *Biomacromolecules*, 8, 3758-3766.

ANDERSON, G. W. & MCGREGOR, A. C. 1957. t-Butyloxycarbonylamino acids and their use in peptide synthesis. *Journal of the American Chemical Society*, 79, 6180-6183.

- ANDRESEN EGUILUZ, R. C., COOK, S. G., BROWN, C. N., WU, F., PACIFICI, N. J., BONASSAR, L. J. & GOURDON, D. 2015. Fibronectin mediates enhanced wear protection of lubricin during shear. *Biomacromolecules*, 16, 2884-2894.
- APPLEYARD, R. C., BURKHARDT, D., GHOSH, P., READ, R., CAKE, M., SWAIN, M. V., 2003. Topographical analysis of the structural, biochemical and dynamic biochemical properties of cartilage in an ovine model of osteoarthritis. *Osteoarthritis and Cartilage*, 11, 65-77.
- APPUKUTTAN, P., DEHAEN, W., FOKIN, V. V. & VAN DER EYCKEN, E. 2004. A microwave-assisted click chemistry synthesis of 1, 4-disubstituted 1, 2, 3-triazoles via a copper (I)-catalyzed three-component reaction. *Organic letters*, 6, 4223-4225.
- ATESHIAN, G., WARDEN, W., KIM, J., GRELSAMER, R. & MOW, V. 1997. Finite deformation biphasic material properties of bovine articular cartilage from confined compression experiments. *Journal of biomechanics*, 30, 1157-1164.
- ATESHIAN, G. A., CHAHINE, N. O., BASALO, I. M. & HUNG, C. T. 2004. The correspondence between equilibrium biphasic and triphasic material properties in mixture models of articular cartilage. *Journal of Biomechanics*, 37, 391-400.
- ATHANASIOU, K. A., DARLING, E. M., HU, J. C., 2009. Articular Cartilage Tissue Engineering. In: ATHANASIOU, K. A. (ed.). University of California.
- AURY-LANDAS, J., MARCELLI, C., LECLERCQ, S., BOUMÉDIENE, K. & BAUGÉ, C. 2016. Genetic determinism of primary early-onset osteoarthritis. *Trends in molecular medicine*, 22, 38-52.
- AYHAN, E., KESMEZACAR, H. & AKGUN, I. 2014. Intraarticular injections (corticosteroid, hyaluronic acid, platelet rich plasma) for the knee osteoarthritis. *World J Orthop*, 5, 351-61.
- BAI, Y. H., LI, J. Y., ZHU, Y. H., XU, J. J. & CHEN, H. Y. 2010. Selective Detection of p-Phenylenediamine in Hair Dyes Based on a Special CE Mechanism Using MnO₂ Nanowires. *Electroanalysis*, 22, 1239-1247.
- BALAKRISHNAN, B. & BANERJEE, R. 2011. Biopolymer-based hydrogels for cartilage tissue engineering. *Chem Rev*, 111, 4453-74.
- BALI, J.-P., COUSSE, H. & NEUZIL, E. 2001. Biochemical basis of the pharmacologic action of chondroitin sulfates on the osteoarticular system. *Seminars in Arthritis and Rheumatism*, 31, 58-68.
- BALI, J. P., COUSSE, H., NEUZIL, E., 2001. Biochemical basis of the pharmacologic action of chondroitin sulfates on osteoarticular system. *Seminars in Arthritis and Rheumatism*, 31, 58-68.
- BARCO, A. 2017. *Self-assembling peptide hydrogels for articular cartilage repair*. University of Leeds.
- BASALO, I. M., CHAHINE, N. O., KAPLUN, M., CHEN, F. H., HUNG, C. T. & ATESHIAN, G. A. 2007a. Chondroitin sulfate reduces the friction coefficient of articular cartilage. *J Biomech*, 40, 1847-54.
- BASALO, I. M., CHAHINE, N. O., KAPLUN, M., CHEN, F. H., HUNG, C. T. & ATESHIAN, G. A. 2007b. Chondroitin sulfate reduces the friction coefficient of articular cartilage. *Journal of biomechanics*, 40, 1847-1854.
- BAYLISS, M. T. 1999. Sulfation of Chondroitin Sulfate in Human Articular Cartilage. THE EFFECT OF AGE, TOPOGRAPHICAL POSITION, AND ZONE OF CARTILAGE ON TISSUE COMPOSITION. *Journal of Biological Chemistry*, 274, 15892-15900.
- BECKER, J. C., DOMSCHKE, W., HERBST, H. AND POHLE, T., 2005. Fibrin glue, healing gastric mucosal injury, and expression of growth factors: results from a human *in vivo* study. *Gastrointestinal Endoscopy*, 61, 560-567.
- BEHRENDT, R., WHITE, P. & OFFER, J. 2016. Advances in Fmoc solid-phase peptide synthesis. *Journal of Peptide Science*, 22, 4-27.

- BELL, C. J., CARRICK, L. M., KATTA, J., JIN, Z., INGHAM, E., AGGELI, A., BODEN, N., WAIGH, T. A. & FISHER, J. 2006. Self-assembling peptides as injectable lubricants for osteoarthritis. *J Biomed Mater Res A*, 78, 236-46.
- BELL, C. J., CARRICK, L. M., KATTA, J., JIN, Z., INGHAM, E., AGGELI, A., BODEN, N., WAIGH, T. A., FISHER, J. 2006. Self-assembling peptides as injectable lubricants for osteoarthritis. *J Biomed Mater Res A*, 78, 236-46.
- BENAM, K. H., DAUTH, S., HASSELL, B., HERLAND, A., JAIN, A., JANG, K.-J., KARALIS, K., KIM, H. J., MACQUEEN, L. & MAHMOODIAN, R. 2015. Engineered in vitro disease models. *Annual Review of Pathology: Mechanisms of Disease*, 10, 195-262.
- BERENBAUM, F. 2013. Osteoarthritis as an inflammatory disease (osteoarthritis is not osteoarthrosis!). *Osteoarthritis Cartilage*, 21, 16-21.
- BERTOLDO, M., NAZZI, S., ZAMPANO, G. & CIARDELLI, F. 2011. Synthesis and photochromic response of a new precisely functionalized chitosan with "clicked" spiropyran. *Carbohydrate polymers*, 85, 401-407.
- BHATTACHARJEE, M., COBURN, J., CENTOLA, M., MURAB, S., BARBERO, A., KAPLAN, D. L., MARTIN, I. & GHOSH, S. 2015. Tissue engineering strategies to study cartilage development, degeneration and regeneration. *Advanced drug delivery reviews*, 84, 107-122.
- BHOSALE, A. M., RICHARDSON, J. B., 2008. Articular cartilage: structure, injuries and review of management. *British Medical Bulletin*, 87, 77-95.
- BINDER, W. H. & SACHSENHOFER, R. 2007. 'Click'chemistry in polymer and materials science. *Macromolecular Rapid Communications*, 28, 15-54.
- BLUTEAU, G., CONROZIER, T., MATHIEU, P., VIGNON, E., HERBAGE, D. & MALLEIN-GERIN, F. 2001. Matrix metalloproteinase-1,-3,-13 and aggrecanase-1 and-2 are differentially expressed in experimental osteoarthritis. *Biochimica et Biophysica Acta (BBA)-General Subjects*, 1526, 147-158.
- BOETTCHER, K., KIENLE, S., NACHTSHEIM, J., BURGKART, R., HUGEL, T. & LIELEG, O. 2016. The structure and mechanical properties of articular cartilage are highly resilient towards transient dehydration. *Acta biomaterialia*, 29, 180-187.
- BOYLE, A. L., BROMLEY, E. H., BARTLETT, G. J., SESSIONS, R. B., SHARP, T. H., WILLIAMS, C. L., CURMI, P. M., FORDE, N. R., LINKE, H., WOOLFSON, D. N. 2012. Squaring the circle in peptide assembly: from fibers to discrete nanostructures by de novo design. *J Am Chem Soc*, 134, 15457-67.
- BOYLE, A. L. & WOOLFSON, D. N. 2011. De novo designed peptides for biological applications. *Chem Soc Rev*, 40, 4295-306.
- BOYLE, A. L. & WOOLFSON, D. N. 2012. Rational Design of Peptide-Based Biosupramolecular Systems.
- BRAND, J., HUHN, T., GROTH, U. & JOCHIMS, J. C. 2006. Nitrosation of Sugar Oximes: Preparation of 2-Glycosyl-1-hydroxydiazene-2-oxides. *Chemistry—A European Journal*, 12, 499-509.
- BRIEF, A. A., MAURER, S. G. & DI CESARE, P. E. 2001. Use of Glucosamine and Chondroitin Sulfate in the Management of Osteoarthritis. *Journal of the American Academy of Orthopaedic Surgeons*, 9, 71-78.
- BROMLEY, E. H., CHANNON, K. J., KING, P. J., MAHMOUD, Z. N., BANWELL, E. F., BUTLER, M. F., CRUMP, M. P., DAFFORN, T. R., HICKS, M. R., HIRST, J. D., RODGER, A., WOOLFSON, D. N. 2010. Assembly pathway of a designed alpha-helical protein fiber. *Biophys J*, 98, 1668-76.
- BRUSTAD, E. M., LEMKE, E. A., SCHULTZ, P. G. & DENIZ, A. A. 2008. A general and efficient method for the site-specific dual-labeling of proteins for single molecule fluorescence resonance energy transfer. *Journal of the American Chemical Society*, 130, 17664-17665.

- BURR, D. B. & GALLANT, M. A. 2012. Bone remodelling in osteoarthritis. *Nature Reviews Rheumatology*, 8, 665-673.
- CAI, X.-D., GOLDE, T. E. & YOUNKIN, S. G. 1993. Release of Excess Amyloid Protein from a Mutant Amyloid Protein Precursor. *SCIENCE-NEW YORK THEN WASHINGTON-*, 259, 514-514.
- CAMPBELL, A. B., PINEDA, M., HARRIS, J. D. & FLANIGAN, D. C. 2016. Return to sport after articular cartilage repair in athletes' knees: A systematic review. *Arthroscopy: The Journal of Arthroscopic & Related Surgery*, 32, 651-668. e1.
- CARNEY, S., BILLINGHAM, M., CATERSON, B., RATCLIFFE, A., BAYLISS, M., HARDINGHAM, T. & MUIR, H. 1992. Changes in proteoglycan turnover in experimental canine osteoarthritic cartilage. *Matrix*, 12, 137-147.
- CARNEY, S. L., BILLINGHAM, M. E., MUIR, H. & SANDY, J. D. 1984. Demonstration of increased proteoglycan turnover in cartilage explants from dogs with experimental osteoarthritis. *Journal of orthopaedic research*, 2, 201-206.
- CARPINO, L. A. 1957. Oxidative Reactions of Hydrazines. IV. Elimination of Nitrogen from 1, 1-Disubstituted-2-arenesulfonylhydrazides1-4. *Journal of the American Chemical Society*, 79, 4427-4431.
- CARPINO, L. A., GHASSEMI, S., IONESCU, D., ISMAIL, M., SADAT-AALAE, D., TRURAN, G. A., MANSOUR, E., SIWRUK, G. A., EYNON, J. S. & MORGAN, B. 2003. Rapid, continuous solution-phase peptide synthesis: application to peptides of pharmaceutical interest. *Organic process research & development*, 7, 28-37.
- CARPINO, L. A. & HAN, G. Y. 1970. 9-Fluorenylmethoxycarbonyl function, a new base-sensitive amino-protecting group. *Journal of the American Chemical Society*, 92, 5748-5749.
- CARRICK, L. M., AGGELI, A., BODEN, N., FISHER, J., INGHAM, E. & WAIGH, T. A. 2007. Effect of ionic strength on the self-assembly, morphology and gelation of pH responsive β -sheet tape-forming peptides. *Tetrahedron*, 63, 7457-7467.
- CARRICK, L. M., AGGELI, A., BODEN, N., FISHER, J., INGHAM, E., WAIGH, T. A., 2007a. Effect of ionic strength on the self-assembly, morphology and gelation of pH responsive beta-sheet tape-forming peptides. *Tetrahedron*, 63, 7457-7467.
- CARRICK, L. M., AGGELI, A., BODEN, N., FISHER, J., INGHAM, E., WAIGH, T. A., 2007b. Effect of ionic strength on the self-assembly, morphology and gelation of pH responsive β -sheet tape-forming peptides. *Tetrahedron*, 63, 7457-7467.
- CASTILLO, G. M., LUKITO, W., WIGHT, T. N. & SNOW, A. D. 1999. The Sulfate Moieties of Glycosaminoglycans Are Critical for the Enhancement of β -Amyloid Protein Fibril Formation. *Journal of neurochemistry*, 72, 1681-1687.
- CAWSTON, T. E. & WILSON, A. J. 2006. Understanding the role of tissue degrading enzymes and their inhibitors in development and disease. *Best Pract Res Clin Rheumatol*, 20, 983-1002.
- CHANDRUDU, S., SIMERSKA, P. & TOTH, I. 2013. Chemical methods for peptide and protein production. *Molecules*, 18, 4373-4388.
- CHARNLEY, J. 1960. The Lubrication of Animal Joints in Relation to Surgical Reconstruction by Arthroplasty. *Annals of the Rheumatic Diseases*, 19, 10-19.
- CHAU, Y., LUO, Y., CHEUNG, A. C., NAGAI, Y., ZHANG, S., KOBLER, J. B., ZEITELS, S. M., LANGER, R., 2008. Incorporation of a matrix metalloproteinase-sensitive substrate into self-assembling peptides- A model for biofunctional scaffolds. *Biomaterials*, 29, 1713-1719.
- CHEN, I., HOWARTH, M., LIN, W. & TING, A. Y. 2005. Site-specific labeling of cell surface proteins with biophysical probes using biotin ligase. *Nature methods*, 2, 99-104.
- CHEN, J. W., LU, S. H., WU, J. Z., GUO, X. M., DUAN, C. M., DONG, L. Z., SONG, Y., ZHANG, J. C., JING, D. Y., WU, L. B., DING, J. D. AND LI, D. X., 2005. *In vivo* chondrogenesis of adult bone-marrow-derived autologous mesenchymal stem cells. *Cell and Tissue Research*, 319, 429-438.

- CHEN, K., HE, P., SIANG, K., TOH, S. L., AND GOH, J. C. H. 2012. A hybrid silk/RADA-based Fibrous Scaffold with Triple Hierachy for Ligament Regeneration. *Tissue Eng Part A*, 18, 1399-1409.
- CHOW, D., NUNALEE, M. L., LIM, D. W., SIMNICK, A. J. AND CHILKOTI, A., 2008. Peptide-based biopolymers in biomedicine and biotechnology. *Materials Science and Engineering R*, 62, 125-155.
- CHUNG, C., 2008. Engineering cartilage tissue. *Advanced Drug Delivery Reviews*, 60, 243-262.
- CHUNG, C., MAUCK, R. L. AND BURDICK, J. A., 2009. The influence of degradation characteristics of hyaluronic acid hydrogels on *in vitro* neocartilage formation by mesenchymal stem cells. *Biomaterials*, 30, 4287.
- CIEPLA, P., KONITSIOTIS, A. D., SERWA, R. A., MASUMOTO, N., LEONG, W. P., DALLMAN, M. J., MAGEE, A. I. & TATE, E. W. 2014. New chemical probes targeting cholesterylation of Sonic Hedgehog in human cells and zebrafish. *Chemical Science*, 5, 4249-4259.
- CITRON, M., VIGO-PELFREY, C., TEFLOW, D. B., MILLER, C., SCHENK, D., JOHNSTON, J., WINBLAD, B., VENIZELOS, N., LANNFELT, L. & SELKOE, D. J. 1994. Excessive production of amyloid beta-protein by peripheral cells of symptomatic and presymptomatic patients carrying the Swedish familial Alzheimer disease mutation. *Proceedings of the National Academy of Sciences*, 91, 11993-11997.
- COLLINS, J. M., SINGH, S. K. & VANIER, G. S. 2012. Microwave technology for solid phase peptide synthesis-It's not just for difficult peptides. *CHIMICA OGGI-CHEMISTRY TODAY*, 30, 26-29.
- COOK, J., HUNG, C., KUROKI, K., STOKER, A., COOK, C., PFEIFFER, F., SHERMAN, S. & STANNARD, J. 2014. Animal models of cartilage repair. *Bone and Joint Research*, 3, 89-94.
- CREAMER, P., SHARIF, M., GEORGE, E., MEADOWS, K., CUSHNAGHAN, J., SHINMEI, M. & DIEPPE, P. 1994. Intra-articular hyaluronic acid in osteoarthritis of the knee: an investigation into mechanisms of action. *Osteoarthritis and Cartilage*, 2, 133-140.
- CUI, H., WEBBER, M. J., STUPP, S. I. 2010a. Self-assembly of peptide amphiphiles: from molecules to nanostructures to biomaterials. *Biopolymers*, 94, 1-18.
- CUI, H., WEBBER, M. J., STUPP, S. I., 2010b. Self-assembly of peptide amphiphiles: from molecules to nanostructures to biomaterials. *Biopolymers*, 94, 1-26.
- CUMPSTEY, I. 2013. Chemical modification of polysaccharides. *ISRN organic chemistry*, 2013.
- DANIEL, M. 2014. Boundary cartilage lubrication: Review of current concepts. *Wiener Medizinische Wochenschrift*, 164, 88-94.
- DAS, A. K., HIRST, A. R.,ULIJN, R. V., 2009. Evolving nanomaterials using enzyme-driven dynamic peptide libraries (eDPL). *Faraday Discussions*, 143, 293-303.
- DAVIES, R. P. & AGGELI, A. 2011. Self-assembly of amphiphilic beta-sheet peptide tapes based on aliphatic side chains. *J Pept Sci*, 17, 107-14.
- DAVIES, R. P. W., AGGELI, A., BEEVERS, A. J., BODEN, N., CARRICK, L. M., FISHWICK, C. W. G., MCLEISH, T. C. B., NYRKOVA, I. & SEMENOV, A. N. 2006. Self-assembling β -Sheet Tape Forming Peptides. *Supramolecular Chemistry*, 18, 435-443.
- DEFAIL, A. J., IZZO, N. AND MARRA, K.G., 2006. Controlled release of bioactive TGF-beta 1 from microspheres embedded within biodegradable hydrogels. *Biomaterials*, 27, 1579-1585.
- DIEPPE, P. A. & LOHMANDER, L. S. 2005. Pathogenesis and management of pain in osteoarthritis. *The Lancet*, 365, 965-973.
- DOHERTY, M., WATT, I. & DIEPPE, P. 1983. Influence of primary generalised osteoarthritis on development of secondary osteoarthritis. *The Lancet*, 322, 8-11.
- DOWSON, D. 1967. Models of Lubrication in Human Joints. *Symposium on Lubrication and Wear in Living and Artificial Human Joints*. Institution of Mechanical Engineers.

- DOWSON, D. 1990. *Bio-tribology of natural and replacement synovial joints*, Springer.
- DOWSON, D. & JIN, Z.-M. 1986. Micro-elastohydrodynamic lubrication of synovial joints. *Engineering in medicine*, 15, 63-65.
- DUMOND, H., PRESLE, N., POTTIE, P., PACQUELET, S., TERLAIN, B., NETTER, P., GEPSTEIN, A., LIVNE, E. & JOUZEAU, J.-Y. 2004. Site specific changes in gene expression and cartilage metabolism during early experimental osteoarthritis. *Osteoarthritis and cartilage*, 12, 284-295.
- ELASHAL, H. E., COHEN, R. D. & RAJ, M. 2016. Fmoc solid-phase synthesis of C-terminal modified peptides by formation of a backbone cyclic urethane moiety. *Chemical Communications*, 52, 9699-9702.
- ELCHINGER, P.H., FAUGERAS, P.A., BOËNS, B., BROUILLETTE, F., MONTPLAISIR, D., ZERROUKI, R. & LUCAS, R. 2011. Polysaccharides: the "click" chemistry impact. *Polymers*, 3, 1607-1651.
- ELISSEFF, J., FU, K., BLUNK, B. T. AND LANGER, R., 2001. Controlled-release of IGF-1 and TGF-beta 1 in a photopolymerizing hydrogel for cartilage tissue engineering. *Journal of Orthopaedic Research*, 19, 1098-1104.
- ERICKSON, G. R., FRANKLIN, D. M., RICE, H. E., AWAD, H. AND GUILAK, F., 2002. Chondrogenic potential of adipose tissue-derived stromal cells *in vitro* and *in vivo* *Biochemical and Biophysical Research Communications*, 290, 763-769.
- ESLAHI, N., ABDORAHIM, M. & SIMCHI, A. A. 2016. Smart Polymeric Hydrogels for Cartilage Tissue Engineering: A Review on the Chemistry and Biological Functions. *Biomacromolecules*.
- FAJARDO, A. R., GUERRY, A., BRITTA, E. A., NAKAMURA, C. V., MUNIZ, E. C., BORSALI, R. & HALILA, S. 2014. Sulfated glycosaminoglycan-based block copolymer: preparation of biocompatible chondroitin sulfate-b-poly (lactic acid) micelles. *Biomacromolecules*, 15, 2691-2700.
- FELSON, D. T. & HODGSON, R. 2014. Identifying and treating preclinical and early osteoarthritis. *Rheumatic Disease Clinics of North America*, 40, 699-710.
- FERMOR, H., MCLURE, S., TAYLOR, S., RUSSELL, S., WILLIAMS, S., FISHER, J. & INGHAM, E. 2015a. Biological, biochemical and biomechanical characterisation of articular cartilage from the porcine, bovine and ovine hip and knee. *Bio-Medical Materials and Engineering*, 25, 381-395.
- FERMOR, H. L., RUSSELL, S. L., WILLIAMS, S., FISHER, J. & INGHAM, E. 2015b. Development and characterisation of a decellularised bovine osteochondral biomaterial for cartilage repair. *Journal of Materials Science: Materials in Medicine*, 26, 1-11.
- FERNANDES, R. J., WILKIN, D. J., WEIS, M. A., WILCOX, W. R., COHN, D. H., RIMOIN, D. L., EYRE, D. R., 1998. Incorporation of structurally defective type II collagen into cartilage matrix in Kniest chondrodysplasia. *Archives of biochemistry and biophysics*, 355, 282-290.
- FISCHER, E. & FOURNEAU, E. 1901. Ueber einige derivate des glykocolls. *Berichte der deutschen chemischen Gesellschaft*, 34, 2868-2877.
- FISHER, J. P., MIKOS, A. G., BRONZINO, J. D., PETERSON, D. R., 2013. *Tissue Engineering Principles and Practices*, CRC Press.
- FLETCHER, J. M., BOYLE, AIMEE L., BRUNING, MARC, BARTLETT, GAIL J., VINCENT, THOMAS L., ZACCAI, NATHAN R., ARMSTRONG, CRAIG T., BROMLEY, ELIZABETH H. C., BOOTH, PAULA J., BRADY, R. LEO, THOMSON, ANDREW R., WOOLFSON, DEREK N. 2012. A Basis Set of de Novo Coiled-Coil Peptide Oligomers for Rational Protein Design and Synthetic Biology. *ACS Synthetic Biology*, 1, 240-250.
- FLOMAN, Y., EYRE, D. R., GLIMCHER, M. J., 1980. Induction of osteoarthrosis in the rabbit knee joint: biochemical studies on the articular cartilage. *Clinical Orthoptometry*, 147, 278-286.
- FORSEY, R. W., FISHER, J., THOMPSON, J., STONE, M. H., BELL, C. & INGHAM, E. 2006. The effect of hyaluronic acid and phospholipid based lubricants on friction within a human cartilage damage model. *Biomaterials*, 27, 4581-4590.

- FOUNDATION, N. 2002. *Tissue Engineering of Cartilage and Bone*, Wiley.
- FRASER, P. E., NGUYEN, J. T., CHIN, D. T. & KIRSCHNER, D. A. 1992. Effects of Sulfate Ions on Alzheimer β /A4 Peptide Assemblies: Implications for Amyloid Fibril-Proteoglycan Interactions. *Journal of neurochemistry*, 59, 1531-1540.
- FRENCH, M. M., CANSECO, J. AND ATHANASIOU, K. A., 2004. Chondrogenic differentiation of adult dermal fibroblasts. *Annals of Biomedical Engineering*, 32, 50-56.
- GAFFEN, J. D., BAYLISS, M. T. & MASON, R. M. 1997. Elevated aggrecan mRNA in early murine osteoarthritis. *Osteoarthritis and Cartilage*, 5, 227-233.
- GAUT, C. & SUGAYA, K. 2015. Critical review on the physical and mechanical factors involved in tissue engineering of cartilage. *Regenerative medicine*, 10, 665-679.
- GENOVE, E., SHEN, C., ZHANG, S., SEMINO, C. E., 2005. The effect of functionalized self-assembling peptide scaffolds on human aortic endothelial cell function. *Biomaterials*, 26, 3341-3351.
- GILBERT, T. W., SELLARO, T. L., BADYLAK, S. F., 2006. Decellularization of tissues and organs. *Biomaterials*, 27, 3675-3683.
- GLOWACKI, J. & THORNHILL, T. S. Osteoporosis and Osteopenia in Patients with Osteoarthritis.
- GOMIS, A., PAWLAK, M., BALAZS, E. A., SCHMIDT, R. F. & BELMONTE, C. 2004. Effects of different molecular weight elastoviscous hyaluronan solutions on articular nociceptive afferents. *Arthritis & Rheumatism*, 50, 314-326.
- GORI, A. & LONGHI, R. 2016. Chemoselective Strategies to Peptide and Protein Bioprobes Immobilization on Microarray Surfaces. *Peptide Microarrays: Methods and Protocols*, 145-156.
- GRENIER, S., BHARGAVA, M. M. & TORZILLI, P. A. 2014. An in vitro model for the pathological degradation of articular cartilage in osteoarthritis. *Journal of biomechanics*, 47, 645-652.
- GRIFFIN, D. J., VICARI, J., BUCKLEY, M. R., SILVERBERG, J. L., COHEN, I. & BONASSAR, L. J. 2014. Effects of enzymatic treatments on the depth-dependent viscoelastic shear properties of articular cartilage. *Journal of Orthopaedic Research*, 32, 1652-1657.
- GUVENTIREN, M., LU, H. D., BURDICK, J. A., 2012. Shear-thinning hydrogels for biomedical applications. *Soft Matter*, 8, 260-273.
- HAMADA, K., HIROSE, M., YAMASHITA, T., OHGUSHI, H. 2007. Spatial distribution of mineralized bone matrix produced by marrow mesenchymal stem cells in self-assembling peptide hydrogel scaffold. *Journal of Biomedical Materials Research Part A*.
- HAMADA K., E. A. 2007. Spatial distribution of mineralized bone matrix produced by marrow mesenchymal stem cells in self-assembling peptide hydrogel scaffold. *Journal of Biomedical Materials Research Part A*, 128-136.
- HAMBACH, L., NEUREITER, D., ZEILER, G., KIRCHNER, T., AIGNER, T., 1998. Severe disturbance of the distribution and expression of type VI collagen chains in osteoarthritic articular cartilage. *Arthritis & Rheumatism*, 41, 986-996.
- HARTGERINK, J. D., BENIASH, E., STUPP, S.I. 2001. Self-assembly and mineralization of peptide-amphiphile nanofibers. *Science*, 294, 1684-1688.
- HAYAMI, T., FUNAKI, H., YAOEDA, K., MITUI, K., YAMAGIWA, H., TOKUNAGA, K., HATANO, H., KONDO, J., HIRAKI, Y. & YAMAMOTO, T. 2003. Expression of the cartilage derived anti-angiogenic factor chondromodulin-I decreases in the early stage of experimental osteoarthritis. *The Journal of rheumatology*, 30, 2207-2217.
- HILBICH, C., KISTERS-WOIKE, B., REED, J., MASTERS, C. L. & BEYREUTHER, K. 1991. Aggregation and secondary structure of synthetic amyloid β A4 peptides of Alzheimer's disease. *Journal of molecular biology*, 218, 149-163.

- HOLMES, T. C. 2002. Novel peptide-based biomaterial scaffolds for tissue engineering. *TRENDS in Biotechnology*, 20, 16-21.
- HOLMES, T. C., DE LACALLE, S., SU, X., LIU, G., RICH, A., ZHANG, S. 2000a. Extensive neurite outgrowth and active synapse formation on self-assembling peptide scaffolds *PNAS*, 97, 6728-6733.
- HOLMES, T. C., DE LACALLE, S., SU, X., LIU, G., RICH, A., ZHANG, S. 2000b. Extensive neurite outgrowth and active synapse formation on self-assembling peptide scaffolds. *PNAS*, 97, 6728-6733.
- HORII, A., WANG, X., GELAIN, F., ZHANG, S., 2007a. Biological Designer Self-Assembling Peptide Nanofiber Scaffolds Significantly Enhance Osteoblast Proliferation, Differentiation and 3-D Migration. *PLoS one*, 2, 1-9.
- HORII, A., WANG, X., GELAIN, F., ZHANG, S., 2007b. Biological designer self-assembling peptide nanofiber scaffolds significantly enhance osteoblast proliferation, differentiation and 3-D migration. *PLoS one*, 2, 1-9.
- HOSSEINI, S., VELDINK, M., ITO, K. & VAN DONKELAAR, C. 2013. Is collagen fiber damage the cause of early softening in articular cartilage? *Osteoarthritis and Cartilage*, 21, 136-143.
- HOSSEININIA, S., LINDBERG, L. R. & DAHLBERG, L. E. 2013. Cartilage collagen damage in hip osteoarthritis similar to that seen in knee osteoarthritis; a case-control study of relationship between collagen, glycosaminoglycan and cartilage swelling. *BMC musculoskeletal disorders*, 14, 1.
- HOSSEININIA, S., WEIS, M., RAI, J., KIM, L., FUNK, S., DAHLBERG, L. & EYRE, D. 2016. Evidence for enhanced collagen type III deposition focally in the territorial matrix of osteoarthritic hip articular cartilage. *Osteoarthritis and Cartilage*, 24, 1029-1035.
- HOSSEINKHANI, H., HONG, P.-D. & YU, D.-S. 2013. Self-assembled proteins and peptides for regenerative medicine. *Chemical reviews*, 113, 4837-4861.
- HU, X., LI, D., ZHOU, F. & GAO, C. 2011. Biological hydrogel synthesized from hyaluronic acid, gelatin and chondroitin sulfate by click chemistry. *Acta biomaterialia*, 7, 1618-1626.
- HU, X., LI, D., ZHOU, F., GAO, C., 2011. Biological hydrogel synthesized from hyaluronic acid, gelatin and chondroitin sulfate by click chemistry. *Acta biomaterialia*, 7, 1618-1626.
- HUANG, C.Y., STANKIEWICZ, A., ATESHIAN, G. A. & MOW, V. C. 2005. Anisotropy, inhomogeneity, and tension-compression nonlinearity of human glenohumeral cartilage in finite deformation. *Journal of biomechanics*, 38, 799-809.
- HUANG, J. I., JONES, N. F., ZHU, M., LORENZ, H. P., HEDRICK, M. H. AND BENHAIM, P., 2004. Chondrogenic potential of multipotential cells from human adipose tissue. *Plastic and Reconstructive Surgery*, 113, 585-594.
- HUANG, Q., HUTMACHER, D. W. AND LEE, E. H., 2002. *In vivo* mesenchymal cell recruitment by a scaffold loaded with transforming growth factor-beta 1 and the potential for *in situ* chondrogenesis. *Tissue Engineering*, 8, 469-482.
- HUEY, D. J., HU, J. C. & ATHANASIOU, K. A. 2012. Unlike bone, cartilage regeneration remains elusive. *Science*, 338, 917-21.
- HUISGEN, R. 1963. 1, 3-dipolar cycloadditions. Past and future. *Angewandte Chemie International Edition in English*, 2, 565-598.
- HUNZIKER, E. B., LIPPUNER, K., KEEL, M. & SHINTANI, N. 2015. An educational review of cartilage repair: precepts & practice-myths & misconceptions-progress & prospects. *Osteoarthritis and Cartilage*, 23, 334-350.
- HUTMACHER, D. W. 2001. Scaffold design and fabrication technologies for engineering tissues—state of the art and future perspectives. *Journal of Biomaterials Science, Polymer Edition*, 12, 107-124.

IFUKU, S., WADA, M., MORIMOTO, M. & SAIMOTO, H. 2011. Preparation of highly regioselective chitosan derivatives via "click chemistry". *Carbohydrate Polymers*, 85, 653-657.

J. W. CHEN., C. Y. W., S. H. LU., J. Z. WU., X. M. GUO., C. M. DUAN., L. Z. DONG., Y. SONG., J. C. ZHANG., D. Y. JING., L. B. WU., J. D. DING., AND D. X. LI. 2005. *In vivo* chondrogenesis of adult bone-marrow-derived autologous mesenchymal stem cells. *Cell and Tissue Research*, 319, 429-438.

JACKSON, D. W. AND SIMON, T. M., 2001. Cartilage Substitutes: Overview of Basic Science and Treatment Options. *Journal of the American Academy of Orthopaedic Surgeons*, 9, 37-51.

JAHN, S., SEROR, J. & KLEIN, J. 2016. Lubrication of Articular Cartilage. *Annual Review of Biomedical Engineering*, 18.

JARRETT, J. T., BERGER, E. P. & LANSBURY JR, P. T. 1993. The carboxy terminus of the beta. amyloid protein is critical for the seeding of amyloid formation: Implications for the pathogenesis of Alzheimer's disease. *Biochemistry*, 32, 4693-4697.

JARRETT, J. T. & LANSBURY, P. T. 1993. Seeding "one-dimensional crystallization" of amyloid: a pathogenic mechanism in Alzheimer's disease and scrapie? *Cell*, 73, 1055-1058.

JAY, G., TORRES, J., WARMAN, M., LADERER, M. & BREUER, K. 2007. The role of lubricin in the mechanical behavior of synovial fluid. *Proceedings of the National Academy of Sciences*, 104, 6194-6199.

JAYAWARNA, V., ALI, M., JOWITT, T. A., MILLER, A. F, SAIANI, A., GOUGH, J. E, ULIJN, R. V 2006. Nanostructured Hydrogels for Three-Dimensional Cell Culture Through Self-Assembly of Fluorenylmethoxycarbonyl-Dipeptides. *Advanced Materials*, 18, 611-614.

JAYAWARNA, V., RICHARDSON, S. M., HIRST, A. R., HODSON, N. W., SAIANI, A., GOUGH, J. E., ULIJN, R. V. 2009. Introducing chemical functionality in Fmoc-peptide gels for cell culture. *Acta Biomaterialia*, 5, 934-943.

JAZRAWI, L. M., ALAIA, M. J., CHANG, G., FITZGERALD, E. F. & RECHT, M. P. 2011. Advances in magnetic resonance imaging of articular cartilage. *Journal of the American Academy of Orthopaedic Surgeons*, 19, 420-429.

JEONG, S. I., LIM, J. I., CHO, S. W., JUNG, Y., SUNG, W. J., KIM, S. H., KIM, Y. H., LEE, Y. M., KIM, B. S., CHOI, C. Y. AND KIM, S. J., 2005. Mechano-active tissue engineering of vascular smooth muscle using pulsatile perfusion bioreactors and elastic PLCL scaffolds. *Biomaterials*, 26, 1405-1411.

JIN, M. & GRODZINSKY, A. J. 2001. Effect of electrostatic interactions between glycosaminoglycans on the shear stiffness of cartilage: a molecular model and experiments. *Macromolecules*, 34, 8330-8339.

JIN, Z. & DOWSON, D. 2011. Development of Early Concepts of Lubrication in Natural Synovial Joints. *Tribology Online*, 6, 168-173.

JOHNSON, C. I., ARGYLE, D. J. & CLEMENTS, D. N. 2016. In vitro models for the study of osteoarthritis. *The Veterinary Journal*, 209, 40-49.

JOHNSON, T. S., ZAPOROJAN, V. V., MESA, J. M., WEINAND, C., RANDOLPH, M. A., BONASSAR, L. J., WINOGRAD, J. M. AND YAREMCHUK, M. J., 2004. Integrative repair of cartilage with articular and nonarticular chondrocytes. *Tissue Engineering*, 10, 1308-1315.

KAKWERE, H., PAYNE, R. J., JOLLIFFE, K. A. & PERRIER, S. 2011. Self-assembling macromolecular chimeras: controlling fibrillization of a β -sheet forming peptide by polymer conjugation. *Soft Matter*, 7, 3754-3757.

KAPOOR, D., LAD, C., VYAS, R. & PATEL, M. 2016. AN OVERVIEW OF VISCOSUPPLEMENTS: THERAPEUTIC MODALITY FOR THE AILMENT OF OSTEOARTHRITIS. *Journal of Drug Delivery and Therapeutics*, 6, 73-78.

- KATTA, J., JIN, Z., INGHAM, E. & FISHER, J. 2009. Chondroitin sulphate: an effective joint lubricant? *Osteoarthritis Cartilage*, 17, 1001-8.
- KAWAMURA, S., KIMURA, T., MAEDA, A., CAPLAN, A. I., SHINO, K. AND OCHI, T., 1998. Articular cartilage repair. Rabbit experiments with a collagen gel-biomatrix and chondrocytes cultured in it. *Acta Orthopaedic Scandanavica*, 69, 56-62.
- KHEIR, E., SHAW, D., 2009. Hyaline Articular Cartilage. *Orthopaedics and Trauma*, 23, 450-455.
- KIENLE, S., BOETTCHER, K., WIEGLEB, L., URBAN, J., BURGKART, R., LIELEG, O. & HUGEL, T. 2015. Comparison of friction and wear of articular cartilage on different length scales. *Journal of biomechanics*, 48, 3052-3058.
- KIM, S. E., CHO, Y. W., CHUNG, H., JEONG, S. Y., LEE, E. B. AND KWON, I. C., 2003. Porous chitosan scaffold containing microspheres loaded with transforming growth factor-beta 1: implications for cartilage tissue engineering. *Journal of Controlled Release*, 91, 1183-1193.
- KIM, J. H. P., Y. W. CHO., H. CHUNG., S. Y. JEONG., E. B. LEE., AND I. C. KWON. 2003. Porous chitosan scaffold containing microspheres loaded with transforming growth factor-beta 1: implications for cartilage tissue engineering. *Journal of Controlled Release*, 91, 1183-1193.
- KIRKHAM, J., FIRTH, A., VERNALS, D., BODEN, N., ROBINSON, C., SHORE, R. C., BROOKES, S. J. & AGGELI, A. 2007. Self-assembling Peptide Scaffolds Promote Enamel Remineralization. *Journal of Dental Research*, 86, 426-430.
- KNAPMAN, T. W., AGGELI, A. & ASHCROFT, A. E. 2008. Critical concentrations of beta-sheet peptide self-assembly quantified directly by nanoelectrospray ionization mass spectrometry. *Rapid Commun Mass Spectrom*, 22, 1611-4.
- KOBAYASHI, K., MATSUZAKA, S., YOSHIDA, Y., MIYAUCHI, S., WADA, Y. & MORIYA, H. 2004. The effects of intraarticularly injected sodium hyaluronate on levels of intact aggrecan and nitric oxide in the joint fluid of patients with knee osteoarthritis. *Osteoarthritis and cartilage*, 12, 536-542.
- KOKUBO, T., KIM, H.-M. & KAWASHITA, M. 2003. Novel bioactive materials with different mechanical properties. *Biomaterials*, 24, 2161-2175.
- KOLB, H. C., FINN, M. & SHARPLESS, K. B. 2001. Click chemistry: diverse chemical function from a few good reactions. *Angewandte Chemie International Edition*, 40, 2004-2021.
- KON, E., ROFFI, A., FILARDO, G., TESEI, G. & MARCACCI, M. 2015. Scaffold-based cartilage treatments: with or without cells? A systematic review of preclinical and clinical evidence. *Arthroscopy: The Journal of Arthroscopic & Related Surgery*, 31, 767-775.
- KRALL, N., DA CRUZ, F. P., BOUTUREIRA, O. & BERNARDES, G. J. 2016. Site-selective protein-modification chemistry for basic biology and drug development. *Nature chemistry*, 8, 103-113.
- KRYSMANN, M. J., CASTELLETTO, V., KELARAKIS, A., HAMLEY, I. W., HULE, R. A., POCHAN, D. J., 2008. Self-Assembly and Hydrogelation of an Amyloid Peptide Fragment. *Biochemistry*, 47, 4597-4605.
- KYLE, S., AGGELI, A., INGHAM, E. & MCPHERSON, M. J. 2009. Production of self-assembling biomaterials for tissue engineering. *Trends Biotechnol*, 27, 423-33.
- KYLE, S., AGGELI, A., INGHAM, E. & MCPHERSON, M. J. 2010. Recombinant self-assembling peptides as biomaterials for tissue engineering. *Biomaterials*, 31, 9395-405.
- KYLE, S., AGGELI, A., INGHAM, E., MCPHERSON, M. J. 2009. Production of self-assembling biomaterials for tissue engineering. *Trends Biotechnol*, 27, 423-33.
- KYLE, S., AGGELI, A., INGHAM, E., MCPHERSON, M. J. 2010. Recombinant self-assembling peptides as biomaterials for tissue engineering. *Biomaterials*, 31, 9395-405.
- KYLE, S., FELTON, S. H., MCPHERSON, M. J., AGGELI, A. & INGHAM, E. 2012. Rational molecular design of complementary self-assembling peptide hydrogels. *Adv Healthc Mater*, 1, 640-5.

- LAI, W., HOU, J. & MOW, V. 1991. A triphasic theory for the swelling and deformation behaviors of articular cartilage. *Journal of biomechanical engineering*, 113, 245-258.
- LALLANA, E., FERNANDEZ-MEGIA, E. & RIGUERA, R. 2009. Surpassing the use of copper in the click functionalization of polymeric nanostructures: a strain-promoted approach. *Journal of the American Chemical Society*, 131, 5748-5750.
- LALLANA, E., RIGUERA, R. & FERNANDEZ-MEGIA, E. 2011. Reliable and efficient procedures for the conjugation of biomolecules through Huisgen azide-alkyne cycloadditions. *Angewandte Chemie International Edition*, 50, 8794-8804.
- LANG, K. & CHIN, J. W. 2014. Bioorthogonal reactions for labeling proteins. *ACS chemical biology*, 9, 16-20.
- LANG, K., DAVIS, L., TORRES-KOLBUS, J., CHOU, C., DEITERS, A. & CHIN, J. W. 2012a. Genetically encoded norbornene directs site-specific cellular protein labelling via a rapid bioorthogonal reaction. *Nature chemistry*, 4, 298-304.
- LANG, K., DAVIS, L., WALLACE, S., MAHESH, M., COX, D. J., BLACKMAN, M. L., FOX, J. M. & CHIN, J. W. 2012b. Genetic encoding of bicyclononynes and trans-cyclooctenes for site-specific protein labeling in vitro and in live mammalian cells via rapid fluorogenic Diels-Alder reactions. *Journal of the American Chemical Society*, 134, 10317-10320.
- LANKE, K., KRENN, B., MELCHERS, W., SEIPELT, J. & VAN KUPPEVELD, F. 2007. PDTC inhibits picornavirus polyprotein processing and RNA replication by transporting zinc ions into cells. *Journal of General Virology*, 88, 1206-1217.
- LEE, J., MACOSKO, C. W. & URRY, D. W. 2001. Elastomeric polypentapeptides cross-linked into matrixes and fibers. *Biomacromolecules*, 2, 170-179.
- LEE, K. H., HWANG, T. S., YI, Y., OH, I. S., LEE, J. Y., CHOI, K. B., CHOI, M. S. AND KIM, S. J., 2001. Regeneration of hyaline cartilage by cell-mediated gene therapy using transforming growth factor beta 1-producing fibroblasts. *Human Gene Therapy*, 12, 1805-1813.
- LEE, S., AND SHIN, H., 2007. Matrices and scaffolds for delivery of bioactive molecules in bone and cartilage tissue engineering. *Advanced drug delivery reviews*, 54, 339-359.
- LEE, S. H. & SHIN, H. 2007. Matrices and scaffolds for delivery of bioactive molecules in bone and cartilage tissue engineering. *Adv Drug Deliv Rev*, 59, 339-59.
- LEE, S. Y., PEREIRA, B. P., YUSOF, N., SELVARATNAM, L., YU, Z., ABBAS, A. A. & KAMARUL, T. 2009. Unconfined compression properties of a porous poly(vinyl alcohol)-chitosan-based hydrogel after hydration. *Acta Biomater*, 5, 1919-25.
- LI, Q., SUN, D. D., WANG, J., LEONG, K. AND ELISSEEFF, J. H., 2004. Photocrosslinkable polysaccharides based on chondroitin sulfate. *Journal of Biomedical Materials Research*, 68, 28-33.
- LI, X., DING, J., ZHUANG, X., CHANG, F., WANG, J. & CHEN, X. 2016. Chitosan-Based Scaffolds for Cartilage Regeneration. *Chitin and Chitosan for Regenerative Medicine*. Springer.
- LI, Y., RUSSELL, A. M., GONZALEZ, K. R., HARDINGHAM, T. E. AND HAWKINS, R. E., 2004. Transduction of passaged human articular chondrocytes with adenoviral, retroviral and lentiviral vectors and the effects of enhanced expression of SOX9. *Tissue Engineering*, 10, 575-584.
- LIPPIELLO, L., HALL, D. & MANKIN, H. J. 1977. Collagen synthesis in normal and osteoarthritic human cartilage. *Journal of Clinical Investigation*, 59, 593.
- LITTLE, C., GHOSH, P. & BELLENGER, C. 1996. Topographic variation in biglycan and decorin synthesis by articular cartilage in the early stages of osteoarthritis: an experimental study in sheep. *Journal of orthopaedic research*, 14, 433-444.
- LIU, C.F., RAO, C. & TAM, J. P. 1996. Orthogonal ligation of unprotected peptide segments through pseudoproline formation for the synthesis of HIV-1 protease analogs. *Journal of the American Chemical Society*, 118, 307-312.

- LIU, L., BUSUTTIL, K., ZHANG, S., YANG, Y., WANG, C., BESENBACHER, F. & DONG, M. 2011. The role of self-assembling polypeptides in building nanomaterials. *Phys Chem Chem Phys*, 13, 17435-44.
- LIU, L., BUSUTTIL, K., ZHANG, S., YANG, Y., WANG, C., BESENBACHER, F., DONG, M., 2011. The role of self-assembling polypeptides in building nanomaterials. *Physical Chemistry Chemical Physics*, 13, 17435-17444.
- LOHMANDER, L. S., DALEN, N., ENGLUND, G., HÄMÄLÄINEN, M., JENSEN, E., KARLSSON, K., ODENSTEN, M., RYD, L., SERNBO, I. & SUOMALAINEN, O. 1996. Intra-articular hyaluronan injections in the treatment of osteoarthritis of the knee: a randomised, double blind, placebo controlled multicentre trial. Hyaluronan Multicentre Trial Group. *Annals of the rheumatic diseases*, 55, 424-431.
- LOMAKIN, A., CHUNG, D. S., BENEDEK, G. B., KIRSCHNER, D. A. & TEPLow, D. B. 1996. On the nucleation and growth of amyloid beta-protein fibrils: detection of nuclei and quantitation of rate constants. *Proceedings of the National Academy of Sciences*, 93, 1125-1129.
- LORENZ, H. & RICHTER, W. 2006. Osteoarthritis: cellular and molecular changes in degenerating cartilage. *Prog Histochem Cytochem*, 40, 135-63.
- LU, X. L., SUN, D. D., GUO, X. E., CHEN, F. H., LAI, W. M., MOW, V. C., 2004. Indentation determined mechanoelectrochemical properties and fixed charge density of articular cartilage. *Annals of Biomedical Engineering*, 32, 370-379.
- MADRY, H., KON, E., CONDELLO, V., PERETTI, G. M., STEINWACHS, M., SEIL, R., BERRUTO, M., ENGBRETSSEN, L., FILARDO, G. & ANGELE, P. 2016. Early osteoarthritis of the knee. *Knee Surgery, Sports Traumatology, Arthroscopy*, 1-10.
- MAHAL, L. K., YAREMA, K. J. & BERTOZZI, C. R. 1997. Engineering chemical reactivity on cell surfaces through oligosaccharide biosynthesis. *Science*, 276, 1125-1128.
- MAJD, S. E., KUIJER, R., KÖWITSCH, A., GROTH, T., SCHMIDT, T. A. & SHARMA, P. K. 2014. Both hyaluronan and collagen type II keep proteoglycan 4 (lubricin) at the cartilage surface in a condition that provides low friction during boundary lubrication. *Langmuir*, 30, 14566-14572.
- MAKRIS, E. A., GOMOLL, A. H., MALIZOS, K. N., HU, J. C. & ATHANASIOU, K. A. 2015. Repair and tissue engineering techniques for articular cartilage. *Nature Reviews Rheumatology*, 11, 21-34.
- MANKIN, H. J. & LIPPIELLO, L. 1971. The glycosaminoglycans of normal and arthritic cartilage. *Journal of Clinical Investigation*, 50, 1712.
- MARIJNISSEN, A., VAN ROERMUND, P., VERZIIL, N., TEKOPPELE, J., BIJLSMA, J. & LAFEBER, F. 2002. Steady progression of osteoarthritic features in the canine groove model. *Osteoarthritis and cartilage*, 10, 282-289.
- MAROUDAS, A. 1979. Physicochemical properties of articular cartilage. *Adult articular cartilage* 2, 2, 215-290.
- MARSHALL, K. W. 2000. Intra-articular hyaluronan therapy. *Current opinion in rheumatology*, 12, 468-474.
- MART, R. J., OSBORNE, R. D., STEVENS, M. M., ULIJN, R. V., 2006. Peptide-based stimuli-responsive biomaterials. *Soft Matter*, 2, 822-835.
- MARTEL-PELLETIER, J. 1998. Pathophysiology of osteoarthritis. *Osteoarthritis and cartilage*, 6, 374-376.
- MARTEL-PELLETIER, J., BOILEAU, C., PELLETIER, J.-P. & ROUGHLEY, P. J. 2008. Cartilage in normal and osteoarthritis conditions. *Best Practice & Research Clinical Rheumatology*, 22, 351-384.
- MATSIKO, A., LEVINGSTONE, T. & O'BRIEN, F. 2013. Advanced Strategies for Articular Cartilage Defect Repair. *Materials*, 6, 637-668.

- MATZAT, S. J., VAN TIEL, J., GOLD, G. E. & OEI, E. H. 2013. Quantitative MRI techniques of cartilage composition. *Quantitative imaging in medicine and surgery*, 3, 162-174.
- MAUDE, S., MILES, D. E., FELTON, S. H., INGRAM, J., CARRICK, L. M., WILCOX, R. K., INGHAM, E. & AGGELI, A. 2011. De novo designed positively charged tape-forming peptides: self-assembly and gelation in physiological solutions and their evaluation as 3D matrices for cell growth. *Soft Matter*, 7, 8085.
- MAUDE, S., TAI, L. R., DAVIES, R. P., LIU, B., HARRIS, S. A., KOCIENSKI, P. J. & AGGELI, A. 2012. Peptide synthesis and self-assembly. *Top Curr Chem*, 310, 27-69.
- MCCUTCHEN, C. W. 1959. Sponge-hydrostatic and weeping bearings. *Nature*, 184, 1284-1285.
- MCDEVITT, C., GILBERTSON, E. & MUIR, H. 1977. An experimental model of osteoarthritis; early morphological and biochemical changes. *Journal of Bone & Joint Surgery, British Volume*, 59, 24-35.
- MCLAURIN, J. & CHAKRABARTTY, A. 1996. Membrane disruption by alzheimer β -amyloid peptides mediated through specific binding to either phospholipids or gangliosides implications for neurotoxicity. *Journal of Biological Chemistry*, 271, 26482-26489.
- MCLAURIN, J., FRANKLIN, T., FRASER, P. E. & CHAKRABARTTY, A. 1998. Structural transitions associated with the interaction of Alzheimer β -amyloid peptides with gangliosides. *Journal of Biological Chemistry*, 273, 4506-4515.
- MCLAURIN, J., FRANKLIN, T., ZHANG, X., DENG, J. & FRASER, P. E. 1999. Interactions of Alzheimer amyloid- β peptides with glycosaminoglycans. *European Journal of Biochemistry*, 266, 1101-1110.
- MERRIFIELD, R. B. 1963. Solid phase peptide synthesis. I. The synthesis of a tetrapeptide. *Journal of the American Chemical Society*, 85, 2149-2154.
- MESA, J. M., WEINAND, C., JOHNSON, T. S., BONASSAR, L., RANDOLPH, M. A., YAREMCHUK, M. J. AND BUTLER, P. E., 2006. Tissue engineering cartilage with aged articular chondrocytes *in vivo*. *Plastic and Reconstructive Surgery*, 118, 41-49.
- MEYER, A. & FISCHER, K. 2015. Oxidative transformation processes and products of para-phenylenediamine (PPD) and para-toluenediamine (PTD)—a review. *Environmental Sciences Europe*, 27, 1-16.
- MIOGGE, N., HARTMANN, M., MAELICKE, C. & HERKEN, R. 2004. Expression of collagen type I and type II in consecutive stages of human osteoarthritis. *Histochemistry and cell biology*, 122, 229-236.
- MOUW, J. K., GULDBERG, R. E., PLAAS, A. H. AND LEVENSTON, M. E., 2005. Variations in matrix composition and GAG fine structure among scaffolds for cartilage tissue engineering. *Osteoarthritis Cartilage*, 13, 828-836.
- MOW, V. C. & HUISKES, R. 2005. *Basic orthopaedic biomechanics & mechano-biology*, Lippincott Williams & Wilkins.
- MOW, V. C., KUEI, S. C., LAI, W. M., ARMSTRONG, C. G., 1980. Biphasic creep and stress relaxation of articular cartilage in compression? Theory and experiments. *Journal of Biomechanical Engineering*, 102, 73-84.
- MUZZARELLI, R. A. A., GRECO, F., BUSILACCHI, A., SOLLAZZO, V. & GIGANTE, A. 2012. Chitosan, hyaluronan and chondroitin sulfate in tissue engineering for cartilage regeneration: A review. *Carbohydrate Polymers*, 89, 723-739.
- NAGY, K. J., GIANO, M. C., JIN, A., POCHAN, D. J., SCHNEIDER, J. P., 2011. Enhanced Mechanical Rigidity of Hydrogels Formed From Enantiomeric Peptide Assemblies. *Journal of American Chemistry Society*, 133, 14975-14977.

NEHRER, S., RAMAPPA, A., YOUNG, G., SHORTKROFF, S., LOUISE, L. K., SLEDGE, C. B., YANNAS, I. V. AND SPECTOR, M., 1997. Matrix collagen type and pore size influence behaviour of seeded canine chondrocytes. *Biomaterials*, 18, 769-776.

NERLICH, A. G., WIEST, I. & VON DER MARK, K. 1993. Immunohistochemical analysis of interstitial collagens in cartilage of different stages of osteoarthritis. *Virchows Archiv B*, 63, 249-255.

NING, X., TEMMING, R. P., DOMMERHOLT, J., GUO, J., ANIA, D. B., DEBETS, M. F., WOLFERT, M. A., BOONS, G. J. & VAN DELFT, F. L. 2010. Protein Modification by Strain-Promoted Alkyne–Nitrene Cycloaddition. *Angewandte Chemie International Edition*, 49, 3065-3068.

NISHIUCHI, Y., INUI, T., NISHIO, H., BÓDI, J., KIMURA, T., TSUJI, F. I. & SAKAKIBARA, S. 1998. Chemical synthesis of the precursor molecule of the Aequorea green fluorescent protein, subsequent folding, and development of fluorescence. *Proceedings of the National Academy of Sciences*, 95, 13549-13554.

NOWAK, A. P., BREEDVELD, V., PAKSTIS, L., OZBAS, B., PINE, D. J., Pochan, D., DEMING, T. J., 2002. Rapidly recovering hydrogel scaffolds from self-assembling diblock copolypeptide amphiphiles. *Nature*, 417, 424-429.

NUKAVARAPU, S. P. & DORCEMUS, D. L. 2013. Osteochondral tissue engineering: current strategies and challenges. *Biotechnol Adv*, 31, 706-21.

NYRKOVA, I., SEMENOV, A., AGGELI, A. & BODEN, N. 2000. Fibril stability in solutions of twisted-sheet peptides: a new kind of micellization in chiral systems. *The European Physical Journal B-Condensed Matter and Complex Systems*, 17, 481-497.

OEGEMA, T. R., DELORIA, L. B., SANDY, J. D. & HART, D. A. 2002. Effect of oral glucosamine on cartilage and meniscus in normal and chymopapain-injected knees of young rabbits. *Arthritis & Rheumatism*, 46, 2495-2503.

OFEK, G., REVELL, C. M., HU, J. C., ALLISON, D. D., GRANDE-ALLEN, K. J. & ATHANASIOU, K. A. 2008. Matrix development in self-assembly of articular cartilage. *PLoS one*, 3, e2795.

ORBACH, R., ADLER-ABRAMOVICH, L., ZIGERSON, S., MIRONI-HARPAZ, I., SELIKTAR, D., GAZIT, E., 2009. Self-Assembled Fmoc-Peptides as a Platform for the Formation of Nanostructures and Hydrogels. *Biomacromolecules*, 10, 2646-2651.

OTT, H. C., CLIPPINGER, B., CONRAD, C., SCHUETZ, C., POMERANTSEVA, I., IKONOMOU, L., KOTTON, D. & VACANTI, J. P. 2010. Regeneration and orthotopic transplantation of a bioartificial lung. *Nature medicine*, 16, 927-933.

OYEN, M. 2014. Mechanical characterisation of hydrogel materials. *International Materials Reviews*, 59, 44-59.

OZBAS, B., RAJAGOPAL, K., HAINES-BUTTERICK, L., SCHNEIDER, J. P., Pochan, D. J., 2007. Reversible Stiffening Transition in Beta-Hairpin Hydrogels Induced by Ion Complexation. *Journal of Physical Chemistry*, 111, 13901-13908.

OZTURK, H., STOFFEL, K., JONES, C. & STACHOWIAK, G. 2004. The effect of surface-active phospholipids on the lubrication of osteoarthritic sheep knee joints: friction. *Tribology Letters*, 16, 283-289.

PAL, K., BANTHIA, A. & MAJUMDAR, D. 2009. Polymeric hydrogels: characterization and biomedical applications. *Designed monomers and polymers*, 12, 197-220.

PANOSSIAN, A., KIRCHHOFF, C. H., RANDOLPH, M. A. AND YAREMCHUK, M. J., 2001. Effects of cell concentration and growth period on articular and ear chondrocyte transplants for tissue engineering. *Plastic and Reconstructive Surgery*, 108, 392-402.

PARTINGTON, L., MORDAN, N., MASON, C., KNOWLES, J., KIM, H., LOWDELL, M., BIRCHALL, M. A. & WALL, I. 2013. Biochemical changes caused by decellularization may compromise mechanical integrity of tracheal scaffolds. *Acta biomaterialia*, 9, 5251-5261.

- PEARLE, A. D., WARREN, R. F., RODEO S. A., 2005. Basic science of articular cartilage and osteoarthritis. *Clin Sports Med*, 24, 1-12.
- PECCHI, E., PRIAM, S., MLADENOVIC, Z., GOSSET, M., SAUREL, A. S., AGUILAR, L., BERENBAUM, F. & JACQUES, C. 2012. A potential role of chondroitin sulfate on bone in osteoarthritis: inhibition of prostaglandin E(2) and matrix metalloproteinases synthesis in interleukin-1beta-stimulated osteoblasts. *Osteoarthritis Cartilage*, 20, 127-35.
- PERERA, J. R., GIKAS, P. D. & BENTLEY, G. 2012. The present state of treatments for articular cartilage defects in the knee. *Ann R Coll Surg Engl*, 94, 381-7.
- PETERSEN, T. H., CALLE, E. A., ZHAO, L., LEE, E. J., GUI, L., RAREDON, M. B., GAVRILOV, K., YI, T., ZHUANG, Z. W. & BREUER, C. 2010. Tissue-engineered lungs for in vivo implantation. *Science*, 329, 538-541.
- PFANDER, D., RAHMANZADEH, R., SCHELLER, E. E., 1999. Presence and distribution of collagen II, collagen I, fibronectin, and tenascin in rabbit normal and osteoarthritic cartilage. *Journal of Rheumatology*, 26, 386-394.
- PIPKORN, R. A. W., P. 2000. NovaGel resins: applications in peptide synthesis. *NoVabiochem Innovations*, 3.
- PITSILLIDES, A. A. & BEIER, F. 2011. Cartilage biology in osteoarthritis--lessons from developmental biology. *Nat Rev Rheumatol*, 7, 654-663.
- PLASS, T., MILLES, S., KOEHLER, C., SCHULTZ, C. & LEMKE, E. A. 2011. Genetically Encoded Copper-Free Click Chemistry. *Angewandte Chemie International Edition*, 50, 3878-3881.
- PUHL, W., BERNAU, A., GREILING, H., KÖPCKE, W., PFÖRRINGER, W., STECK, K. J., ZACHER, J. & SCHARF, H. P. 1993. Intra-articular sodium hyaluronate in osteoarthritis of the knee: a multicenter, double-blind study. *Osteoarthritis and Cartilage*, 1, 233-241.
- RAJAGOPAL, K., LAMM, M. S., HAINES-BUTTERICK, L. A., PCHAN, D. J., SCHNEIDER, J. P., 2009. Tuning the pH Responsiveness of Beta-Hairpin Peptide Folding, Self-Assembly, and Hydrogel Material Formation. *Biomacromolecules*, 10, 2619-2625.
- RAJAGOPAL, K., OZBAS, B., PCHAN, D. J., SCHNEIDER, J. P., 2006. Probing the importance of lateral hydrophobic association in self-assembling peptide hydrogelators. *European Biophysics Journal*, 35, 162-169.
- REYNOLDS, O. 1886. On the Theory of Lubrication and Its Application to Mr. Beauchamp Tower's Experiments, Including an Experimental Determination of the Viscosity of Olive Oil. *Proceedings of the Royal Society of London*, 40, 191-203.
- RIDEOUT, D. 1986. Self-assembling cytotoxins. *Science*, 233, 561-563.
- RILEY, J. M., AGGELI, A., KOOPMANS, R. J. & MCPHERSON, M. J. 2009. Bioproduction and characterization of a pH responsive self-assembling peptide. *Biotechnol Bioeng*, 103, 241-51.
- RILEY, J. M., AGGELI, A., KOOPMANS, R. J., MCPHERSON, M. J. 2009. Bioproduction and characterization of a pH responsive self-assembling peptide. *Biotechnology and Bioengineering*, 103, 241-51.
- SALTZMANN, W. M. 2004. *Tissue Engineering: Principles for the Design of Replacement Organs and Tissues*, Oxford University Press.
- SARGEANT, T. D., APARICIO, C., GOLDBERGER, J. E., CUI, H., STUPP, S. I. 2012. Mineralization of peptide amphiphile nanofibers and its effect on the differentiation of human mesenchymal stem cells. *Acta Biomaterialia*, 8, 2456-2465.
- SARGEANT, T. D., GULER, M. O., OPPENHEIMER, S. M., MATA, A., SATCHEL, R. L., DUNAND, D. C., STUPP, S. I. 2008. Hybrid bone implants: Self-assembly of peptide amphiphile nanofibers within porous titanium. *Biomaterials*, 29, 161-171.

SARZI-PUTTINI, P., CIMMINO, M. A., SCARPA, R., CAPORALI, R., PARAZZINI, F., ZANINELLI, A., ATZENI, F. & CANESI, B. Osteoarthritis: an overview of the disease and its treatment strategies. *Seminars in arthritis and rheumatism*, 2005. Elsevier, 1-10.

SCHUMACHER, B. L., BLOCK, J., SCHMID, T., AYDELOTTE, M. & KUETTNER, K. 1994. A novel proteoglycan synthesized and secreted by chondrocytes of the superficial zone of articular cartilage. *Archives of biochemistry and biophysics*, 311, 144-152.

SEITCHIK, J. L., PEELER, J. C., TAYLOR, M. T., BLACKMAN, M. L., RHOADS, T. W., COOLEY, R. B., REFAKIS, C., FOX, J. M. & MEHL, R. A. 2012. Genetically encoded tetrazine amino acid directs rapid site-specific in vivo bioorthogonal ligation with trans-cyclooctenes. *Journal of the American Chemical Society*, 134, 2898-2901.

SHIN, H. J., CHO, I. H., KIM, Y. J., LEE, Y. J., KIM, I. A., PARK, K. D., YUI, N. AND SHIN, J. W., 2006. Electrospun PLGA nanofiber scaffolds for articular cartilage reconstruction: mechanical stability, degradation and cellular responses under mechanical stimulation *in vitro*. *Journal of Biomaterials Science-Polymer Edition*, 17, 103-119.

SIEBER, P. 1987. An improved method for anchoring of 9-fluorenylmethoxycarbonyl-amino acids to 4-alkoxybenzyl alcohol resins. *Tetrahedron letters*, 28, 6147-6150.

SOLIS, V., IWASITA, T. & GIORDANO, M. 1976. Para-phenylenediamine oxidation at a platinum electrode in acetonitrile solutions. *Journal of Electroanalytical Chemistry and Interfacial Electrochemistry*, 73, 91-104.

SONG, J. J. & OTT, H. C. 2011. Organ engineering based on decellularized matrix scaffolds. *Trends in molecular medicine*, 17, 424-432.

SOPHIA FOX, A. J., BEDI, A., RODEO, S. A., 2009. The basic science of articular cartilage: structure, composition, and function. *Sports Health*, 1, 461-8.

SPILLER, K. L., MAHER, S. A. & LOWMAN, A. M. 2011. Hydrogels for the repair of articular cartilage defects. *Tissue Eng Part B Rev*, 17, 281-99.

SQUIRES, G. R., OKOUNEFF, S., IONESCU, M. & POOLE, A. R. 2003. The pathobiology of focal lesion development in aging human articular cartilage and molecular matrix changes characteristic of osteoarthritis. *Arthritis & Rheumatism*, 48, 1261-1270.

STETSENKO, D. A. & GAIT, M. J. 2000. Efficient conjugation of peptides to oligonucleotides by "native ligation". *The Journal of organic chemistry*, 65, 4900-4908.

STUPP, S. I. 2010. Self-Assembly and Biomaterials. *Nano Letters*, 10, 4783-4786.

TAN, H., CHU, C. R., PAYNE, K. A. & MARRA, K. G. 2009. Injectable in situ forming biodegradable chitosan-hyaluronic acid based hydrogels for cartilage tissue engineering. *Biomaterials*, 30, 2499-2506.

TAY, A. G., SUETTERLIN, R., PIERER, G., HEBERER, M., AND MARTIN, I., 2004. Cell yield, proliferation, and post expansion differentiation capacity of human ear, nasal, and rib chondrocytes. *Tissue Engineering*, 10, 762-770.

TERZI, E., HÖLZEMANN, G. & SEELIG, J. 1995. Self-association of β -amyloid peptide (1-40) in solution and binding to lipid membranes. *Journal of molecular biology*, 252, 633-642.

TESHIMA, R., ONO, M., YAMASHITA, Y., HIRAKAWA, H., NAWATA, K. & MORIO, Y. 2004. Immunohistochemical collagen analysis of the most superficial layer in adult articular cartilage. *Journal of Orthopaedic Science*, 9, 270-273.

THIEDE, R. M., LU, Y. & MARKEL, M. D. 2012. A review of the treatment methods for cartilage defects. *Vet Comp Orthop Traumatol*, 25, 263-72.

TIBBITT, M. W. & ANSETH, K. S. 2009. Hydrogels as extracellular matrix mimics for 3D cell culture. *Biotechnology and bioengineering*, 103, 655-663.

- TREVINO, R. L., STOIA, J., LAURENT, M. P., PACIONE, C. A., CHUBINSKAYA, S. & WIMMER, M. A. 2016. Establishing a live cartilage-on-cartilage interface for tribological testing. *Biotribology*.
- UEMATSU, K., ISHIMOTO, Y., YAMAUCHI, J., HABATA, T., TAKAKURA, Y., OHGUSHI, H., FUKUCHI, T. AND SATO, M., 2005. Cartilage regeneration using mesenchymal stem cells and a three-dimensional poly-lactic-glycolic acid (PLGA) scaffold. *Biomaterials*, 26, 4273-4279.
- UPADHYAY, K. K., MEINS, J. F. L., MISRA, A., VOISIN, P., BOUCHAUD, V., IBARBOURE, E., SCHATZ, C. & LECOMMANDOUX, S. 2009. Biomimetic doxorubicin loaded polymersomes from hyaluronan-block-poly (γ -benzyl glutamate) copolymers. *Biomacromolecules*, 10, 2802-2808.
- URBAN, J. P. G. 1994. The chondrocyte - a cell under pressure. *British Journal of Rheumatology*, 33, 901-908.
- USHIDA, T., TOITA, K. AND TATEISHI, T., 2002. Three-dimensional seeding of chondrocytes encapsulated in collagen gel into PLLA scaffolds. *Cell Transplant*, 11, 489-494.
- UTTAMAPINANT, C., TANGPEERACHAIKUL, A., GRECIAN, S., CLARKE, S., SINGH, U., SLADE, P., GEE, K. R. & TING, A. Y. 2012. Fast, Cell-Compatible Click Chemistry with Copper-Chelating Azides for Biomolecular Labeling. *Angewandte Chemie International Edition*, 51, 5852-5856.
- VAN BLITTERSWIJK, W. J., VAN DE NES, J. C. & WUISMAN, P. I. 2003. Glucosamine and chondroitin sulfate supplementation to treat symptomatic disc degeneration: biochemical rationale and case report. *BMC Complementary and alternative Medicine*, 3, 1.
- VAN OSCH, G. J. V. M., JAHR, H., KOEVOET, W., NOLST-TRENITE, G. AND VERHAAR, J. A., 2004. Considerations on the use of ear chondrocytes as donor chondrocytes for cartilage tissue engineering. *Biorheology*, 41, 411-421.
- VERMA, G. P. 2001. *Cartilage and Bone. Fundamentals of Histology*, New Delhi, New Age International Limited.
- VIOLA, J., LAL, B. & GRAD, O. 2003. The emergence of tissue engineering as a research field. *National Science Foundation, Arlington, VA*.
- VON DER MARK, K., KIRSCH, T., NERLICH, A., KUSS, A., WESELOH, G., GLÜCKERT, K. & STÖSS, H. 1992. Type X collagen synthesis in human osteoarthritic cartilage. Indication of chondrocyte hypertrophy. *Arthritis & Rheumatism*, 35, 806-811.
- W. J. LI., R. T., C. OKAFOR., A. DERFOUL., K. G. DANIELSON., D. J. HALL., AND R. S. TUAN. 2005. A three-dimensional nanofibrous scaffold for cartilage tissue engineering using human mesenchymal stem cells. *Biomaterials*, 26, 599-609.
- WAMBACH, B. A. AND JOSEPHSON, G. D., 2000. Cartilage tissue engineering using thyroid chondrocytes on a type I collagen matrix. *Laryngoscope*, 110, 2008-2011.
- WAYNE, J., BRODRICK, C. & MUKHERJEE, N. 1998. Measurement of articular cartilage thickness in the articulated knee. *Annals of biomedical engineering*, 26, 96-102.
- WENDELER, M., GRINBERG, L., WANG, X., DAWSON, P. E. & BACA, M. 2013. Enhanced catalysis of oxime-based bioconjugations by substituted anilines. *Bioconjugate chemistry*, 25, 93-101.
- WILLIAMS, R. J., SMITH, A. M., COLLINS, R., HODSON, N., DAS, A. K., ULIJN, R. V., 2008. Enzyme-assisted self-assembly under thermodynamic control. *Nature Nanotechnology*, 4, 19-25.
- WILUSZ, R. E., SANCHEZ-ADAMS, J. & GUILAK, F. 2014. The structure and function of the pericellular matrix of articular cartilage. *Matrix Biology*, 39, 25-32.
- WÖHR, T., WAHL, F., NEFZI, A., ROHWEDDER, B., SATO, T., SUN, X. & MUTTER, M. 1996. Pseudo-prolines as a solubilizing, structure-disrupting protection technique in peptide synthesis. *Journal of the American Chemical Society*, 118, 9218-9227.
- WU, E. C., ZHANG, S., HAUSER, C. A. E., 2011. Self-Assembling Peptides as Cell-Interactive Scaffolds. *Advanced Functional Materials*, 22, 456-468.

- XIA, B., CHEN, D., ZHANG, J., HU, S., JIN, H. & TONG, P. 2014. Osteoarthritis pathogenesis: a review of molecular mechanisms. *Calcified tissue international*, 95, 495-505.
- YAMAGUCHI, M., KOJIMA, K., HAYASHI, N., KAKIZAKI, I., KON, A. & TAKAGAKI, K. 2006. Efficient and widely applicable method of constructing neo-proteoglycan utilizing copper (I) catalyzed 1, 3-dipolar cycloaddition. *Tetrahedron letters*, 47, 7455-7458.
- YAMAGUCHI, M., TAKAGAKI, K., KOJIMA, K., HAYASHI, N., CHEN, F., KAKIZAKI, I., KON, A. & ENDO, M. 2010. Novel proteoglycan glycochemistry: chemoenzymatic synthesis of chondroitin sulfate-containing molecules and its application. *Glycoconjugate journal*, 27, 189-198.
- YANG, X. B., SEBALD, W., CLARKE, N., HOWDLE, S. M., SHAKESHEFF, K. M. AND OREFFO, R. O., 2004. Human osteoprogenitor bone formation using encapsulated bone morphogenetic protein 2 in porous polymer scaffolds. *Tissue Engineering*, 10, 1037-1045.
- YOSHIKUMI, A., FLETCHER, J. M., YU, Z., PERSIKOV, A. V., BARTLETT, G. J., BOYLE, A. L., VINCENT, T. L., WOOLFSON, D. N., BRODSKY, B. 2011. Designed coiled coils promote folding of a recombinant bacterial collagen. *J Biol Chem*, 286, 17512-20.
- YOON, B. S., 2004. Multiple functions of BMPs in chondrogenesis. *Journal of Cell Biochemistry*, 93, 93-103.
- YOUNG, D. A., LAKEY, R. L., PENNINGTON, C. J., JONES, D., KEVORKIAN, L., EDWARDS, D. R., CAWSTON, T. E. & CLARK, I. M. 2005. Histone deacetylase inhibitors modulate metalloproteinase gene expression in chondrocytes and block cartilage resorption. *Arthritis Res Ther*, 7, R503-R512.
- ZHANG, L., MIRAMINI, S., SMITH, D. W., GARDINER, B. S. & GRODZINSKY, A. J. 2015. Time evolution of deformation in a human cartilage under cyclic loading. *Annals of biomedical engineering*, 43, 1166-1177.
- ZHANG, S. 2003. Fabrication of novel biomaterials through molecular self-assembly. *Nature Biotechnology*, 21, 1171-1178.
- ZHAO, W., JIN, X., CONG, Y., LIU, Y. & FU, J. 2013. Degradable natural polymer hydrogels for articular cartilage tissue engineering. *Journal of Chemical Technology & Biotechnology*, 88, 327-339.
- ZHU, W., MOW, V. C., KOOB, T. J. & EYRE, D. R. 1993. Viscoelastic shear properties of articular cartilage and the effects of glycosidase treatments. *Journal of Orthopaedic Research*, 11, 771-781.
- ZUIDEMA, J. M., RIVET, C. J., GILBERT, R. J. & MORRISON, F. A. 2014. A protocol for rheological characterization of hydrogels for tissue engineering strategies. *Journal of Biomedical Materials Research Part B: Applied Biomaterials*, 102, 1063-1073.
-

Chapter 8

Appendices

Appendix 1

Table 1: Equipment

Equipment	Model	Supplier
Automatic Pipettes	Gilson P2-P1000	Anachem Ltd
Balances (Accuracy: 0.01g/0.0001g)	GR200/GX2000	Jencons PLC
Bench top centrifuge	5415R	Eppendorf
Class II safety cabinet	Heraeus 85	Kendro
CO ₂ Incubator	MCO-20AIC	SANYO Biomedical Europe BV
Cryostat	CM3050S	Leica
Flame atomic absorption spectrophotometer	Aanalyst 200	Perkin Elmer
FT-IR spectrometer	Spectrum 100S	Perkin Elmer
Freeze drier	Modulyod-230	Thermo Savant
	Powerdry LL1500	Thermo Heto
	Benchtop BTP 82L	VirTis
Freezer (-20 °C)	Electrolux 3000	Jencons PLC
Fridge	Electrolux ER8817C	Jencons PLC

Fume cupboard/Fume hood	-	Whiteley
Histology cassettes	CMB-160-030R	Thermo Fisher Scientific Ltd
Histology water bath	MH8515	Barnstead
Hot plate	E18.1 hotplate	Raymond A Lamb
Hot wax dispenser	E66 was dispenser	Raymond A Lamb
Incubator	Heraeus	Jencons PLC
Instron material testing machine	3365	Instron
Inverted confocal microscope	LSM 510 META	Zeiss
Linear variable differential transformer (LVDT)	RDP DS-200H	Electrosence
Liquid chromatography – mass spectrometer	HCT-Ultra	Bruker
Liquid nitrogen Dewar	BIO65	Jencons PLC
Luminescence counter and liquid scintillation counter	Packard TopCount NX	Perkin Elmer
Magnetic stirrer	Stuart SB161	Scientific Laboratory Systems Ltd
Mass Spectrometer	MaXis Impact	Bruker
Micro-plate spectrophotometer	Multiscan Spectrum 1500 Chameleon V	Thermo Scientific Hidex
Microscope (Inverted)	Olympus IX71	Microscopes, Medical Diagnostics Systems and Olympus Patient Systems

		Ltd
Microscope (upright)	Olympus BX51	Microscopes, Medical Diagnostics Systems and Olympus Patient Systems
		Ltd
Microtome	RM2125 RTR	Leica Microsystems
Neubauer	MNK-420-010N	Fischer scientific
haemocytometer		
NMR spectrometer	Avance 400	Bruker
	Avance 500	Bruker
Orbital Shaker	IKA KS130 basic	Jencons PLC
Oven (hot air)		
pH meter	Jenway 3010	VWR International
	Docu-pH	Satorus
	CD720	WPA
Piezo-electric force transformer	060-1896-02	Electrosence
Pipette boy	Acu	Integra biosciences
Plate Shaker	IKA KS130 basic	Jencons PLC
Rheometer	Pro Rheometer	Malvern
Slide holder	E102	Raymond A Lamb
Transmission electron microscope	1400	JEOL
Tissue Processor	TP11020	Leica Microsystems

Vortexer	Topmix FB15024	Fisher Scientific
Water Bath	Grant	Jencons PLC
Water purifier	Option 7	ELGA
Wax oven	Windsor E18/31	Scientific Laboratory
		Supplies

Table 2: Chemical Reagents

Chemical/Reagent	Cat No.	Supplier
1,2-Ethenediol	324558	Sigma-Aldrich
1,9 dimethylene blue	34108-8	Sigma-Aldrich
4-ethynylbenzyl alcohol	519235	Sigma-Aldrich
6-Bromohexanoic acid	150452	Sigma-Aldrich
Acetic acid (glacial)	A/0400/PB17	Fisher Scientific
Aniline	242284	Sigma-Aldrich
Anisole	296295	Sigma-Aldrich
ATPLite-M assay	6016941	Perkin-Elmer
Chondroitin sulfate from shark cartilage	C4384	Sigma-Aldrich
Chondroitin sulphate B	C-3788	Sigma-Aldrich
DIAD	225541	Sigma-Aldrich
Diaminoethanetetra-acetic acid disodium salt (EDTA)	E/P140/65	Fisher Scientific Ltd
Dimethyl sulfoxide (DMSO)	D26650	Sigma-Aldrich
Di-sodium hydrogen orthophosphate (anhydrous)	1.06586.0500	Merck Millipore
DPX mountant	RRSP29	Atom Scientific
Dulbecco's minimal essential media (DMEM)	D6546	Sigma-Aldrich
Dulbecco's PBS tablets	BR0014	Oxoid
Eosin Y	1.09844.1000	Merck Millipore
Ethanol	10107	VWR International
Ethanol	E/0555DF/25	Fisher Scientific
Fast green	F7258	Sigma-Aldrich
Fmoc-Arg(Pbf)-OH	852067	Novabiochem
Fmoc-Gln(Trt)-OH	852045	Novabiochem
	47674	Sigma-Aldrich
Fmoc-Glu(OtBu)-OH	852009	Novabiochem
Fmoc-Lys(Mca)-OH	852095	Novabiochem
Fmoc-NH-PEG-COOH	851037	Novabiochem
Fmoc-Orn(Boc)-OH	852015	Novabiochem
Fmoc-Phe-OH	852016	Novabiochem

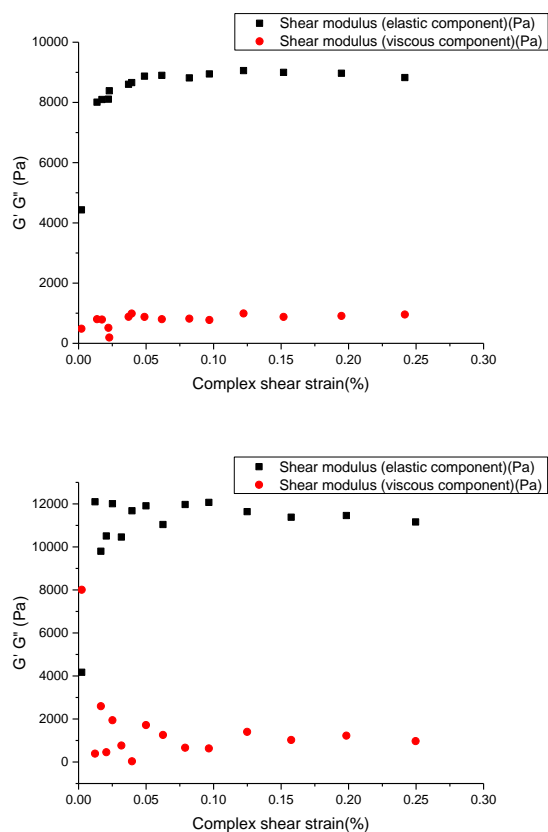
Fmoc-Trp(Boc)-OH	852050	Novabiochem
Foetal bovine serum (FBS)	EU-000	Sera Lab
Formic acid	F-4166	Sigma-Aldrich
Glasgow's minimal essential media (GMEM)	G5154	Sigma-Aldrich
HCTU	04936	Sigma-Aldrich
Hydrazine monohydrate	207942	Sigma-Aldrich
Hydrochloric Acid	H/1200/PB17	Fisher Scientific
Hydrochloric acid (6 M)	2611.500	VWR International
L-cysteine hydrochloride anhydrous	C1276	Sigma-Aldrich
L-Glutamine (200mM)	G7513	Sigma-Aldrich
Mayer's Haematoxylin (Mayer's Haemalum)	RRSP60	Atom Scientific
<i>N,N'</i> -Diisopropylcarbodiimide	D125407	Sigma-Aldrich
<i>N,N</i> -Diisopropylethylamine	387649	Sigma-Aldrich
<i>N</i> -hydroxy phthalimide	H53704	Sigma-Aldrich
NovaSyn® TG Sieber Resin	855013	Novabiochem
Oxyma Pure	851086	Novabiochem
P ₁₁ -4-PEG-Hex-N ₃	-	Cambridge Bioscience
P ₁₁ -8-PEG-Hex-N ₃	-	Cambridge Bioscience
Papain	A3824,0100	Applichem
PBS without Ca ² /Mg ²⁺	D8537	Sigma-Aldrich
Penicillin (5000U/ml) / Streptomycin (5 mg ml ⁻¹)	P4458	Sigma-Aldrich
Phenol	185450	Sigma-Aldrich
Piperidine	411027	Sigma-Aldrich
<i>p</i> -phenylenediamine	P6001	Sigma-Aldrich
Rink Amide Novagel™ Resin	855031	Novabiochem
Rink Amide PEGA Resin	855016	Novabiochem
Safranin O	S305-2 or S305-3	Raymond Lamb
Scott's tap water substitute 10x concentrate	RRSP190	Atom Scientific
Sodium Azide	S2002	Sigma-Aldrich
Sodium cyanoborohydride	156159	Sigma-Aldrich
Sodium di-hydrogen orthophosphate	102454R	VWR International
Sodium formate	30142LN	VWR International
Sodium hydroxide	S/4920/53	Thermo Fisher Scientific Ltd
Sodium hydroxide (6 M)	102525P	VWR International
TFA	808260	Novabiochem
TIPS	233781	Sigma-Aldrich
Tris(2-carboxyethyl)phosphine hydrochloride	C4706	Sigma-Aldrich
Tris[(1-benzyl-1 <i>H</i> -1,2,3-triazol-4-yl)methyl]amine	678937	Sigma-Aldrich
Trypsin/EDTA	T3924	Sigma-Aldrich
Tryptone phosphate broth (TPB)	T8782	Sigma-Aldrich
Weigert Haematoxylin Solution A	RRSP72-D	Atom Scientific
Solution B	RRSP73-D	

Appendix 2: Rheological data

P₁₁-4 only

130 mM Na⁺ buffer

The two amplitude sweeps indicated the LVER laid between 0.05 – 0.2% shear strains, where 0.15% shear strain was selected at which to carry out the frequency sweep at. The frequency sweep was carried out in triplicate to ensure the measured moduli was sample preparation independent. The average moduli obtained was as follows: G' – 15443.1 ± 3104.3 Pa, G'' – 1431.4 ± 330.1 Pa. The data from each amplitude sweep and the average frequency sweep is shown in **Fig A2.1**.



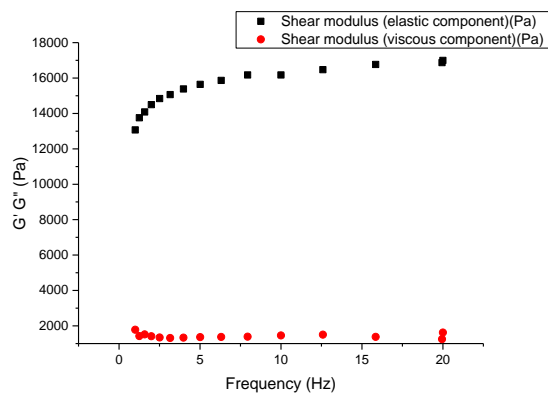


Fig A2.1: Rheological sweeps for P₁₁-4 130 mM Na⁺. A) Amplitude sweep 0.01 – 100% shear strain at 1Hz B) Amplitude sweep 0.01 – 100% shear strain at 20Hz C) Frequency sweep 1-20Hz at 0.15% shear strain – all at 37°C.

P₁₁-4 + CS

230 mM Na⁺ buffer 32:1 P₁₁-4: CS

The two amplitude sweeps indicated the LVER laid between 0.05 – 0.2% shear strains, where 0.15% shear strain was selected at which to carry out the frequency sweep at. The frequency sweep was carried out in triplicate to ensure the measured moduli was sample preparation independent. The average moduli obtained was as follows: $G' - 19198.3 \pm 627.7$ Pa, $G'' - 1770.0 \pm 212.2$ Pa. The data from each amplitude sweep and the average frequency sweep is shown in **Fig A2.2**.

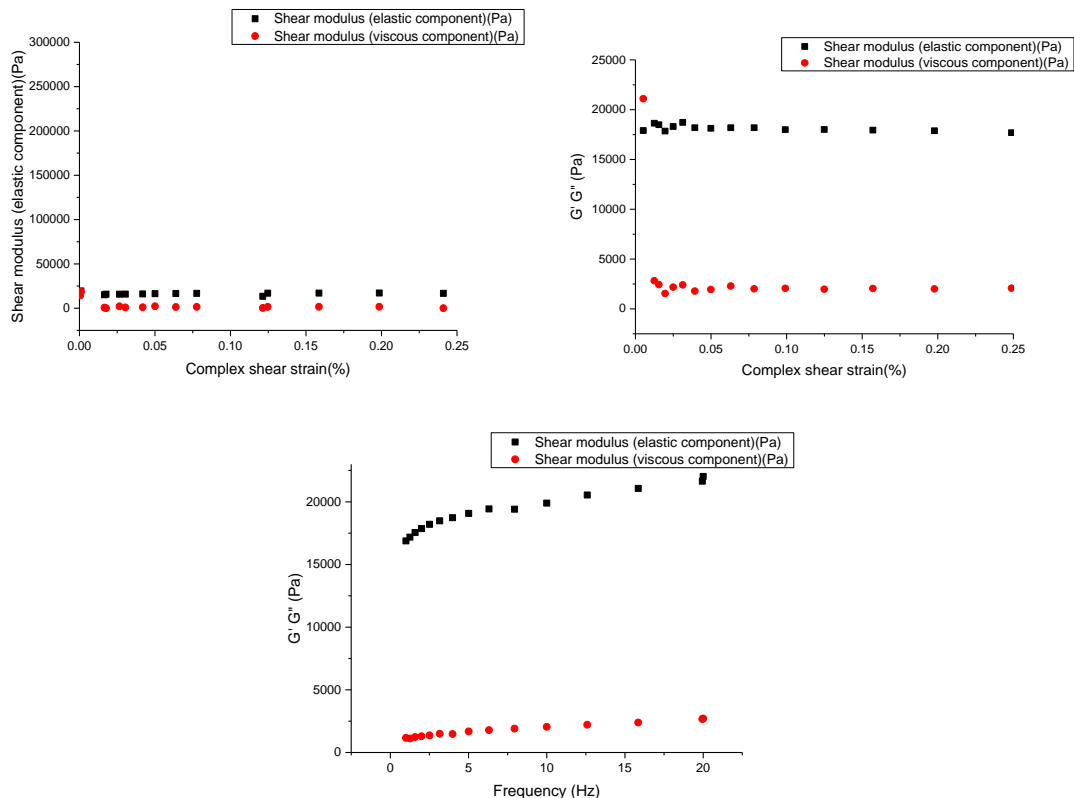


Fig A2.2: Rheological sweeps for P₁₁-4 + CS 32:1 molar ratio 230 mM Na⁺. A) Amplitude sweep 0.01 – 100% shear strain at 1Hz B) Amplitude sweep 0.01 – 100% shear strain at 20Hz C) Frequency sweep 1-20Hz at 0.15% shear strain – all at 37°C.

230 mM Na⁺ buffer 64:1 P₁₁-4: CS

The two amplitude sweeps indicated the LVER laid between 0.05 – 0.1% shear strains, where 0.08% shear strain was selected at which to carry out the frequency sweep at. The frequency sweep was carried out in triplicate to ensure the measured moduli was sample preparation independent. The average moduli obtained was as follows: $G' - 7343.2 \pm 1756.9$ Pa, $G'' - 862.5 \pm 220.3$ Pa. The data from each amplitude sweep and the average frequency sweep is shown in **Fig A2.3**.

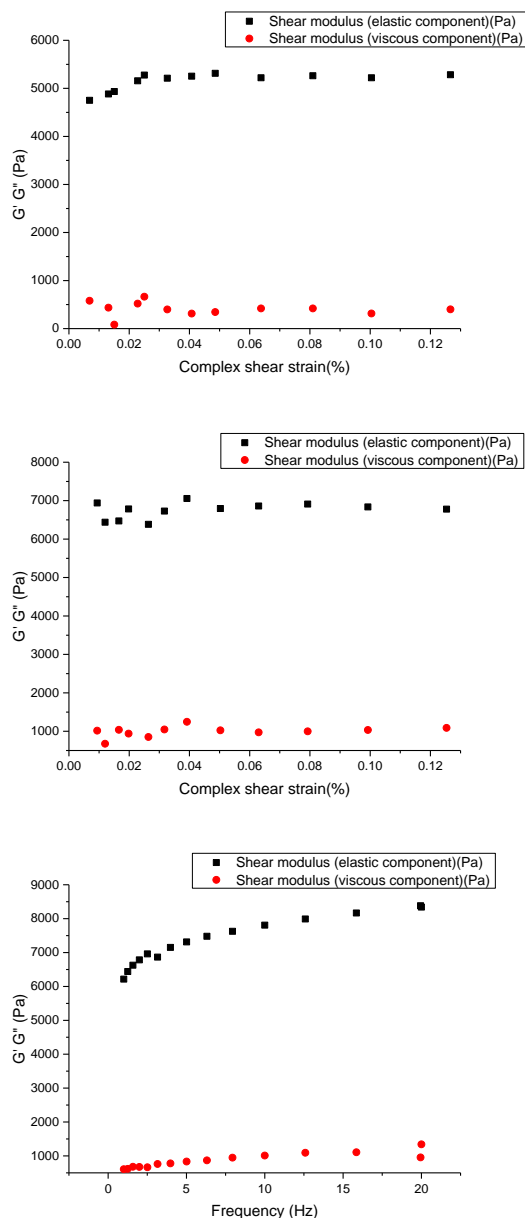


Fig A2.3: Rheological sweeps for P₁₁₋₄ + CS 64:1 molar ratio 230 mM Na⁺. A) Amplitude sweep 0.01 – 100% shear strain at 1Hz B) Amplitude sweep 0.01 – 100% shear strain at 20Hz C) Frequency sweep 1-20Hz at 0.08% shear strain – all at 37°C.

130 mM Na⁺ buffer 32:1 P₁₁₋₄: CS

The two amplitude sweeps indicated the LVER laid between 0.05 – 0.3% shear strains, where 0.25% shear strain was selected at which to carry out the frequency sweep at. The frequency sweep was carried out in triplicate to ensure the measured moduli was sample preparation independent. The average moduli obtained was as follows: $G' - 11579.8 \pm 6312.3$ Pa, $G'' - 1843.3 \pm 977.7$ Pa. The data from each amplitude sweep and the average frequency sweep is shown in **Fig A2.4**.

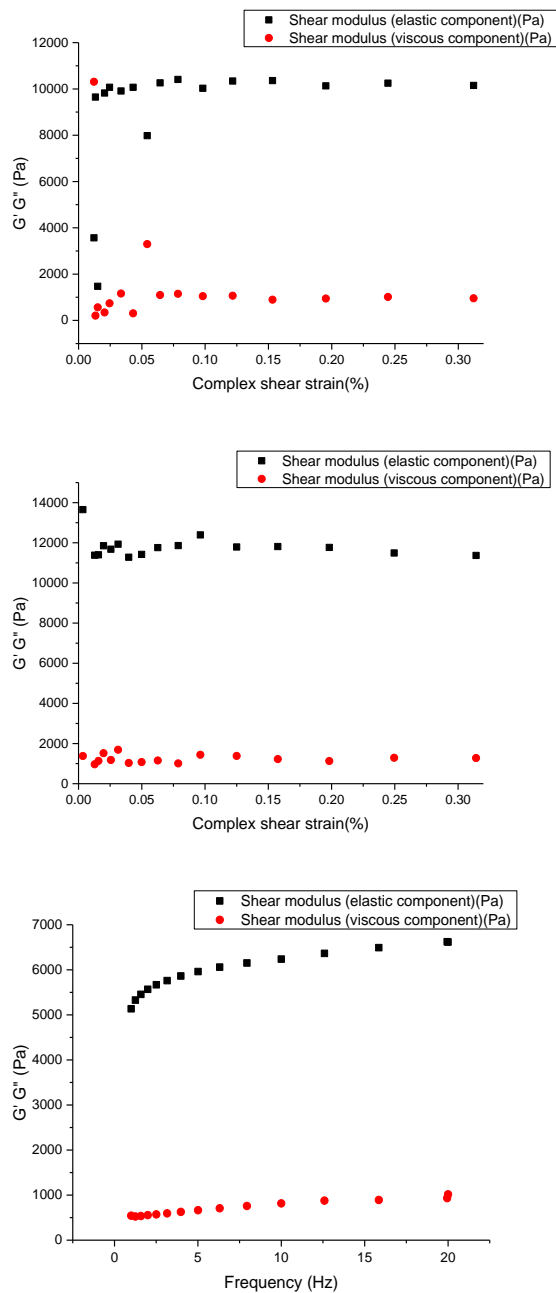


Fig A2.4: Rheological sweeps for P_{11-4} + CS 32:1 molar ratio 130 mM Na^+ . A) Amplitude sweep 0.01 – 100% shear strain at 1Hz B) Amplitude sweep 0.01 – 100% shear strain at 20Hz C) Frequency sweep 1-20Hz at 0.25% shear strain – all at 37°C.

130 mM Na^+ buffer 64:1 P_{11-4} : CS

The two amplitude sweeps indicated the LVER laid between 0.05 – 0.2% shear strains, where 0.15% shear strain was selected at which to carry out the frequency sweep at. The frequency sweep was carried out in triplicate to ensure the measured moduli was sample preparation independent. The average moduli obtained was as follows: $G' - 5952.3 \pm 3816.2$ Pa, $G'' - 707.5$

± 289.3 Pa. The data from each amplitude sweep and the average frequency sweep is shown in Fig A2.5.

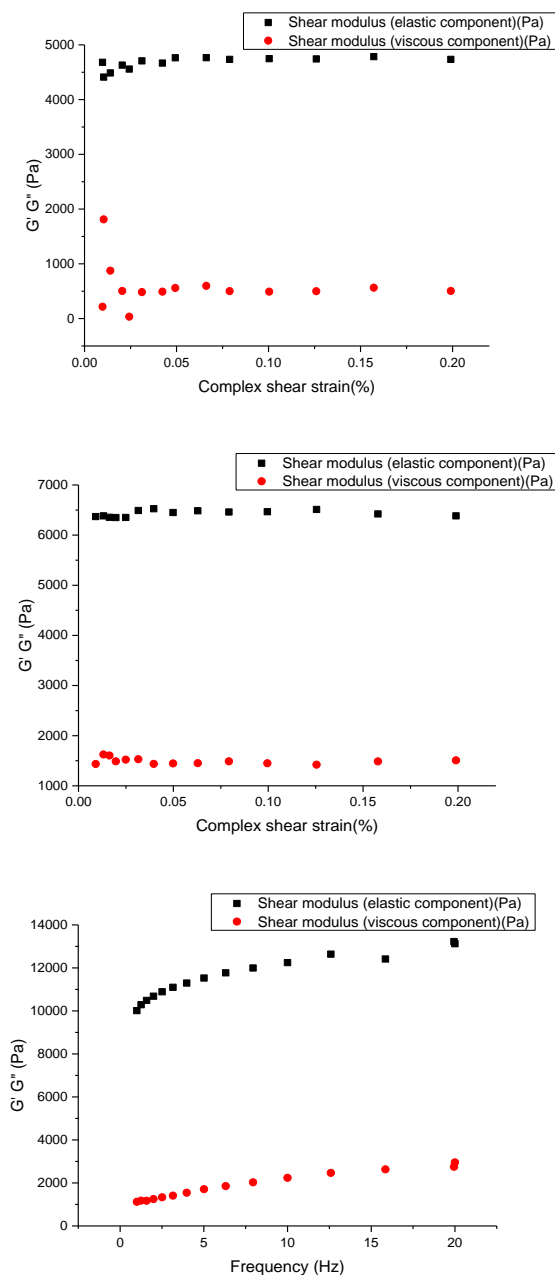


Fig A2.5: Rheological sweeps for P₁₁-4 + CS 64:1 molar ratio 130 mM Na⁺. A) Amplitude sweep 0.01 – 100% shear strain at 1Hz B) Amplitude sweep 0.01 – 100% shear strain at 20Hz C) Frequency sweep 1-20Hz at 0.15% shear strain – all at 37°C.

P₁₁-4 + P₁₁-4-CS

230 mM Na⁺ buffer 32:1 P₁₁-4: P₁₁-4-CS

The two amplitude sweeps indicated the LVER laid between 0.05 – 0.3% shear strains, where 0.23% shear strain was selected at which to carry out the frequency sweep at. The frequency

sweep was carried out in triplicate to ensure the measured moduli was sample preparation independent. The average moduli obtained was as follows: $G' - 234824.4 \pm 12606.0$ Pa, $G'' - 25902.4 \pm 3046.1$ Pa. The data from each amplitude sweep and the average frequency sweep is shown in **Fig A2.6**.

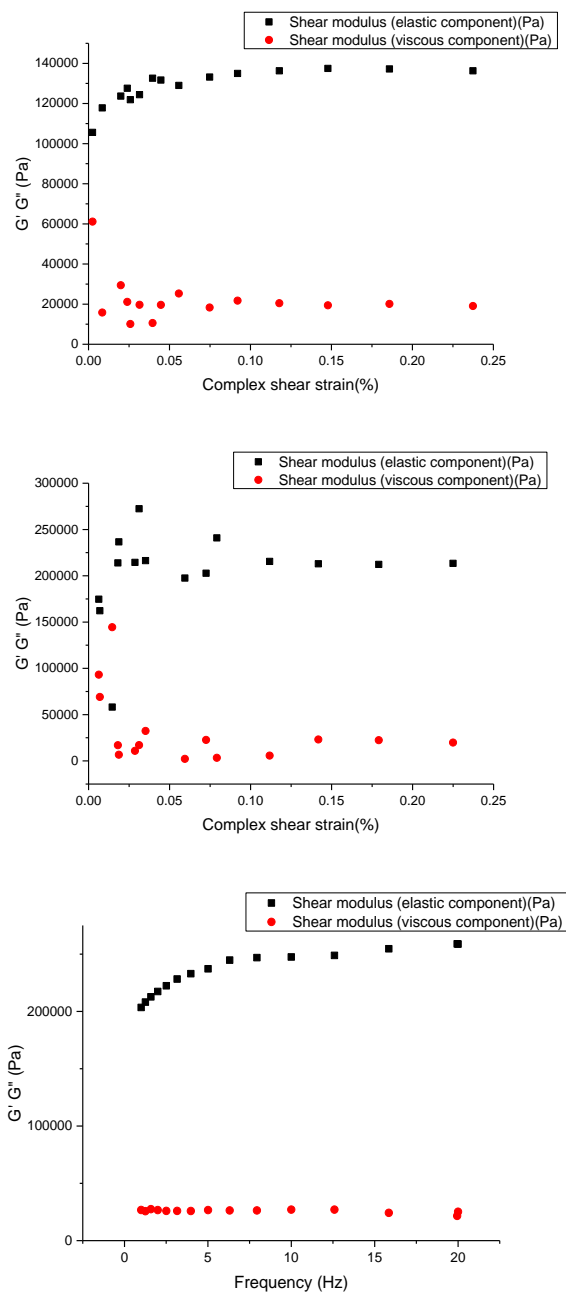


Fig A2.6: Rheological sweeps for $P_{11-4} + P_{11-4-CS}$ 32:1 molar ratio 230 mM Na^+ . A) Amplitude sweep 0.01 – 100% shear strain at 1Hz B) Amplitude sweep 0.01 – 100% shear strain at 20Hz C) Frequency sweep 1–20Hz at 0.23% shear strain – all at 37°C.

230 mM Na⁺ buffer 64:1 P₁₁-4: P₁₁-4-CS

The two amplitude sweeps indicated the LVER laid between 0.05 – 0.3% shear strains, where 0.23% shear strain was selected at which to carry out the frequency sweep at. The frequency sweep was carried out in triplicate to ensure the measured moduli was sample preparation independent. The average moduli obtained was as follows: G' – 63075.6 ± 34272.5 Pa, G'' – 7636.0 ± 3983.0 Pa. The data from each amplitude sweep and the average frequency sweep is shown in **Fig A2.7**.

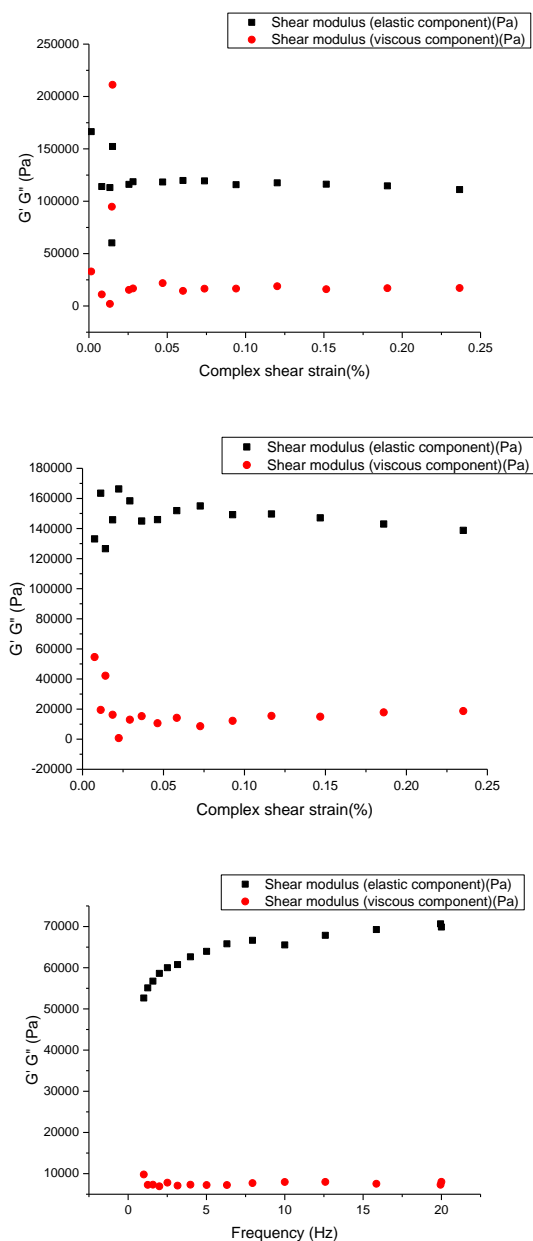


Fig A2.7: Rheological sweeps for P₁₁-4 + P₁₁-4-CS 64:1 molar ratio 230 mM Na⁺. A) Amplitude sweep 0.01 – 100% shear strain at 1Hz B) Amplitude sweep 0.01 – 100% shear strain at 20Hz C) Frequency sweep 1-20Hz at 0.23% shear strain – all at 37°C.

130 mM Na⁺ buffer 32:1 P₁₁-4: P₁₁-4-CS

The two amplitude sweeps indicated the LVER laid between 0.05 – 0.3% shear strains, where 0.27% shear strain was selected at which to carry out the frequency sweep at. The frequency sweep was carried out in triplicate to ensure the measured moduli was sample preparation independent. The average moduli obtained was as follows: G' – 277475.6 ± 8105.0 Pa, G'' – 36057.8 ± 3189.8 Pa. The data from each amplitude sweep and the average frequency sweep is shown in **Fig A2.8**.

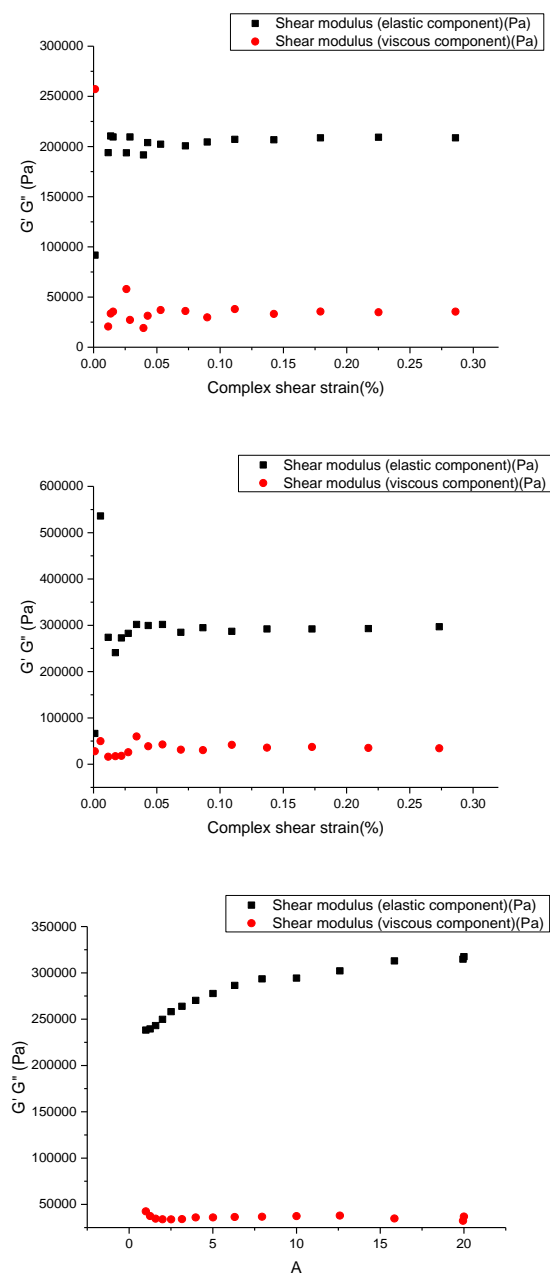


Fig A2.8: Rheological sweeps for P₁₁-4 + P₁₁-4-CS 32:1 molar ratio 130 mM Na⁺. A) Amplitude sweep 0.01 – 100% shear strain at 1Hz B) Amplitude sweep 0.01 – 100% shear strain at 20Hz C) Frequency sweep 1-20Hz at 0.27% shear strain – all at 37°C.

130 mM Na⁺ buffer 64:1 P₁₁-4: P₁₁-4-CS

The two amplitude sweeps indicated the LVER laid between 0.05 – 0.2% shear strains, where 0.15% shear strain was selected at which to carry out the frequency sweep at. The frequency sweep was carried out in triplicate to ensure the measured moduli was sample preparation independent. The average moduli obtained was as follows: G' – 95031.8 ± 44844.4 Pa, G'' – 12235.9 ± 5083.4 Pa. The data from each amplitude sweep and the average frequency sweep is shown in **Fig A2.9**.

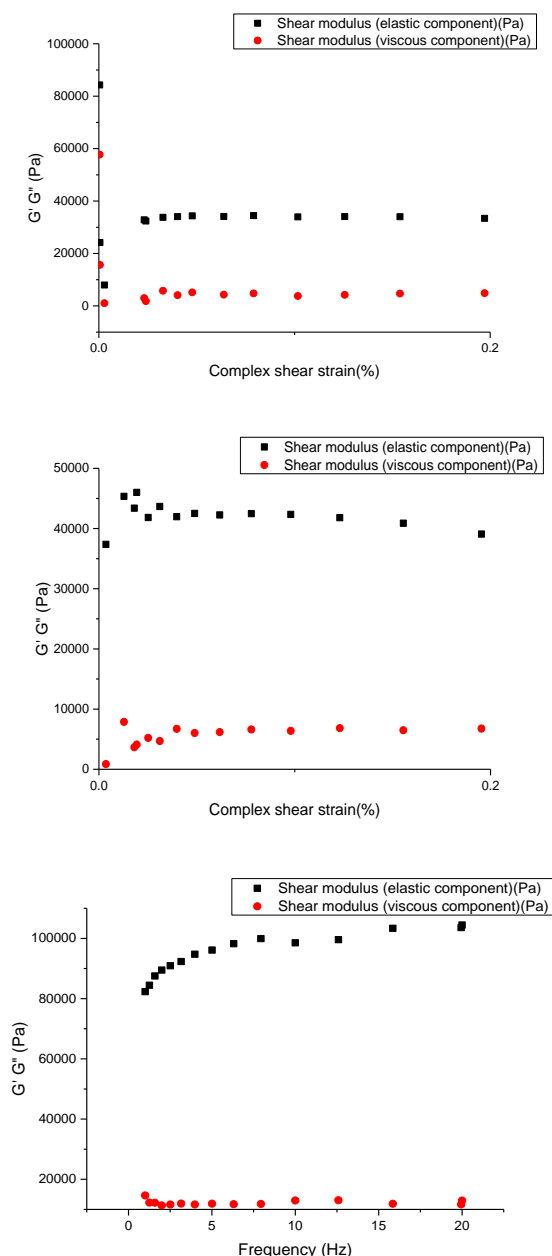


Fig A2.9: Rheological sweeps for P₁₁-4 + P₁₁-4-CS 64:1 molar ratio 130 mM Na⁺. A) Amplitude sweep 0.01 – 100% shear strain at 1Hz B) Amplitude sweep 0.01 – 100% shear strain at 20Hz C) Frequency sweep 1-20Hz at 0.15% shear strain – all at 37°C.

130 mM Na⁺ buffer P₁₁-4 30 mg ml⁻¹

The two amplitude sweeps indicated the LVER laid between 0.05 – 0.3% shear strains, where 0.27% shear strain was selected at which to carry out the frequency sweep at. The frequency sweep was carried out in triplicate to ensure the measured moduli was sample preparation independent. The average moduli obtained was as follows: $G' - 143447.5 \pm 21984.0$ Pa, $G'' - 20576.4 \pm 2857.9$ Pa. The data from each amplitude sweep and the average frequency sweep is shown in **Fig A2.10**.

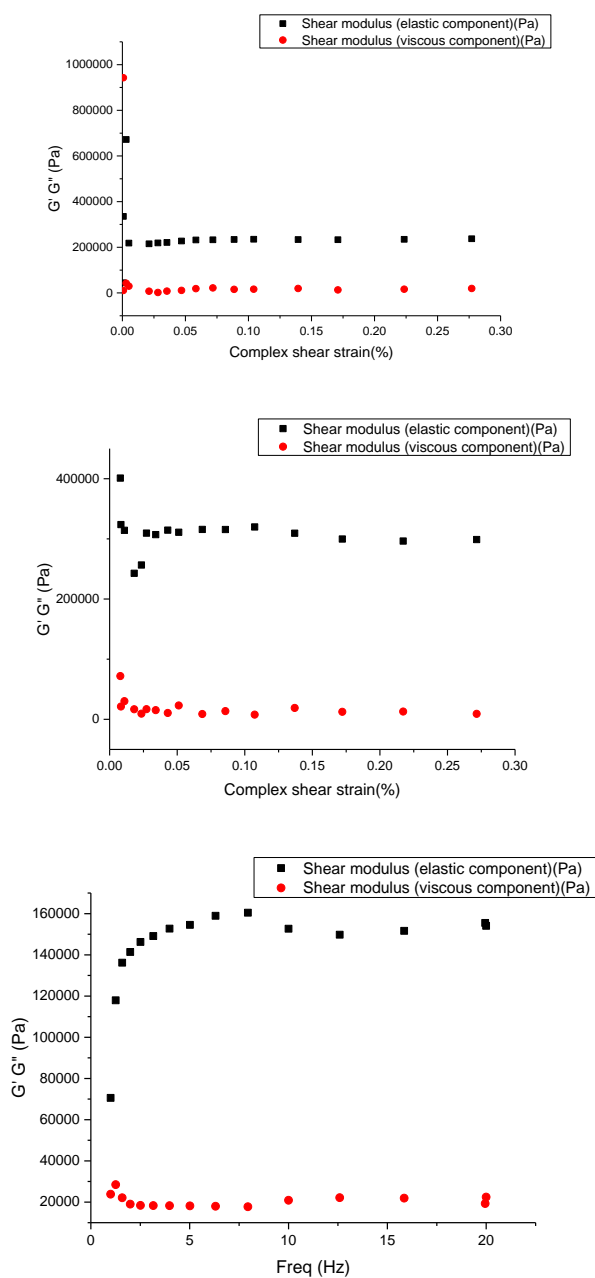


Fig A2.10: Rheological sweeps for P₁₁-4 130 mM Na⁺ at 30 mg ml⁻¹. A) Amplitude sweep 0.01 – 100% shear strain at 1Hz B) Amplitude sweep 0.01 – 100% shear strain at 20Hz C) Frequency sweep 1-20Hz at 0.27% shear strain – all at 37°C.

130 mM Na⁺ buffer P₁₁-4 + CS 30 mg ml⁻¹

The two amplitude sweeps indicated the LVER laid between 0.05 – 0.3% shear strains, where 0.28% shear strain was selected at which to carry out the frequency sweep at. The frequency sweep was carried out in triplicate to ensure the measured moduli was sample preparation independent. The average moduli obtained was as follows: $G' - 207008.9 \pm 13692.5$ Pa, $G'' - 20181.8 \pm 2161.4$ Pa. The data from each amplitude sweep and the average frequency sweep is shown in **Fig A2.11**.

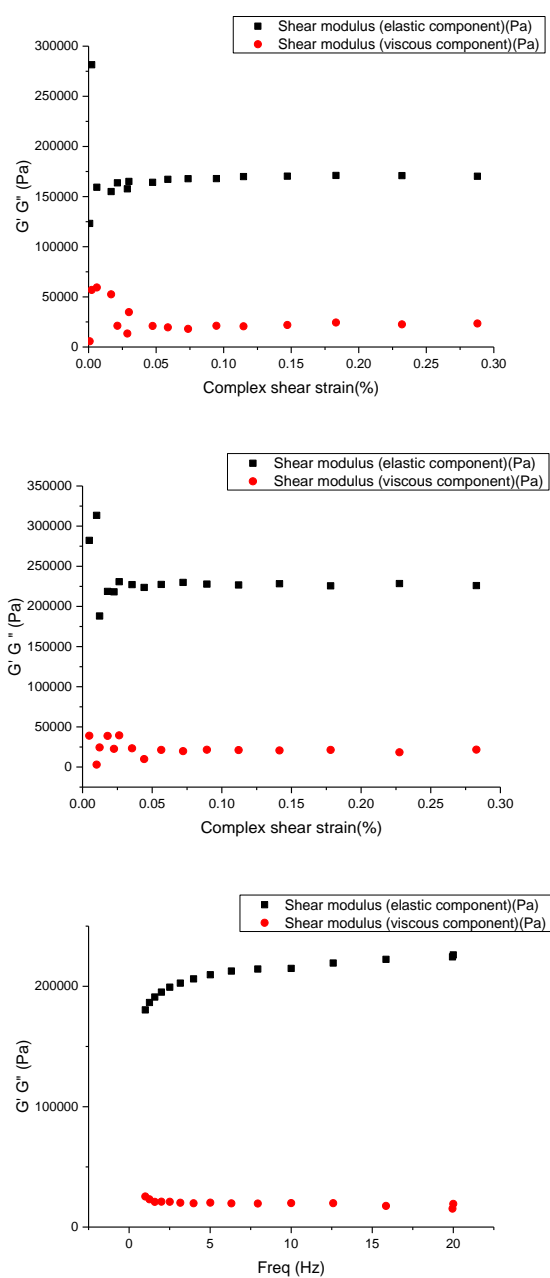


Fig A2.11: Rheological sweeps for P₁₁-4 + CS 32:1 molar ratio 130 mM Na⁺ at 30 mg ml⁻¹. A) Amplitude sweep 0.01 – 100% shear strain at 1Hz B) Amplitude sweep 0.01 – 100% shear strain at 20Hz C) Frequency sweep 1-20Hz at 0.28% shear strain – all at 37°C.

130 mM Na⁺ buffer P₁₁-4 + P₁₁-4-CS 32:1 30 mg ml⁻¹

The two amplitude sweeps indicated the LVER laid between 0.05 – 0.35% shear strains, where 0.31% shear strain was selected at which to carry out the frequency sweep at. The frequency sweep was carried out in triplicate to ensure the measured moduli was sample preparation independent. The average moduli obtained was as follows: $G' - 434555.9 \pm 51345.0$ Pa, $G'' - 58665.7 \pm 10214.6$ Pa. The data from each amplitude sweep and the average frequency sweep is shown in **Fig A2.12**.

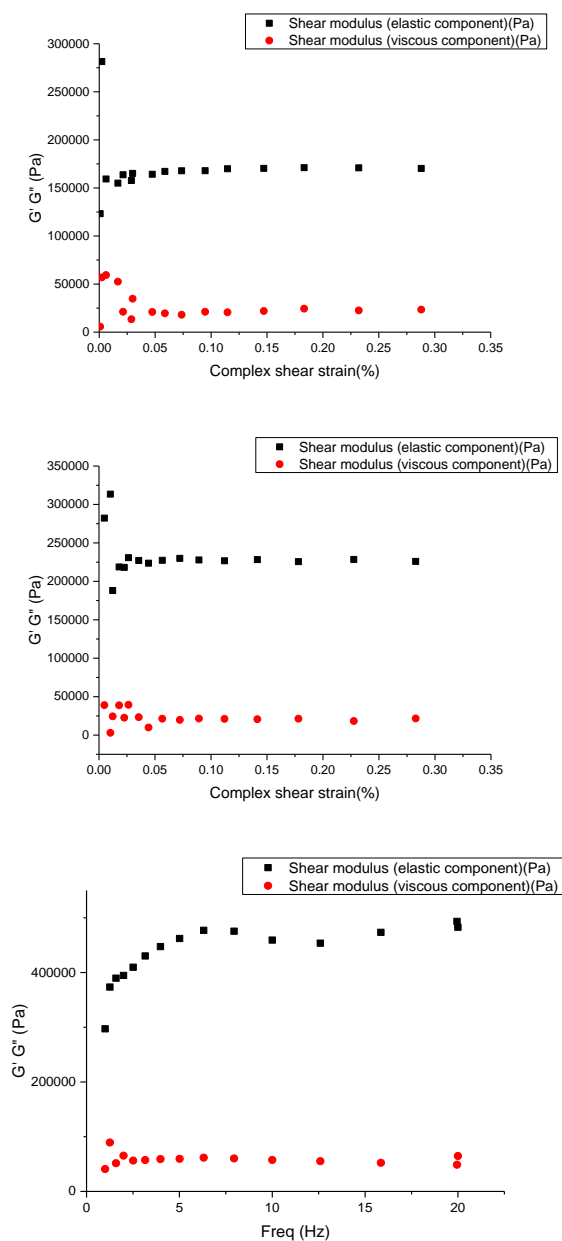


Fig A2.12: Rheological sweeps for P₁₁-4 + P₁₁-4-CS 32:1 molar ratio 130 mM Na⁺ at 30 mg ml⁻¹. A) Amplitude sweep 0.01 – 100% shear strain at 1Hz B) Amplitude sweep 0.01 – 100% shear strain at 20Hz C) Frequency sweep 1-20Hz at 0.31% shear strain – all at 37°C.

P₁₁-8 only

230 mM Na⁺ buffer

The two amplitude sweeps indicated the LVER laid between 0.05 – 0.2% shear strains, where 0.15% shear strain was selected at which to carry out the frequency sweep at. The frequency sweep was carried out in triplicate to ensure the measured moduli was sample preparation independent. The average moduli obtained was as follows: $G' - 25161.6 \pm 7358.7$ Pa, $G'' - 2041.7 \pm 670.5$ Pa. The data from each amplitude sweep and the average frequency sweep is shown in **Fig A2.13**.

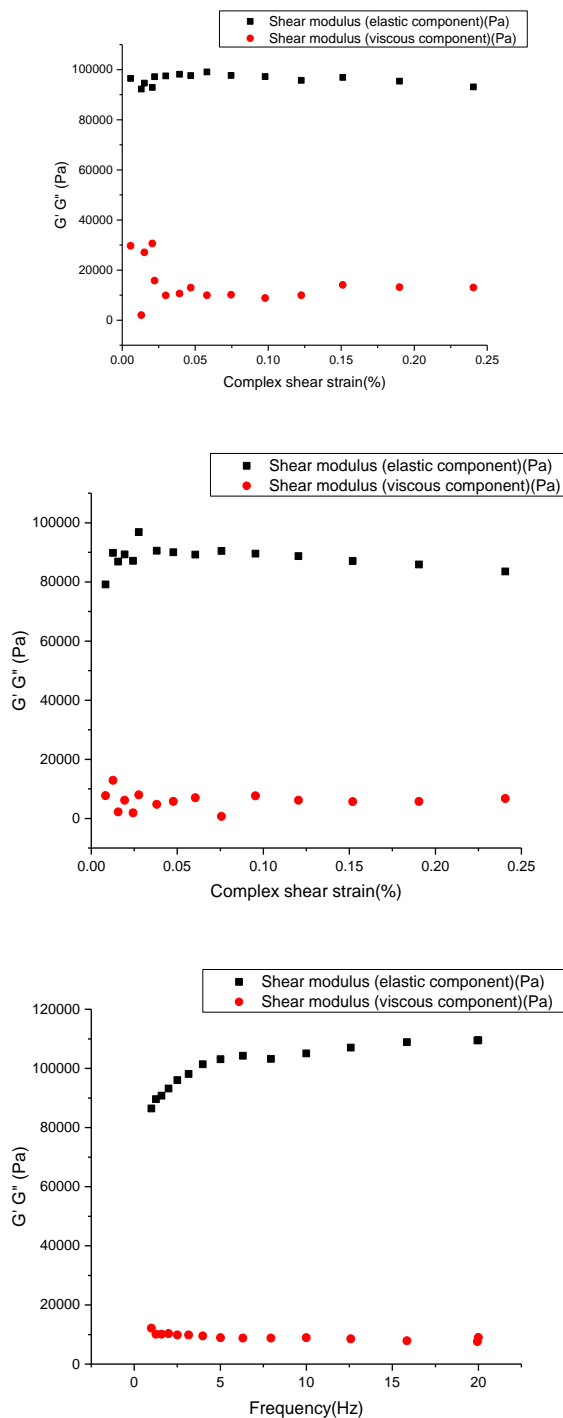


Fig A2.13: Rheological sweeps for P₁₁₋₈ 230 mM Na⁺. A) Amplitude sweep 0.01 – 100% shear strain at 1Hz B) Amplitude sweep 0.01 – 100% shear strain at 20Hz C) Frequency sweep 1-20Hz at 0.15% shear strain – all at 37°C.

130 mM Na⁺ buffer

The two amplitude sweeps indicated the LVER laid between 0.05 – 0.2% shear strains, where 0.1% shear strain was selected at which to carry out the frequency sweep at. The frequency sweep was carried out in triplicate to ensure the measured moduli was sample preparation independent. The average moduli obtained was as follows: $G' - 15443.1 \pm 3104.3$ Pa, $G'' - 1431.4$

± 330.1 Pa. The data from each amplitude sweep and the average frequency sweep is shown in Fig A2.14.

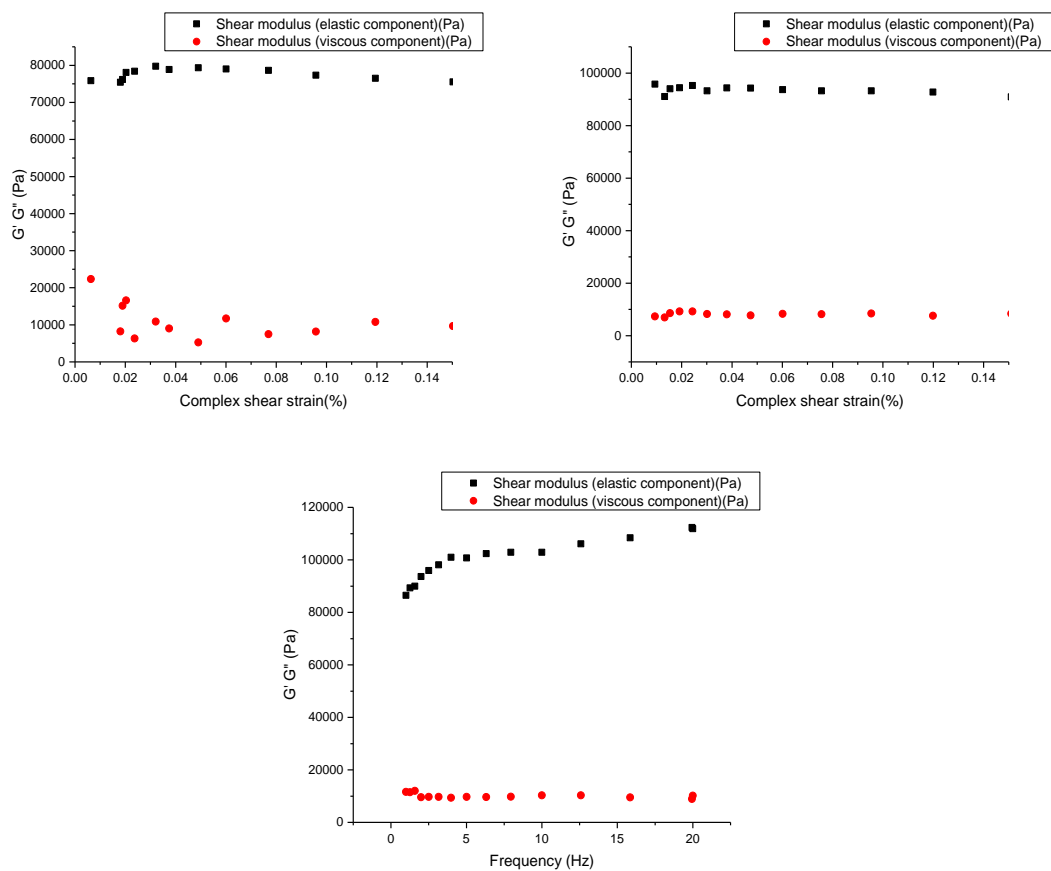


Fig A2.14: Rheological sweeps for P_{11-8} 130 mM Na^+ . A) Amplitude sweep 0.01 – 100% shear strain at 1Hz B) Amplitude sweep 0.01 – 100% shear strain at 20Hz C) Frequency sweep 1-20Hz at 0.1% shear strain – all at 37°C.

$P_{11-8} + CS$

230 mM Na^+ buffer 32:1 P_{11-8} : CS

The two amplitude sweeps indicated the LVER laid between 0.05 – 0.35% shear strains, where 0.3% shear strain was selected at which to carry out the frequency sweep at. The frequency sweep was carried out in triplicate to ensure the measured moduli was sample preparation independent. The average moduli obtained was as follows: $G' - 19198.3 \pm 627.7$ Pa, $G'' - 1770.0 \pm 212.2$ Pa. The data from each amplitude sweep and the average frequency sweep is shown in Fig A2.15.

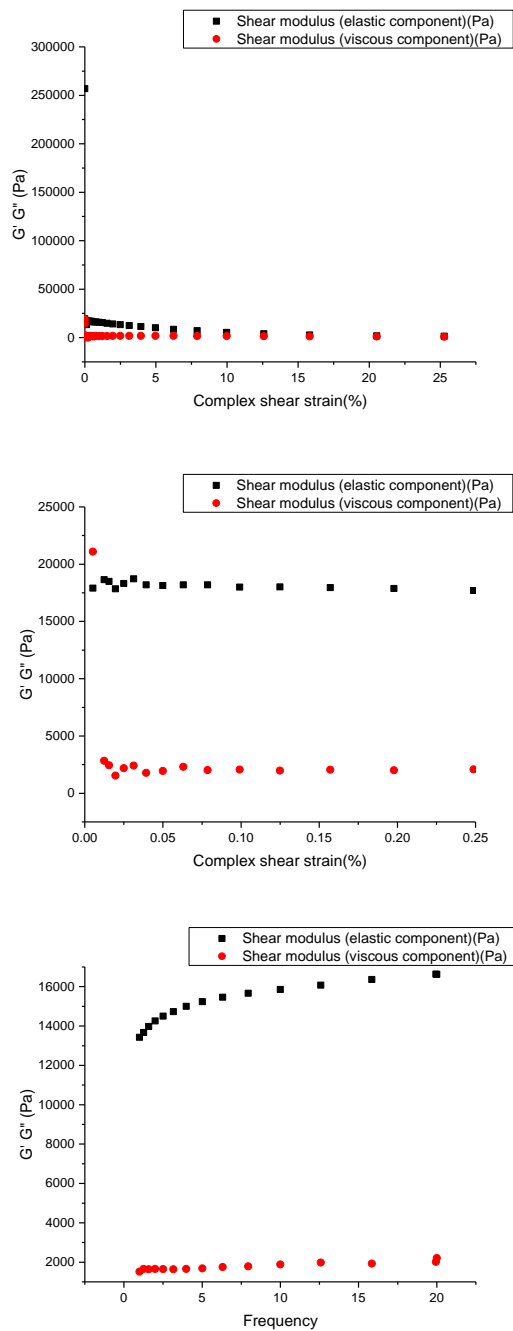


Fig A2.15: Rheological sweeps for P₁₁-8 + CS 32:1 molar ratio 230 mM Na⁺. A) Amplitude sweep 0.01 – 100% shear strain at 1Hz B) Amplitude sweep 0.01 – 100% shear strain at 20Hz C) Frequency sweep 1-20Hz at 0.3% shear strain – all at 37°C.

230 mM Na⁺ buffer 64:1 P₁₁-8: CS

The two amplitude sweeps indicated the LVER laid between 0.05 – 0.35% shear strains, where 0.3% shear strain was selected at which to carry out the frequency sweep at. The frequency sweep was carried out in triplicate to ensure the measured moduli was sample preparation independent. The average moduli obtained was as follows: $G' = 7343.2 \pm 1756.9$ Pa, $G'' = 862.5$

± 220.3 Pa. The data from each amplitude sweep and the average frequency sweep is shown in Fig A2.16.

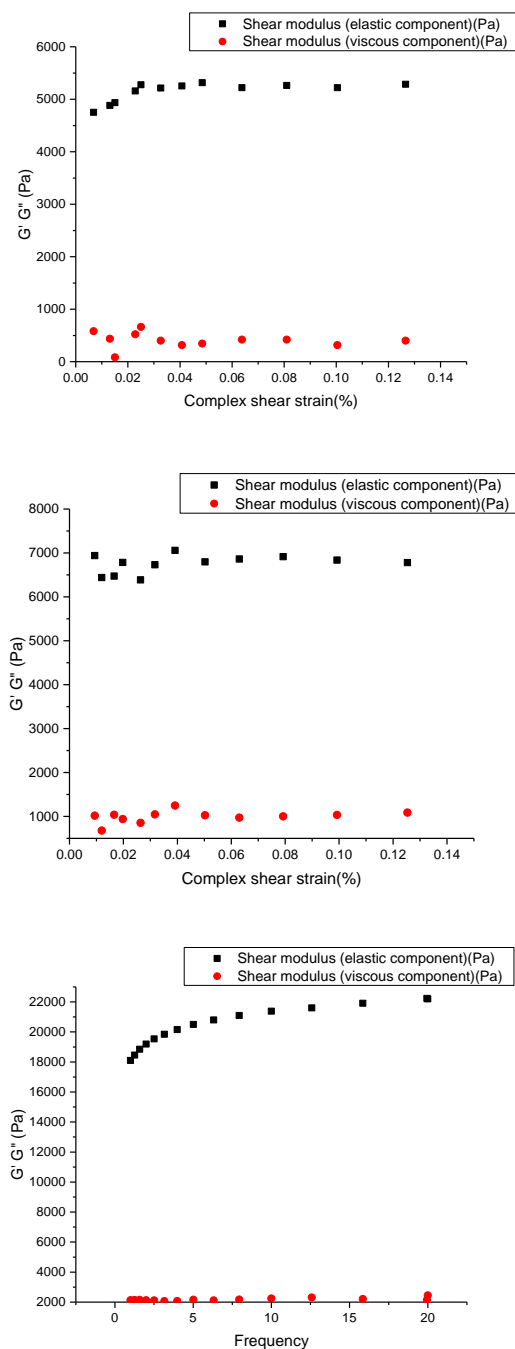


Fig A2.17: Rheological sweeps for P₁₁₋₈ + CS 64:1 molar ratio 230 mM Na⁺. A) Amplitude sweep 0.01 – 100% shear strain at 1Hz B) Amplitude sweep 0.01 – 100% shear strain at 20Hz C) Frequency sweep 1-20Hz at 0.3% shear strain – all at 37°C.

130 mM Na⁺ buffer 32:1 P₁₁₋₈: CS

The two amplitude sweeps indicated the LVER laid between 0.05 – 0.35% shear strains, where 0.3% shear strain was selected at which to carry out the frequency sweep at. The frequency

sweep was carried out in triplicate to ensure the measured moduli was sample preparation independent. The average moduli obtained was as follows: $G' - 11579.8 \pm 6312.3$ Pa, $G'' - 1843.3 \pm 977.7$ Pa. The data from each amplitude sweep and the average frequency sweep is shown in **Fig A2.18**.

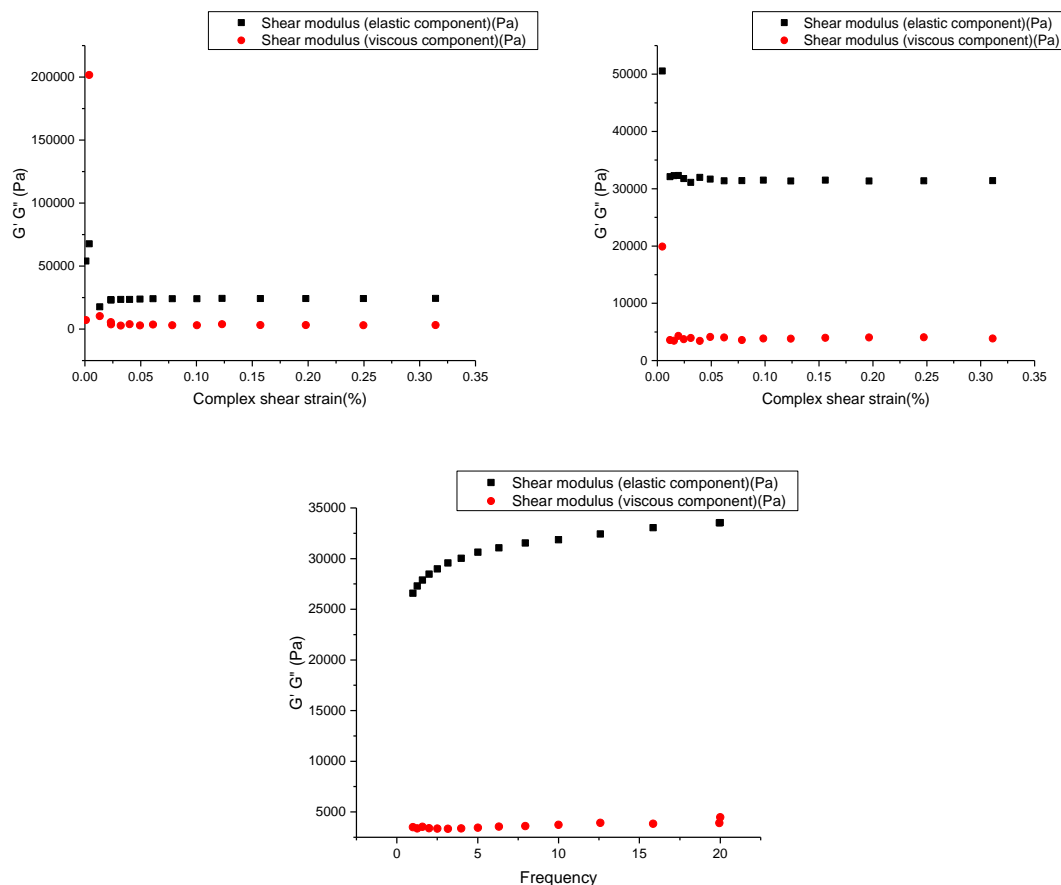


Fig A2.18: Rheological sweeps for $P_{11-8} + CS$ 32:1 molar ratio 130 mM Na^+ . A) Amplitude sweep 0.01 – 100% shear strain at 1Hz B) Amplitude sweep 0.01 – 100% shear strain at 20Hz C) Frequency sweep 1-20Hz at 0.3% shear strain – all at 37°C.

130 mM Na^+ buffer 64:1 P_{11-8} : CS

The two amplitude sweeps indicated the LVER laid between 0.05 – 0.35% shear strains, where 0.3% shear strain was selected at which to carry out the frequency sweep at. The frequency sweep was carried out in triplicate to ensure the measured moduli was sample preparation independent. The average moduli obtained was as follows: $G' - 5952.3 \pm 3816.2$ Pa, $G'' - 707.5 \pm 289.3$ Pa. The data from each amplitude sweep and the average frequency sweep is shown in **Fig A2.19**.

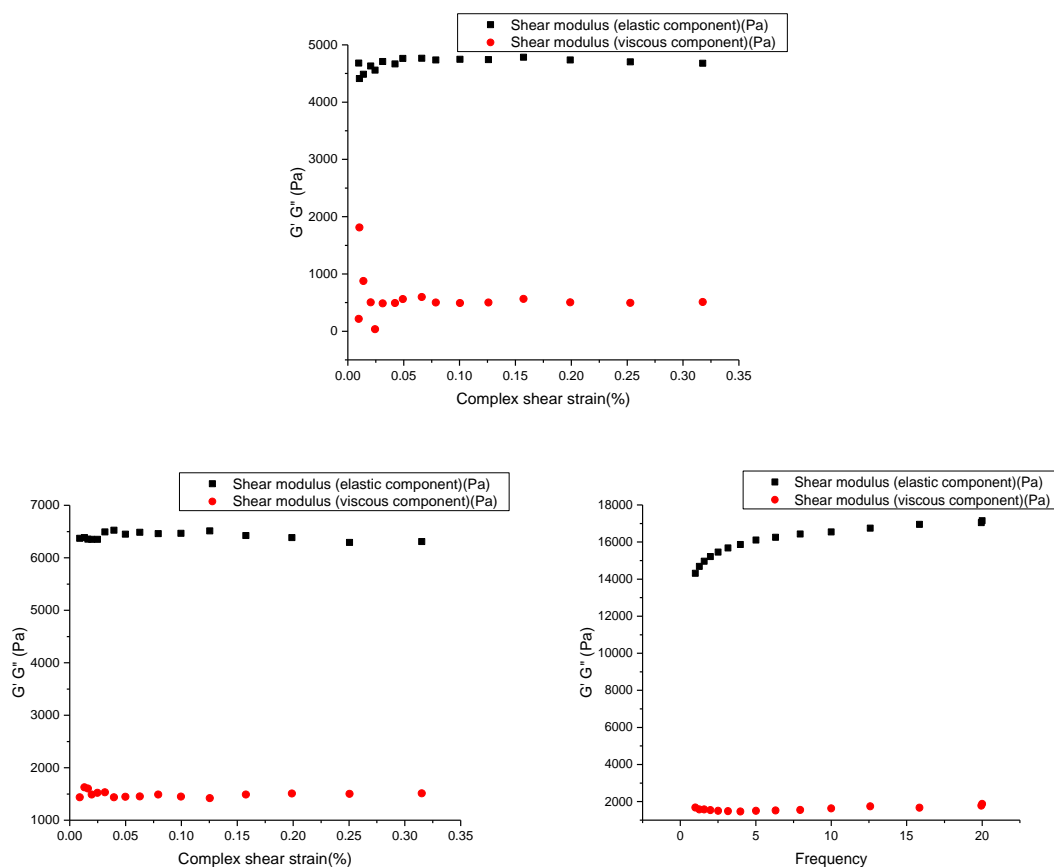


Fig A2.19: Rheological sweeps for P₁₁-8 + CS 64:1 molar ratio 130 mM Na⁺. A) Amplitude sweep 0.01 – 100% shear strain at 1Hz B) Amplitude sweep 0.01 – 100% shear strain at 20Hz C) Frequency sweep 1-20Hz at 0.15% shear strain – all at 37°C.

P₁₁-8 + P₁₁-8-CS

230 mM Na⁺ buffer 32:1 P₁₁-8: P₁₁-8-CS

The two amplitude sweeps indicated the LVER laid between 0.05 – 0.25% shear strains, where 0.22% shear strain was selected at which to carry out the frequency sweep at. The frequency sweep was carried out in triplicate to ensure the measured moduli was sample preparation independent. The average moduli obtained was as follows: $G' - 234824.4 \pm 12606.0$ Pa, $G'' - 25902.4 \pm 3046.1$ Pa. The data from each amplitude sweep and the average frequency sweep is shown in **Fig A2.20**.

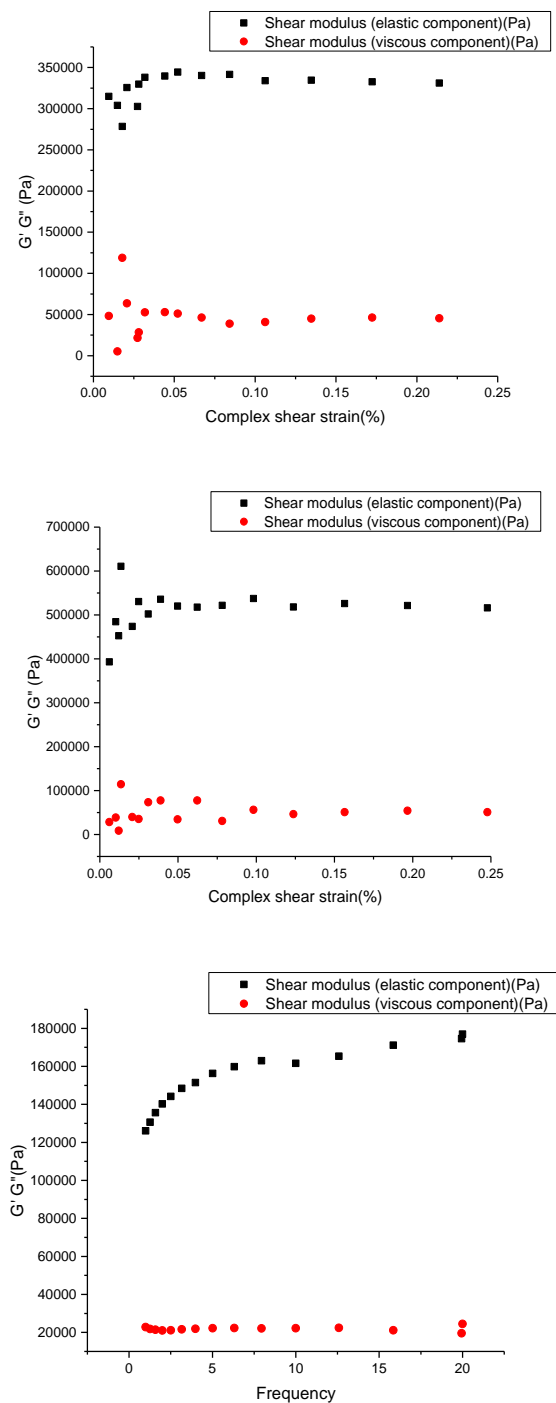


Fig A2.20: Rheological sweeps for P₁₁-8 + P₁₁-8-CS 32:1 molar ratio 230 mM Na⁺. A) Amplitude sweep 0.01 – 100% shear strain at 1Hz B) Amplitude sweep 0.01 – 100% shear strain at 20Hz C) Frequency sweep 1-20Hz at 0.22% shear strain – all at 37°C.

230 mM Na⁺ buffer 64:1 P₁₁-8: P₁₁-8-CS

The two amplitude sweeps indicated the LVER laid between 0.05 – 0.3% shear strains, where 0.25% shear strain was selected at which to carry out the frequency sweep at. The frequency sweep was carried out in triplicate to ensure the measured moduli was sample preparation

independent. The average moduli obtained was as follows: G' – 63075.6 ± 34272.5 Pa, G'' – 7636.0 ± 3983.0 Pa. The data from each amplitude sweep and the average frequency sweep is shown in **Fig A2.21**.

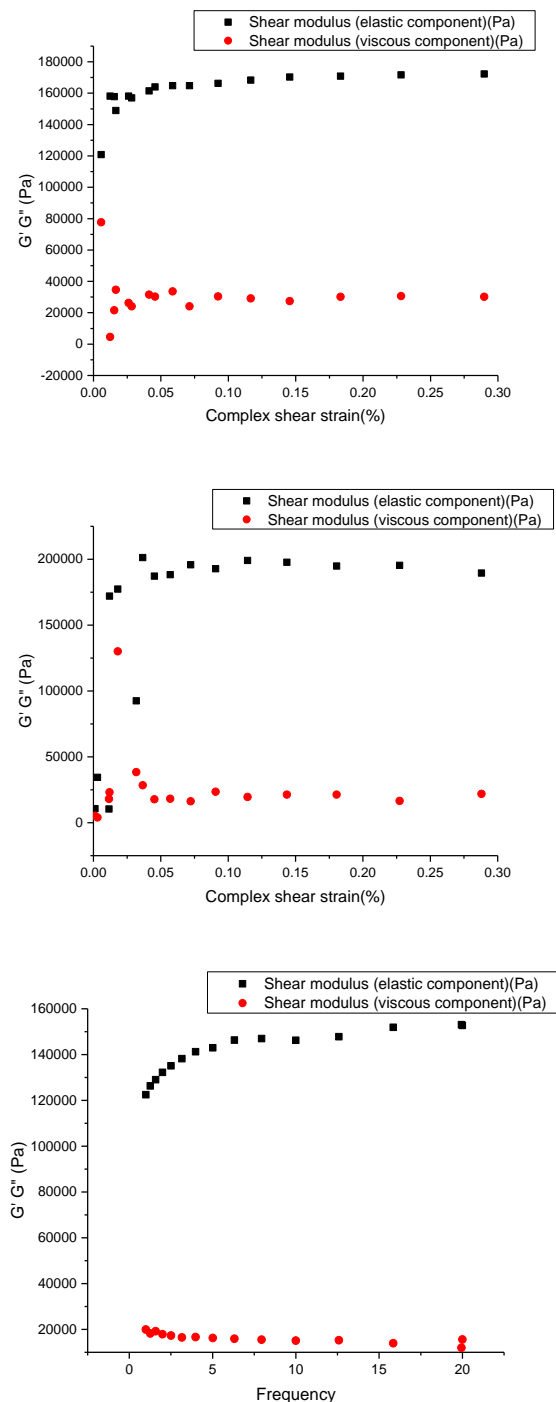


Fig A2.21: Rheological sweeps for P₁₁-8 + P₁₁-8-CS 64:1 molar ratio 230 mM Na⁺. A) Amplitude sweep 0.01 – 100% shear strain at 1Hz B) Amplitude sweep 0.01 – 100% shear strain at 20Hz C) Frequency sweep 1-20Hz at 0.25% shear strain – all at 37°C.

130 mM Na⁺ buffer 32:1 P₁₁-8: P₁₁-8-CS

The two amplitude sweeps indicated the LVER laid between 0.05 – 0.3% shear strains, where 0.24% shear strain was selected at which to carry out the frequency sweep at. The frequency sweep was carried out in triplicate to ensure the measured moduli was sample preparation independent. The average moduli obtained was as follows: G' – 277475.6 ± 8105.0 Pa, G'' – 36057.8 ± 3189.8 Pa. The data from each amplitude sweep and the average frequency sweep is shown in **Fig A2.22**.

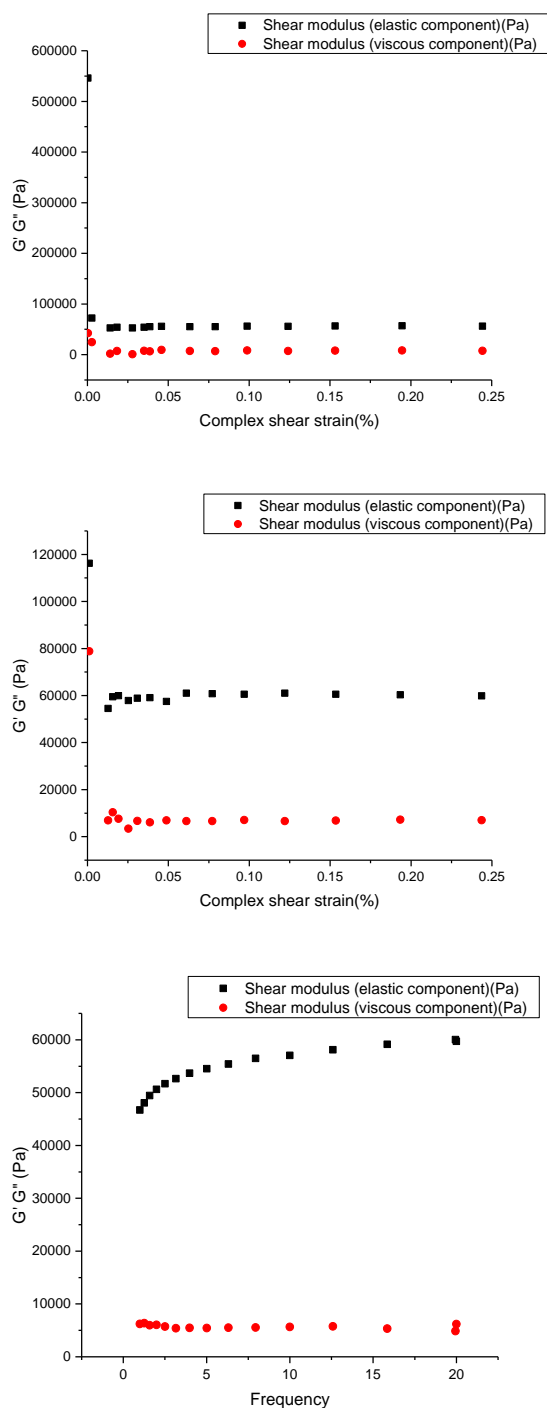


Fig A2.22: Rheological sweeps for P₁₁-8 + P₁₁-8-CS 32:1 molar ratio 130 mM Na⁺. A) Amplitude sweep 0.01 – 100% shear strain at 1Hz B) Amplitude sweep 0.01 – 100% shear strain at 20Hz C) Frequency sweep 1-20Hz at 0.24% shear strain – all at 37°C.

130 mM Na⁺ buffer 64:1 P₁₁-8: P₁₁-8-CS

The two amplitude sweeps indicated the LVER laid between 0.05 – 0.3% shear strains, where 0.24% shear strain was selected at which to carry out the frequency sweep at. The frequency sweep was carried out in triplicate to ensure the measured moduli was sample preparation independent. The average moduli obtained was as follows: G' – 95031.8 ± 44844.4 Pa, G'' – 12235.9 ± 5083.4 Pa. The data from each amplitude sweep and the average frequency sweep is shown in **Fig A2.23**.

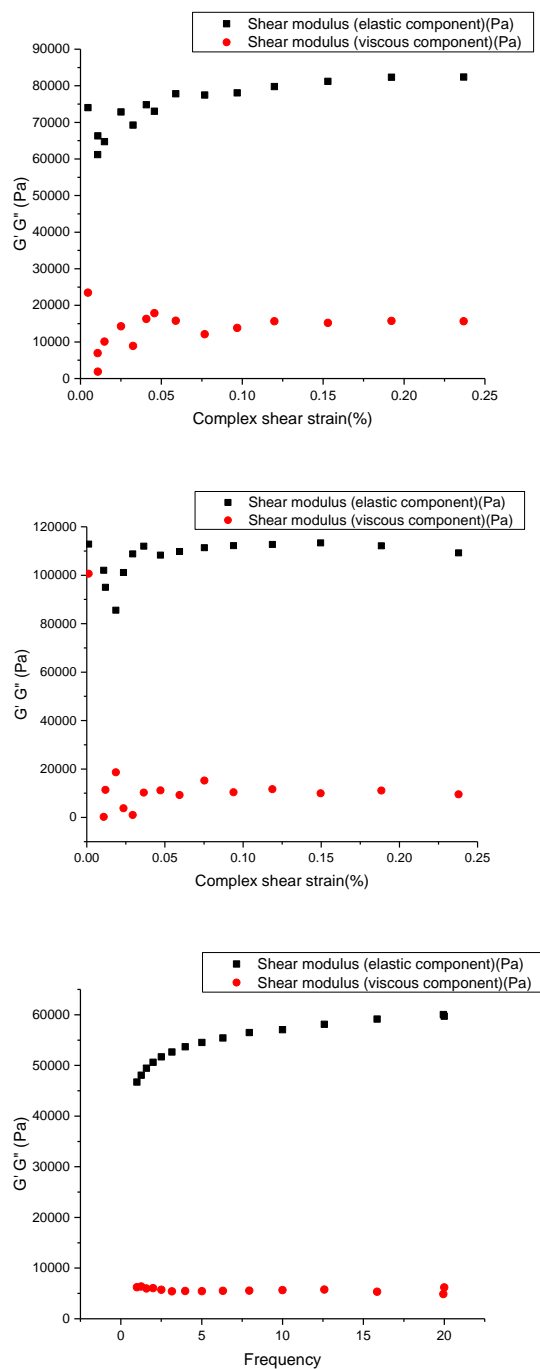


Fig A2.23: Rheological sweeps for P₁₁-8 + P₁₁-8-CS 64:1 molar ratio 130 mM Na⁺. A) Amplitude sweep 0.01 – 100% shear strain at 1Hz B) Amplitude sweep 0.01 – 100% shear strain at 20Hz C) Frequency sweep 1-20Hz at 0.24% shear strain – all at 37°C.

P₁₁-8 130 mM 30 mg ml⁻¹

The two amplitude sweeps indicated the LVER laid between 0.05 – 0.35% shear strains, where 0.3% shear strain was selected at which to carry out the frequency sweep at. The frequency sweep was carried out in triplicate to ensure the measured moduli was sample preparation independent. The average moduli obtained was as follows: $G' - 205046.7 \pm 14572.2$ Pa, $G'' -$

23325.1 \pm 1099.5 Pa. The data from each amplitude sweep and the average frequency sweep is shown in **Fig A2.24**.

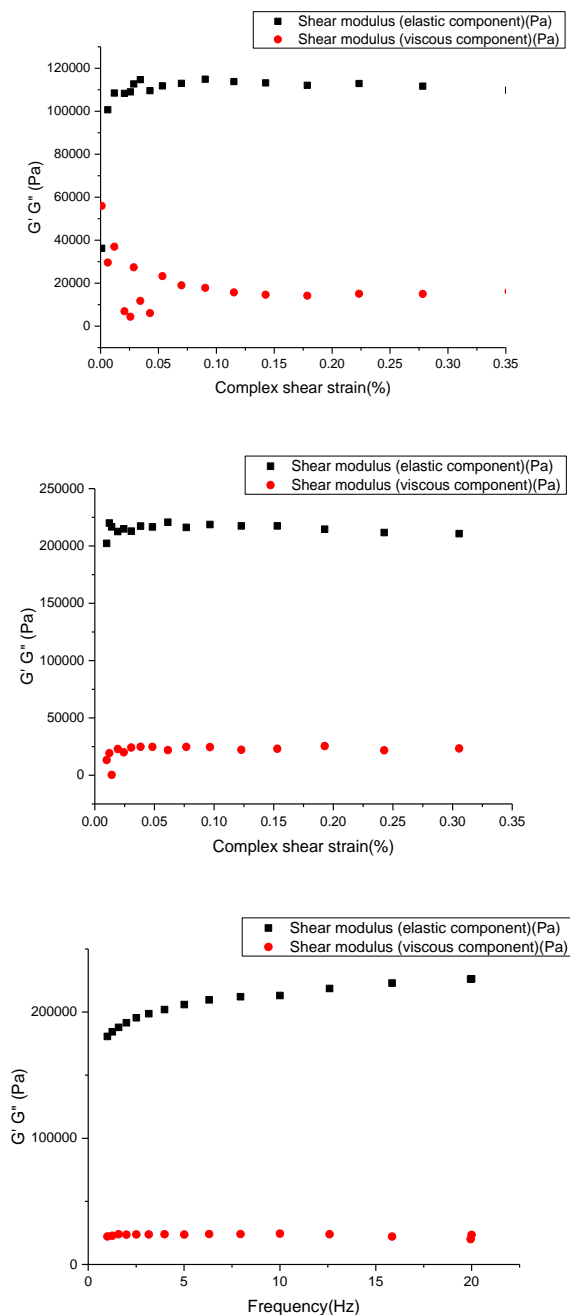


Fig A2.24: Rheological sweeps for P₁₁₋₈ 130 mM Na⁺ 30 mg ml⁻¹. A) Amplitude sweep 0.01 – 100% shear strain at 1Hz B) Amplitude sweep 0.01 – 100% shear strain at 20Hz C) Frequency sweep 1-20Hz at 0.3% shear strain – all at 37°C.

P₁₁₋₈ + CS 130 mM 30 mg ml⁻¹

The two amplitude sweeps indicated the LVER laid between 0.05 – 0.4% shear strains, where 0.35% shear strain was selected at which to carry out the frequency sweep at. The frequency sweep was carried out in triplicate to ensure the measured moduli was sample preparation

independent. The average moduli obtained was as follows: $G' - 207813.3 \pm 19964.5$ Pa, $G'' - 31477.3 \pm 2257.0$ Pa. The data from each amplitude sweep and the average frequency sweep is shown in **Fig A2.25**.

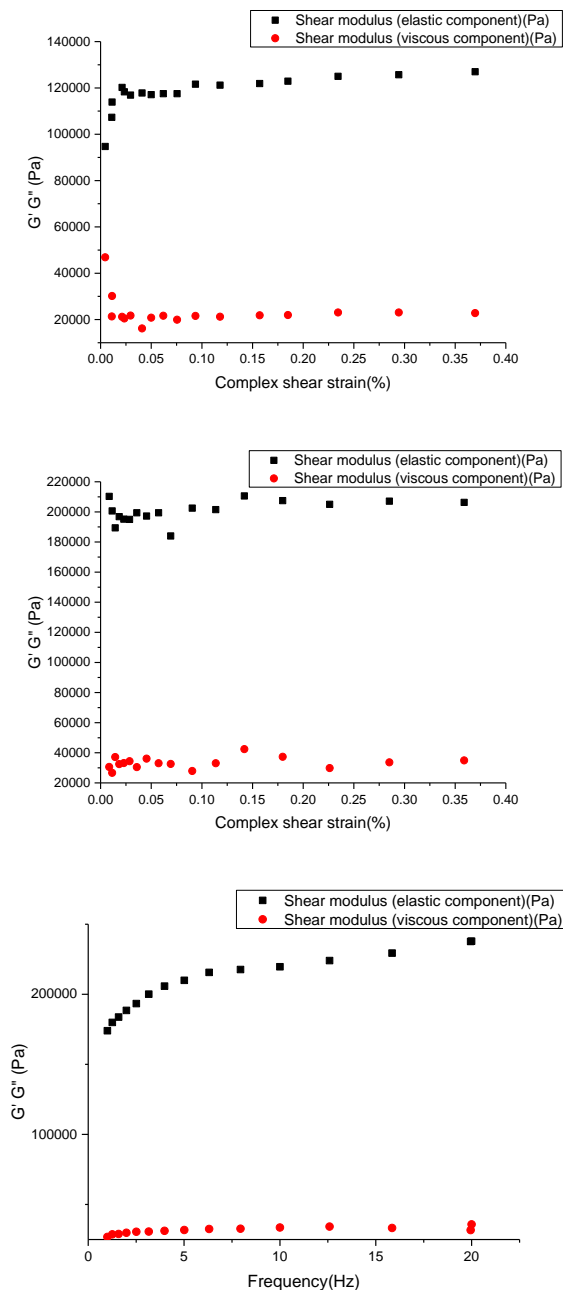


Fig A2.25: Rheological sweeps for $P_{11-8} + CS$ 32:1 molar ratio 130 mM Na^+ at 30 mg ml^{-1} . A) Amplitude sweep 0.01 – 100% shear strain at 1Hz B) Amplitude sweep 0.01 – 100% shear strain at 20Hz C) Frequency sweep 1-20Hz at 0.35% shear strain – all at 37°C .

$P_{11-8} + P_{11-8-}CS$ 130 mM 30 mg ml^{-1}

The two amplitude sweeps indicated the LVER laid between 0.05 – 0.35% shear strains, where 0.3% shear strain was selected at which to carry out the frequency sweep at. The frequency

sweep was carried out in triplicate to ensure the measured moduli was sample preparation independent. The average moduli obtained was as follows: G' – 101644.4 ± 8543.0 Pa, G'' – 13542.7 ± 953.3 Pa. The data from each amplitude sweep and the average frequency sweep is shown in **Fig A2.26**.

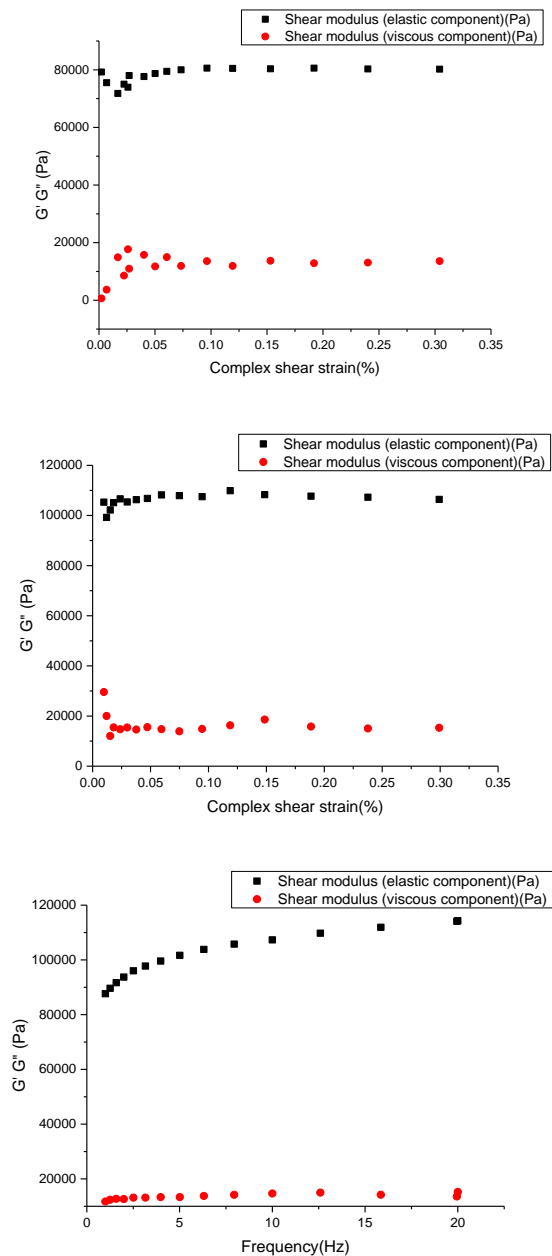


Fig A2.26: Rheological sweeps for $P_{11-8} + P_{11-8-CS}$ 32:1 molar ratio 130 mM Na^+ at 30 mg ml^{-1} . A) Amplitude sweep 0.01 – 100% shear strain at 1Hz B) Amplitude sweep 0.01 – 100% shear strain at 20Hz C) Frequency sweep 1-20Hz at 0.3% shear strain – all at 37